Signatures of Majorana bound states in one-dimensional topological superconductors

Im Fachbereich Physik

der Freien Universität Berlin

eingereichte

Dissertation

von

Falko Pientka

Berlin, im August 2014

Erstgutachter:	Felix von Oppen
Zweitgutachter:	Piet Brouwer
Disputationstermin:	3. November 2014

Selbstständigkeitserklärung

Hiermit versichere ich, dass ich in meiner Dissertation alle Hilfsmittel und Hilfen angegeben habe, und auf dieser Grundlage die Arbeit selbstständig verfasst habe. Diese Arbeit habe ich nicht schon einmal in einem früheren Promotionsverfahren eingereicht.

Berlin, 14. August 2014

Zusammenfassung

Topologische Phasen in kondensierter Materie faszinieren Physiker seit mehr als drei Jahrzehnten. Die beispiellose Quantisierung der Leitfähigkeit durch den Quanten-Hall-Effekt oder die vielbeachteten Dirac-Randzustände in topologischen Isolatoren gehen auf topologische Eigenschaften zurück. Seit kurzem sind neuartige topologische Phasen in Supraleitern im Fokus intensiver experimenteller und theoretischer Forschung. Von besonderem Interesse sind eindimensionale topologische Supraleiter, da hier exotische Majoranateilchen als Randzustände auftreten. Dabei handelt es sich um gebundene Zustände verschwindender Energie mit nichtabelscher Vertauschungsstatistik, die vielversprechende Anwendungen in der Quanteninformationsverarbeitung ermöglicht.

Durch jüngste theoretische und experimentelle Fortschritte erscheint die Realisierung von Majoranazuständen im Labor möglich. Das Ziel dieser Arbeit ist einerseits eine realistische theoretische Beschreibung aktueller experimenteller Bemühungen. Andererseits schlagen wir neue Versuchsaufbaue mit charakteristischen Signaturen von Majoranateilchen vor. Ein besonderer Fokus liegt hierbei auf nicht idealen experimentellen Bedingungen und neuen Effekten, die daraus entstehen.

Signaturen von Majoranateilchen können im Josephsonstrom zwischen zwei topologischen Supraleitern auftreten, obgleich diese Signaturen im DC-Josephson-Effekt meist durch unvermeidbare Quasiteilchenrelaxationen im Supraleiter vernichtet werden. In dieser Arbeit entwerfen wir einen Messaufbau basierend auf mesoskopischen supraleitenden Ringen, in dem die Majorana-Signaturen selbst für beliebig schnelle Relaxation erhalten bleiben. In einem weiteren Projekt beschreiben wir eine alternative Methode zum Nachweis von Majoranas im Rahmen des Josephson-Effekts. Dabei werden Supraströme nicht durch eine Phasendifferenz der Supraleiter induziert, sondern durch gegeneinander verdrehte Magnetfelder auf den zwei Seiten des Josephsonkontakts.

Eine weitere wichtige Nachweismöglichkeit für Majoranas im Experiment liefert die Messung des differentiellen Leitwerts. Wir zeigen, dass der für Majoranateilchen charakteristische Peak im Leitwert kleiner ausfällt, wenn in dem topologischen Supraleiterdraht mehrere Teilbänder besetzt sind. Dies bietet eine plausible Erklärung für jüngste experimentelle Ergebnisse. Darüber hinaus erläutern wir, wie geeignet plazierte Störstellen die Signatur verstärken und so einen überzeugenden Nachweis für Majoranas liefern können.

Ein aktueller Vorschlag für die Realisierung von Majoranateilchen basiert auf Ketten magnetischer Störstellen auf der Oberfläche von konventionellen Supraleitern. Dazu leiten wir ein mikroskopisches Modell her, das die Kette durch sogenannte Shibazustände beschreibt, die an die einzelnen Störstellen gebunden sind. Unter realistischen Bedingungen weist dieses Modell langreichweitige Kopplungen auf, welche einen neuartigen Phasenübergang und erstaunliche Lokalisierungseigenschaften der Majoranas zur Folge haben. Abschließend untersuchen wir die Tunnelspektroskopie von lokalisierten Zuständen in Supraleitern. Dazu entwickeln wir eine Theorie für den differentiellen Tunnelleitwert für eine supraleitende Tunnelspitze unter Berücksichtigung thermischer Relaxationsprozesse von Quasiteilchen im Supraleiter. Unsere Ergebnisse stimmen gut mit Messungen zu Shibazuständen überein und erlauben die Bestimmung zentraler Eigenschaften wie die lokale Zustandsdichte oder die Art der Relaxationsprozesse.

Abstract

Topological states of matter have fascinated condensed matter physicists for the past three decades. Famous examples include the integer and fractional quantum Hall states exhibiting a spectacular conductance quantization as well as topological insulators in two and three dimensions featuring gapless Dirac fermions at the boundary. Very recently, novel topological phases in superconductors have been subject of intense experimental and theoretical investigation. One-dimensional topological superconductors are particularly intriguing as they host exotic Majorana end states. These are zero-energy bound states with nonabelian exchange statistics potentially useful for topologically protected quantum computing.

Recent theoretical and experimental advances have put the realization of Majorana states within reach of current measurement techniques. In this thesis we investigate signatures of Majorana bound states in realistic experiments aiming to improve the theoretical understanding of ongoing experimental efforts and to design novel measurement schemes, which exhibit convincing signatures of Majoranas. In particular we account for nonideal experimental conditions which can lead to qualitatively new features.

Possible signatures of Majoranas can be accessed in the Josephson current through a weak link between two topological superconductors although the signatures in the dc Josephson effect are typically obscured by inevitable quasiparticle relaxation in the superconductor. Here we propose a measurement scheme in mesoscopic superconducting rings, where Majorana signatures persist even for infinitely fast relaxation. In a separate project we outline an alternative to the standard Josephson experiment in topological superconductors based on quantum wires. We delineate how Majoranas can be detected, when the Josephson current is induced by noncollinear magnetic fields applied to the two banks of the junction instead of a superconducting phase difference.

Another important experimental manifestation of Majoranas is a zero-bias peak in the differential conductance. Here we show that in multi-subband wires the Majorana conductance peak can be suppressed compared to a strictly one-dimensional system, thereby providing a plausible explanation for recent experimental results. Based on this analysis, we furthermore predict an enhancement of the signature by deliberately introducing disorder, which could establish strong evidence for a Majorana bound state.

A very recent proposal to realize a topological superconductor is based on a chain of magnetic impurities on the surface of a conventional superconductor. Here we derive a microscopic model in terms of the Shiba states bound to the individual impurities in the superconductor. Under realistic experimental conditions, the model involves long-range couplings leading to a new kind of topological phase transition and remarkable localization properties of the Majoranas. Finally, we investigate the tunneling spectroscopy of subgap states in superconductors. We develop a theory to describe the differential tunneling conductance from a superconducting tip into a localized quasiparticle state including relaxation processes present at nonzero temperature. Our result are in good agreement with experimental data on Shiba states and give access to properties of the bound state such as the local density of states and the nature of the relevant relaxation processes.

Contents

1. Introduction

In 2012 popular and scientific media celebrated the discovery of Majorana particles after a seven-decade-long chase [Wilc 09, Fran 10b, Ster 10, Hugh 11, Serv 11, Fran 13, Spei 12, Nest 13] when the group of L. Kouwenhoven in Delft reported signatures of Majorana particles in a superconductor–quantum wire hybrid device [Mour 12]. The existence of Majorana *fermions* is certainly among the major puzzles in particle physics. Already in 1937 Ettore Majorana had shown [Majo 37] that the Dirac equation, which describes fermions, allows for purely real solutions. As particles and antiparticles in Dirac's theory are related by complex conjugation, Majorana's fermion is described by real operators and must be identical to its own antiparticle. This initiated a long search for Majorana fermions in the zoo of elementary particles with neutrinos being the prime candidate, but no evidence has been found to date [Avig 08].

In contrast the interest in the condensed matter realization of emergent Majorana *quasiparticles* is much younger and of an entirely different background [Alic 12, Been 13, Elli 14]. The existence of Majorana quasiparticles has first been predicted in $\nu = 5/2$ fractional quantum Hall systems [Moor 91] and later in superfluid Helium-3 [Volo 99, Volo 03], while the Majoranas investigated in Delft are midgap excitations in superconductors whose theoretical discovery dates back little more than a decade [Read 00, Kita 01]. While the possibility of an *elementary* fermionic particle being its own antiparticle is of fundamental importance this concept is not unusual for *emergent* particles in many-body systems. In fact the ubiquitous Bogoliubov particles, the elementary excitations of superconductors, are their own antiparticle [Cham 10] and could be called Majorana fermions. In contrast the claimed signatures of the Delft experiment belong to a very different species, which we will refer to as Majorana bound states or Majorana zero modes. These particles are not fermions (although they are frequently referred to as such), which clearly distinguishes them from Majorana's original proposal.

In fact Majorana bound states are interesting to condensed matter physicists precisely because they are neither fermions nor bosons but nonabelian anyons. To illustrate the difference between these types of particles we consider a two-dimensional system with a degenerate ground state. While the exchange of two fermions or bosons leaves the ground state invariant up to a sign, exchanging nonabelian anyons effects a unitary

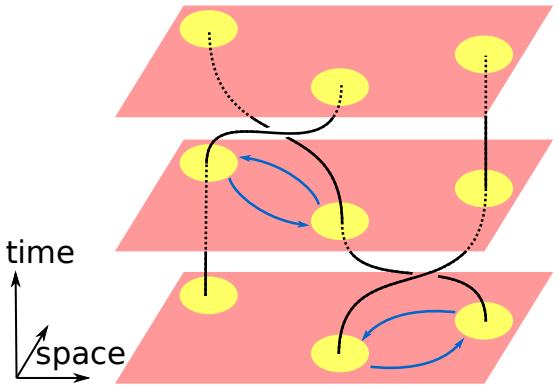

Figure 1.1.: Exchanging Majoranas is a nonabelian operation transforming the ground state of the system. The exchange operations can be imagined as braiding the worldlines of the Majoranas in two spatial and one time dimension.

transformation in the degenerate subspace of ground states. Two such transformations generally do not commute and thus the final state of the system after interchanging several pairs of Majorana bound states depends on the order of the exchange operations much like braiding strings (see Fig. 1.1). This property is unique to emergent particles in many-body systems and is only possible in two dimensions.

Along with their unusual exchange statistics Majorana bound states exhibit another remarkable feature: they are topologically protected zero-energy excitations. Hence the system's ground state has a degeneracy in the presence of Majoranas, which cannot be broken by weak local perturbations. Accordingly superconductors hosting Majorana bound states are called 'topological superconductors'. Our considerations above demonstrate that a ground state degeneracy is a prerequisite for nonabelian exchange statistics and therefore nonabelian anyons are always accompanied by protected zero-energy excitations.

Majorana zero modes constitute the boundary excitations associated with a bulk topological phase in superconductors, similar to the massless Dirac edge states inherent to topological insulators. Like the Dirac edges states Majorana modes mediate quantized transport phenomena characteristic of topological phases. Recent progress towards the realization of Majorana bound states has renewed the excitement about topological phases, which have captivated condensed matter physicists since the discovery of topological insulators almost a decade ago.

Besides the fundamental importance of realizing nonabelian anyons potential applications in quantum computation motivate the quest for Majorana particles in condensed matter physics. Pairs of Majoranas form qubits, the quantum version of a classical bit and information storage unit of a quantum computer. In contrast to conventional qubits

(e.g., two energy levels of a quantum dot) the two Majorana states comprising *a single* qubit can be separated on macroscopic length scales. Hence Majorana qubits store the information nonlocally and are immune to local sources of decoherence such as noise of a gate potential. Furthermore, we have already seen that exchanging Majoranas results in nontrivial unitary transformations and therefore realizes qubit manipulations. If the exchange operations are adiabatic the final state of the system depends only on the topology of the trajectories and not on their exact shape. Hence the nonabelian exchange statistics of the Majorana bound states allows for fault-tolerant quantum computation.[1]

Although Majorana bound states in superconductors are just one incarnation of nonabelian anyons, they are a particularly promising candidate to be realized experimentally owing to the simplicity of the host system. In a seminal work Fu and Kane [Fu 08] predicted Majorana states in hybrid structures of conventional superconductors and topological insulators. The basic principle of this proposal is to combine the properties of different systems, namely a pairing potential and helical edge states, to engineer topological superconductors. Following this line of thought numerous hybrid systems have been suggested to host Majorana bound states exploiting that the requirements for a topological superconductor are surprisingly generic: it suffices to realize a 'spinless' superconductor, i.e., a superconductor with only a single band without spin degeneracy at the Fermi level.

This abundance of theoretical proposals has triggered substantial efforts to realize topological superconductors in the laboratory, in particular since many of the model systems and measurement schemes are within reach of current experiments. The topological origin of Majoranas facilitates this search as it guarantees robustness to a fair amount of disorder and other imperfections of the system. In addition to the broad range of tentative host systems, Majorana bound states are also predicted to give rise to various experimental signatures. Most prominently transport measurements can identify zero-energy bound states. Here the special nature of the Majoranas as robust zero modes irrespective of external manipulations leads to very distinct signatures. Nevertheless, it typically remains a challenge to exclude other effects possibly mimicking the Majorana signatures. The experimentally most relevant systems and signatures are reviewed in Sec. 3.2, the Delft experiment being only the first of several detailed investigations.

Despite the excitement about the first reports on signatures of Majorana bound states in the condensed matter community and beyond, crystal-clear evidence remains to be found. The aim of this thesis is to improve the theoretical understanding of concrete ex-

[1] The exchange statistics of Majorana bound states do not generate all qubit operations necessary for universal quantum computation. Hence a quantum computer based on Majoranas needs to be supplemented by unprotected qubit gates (see [Naya 08] for details).

perimental realizations and the corresponding signatures of Majorana bound states. On the one hand we extend the theoretical description of existing experiments by developing realistic models, which allow us to predict qualitatively new features. On the other hand we theoretically design new measurement schemes that can give rise to distinct signatures of Majorana bound states and determine realistic conditions for such experiments. The specific projects covered in this thesis will be outlined in the remainder of this introduction.

1.1. Outline

In the introductory Chapter 2 we show that superconductors in one and two dimensions can host robust Majorana bound states with exotic exchange statistics. We further give a basic account of generic topological superconducting phases in one-dimensional systems (wires) and show that Majorana bound states emerge at the wires' ends. The topological phase can be characterized by integer quantum numbers which directly relate to experimental observables. We further discuss the stability of the topological phase with respect to disorder. Throughout most of the discussion we illustrate these general concepts by considering a simple model of a p-wave superconductor wire, which contains all essential features of a topological superconductor and therefore serves as a prototype of the various systems discussed in this thesis.

Various more realistic manifestations of topological superconductors are presented in Ch. 3. We first briefly introduce the proximity effect by which a superconducting gap can be opened in ordinary metals. This phenomenon enables engineering effective p-wave superconductors in hybrid structures and thereby gives rise to a plethora of physical realizations of topological superconductors. As this thesis is primarily motivated by experimental efforts to find Majorana bound states we focus on three systems which are currently actively investigated in the laboratory, namely topological insulator edges, quantum wires, and chains of magnetic impurities all in contact with a conventional superconductor. We discuss specific experiments exhibiting signatures of Majorana bound states and comment on the progress of ongoing experimental work aimed at detecting topological superconducting phases.

The main part of the thesis comprises Chs. 4–8. In several independent projects we investigate signatures of Majorana bound states taking into account realistic experimental conditions. In Ch. 4 we investigate multichannel effects on the conductance signatures of Majorana bound states in proximity-coupled quantum wires. We show that under realistic conditions the Majorana conductance peak can be suppressed by additional topologically trivial subbands in the wire providing a possible explanation for recent

experimental findings. Furthermore we predict an enhancement of the signature by the deliberate introduction of disorder which results in a mixing of subbands. We quantify this effect by a combination of numerical calculations and analytical considerations and also discuss other mechanisms that can lead to an enhancement of the Majorana peak.

Chapter 5 reports on signatures of the topological phase in the Josephson current. The current through a Josephson junction hosting Majorana states on either side of the junction exhibits a unique 4π periodicity in the superconducting phase difference. Inevitable quasiparticle relaxation processes in the superconductor typically obscure this signature of Majorana states. In this chapter we show that in mesoscopic p-wave superconductor rings the signature is recovered as a peak in the 4π periodic Josephson current in the vicinity of the topological critical point. The peak results from the competition of two couplings between the two Majorana states across the insulating junction *and* through the interior of the superconducting ring. Such a system can emerge in semiconductor rings with induced superconductivity, which have been experimentally realized in [Forn 13]. To make this prediction more reliable we demonstrate the robustness of this signature with respect to disorder. Interestingly we find as a byproduct of this work that weak disorder can drive the system further into the topological phase.

We remain with the topological Josephson effect in Ch. 6 and discuss supercurrents driven by a twist of the magnetic field direction instead of a superconducting phase gradient. The so-called magneto-Josephson effect serves as an alternative to the elusive ordinary Josephson effect, whose 4π periodicity signals the presence of Majorana states. It has been previously investigated for topological superconductor realized on the edge of topological insulator. Here we study the magneto-Josephson effect for quantum-wire-based topological superconductors. We show that signatures of Majorana states in the magneto-Josephson effect occur only for a certain domain configuration of the Josephson junction. We furthermore contrast the ordinary and magneto-Josephson effects in the two realizations based on quantum wires and topological-insulator edges. We find that the bound state spectrum can be markedly different in the two cases even when the low-energy bulk spectra are identical. To draw the connection to possible experiments we estimate the magnitude of the topological Josephson effect for realistic parameters.

Finally, Chs. 7 and 8 are dedicated to Shiba states, i.e., localized states induced by magnetic impurities in s-wave superconductors, and their relation to topological superconductivity. Chapter 7 contains a detailed analysis of chains of magnetic impurities forming a spin helix on top of a conventional superconductor possibly hosting Majorana bound states. Such systems are currently investigated in experiment and first claims of signatures of Majorana states have been made. Here, we derive an effective tight-binding model of the impurity band formed by the individual Shiba states in the gap of

the substrate superconductor. This Shiba band constitutes an effective one-dimensional topological superconductor and supports Majorana bound states at the chain ends. We show that under realistic conditions the system involves long-range couplings giving rise to power-law (rather than exponentially) localized Majoranas with important consequences for experimental observations and possible applications. Furthermore the model exhibits an unconventional topological phase transition unparalleled in other systems. Quite remarkably, Majorana states become more strongly localized at the critical point in stark contrast to the usual delocalization of the Majorana wavefunction when approaching the phase transition.

In Ch. 8 we investigate the tunneling conductance of generic subgap states in superconductors. Tunneling spectroscopy is a major tool for the characterization of Shiba states and has also proven to be a valuable technique in the quest for Majorana bound states. This work combines a theoretical calculation of the differential tunneling conductance with scanning tunneling spectroscopy measurements on Shiba states using a superconducting tip. In particular we discuss competing transport mechanisms, which can give rise to multiple resonances and qualitative changes in the differential conductance maps as a function of tunneling strength. Our theoretical results are in good agreement with experimental findings and allow us to quantitatively determine system parameters such as the local density of states and the quasiparticle relaxation rate. An important implication of our work is that careful investigations are required to determine the local density of states of Shiba states, which cannot be extracted immediately from the tunneling conductance.

Finally we summarize our findings in the concluding chapter 9 and provide an outlook to future research directions.

2. Topological superconductors and Majorana bound states

2.1. Majorana excitations in superconductors

The Bogoliubov–de Gennes spectrum of superconductors has particle-hole symmetry and thus for each particle excitation γ_ϵ at energy ϵ there must be a hole excitation at the negative energy $\gamma_{-\epsilon}^\dagger$. This requires all levels with the exception of zero modes to come in pairs symmetric in energy. States at zero energy cannot be extended in gapped superconductors and must therefore be localized at defects or boundaries. Imagine an isolated defect with one zero-energy state bound to it. This state must remain precisely at zero energy even when weak local perturbations are introduced. A shift of the bound state energy to, say, positive energies would require a second state at negative energies to satisfy particle-hole symmetry. Other subgap states crossing zero energy as a function of some external parameter (e.g., an external magnetic field) may exist but they will always come in pairs and symmetry requires that at least one zero mode always exists for an odd number of levels.

Another interesting property is that an isolated zero mode must satisfy $\gamma^\dagger = \gamma$, and therefore the creation is equivalent to the annihilation of this quasiparticle. In high-energy physics fermionic particles that are their own antiparticles are known as Majorana fermions [Majo 37], however, the zero modes in our case are not fermions and we hence refer to them as Majorana zero modes. In writing the Bogoliubov–de Gennes Hamiltonian one doubles the number of fermions. This leads to a redundancy that the particle excitation γ_ϵ and the symmetric hole excitation $\gamma_{-\epsilon}^\dagger$ describe the same fermionic state, in contrast to the Dirac equation where particle and antiparticles are separate fermions. In this sense a Majorana zero mode represents only half a fermion and two Majorana zero modes are required to form one fermionic state $d = \gamma_1 + i\gamma_2$. One remarkable consequences of the Majorana nature of the zero modes γ_i are the unusual anticommutation relations

$$\{\gamma_i, \gamma_j^\dagger\} = 2\delta_{ij}, \quad \{\gamma_i, \gamma_j\} = 2\delta_{ij}. \tag{2.1}$$

Using $\gamma_i = \gamma_i^\dagger$ one readily verifies that the fermions d_i constructed from pairs of Majorana zero modes satisfy the usual Dirac anticommutation relations

$$\{d_i, d_j^\dagger\} = 2\delta_{ij}, \quad \{d_i, d_j\} = 0. \tag{2.2}$$

We will see below that indeed Majorana zero modes are not fermions but nonabelian anyons, i.e., they exhibit nonabelian exchange statistics. Furthermore Majorana zero modes in superconductors only exist in one or two dimensions and do not have a dispersion, which distinguishes them from three-dimensional Majorana fermions in particle physics. The latter also occur as emergent particles in superconductors. Particle-hole symmetry ensures that all Bogoliubov quasiparticles, the elementary excitations of a superconductor, can be written in a real form and are therefore Majorana fermions satisfying $\gamma_\epsilon = \gamma_{-\epsilon}^\dagger$ [Cham 10]. Two Bogoliubov excitations can annihilate and their Majorana nature can be tested by interferometry [Been 14].

In contrast single Majorana bound states are tied to the middle of the gap. Their energy can move away from zero only if a second defect with an attached zero mode is brought close to the first one. The two Majorana bound states can hybridize and form a finite energy excitation, which is exponentially small in the distance. Another way to remove the single level at zero is to close the gap so that the zero mode becomes extended. It can then couple to other spatially separated zero modes. Thus superconductors with isolated Majorana bound states (i.e., all defects with zero modes are infinitely far away from each other) cannot be deformed by a smooth variation of parameters into superconductors without zero modes unless the gap closes during the deformation. They are in two topologically distinct phases and the phase transition between them is accompanied by a closing of the bulk gap. This parallels well-known topological phases in integer quantum Hall systems and topological insulators, where gapless modes appear at well-separated defects in an otherwise gapped system. In general transitions between phases with different topological indices require a closing of the gap.

As stated above Majoranas are nonabelian anyons meaning that the final state of the system after exchanging several pairs of Majoranas depends on the order of the exchange operations. In order to illustrate the exotic exchange statistics of Majorana bound states we consider a concrete example where Majorana bound states arise. A superconducting flux quantum $h/2e$ penetrating a 2d superconductor creates an Abrikosov vortex. Due to the suppression of the superconducting gap by the magnetic flux such a vortex binds localized states with equidistant energy levels $E_n = (n + \alpha)\delta$ with n an integer and $\delta \sim \Delta^2/E_F$ [Caro 64, Genn 99], where Δ is the superconducting gap and E_F the Fermi energy. Particle-hole symmetry restricts α to 0 or $1/2$. For massive electrons as in an s-wave superconductor zero point motion enforces $\alpha = 1/2$. In contrast, a p-

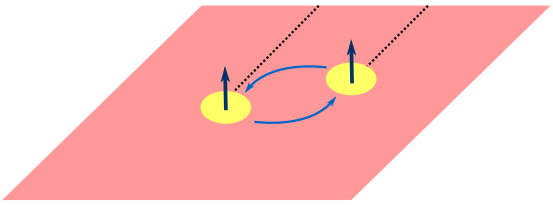

Figure 2.1.: Exchanging Majoranas bound to $h/2e$ vortices in p-wave superconductor. Each vortex has a branch cut where the superconducting phase jumps by 2π (dotted line).

wave superconductor with the pairing potential $\Delta'(p_x + ip_y)$ features a linear dispersion describing massless Dirac fermions where $\alpha = 0$ and thus a zero mode is bound to the vortex [Jack 81]. The origin of this shift by $1/2$ can be understood semiclassically as an additional Berry phase π accumulated by electrons moving around closed orbits due to the locking of the momentum and the superconducting phase in p-wave superconductors. This yields an energy shift canceling the zero-point energy. [1]

We can obtain an intuitive understanding of the nonabelian nature of the Majoranas bound to vortices following Ivanov [Ivan 01, Ster 04, Alic 12]. The penetrating flux leads to a winding of the superconducting phase around the vortex and creates a branch cut where the phase jumps by 2π. When two vortices with Majoranas $\gamma_{1,2}$ are exchanged as shown in Fig. 2.1, one vortex has to cross a branch cut and the phase of the Majorana wavefunction jumps by π, i.e., half of the superconducting phase change. Accordingly the corresponding annihilation operators transform[2] as $\gamma_1 \to \gamma_2$, $\gamma_2 \to -\gamma_1$. This transformation can be described by the unitary operator $U_{12} = (1 + \gamma_1\gamma_2)/\sqrt{2}$. Indeed one readily confirms that $U_{12}\gamma_{1/2}U_{12}^\dagger = \mp\gamma_{2/1}$. We now consider two processes: exchanging γ_1 and γ_2 and exchanging γ_2 and a third Majorana γ_3. The corresponding unitary transformations do not commute $[U_{12}, U_{23}] = \gamma_1\gamma_3$ confirming that Majoranas are nonabelian anyons.

In this thesis we focus on Majorana bound states in one-dimensional systems. We commence by discussing a model for p-wave superconducting wires in detail in the next section showing that Majorana bound states manifest themselves at domain walls. The exceptional exchange statistics of Majoranas can also be accessed in wires although braiding is ill defined in strictly one dimension. A way out is provided in [Alic 11] by

[1] This result is well known in the context of Graphene and surface states of topological insulators where due to the massless Dirac fermions and spin-momentum locking the Landau levels have energies $E_n \sim \sqrt{n}$ instead of $E_n \sim (n + 1/2)$ for massive fermions.

[2] This transformation already illustrates that Majoranas are neither bosons nor fermions. Exchanging bosons once or fermions twice will leave the system's ground state unchanged. In contrast for Majorana bound states four exchanges are necessary to return to the initial state consistent with calling them "half fermions."

considering wire networks (e.g., T-junctions). For the experimental realization of Majorana bound states the one-dimensional realization is advantageous, since accessing and manipulating vortices in 2d superconductors is presumably much more challenging than contacting or moving domain walls in wires.

2.2. Topological phases in one-dimensional p-wave superconductors

We can readily convince ourselves that topologically distinct phases cannot be realized in plain s-wave superconductors. The s-wave gap is always nonzero and the superconductor can be smoothly deformed into a (trivial) vacuum phase by decreasing the chemical potential $\mu \to -\infty$. Whenever two phases can be deformed into each other without closing of the gap we call them topologically connected. This is different for a spinless p-wave superconductor with a BdG Hamiltonian

$$\mathcal{H} = \left(\frac{p^2}{2m} - \mu \right) \tau_z + \Delta' p \tau_x \tag{2.3}$$

in one dimension. Here Δ' is the p-wave pairing strength and τ_j are Pauli matrices in Nambu space. The excitation spectrum is readily obtained by squaring the Hamiltonian. We find

$$E_\pm = \pm \sqrt{\left(\frac{p^2}{2m} - \mu \right)^2 + (\Delta' p)^2}. \tag{2.4}$$

The Pauli principle forbids p-wave pairing at zero momentum and thus the gap closes at $\mu = 0$. For $\mu < 0$ the chemical potential is outside of the band and the system can be adiabatically deformed into a trivial insulator. We now show that the superconducting phase with $\mu > 0$ is indeed topological.

Two phases are topologically distinct if an integer invariant exists, which takes different values in the two phases. We can indeed construct such an integer for one-dimensional spinless p-wave superconductor. To this end we define the unit vector $\hat{h} = \mathbf{h}/|\mathbf{h}|$ that describes the matrix structure of the Hamiltonian in particle-hole space as $\mathcal{H} = h_z(p)\tau_z + h_x(p)\tau_x$. The two components of this vector are plotted in Fig. 2.2(a). Figures 2.2(b) and (c) illustrate the winding of this vector when the momentum p is tuned from $-\infty$ to ∞. While there is no winding in the insulating phase $\mu < 0$, $\hat{h}$ winds once in the superconducting phase $\mu > 0$. Since the winding number takes integer values it cannot be changed by small variations of parameters. It thus defines a topological index ν and proves that the gap closing at $\mu = 0$ marks a topological phase transition to a nontrivial phase for $\mu > 0$. Indeed we note that $\hat{h}$ becomes ill-defined at gap clos-

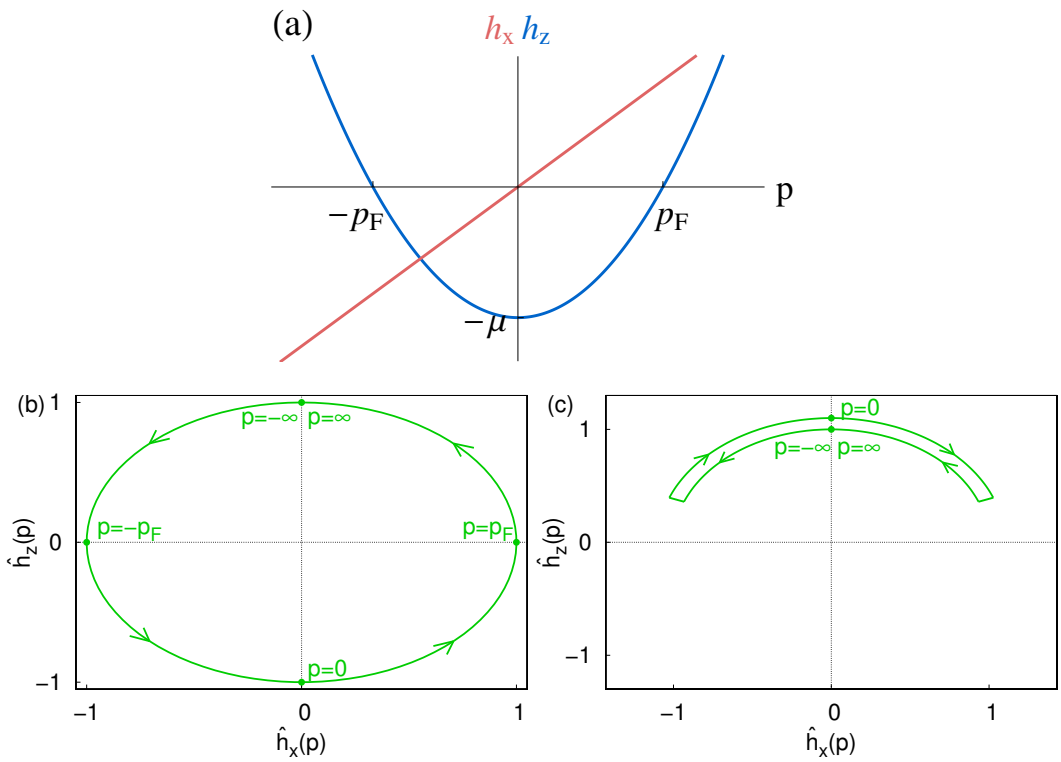

Figure 2.2.: (a) Normal state spectrum $h_z(p) = p^2/2m - \mu$ and pairing $h_x(p) = \Delta' p$ of the p-wave superconductor forming the two components of the vector $\mathbf{h}$. (b+c) Winding of the normalized vector $\hat{h}$ in the (b) topological phase ($\mu > 0$) and (c) the trivial phase ($\mu < 0$).

ings, where $\mathcal{H} = 0$. This is a manifestation of the fact that a change of topological index must involve a closing of the gap. In Fig. 2.3 we display the entire phase diagram of the p-wave superconductor described by Eq. (2.3).

This simple construction of a topological index is limited to systems with translation symmetry. In order to detect the topology in experiments the sample must have boundaries (e.g., where a lead is attached) and the topological phase needs to be stable to a certain amount of disorder. To this end we will discuss more general constructions of topological indices in terms of scattering matrices or in terms of boundary conditions (similar to Laughlin's argument for the quantum Hall effect) in Sec. 2.3 below. Nevertheless, this basic definition of a topological index is very helpful to understand several more general concepts important for the classification of topological insulators and superconductors [Ryu 10, Hasa 10].

(i) The topological index ν defined here is a winding number and can therefore take any integer value. For the simple model in Eq. (2.3) only the values -1,0, and 1 are possible as indicated in the phase diagram in Fig. 2.3. In accordance with earlier obser-

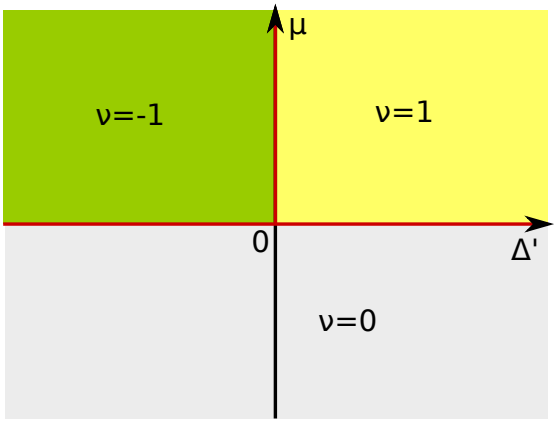

Figure 2.3.: Phase diagram of the spinless p-wave superconductor. For $\mu < 0$ the system is trivial (gray area) and for $\mu > 0$ there are two topologically nontrivial phases (green and yellow). The gap closings signaling topological phase transitions are marked by red lines. The vector $\hat{h}$ shown in Fig. 2.2(b) winds in opposite directions for different signs of the pairing Δ' indicating a topological quantum number $\nu = \pm 1$. The two nontrivial phases are separated by a metallic line $\Delta' = 0$.

vations the transition between the two nontrivial phases ± 1 occurring at $\Delta' = 0$ and $\mu > 0$ involves a closing of the gap. In fact, since the topological index changes by two, also the gap closes at two distinct points in momentum space $p = \pm p_F$. This differs from the $\mu = 0$ transition with only a single gap closing at $p = 0$. Higher indices can in principle also be realized when terms of order higher order in p are present in the Hamiltonian. For instance, a band structure with more than two Fermi points and induced f-wave pairing may yield a topological index ± 3. A two-dimensional realization of such a system is discussed in Ref. [Mao 11].

(ii) The symmetry of the Hamiltonian determines the topological phase. Eq. (2.3) has time-reversal symmetry (TR) $[\mathcal{H}, T] = 0$. Together with particle-hole symmetry this puts the system in the symmetry class BDI [Altl 97][3]. When a term $\sim \tau_y$ is added to the Hamiltonian in way that cannot be removed by a simple gauge transformation, time-reversal symmetry is broken and the system is now in class D. For instance, the multichannel generalization of Eq. (2.3) reads

$$\mathcal{H}_{\text{quasi}-1\text{d}} = \left(\frac{\mathbf{p}^2}{2m} - \mu \right) \tau_z + \Delta'(p_x \tau_x - p_y \tau_y). \tag{2.5}$$

In a quasi one-dimensional system, where p_y is quantized, we could in principle still use the winding number definition of the topological index as the Hamiltonian depends only on one momentum component p_x, but time-reversal symmetry is broken due to the

[3] In a spinless model time reversal only involves complex conjugation, $T = K$, and thus $T^2 = 1$

interchannel pairing $\Delta' p_y \tau_y$.[4] Our definition of ν ceases to describe a topological index since the vector $\hat{h}$ now lives on a sphere instead of a circle and all windings are trivial. It is possible to define a different topological index for Eq. (2.5). The vector $\hat{h}$ points towards the north pole of the sphere $\hat{h}_\infty \to \hat{z}$ for $p \to \pm\infty$. At $p = 0$ the pairing vanishes and thus $\hat{h}_0 = \pm\hat{z}$ points either to the north or south pole depending on whether the band is empty or partially filled. Hence $\nu = \hat{h}_\infty \cdot \hat{h}_0$ defines a $\mathbb{Z}_2$ index. This shows that the change of symmetry class usually comes along with a change of topological index.[5]

(iii) The definition of the winding number ν is restricted to a (quasi) one-dimensional system as it assumes only one momentum component p. There are higher order generalization of a winding number. For instance, the Chern number in two dimensions $\nu = \int d^2p/4\pi(\hat{h} \cdot (\partial_{p_x}\hat{h} \times \partial_{p_y}\hat{h})$ can only assume integer values that count the twists in the mapping of the 2d plane onto a 2-sphere. The Hamiltonian of a two dimensional p-wave superconductor is the same as the one in Eq. (2.5) and the corresponding vector $\hat{h}$ lives on a 2-sphere. Thus a $p + ip$-wave superconductor in 2d (which breaks time-reversal symmetry) also has an integer invariant given by the Chern number. Phases with indices higher than 1 are again only realized in the presence of higher order pairing and a more complicated band structure [Mao 11].

The relation between the one- and two-dimensional p-wave superconductors is an example of the dimensional hierarchy that is at the basis of the periodic table of topological insulators [Kita 09, Schn 08, Ryu 10, Qi 08]. We have seen that a two-dimensional system in class D (without time-reversal symmetry) has the same topological structure as a one-dimensional system in class BDI (with time-reversal symmetry). A topological index similar to a winding number can also be defined in higher dimensions as the number of twists in the mapping of the n-sphere onto itself. [6] In each dimension this is realized in a different symmetry class. This can be formalized in various ways including K-theory [Kita 09] as well as topological field theories and nonlinear σ-models [Qi 08, Schn 08, Ryu 10]. A less rigorous but insightful derivation of the dimensional hierarchy in terms of scattering theory showing the transformation of the symmetry classes under a dimensional reduction procedure has been given in [Fulg 12].

The discussion so far has focused on the topological properties of the bulk system.

[4] Another example of time-reversal breaking in 1d occurs in effective p-wave superconductors that can be formed by the proximity effect in superconducting heterostructures in the presence of a magnetic field (cf. Sec. 3.2). The effective model is spinless and therefore the magnetic field is not enough to break TR, but a supercurrent flowing in the superconducting substrate induces a phase gradient in the pairing and thus breaks TR [Romi 12]. The conditions for a supercurrent to break TR are discussed in Sec. 5.

[5] This definition can be easily extended to arbitrary lattice Hamiltonians with odd-momentum pairing [Alic 12]. The pairing term vanishes at the Brillouin zone center and boundary and thus $\hat{h}_{p=\pm\pi/a}, \hat{h}_{p=0} = \pm\hat{z}$. The relative sign $\hat{h}_{p=\pm\pi/a} \cdot \hat{h}_{p=0}$ defines a $\mathbb{Z}_2$ topological index.

[6] More formally, the n-th homotopy group of the n-sphere is isomorphic to the integer numbers, $\pi_n(S^n) = \mathbb{Z}$.

The most important manifestation of the topology, however, are edge states associated with the topological phase—in this case Majorana bound states. In the previous section we have seen that the number of Majorana bound states at one edge (or defect) can also define a topological index. We will see here and in the next section that the index in terms of Majorana bound states is equivalent to the bulk topological quantum number. In order to first understand how Majoranas emerge in p-wave superconductors we consider a tight-binding (TB) version [Kita 01, Motr 01] of Eq. (2.3)

$$\mathcal{H}_{\mathrm{TB}} = -\mu_{\mathrm{TB}} \sum_{i=1}^{N} c_i^\dagger c_i - \sum_{i=1}^{N-1} (t c_i^\dagger c_{i+1} + \mathrm{h.c.}) - \sum_{i=1}^{N-1} (\Delta_{\mathrm{TB}} c_i c_{i+1} + \Delta_{\mathrm{TB}}^* c_{i+1}^\dagger c_i^\dagger). \tag{2.6}$$

This Hamiltonian describes a chain of spinless fermions and consequently on-site pairing $\sim c_i c_i$ is ruled out by the Pauli principle. Therefore nearest neighbor pairing terms have to be taken into account and the order parameter has p-wave symmetry. The Hamiltonian (2.6) is also called Kitaev chain for its use in Kitaev's seminal work [Kita 01] on Majoranas and their use as topologically protected qubits. The bulk spectrum can be obtained by Fourier transformation

$$\epsilon_{\mathrm{TB}}(k) = \sqrt{(2t \cos ka + \mu_{\mathrm{TB}})^2 + 4\Delta_{\mathrm{TB}}^2 \sin^2 ka} \tag{2.7}$$

with lattice spacing a. The continuum limit $c_i \to \psi(x)$ of the lattice model (2.6) reads

$$\int_0^L dx \left[\psi^\dagger(x) \left(\frac{p^2}{2m} - \mu \right) \psi(x) - \psi(x) \frac{\Delta'}{2} p\psi(x) - \psi^\dagger(x) \frac{\Delta'^*}{2} p\psi^\dagger(x) \right] \tag{2.8}$$

with the substitutions $aN \to L$, $a^2 t \to 1/2m$, $\mu_{\mathrm{TB}} + 2t \to \mu$, and $a\Delta_{\mathrm{TB}} \to \Delta'/2$. The Fourier transformation of Eq. (2.8) can be written in Nambu notation, which yields the Bogoliubov–de Gennes Hamiltonian of the p-wave superconducting wire in Eq. (2.3). Similar to the continuum case the TB model is in a topologically nontrivial phase when the chemical potential is inside the band. Since the TB dispersion is bound from above and below the system has two topological phase transitions at $\mu_{\mathrm{TB}} = \pm 2t$.

We can find the solution to this Hamiltonian for specific sets of parameters illustrating how the change of topological phase manifests itself in samples with boundaries. To this end we perform a transformation to the Majorana basis $c_i = (\gamma_{A,i} + i\gamma_{B,i})/2$ with Hermitian operators $\gamma = \gamma^\dagger$. The γ operators formally describe Majorana particles, but their occurrence is purely mathematical so far as two such operators can be recombined to form a Dirac fermion. In the insulating phase for $t = \Delta = 0$ and $\mu < 0$, Eq. (2.6) reads

$$\mathcal{H}_{\mathrm{TB}} = -\mu_{\mathrm{TB}} \sum_{i=1}^{N} c_i^\dagger c_i = -i \frac{\mu_{\mathrm{TB}}}{2} \sum_{i=1}^{N} \gamma_{A,i} \gamma_{B,i}. \tag{2.9}$$

Here Majorana particles on the same site pair up to form Dirac fermions. With the choice of parameters $t = \Delta$ and chemical potential at the center of the band, $\mu = 0$, which places the system in the topological phase, the Hamiltonian (2.6) takes the form

$$\mathcal{H}_{\mathrm{TB}} = -it \sum_{i=1}^{N-1} \gamma_{A,i}\gamma_{B,i+1} = 2t \sum_{i=1}^{N-1} \left(d_i^\dagger d_i - \frac{1}{2} \right), \tag{2.10}$$

where we have introduced new fermion operators $d_i = \gamma_{A,i} + i\gamma_{B,i+1}$. Now the Majoranas from different sites are paired. Two Majorana operator have dropped out of the Hamiltonian leaving only $N - 1$ excitations of energy $2t$. The N-th fermion $d_N = \gamma_{A,N} + i\gamma_{B,1}$ has zero energy, but different from the other d operators it is delocalized with contributions at both ends of the chain. The two operators $\gamma_{A,N}$ and $\gamma_{B,1}$ now represent two uncoupled Majorana states each forming one zero-energy excitation in the Bogoliubov–de Gennes spectrum as discussed in the previous section.

These two states exactly at zero energy exist only at $t = \Delta$ and $\mu = 0$. Let us consider a semi-infinite chain for this special choice of parameters with one zero-energy state localized on the last site. When tuning away from this point in parameter space the energy of this state must remain at zero due to particle-hole symmetry, but the wavefunction may be extended over several sites. Because of the gap in the bulk of the wire, the Majorana wavefunction decays exponentially. The behavior in finite chains, where the two end state can hybridize, can then be inferred from a perturbative argument: the overlap of the Majorana states is exponentially small in the length of the wire, which generically leads to an exponentially small energy splitting. The exponential decay of the Majorana wavefunction of the lattice model (2.6) has been given in [Kita 01]. Details of the result for the continuum model (2.3) are discussed in Ch. 5 and the corresponding energy splitting is derived from perturbation theory in App. A.

Hence the topological phase is characterized by end states with an energy exponentially small in system size. They are protected in the sense that the energy of the two Majoranas cannot be increased by any local perturbation added to the Hamiltonian. This is very different from other subgap states such as Andreev bound states whose energy can be changed by locally changing the Hamiltonian.

The existence of Majorana bound states in the TB model and their use as qubits discussed in a seminal work by Kitaev [Kita 01] has initiated a series of realistic proposals for realizations of topological superconductors. We will discuss various realizations and corresponding experimental signatures in Ch. 3.

2.3. Definitions of topological indices and robustness to disorder

We have seen that the Majorana bound states at the ends of a wire are robust to disorder. To see that also the bulk topological phases persist in disordered systems we define a topological index in terms of the scattering matrix at the Fermi level [Merz 02, Akhm 11, Fulg 12]. To this end we assume a semi-infinite (quasi) one-dimensional p-wave superconductor attached to a lead. For subgap energies the transmission amplitude vanishes and due to the unitarity of the S matrix we have $|\det r| = 1$, where r is the reflection matrix. In the presence of particle-hole symmetry we can choose a basis[7] in which the reflection matrix satisfies $r(\epsilon) = r^*(-\epsilon)$, thus at the Fermi level the reflection matrix is real, i.e., $\det r = \pm 1$. This allows us to define a $\mathbb{Z}_2$ topological index $Q = \det r$, which distinguishes between the two phases in class D. Consistent with our previous observation the index can only change when the gap closes and finite transmission leads to $|\det r| \neq 1$.

Similar definitions of topological indices in terms of the scattering matrix can be found for other symmetry classes and dimensions [Fulg 11, Fulg 12]. For instance, the reflection matrix of a time-reversal symmetric p-wave superconductor in class BDI is real and symmetric in the Majorana basis. Thus it has real eigenvalues and $|\det r| = 1$ ensures that none of the eigenvalues changes sign within a gapped region of parameter space. Hence the number of, say, negative eigenvalues constitutes a topological quantum number. It can assume any integer value, which is compatible with the topological index defined in terms of the band structure in Sec. 2.2.[8]

The topological indices in terms of scattering matrices are particularly useful as they directly relate to experimentally observable phenomena. The number of bound states at the end of the wire can be determined by placing a lead between the superconductor with reflection matrix r and a hard wall with $r_0 = \mathrm{diag}(-1, \ldots, -1)$. A bound state ψ in the lead must obey $r_0 r \psi = \psi$ and, hence, each zero-energy end state corresponds to an eigenvalue -1 of the reflection matrix r evaluated at the Fermi level. Thus the topological index in class BDI counts the number of zero-energy bound states at the end of the wire.[9] A similar statement holds for class D: In the nontrivial phase with $\det r = -1$ there is an odd number of bound states, while the trivial phase supports an even number. [10]

[7] This is equivalent to the transformation to the Majorana basis we used for the Kitaev chain.

[8] Here we see again that indices higher than 1 can only be realized in p-wave superconductor wires with several channels where the reflection matrix has multiple rows.

[9] There is some ambiguity for the termination of the normal lead in the chiral classes that can lead to additional unprotected bound states (see Ref. [Fulg 11]).

[10] In class D, r is orthogonal in the Majorana basis and its eigenvalues are ± 1 or come in complex conjugate pairs. Hence the condition $\det r = -1$ requires an odd number of eigenvalues -1.

The S matrix formulation of the topological index remains well defined for disordered systems, which immediately establishes the robustness of Majorana states to a small amount of disorder. For very large disorder, on the other hand, superconductivity is suppressed and the system turns trivial. Therefore a topological phase transition must occur at some intermediate strength of disorder. This result has originally been published in 2001 [Motr 01], independent of Kitaev's work, based on a strong disorder renormalization group approach. The critical disorder strength has been determined in Ref. [Brou 11a] using scattering theory. Deep inside the topological phase the transition to the trivial phase occurs when the coherence length of the clean superconductor is twice the mean free path, $\xi = 2l$, i.e., when disorder starts to suppress superconducting correlations.

Based on the results of Ref. [Brou 11a], we show in Sec. 5 (originally published as Ref. [Pien 13c]) how weak disorder may also drive a system further into the topological phase. In fact, a small region in the trivial phase becomes topological when weak disorder is introduced. The phase diagram of the disordered p-wave superconductor is shown in Fig. 5.8. An analytical theory for the phase diagram of individual disordered samples has been developed later [Adag 14] confirming and extending these results. The phase diagram of multichannel p-wave superconductors can be obtained along similar lines [Ried 13]. In systems with N topological channels generically a sequence of N disorder-induced phase transitions occurs, which can be understood from simple arguments. Consider first a collection of N uncoupled strictly one-dimensional p-wave wires in the topological phase. Each channel then exhibits a disorder-induced transition to the trivial phase, where the critical disorder strength depends on the chemical potential relative to the bottom of the band. When weak hopping between different chains is allowed the system is in class BDI and has an integer index which directly connects to the number of topological channels in the uncoupled system. Therefore also the sequence of N disorder-induced phase transitions persists. When inter- and intrachannel hopping have the same strength (which is equivalent to Eq. (2.5) with the interchannel pairing $\Delta' p_y \tau_y$ set to zero) there are still N phase transitions, but the topological phases persist up to much higher disorder strengths. The transitions occur at $\xi = l(N+1)/n$ with $n = 1, \ldots, N$ and thus the upper critical disorder strength above which the system is trivial is $\xi/l = (N+1)$ instead of $\xi/l = 2$ for the uncoupled channels. When interchannel pairing $\Delta' p_y \tau_y$ is present the system is in class D with a $\mathbb{Z}_2$ index. Thus the Majorana end states gap out in pairs and the odd (even) integer phases are mapped to the topological (trivial) phase. This results in a sequence of N transitions between topological and trivial phases [Ried 13].

Finally, we discuss a third possibility to define a topological index for superconductors in class D by means of the Josephson effect. Consider a Josephson junction of two

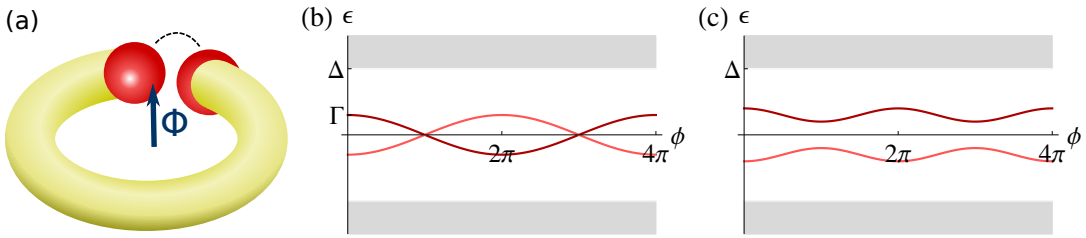

Figure 2.4.: (a) Superconducting ring with a Josephson junction possibly hosting coupled Majorana bound states. Threading a flux through the ring causes a phase difference at the junction. (b+c) Typical subgap spectrum of a Josephson junction as a function of phase difference ϕ in (a) a topological superconductor ring hosting Majorana bound states and (b) a trivial superconductor ring hosting Andreev bound states. The dark and light red states denote particle and hole levels of the same fermionic excitation related by particle-hole symmetry. The subgap contribution of the Majoranas is 4π periodic whereas a trivial junction exhibits 2π periodicity. The continuum (grey) depends only very weakly on the superconducting phase difference with period 2π.

superconductors with a phase difference ϕ across the junction. The energy spectrum is 2π periodic in ϕ and particle-hole symmetry furthermore ensures the spectrum to be symmetric about zero energy. These two properties allow for two distinct phases in which the spectrum has an even or odd number of zero-energy crossings when the phase difference is tuned from 0 to 2π as shown in Fig. 2.4(b) and (c) . Here, a "single" crossing involves two states related by particle-hole symmetry. Transitions between the two states require the addition of single electrons and single crossings are therefore protected by fermion parity conservation. For an odd number of crossings between 0 and 2π the ground state changes its parity while for an even number of crossings the initial and final ground states are identical. In the latter case the spectrum can be smoothly deformed so that all crossings gap out in pairs leaving the system gapless throughout the cycle.

Instead of using two superconductors we can bend a single superconducting wire into a ring and couple the two ends by introducing end-to-end hopping as shown in Fig. 2.4(a). The topological phase is then characterized by a change of the ground state parity when the flux threading the ring is tuned adiabatically from zero to the superconducting flux quantum $h/2e$, which corresponds to a phase difference of 2π. This property can be viewed as a manifestation of the nonabelian statistics and is equivalent to the change of the ground state when moving one Majorana around another in two dimensions (cf. discussion on nonabelian exchange in Sec. 2.1). The change of parity remains unaffected by disorder as long as the bulk gap does not close and thus provides a valid definition of a topological index in non-ideal systems. This index is equivalent to the indices defined above in terms of the winding of the BdG Hamiltonian or the scat-

tering matrix. In Sec. 3.3.2 we show that the presence of Majorana bound states at the junction indeed implies an odd number of zero-energy crossings.

The change of the ground state by threading a flux quantum through a ring is closely related Laughlin's argument [Laug 81] for the integer quantum Hall effect. Similar arguments can be used for the characterization of topological insulators in class AII [Fu 06], or as a general scheme for a dimensional reduction procedure used for the construction of the periodic table of topological insulators, where the flux is considered as a momentum component in d+1 dimensions [Qi 08]. The change of parity can also be used for detection of the topological phase, since the current in a topological Josephson junction has a period of h/e instead of the usual $h/2e$ period as long as parity is conserved. This is discussed in detail in Sec. 3.3.2. Section 5 describes signatures of the topological phase in the Josephson current even for systems where the fermion parity is not conserved.

The general properties of the topological phase and Majorana bound states arising in p-wave superconductors apply to all models of topological superconductors discussed in this thesis.[11] The topology is determined by the dimension and symmetry class. Here we consider the chiral class BDI (e.g., a p-wave superconductor in one dimension) and class D (e.g., a quasi-one-dimensional p-wave superconducting wire), where the effective time-reversal symmetry is broken. Nevertheless in experiments also nontopological properties may be important and seriously affect the physical manifestations of topology. We therefore elucidate the most relevant systems hosting Majorana bound states in the next chapter, in particular, addressing realization specific phenomena.

[11] An exception occurs in the context of helical Shiba chains elucidated in Sec. 7. In a certain limit the effective description of such chains involves long-range couplings and therefore a mapping to a simple p-wave superconductor is impossible.

3. Physical realizations of one-dimensional topological superconductors

In this chapter we review various proposals for systems hosting a topological superconducting phase and discuss how signatures of Majorana bound states can be detected in experiment. We have seen in the previous chapter that one dimensional p-wave superconductors support a topological phase hosting Majorana bound states. Although intrinsic p-wave superconductors have not been unambiguously identified to date (for a review on the prime candidate for intrinsic p-wave superconductivity Sr_2RuO_4, see [Kall 12]), the realization of topological superconductors is within reach of state-of-the-art experimental techniques. An important observation that goes back to Fu and Kane [Fu 08] is that an effective p-wave superconductor can be engineered in superconducting hybrid systems. The strategy is to induce superconductivity by proximity in a system where the Fermi level crosses only a single spin-split band. In such an effectively spinless superconductor pairing of states at $k = 0$ is impossible (as there is only one available state) and thus the gap closes when the chemical potential crosses the dispersion at $k = 0$. Assuming that the pairing potential is linear around $k = 0$, the system is topologically equivalent to a p-wave superconductor and the gap closing marks the topological phase transition. Hence superconductors with a single band at the Fermi level generically support a topological phase.

The prospect of realizing Majorana bound states in superconducting hybrids has triggered much experimental effort. Before discussing particular examples of effective p-wave superconductors in Sec. 3.2 we briefly introduce the proximity effect by which normal metals can inherit pairing correlations from neighboring superconductors. The most relevant signatures of Majoranas and the current status of experiments are reviewed in Ch. 3.3

3.1. Proximity effect

Due to recent advances in nanotechnology it has become possible to artificially design superconducting materials by means of the proximity effect [Doh 05, Fran 10a, Nish 11,

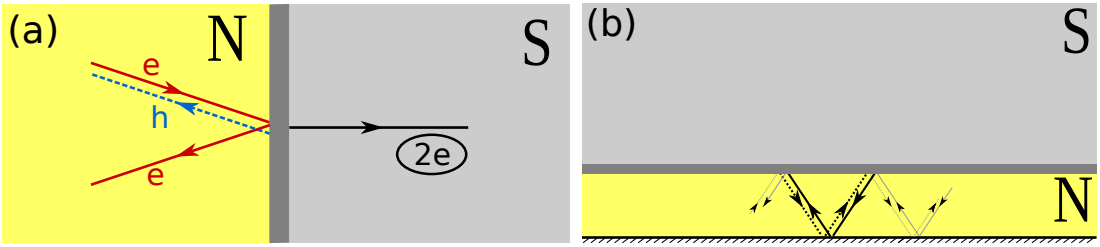

Figure 3.1.: (a) Incident electrons are Andreev reflected as holes at an interface between a normal metal (N) and a superconductor (S) creating a Cooper pair in the superconductor. The electrons may also be partially normal reflected by an opaque interface. (b) Proximity effect in a wire. Sequential normal and Andreev reflection lead to electron-hole correlations and thus a superconducting gap throughout the wire. An opaque interface leads to repeated normal reflections which increase the dwell time and reduce pairing correlations in the wire.

Nils 12]. To understand this phenomenon we consider an interface between a normal metal (N) and a superconductor (S) as shown in Fig. 3.1(a). Single electrons near the Fermi energy in the normal metal cannot enter the superconductor due to the gap. Pairs of electrons, however, may form Cooper pairs and pass into the condensate of the superconductor. This can alternatively be viewed as an Andreev reflection, where incident spin up electrons are reflected from a superconductor as spin down holes with the opposite energy relative to the Fermi level. Such reflection processes create correlations between electronic states in the normal metal close to the interface, which can be described by a correlator $\langle\psi_\uparrow\psi_\downarrow\rangle$. This effectively creates an order parameter $\Delta_{\mathrm{ind}} \propto \langle\psi_\uparrow\psi_\downarrow\rangle$ in the normal metal even in the absence of attractive interactions between electrons.

Here we are interested in wires with only a few transverse modes placed on top of a superconductor depicted in Fig. 3.1(b). In this case the entire system becomes superconducting. The induced gap is mainly determined by the interface transparency. For an ideal interface to a strictly one-dimensional wire the induced gap is equal to Δ, the gap of the host superconductor [Alic 12]. When the interface transmission is small the energy scale of the lowest excitation is set by the Thouless energy, i.e., by the inverse time electrons spend in the normal metal [McMi 68]. This estimate remains valid as long as the Thouless energy remains small compared to Δ. This is typically the case for Andreev billiards, where the extension of the normal system determines the lowest excitation energy [Been 05]. In case of a 1d wire the Thouless energy is set by the tunneling rate. Thus if $\Gamma \ll \Delta$ the induced gap $\Delta_{\mathrm{ind}} \sim \Gamma$ becomes independent of the host superconductor. The same result can be obtained from second-order perturbation theory in the tunneling amplitude. A more accurate theory involves integrating out the supercon-

ductor's degrees of freedom from the action [Pott 11, Alic 12], which yields the induced gap also for intermediate interface transparencies. In addition to the proximity effect, the coupling to the superconductor also renormalizes the bare energy scales of the 1d wire downwards (i.e., it reduces the quasiparticle weight) due to electrons leaking into the superconductor [Pott 11, Alic 12]. Thus a stronger coupling to the superconductor enhances pairing but diminishes all other energy scales of the 1d system.

3.2. Topological phases in superconducting hybrid systems

To open a proximity-induced gap in a metal requires the metallic states of opposite momentum to have different spin orientations because incident electrons can only be Andreev reflected from the superconductor as holes with opposite spin. This poses a major complication to several Majorana proposals as an external magnetic field required to break spin degeneracy generally renders the s-wave proximity effect inefficient. At the same time the competition between a spin-polarizing magnetic field and spin-singlet superconductivity that antialigns spins may be beneficial as it allows tuning through the topological phase transition. In this section we elucidate three suitable systems with a single partially-occupied band, which have received much attention. Although the observation of Majorana bound states has not yet been proven indisputably, experimental progress has been achieved in all of these systems.

3.2.1. Topological insulator edge

In a seminal work Fu and Kane [Fu 08] realized that the surface of a three-dimensional topological insulator (TI) coupled to a superconductor realizes an effective two dimensional $p+ip$ superconductor. In a subsequent paper [Fu 09a], the same authors proposed the realization of a one-dimensional p-wave superconductor on the proximity-coupled edge of a 2d topological insulator. The 1d edge channels can be described by a Dirac Hamiltonian, where opposite momenta have antiparallel spins. Due to this favorable relation between spin and momentum the proximity effect can open a sizable gap in the edge channel comparable to the gap of the nearby superconductor itself. We can readily convince ourselves that the induced pairing has indeed p-wave symmetry as a consequence of the broken spin degeneracy: $\Delta_k = \langle \psi_{k\uparrow} \psi_{-k\downarrow} \rangle = - \langle \psi_{-k\downarrow} \psi_{k\uparrow} \rangle = -\Delta_{-k}$.

In order to realize Majorana bound states the effective topological superconductor on the edge needs to be terminated. This can be achieved by inducing a Zeeman term either by applying a magnetic field or placing a ferromagnet next to the edge. The Zeeman term breaks the time-reversal symmetry protecting the edge states and therefore opens

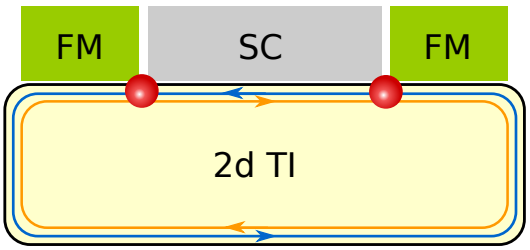

Figure 3.2.: Two dimensional topological insulator with counterpropagating edge modes. The edge channels can be gapped by a superconductor or a ferromagnet with Majorana bound states existing at the interfaces between different gapped regions.

a gap by introducing backscattering between the counterpropagating modes. The Zeeman gap has a very different nature than the superconducting gap as the former tends to align spins whereas the latter favors an antiparallel spin configuration. This leads to a competition between the two mechanisms, which results in an intermediate gap closing when the system is adiabatically tuned from a magnetically gapped state to one with a superconducting gap.

To make these arguments more quantitative we consider the effective Bogoliubov–de Gennes Hamiltonian describing the 2d topological insulator edge [Fu 09a]

$$\mathcal{H}_{\mathrm{TI}} = up\sigma_z\tau_z - \mu\tau_z + \Delta\tau_x + B\sigma_x \tag{3.1}$$

in the Nambu spinor basis $(\psi_\uparrow, \psi_\downarrow, \psi_\downarrow^\dagger, -\psi_\uparrow^\dagger)$, where σ and τ denote Pauli matrices in spin and particle-hole space, u is the edge-state velocity, B is the Zeeman field, Δ the proximity strength, and μ the chemical potential. The energy spectrum can be obtained by squaring the Hamiltonian twice $E_{\mathrm{TI}}^2 = (up)^2+\mu^2+\Delta^2+B^2\pm 2\sqrt{B^2\Delta^2 + B^2\mu^2 + (up)^2\mu^2}$. At $p = 0$ we find for the energy of the lower band involving the minus sign

$$E_{\mathrm{TI},-}(p=0) = \left|B - \sqrt{\Delta^2+\mu^2}\right| \tag{3.2}$$

and the gap closes when $B^2 = \Delta^2+\mu^2$. We can therefore distinguish two gapped phases dominated by B or $(\Delta^2+\mu^2)^{1/2}$ which are separated by a gapless critical point where the two quantities are equal.

We now show that interfaces between the B and Δ dominated phases support Majorana bound states as shown schematically in Fig. 3.2. We follow [Oreg 10] setting $\mu = 0$ and $B = \Delta + bx$ with the spatial coordinate x so that the phase boundary lies at $x = 0$.

By squaring the Hamiltonian we obtain

$$\mathcal{H}_{\mathrm{TI}}^2 = B^2 + \Delta^2 + 2B\Delta\tau_x\sigma_x + ub\sigma_y\tau_z + (up)^2. \tag{3.3}$$

Using $U^\dagger = (\tau_z - i\tau_x - i\sigma_x\tau_z + \sigma_x\tau_x)/2$ we find that $U\mathcal{H}_{\mathrm{TI}}^2U^\dagger$ is diagonal with entries $(up)^2+(B\pm\Delta)^2\pm ub$. The entries that involve $B-\Delta$ have the form of a harmonic oscillator with energies $E^2 = 2ub(n+1/2) \pm ub$. Thus there is exactly one zero mode localized at the interface whose wavefunction is a Gaussian $\sim \exp(-x^2/2l^2)$ with a localization length $l = \sqrt{u/|b|}$. Undoing the rotation shows that the lowest excitation is indeed a Majorana state $\gamma = \gamma^\dagger = (\psi_\uparrow + \psi_\uparrow^\dagger - i\psi_\downarrow + i\psi_\downarrow^\dagger)/2$. The shift $-ub$ in the bound state energies from half integer to integer quanta and the occurrence of a single zero mode is due to the Dirac spectrum and parallels the shift of bound state energies in Abrikosov vortices in 2d p-wave superconductors discussed in Sec. 2.1.

As argued above the Δ dominated phase can be mapped onto a p-wave superconductor, for which Majorana end states are expected to occur. Thus one is tempted to associate the B dominated phase with the trivial vacuum. This is refuted by an interesting duality of the model in Eq. (3.1): for $\mu = 0$ the Hamiltonian is invariant under the exchange of magnetic and superconducting quantities $(\Delta, \tau) \leftrightarrow (B, \sigma)$ [Nils 08, Jian 13]. The duality of the two gapped phases thus suggests that both phases have topological properties.[1] When discussing the topological 4π Josephson effect in Sec. 3.3.2, we will see that both phases indeed exhibit signatures of a nontrivial phase either in the conventional or the magneto-Josephson effect [Jian 13]. Note that the nonexistence of a trivial phase is a consequence of the Dirac spectrum of the TI edge. This model does not have a genuine vacuum phase corresponding to the atomic limit of the Kitaev chain as it remains gapless for $B = \Delta = 0$ even in the limit $\mu \to -\infty$.

Although topological insulators in two and three dimensions are readily available in experiment, only little progress has been made towards the realization of effective p-wave superconductors via the proximity effect since the proposal of Fu and Kane [Fu 08]. Several groups have studied the Josephson effect on top of a 3d TI [Will 12, Maie 12, Veld 12, Oost 13, Cho 13, Soch 13, Kurt 13], but clear signatures of Majorana modes have not been observed. In two recent works [Hart 13, Prib 14] the authors report a supercurrent induced in the edge of a 2d topological insulator. This may represent a major step towards the realization of zero-dimensional Majorana bound states. Possible signatures of Majorana states in Josephson junctions on a TI edge have been discussed, e.g., in [Fu 09a] (see also Sec. 3.3.2).

[1] In a mapping of the TI edge low-energy degrees of freedom to a p-wave superconductor the B dominated phase indeed corresponds to the trivial phase. Nevertheless, the B phase can also be mapped to a topological phase in a different model.

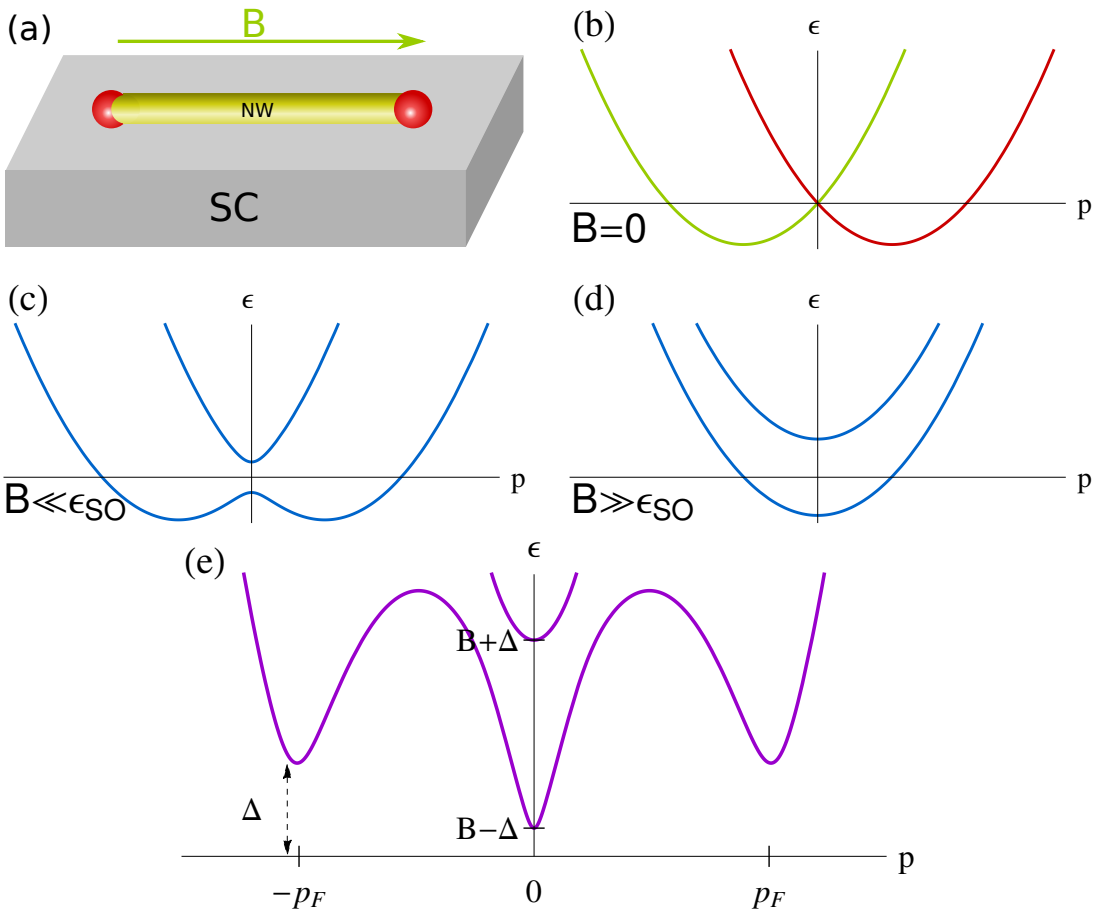

Figure 3.3.: (a) A semiconductor quantum wire placed on top of a superconductor and subject to a magnetic field perpendicular to the direction of the effective Rashba spin-orbit field may exhibit Majorana bound states at its ends. (b-d): Normal band structure of a semiconductor quantum wire for (b) $B = 0$ (with the two spin components marked by different colors), (c) $B \ll \epsilon_{so} = mu^2$ and (d) $B \gg \epsilon_{so}$. (e) Excitation spectrum of the superconducting quantum wire for $\Delta \lesssim B \ll \epsilon_{so}$. The spectrum has three low-energy subspaces at $p = 0$ and $p = \pm p_F$.

3.2.2. Semiconductor quantum wires

Following earlier work on two-dimensional semiconductor structures [Alic 10, Sau 10] two seminal papers [Oreg 10, Lutc 10] proposed that proximity-coupled semiconductor quantum wires host a topological superconducting phase in the presence of a magnetic field. This setup is shown schematically in Fig. 3.3(a). To understand how a topological phase can arise in this system we consider a single channel of free electrons in 1d with a Zeeman field B that pushes one spin band above the Fermi level so that only one pair of Fermi points remains [cf. Fig. 3.3(d)]. The spins at these two Fermi points are parallel

and proximity coupling to an s-wave superconductor is frustrated. If in addition Rashba spin-orbit coupling is present, the spins are tilted away from the parallel configuration, enabling proximity coupling to an s-wave superconductor. The system thus forms an effective spinless superconductor. The resulting Hamiltonian reads

$$\mathcal{H}_{\mathrm{QW}} = \left(\frac{p^2}{2m} - \mu\right)\tau_z + up\sigma_z\tau_z + \Delta\tau_x + B\sigma_x \tag{3.4}$$

in the same Nambu basis as Eq. (3.1) with Zeeman strength B, spin-orbit velocity u, proximity strength Δ, and chemical potential μ. In writing Eq. (3.4) we have assumed the magnetic field (along $\hat{x}$) to be perpendicular to the effective spin-orbit field (along $\hat{z}$) resulting in the mixing of the two spin components required for the proximity effect. We can find the eigenvalues by squaring the Hamiltonian twice $E^2 = \xi_p^2 + \Delta^2 + B^2 + (up)^2 \pm 2\sqrt{\Delta^2 B^2 + B^2\xi_p^2 + (up)^2\xi_p^2}$ with $\xi_p = p^2/2m - \mu$. At $p = 0$ we find $E = \pm B \pm \sqrt{\Delta^2 + \mu^2}$ and the gap closes when $B^2 = \Delta^2 + \mu^2$. Similar to the TI edge the competition between Zeeman field and superconductivity induces a phase transition between the two gapped phase. We can easily convince ourselves that the gap does not close at any other value of the momentum.

An important difference to the TI-edge proposal, however, is the nature of the phases. In the limit of large B the normal dispersion has only a single band crossing the Fermi level. Therefore the B phase ($B^2 > \Delta^2 + \mu^2$) can be identified with the topological p-wave superconductor. On the other hand the Δ phase ($B^2 < \Delta^2 + \mu^2$) is trivial. This reversal of the phases with respect to the TI-edge proposal can be understood from the spectrum shown in Figs. 3.3(b), (c), and (e) for the case $\mu = 0$ and $B \ll \epsilon_{so}$, where $\epsilon_{so} = mu^2/2$ is the spin-orbit energy. The dispersion for $B = 0$ in Fig. 3.3(b) has three crossing points with the Fermi level at zero energy at $p = 0$ and $p = \pm p_F$ with $p_F = 2mu$. For $0 < B \ll \epsilon_{so}$ a small gap of magnitude B opens at $p = 0$ [Fig. 3.3(c)]. A pairing potential additionally opens gaps of magnitude Δ at the wings $p = \pm p_F$ and modifies the gap at the central Fermi point, which becomes $|B - \Delta|$ [Fig. 3.3(e)]. As detailed in Sec. 6 (see also App. B) the model can be effectively described in this limit by two weakly coupled low-energy subspaces: a p-wave superconductor at the wings $p = \pm p_F$ and a 2d TI edge described by Eq. (3.1) at $p = 0$. The topological invariant of the quantum wire is then determined by the sum of the individual quantum numbers of the two subspaces. While the outer subspace represents a p-wave superconductor deep in the topological phase (i.e., the chemical potential is inside the band), the inner subspace at $p = 0$ depends on the competition of B and Δ as we have seen in the previous section. In the Δ phase the inner subspace is equivalent to another topological p-wave superconductor with opposite sign of the effective p-wave pairing amplitude and the topological quantum numbers add up to zero. Thus the presence of the wings of the spectrum at $p = \pm p_F$

are responsible for the reversal of the topological phases between the quantum-wire and TI-edge models. In Sec. 6 we substantiate this interpretation by numerically calculating the subgap spectrum of topological Josephson junctions. Indeed, we can identify hybridized Majorana bound states originating from both low-energy subspaces in the Δ phase.

This discussion suggests that an s-wave superconductor [corresponding to Eq. (3.4) with B and u set to zero] can be thought of as a two-band p-wave superconductor with topological indices ± 1. In such a (topologically trivial) system the two Majorana states at each end are coupled and form a finite-energy excitation. The energy depends on details of the termination of the wire which determines the coupling between the two Majorana states [Kell 12b].

Semiconductor quantum wires are well-studied in experiment and provide a promising venue for the realization of topological phases. Proximity induced superconductivity in quantum wires with very high interface transparencies has been shown experimentally [Doh 05, Dam 06]. Driving semiconductor–superconductor hybrid systems into a topological phase furthermore requires a large Zeeman splitting to overcome superconductivity as well as strong spin-orbit coupling to twist the spins away from the direction dictated by the magnetic field and to allow for a sizable superconducting gap. Particularly promising candidates are InSb or InAs quantum wires, which exhibit considerable Rashba spin-orbit coupling with a spin-orbit energy $\epsilon_{so} \sim 250 \mu eV$ and large g factors $g_{\mathrm{InAs}} \sim 8$ and $g_{\mathrm{InSb}} \sim 50$ [Fast 07, Nils 09]. Several groups have attempted the realization of a topological phase in semiconductor wires. The current experimental status in reviewed in Sec. 3.3.

3.2.3. Chains of magnetic impurities

A third promising venue for topological superconductors involves a spatially rotating magnetic field creating a noncollinear spin configuration in a one-dimensional system. Similar to the quantum wire proposal such a system is effectively spinless but pairing can be induced via proximity to an s-wave superconductor due to the twisted spins. Indeed, a constantly winding field applied to a 1d superconductor yields the Hamiltonian

$$\mathcal{H} = \left(\frac{p^2}{2m} - \mu \right) \tau_z + \Delta \tau_x + B \cos(x \nabla \theta) \sigma_x - B \sin(x \nabla \theta) \sigma_y, \tag{3.5}$$

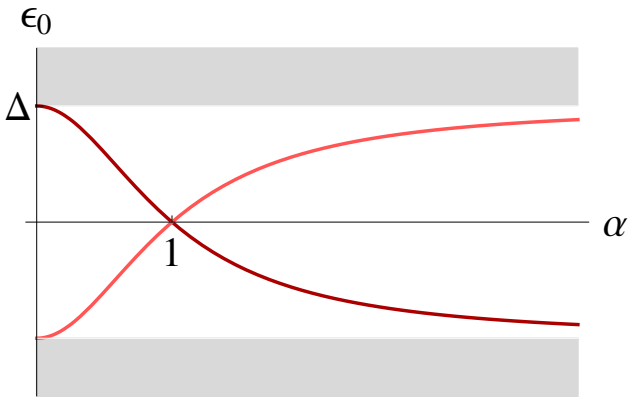

Figure 3.4.: Bogoliubov–de Gennes spectrum of a single Shiba bound state as a function of exchange splitting.

where x is the position and θ is the magnetic field angle with $\nabla\theta = \text{const}$. Performing a gauge transformation $U = \exp(ix\nabla\theta/2\sigma_z)$ yields

$$U^\dagger \mathcal{H} U = \left(\frac{p^2}{2m} - \mu + \frac{(\nabla\theta)^2}{8m}\right)\tau_z + \frac{\nabla\theta}{2m} p\sigma_z\tau_z + \Delta\tau_x + B\sigma_x, \tag{3.6}$$

which has just the same structure as the quantum wire Hamiltonian (3.4) with the winding of the magnetic field taking the role of spin-orbit interaction. This can be used to construct various alternative realizations of topological superconductors in hybrid structures without strong spin-orbit interaction, for instance, proximity-coupled quantum wires close to arrays of nanomagnets [Kjae 12] or rare earth compounds with coexisting superconductivity and helical magnetism [Mart 12].

The perhaps most promising candidate involves a chain of magnetic impurities on top of a conventional s-wave superconductor [Choy 11, Nadj 13, Nako 13b, Klin 13, Vazi 13, Brau 13, Pien 13a, Pien 14]. A classical impurity with pure exchange interaction in a 3d superconductor can be described by the BdG Hamiltonian

$$H_{\text{imp}} = \left(\frac{\mathbf{p}^2}{2m} - \mu\right)\tau_z + \Delta\tau_x + JS\delta(\mathbf{r})\sigma_z, \tag{3.7}$$

where J is the exchange coupling and S the impurity spin. Such impurities bind localized states at subgap energies called Shiba states [Yu 65, Shib 68, Rusi 69, Bala 06]. The bound state energy is

$$\epsilon_0 = \pm\Delta\frac{1-\alpha^2}{1+\alpha^2} \tag{3.8}$$

with $\alpha = \pi\nu_0 SJ$, where ν_0 the normal density of states. The Shiba state wavefunction has the form $\phi_{\text{Shiba}} \sim \exp(-r\sqrt{\Delta^2 - \epsilon_0^2}/v_F)/r$. It decays exponentially on the scale

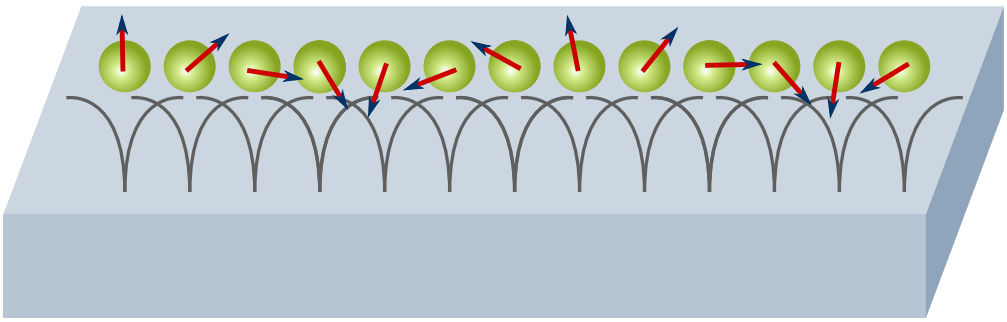

Figure 3.5.: A chain of magnetic impurities forming a spin helix. The impurities induce overlapping subgap states in the superconductor, which may form a one-dimensional topological superconductor.

of the superconducting coherence length and as a $1/r$ power-law on shorter scales. Conveniently such states can be probed directly by scanning tunneling spectroscopy [Yazd 97, Yazd 99], which considerably facilitates the detection of possible Majorana bound states. Chapter 8 examines tunneling spectroscopy of Shiba states in detail showing how competing transport mechanisms determine the differential tunneling conductance.

The Shiba state generates a quantum phase transition at $\alpha = 1$, where the Shiba state energy changes sign as shown in Fig. 3.4. At the transition the spin of the ground state of the superconductor changes by $1/2$. For quantum spins a very similar phase transition occurs between the BCS ground state at weak exchange coupling and a Kondo state when the exchange coupling is strong enough to break a Cooper pair in order to screen the impurity [Bala 06, Fran 11, Baue 13, Yao 14]. A chain of impurities leads to the formation of an impurity band in the gap of the superconductor. For deep Shiba states when $\alpha \sim 1$ the band crosses zero energy and a topological phase is supported once the impurity band itself turns superconducting.

In order to induce superconductivity in the impurity band it is envisioned that the impurities' magnetic moments form a spin helix due to RKKY interaction. While for the one-dimensional RKKY interaction a spin helix with wavevector $2k_F$ is stable [Kitt 68], a one-dimensional chain on a three-dimensional substrate generally exhibits ferromagnetic or antiferromagnetic ordering. Here the substrate is superconducting which suppresses the susceptibility at wavevector $q = 0$ (this has been first discussed for the 3d susceptibility in [Ande 59]) making ferromagnetism unfavorable and supporting the formation of a spin helix. In addition, spin-orbit interaction in the substrate can cause helical ordering of spins by inducing a Dzyaloshinsky–Moriya interaction (for one and two-dimensional systems see [Imam 04]). There is some evidence for such a spin helix on three dimensional metal surfaces [Menz 12].

Assuming that a spin helix forms one can derive an effective tight-binding model in terms of the helical Shiba states induced by the spin chain as shown in Fig. 3.5. In this model on-site pairing is suppressed since the individual impurities are spin polarized, but the noncollinear spins on neighboring atoms allow for nearest neighbor pairing. If the electron and hole branches of the impurity band inside the gap overlap at the Fermi level the pairing correlations open a gap in the impurity band turning it into an effective one dimensional spinless superconductor. This suggests that the impurity chain can effectively be described by the Kitaev model (2.6). This is indeed the case for very short coherence lengths comparable to the lattice spacing $\xi \sim a$ when the Shiba states decay exponentially $\sim \exp(-x/\xi)$. In contrast, for long coherence lengths $\xi \gg a$, which is typically the case in experiments, the Shiba states have a power-law decay on scales shorter than ξ giving rise to long-range hopping and pairing terms. In Ch. 7 we derive the corresponding effective tight-binding model and discuss the remarkable implications of the long-range terms on the topological phase diagram and the Majorana bound states.

Finally we point out that a ferromagnetic chain can also host a topological superconducting phase in the presence of spin-orbit coupling in the superconducting substrate. A similar setup has been studied in [Duck 11, Chun 11], where a halfmetallic wire in proximity to a spin-orbit-coupled superconductor has been shown to host a topological phase. By virtue of the transformation U in Eq. 3.6 the model for the helical spin chain derived in Ch. 7 equally describes a ferromagnetic chain on top of a superconductor with Rashba spin-orbit coupling, where the helix pitch corresponds to the spin-orbit length λ_{so}. This mapping is valid in the case of large impurity spacing $k_F a \gg 1$ and not too strong spin-orbit interaction $k_F \lambda_{\mathrm{so}} \gg 1$, where k_F is the Fermi momentum.

3.3. Experimental signatures of topological superconductivity

For experimental purposes the one-dimensional realizations of topological superconductors are most promising. In the proposals outlined in the previous section the Majorana bound states are pinned to domain walls and it is possible to tune through the topological phase transition with gates [Oreg 10, Lutc 10], magnetic fields [Fu 08, Li 14], or supercurrents [Romi 12, Ront 14]. Moreover a variety of methods for the characterization and manipulation of bound states in one-dimensional superconductors exist. In this section we discuss the most important experimental signatures in one dimension and provide an overview over the current status of experimental work.

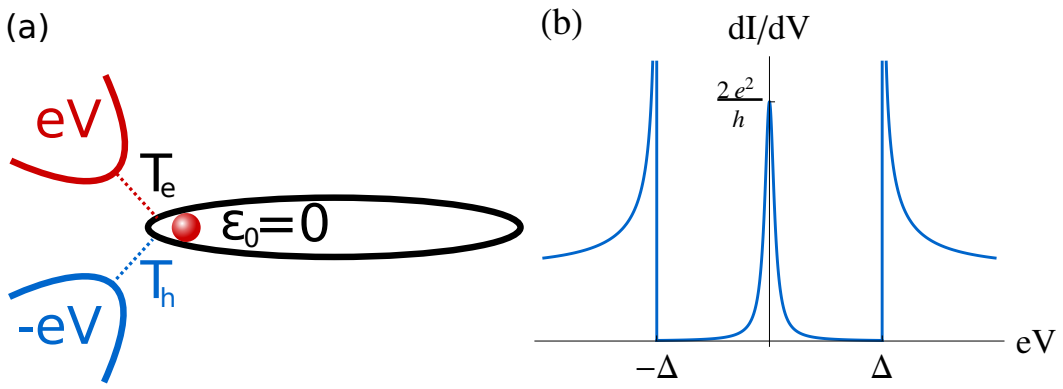

Figure 3.6.: (a) Resonant Andreev reflection in an $N-S$ junction can be seen as coupling an isolated level at ϵ_0 to an electron lead at energy eV (red) and a hole lead at energy $-eV$ (blue). For a Majorana state the ingoing electrons and outgoing holes have equal transmission probability through the tunneling barrier, which results in a quantized zero-bias peak in the differential conductance. (b) Typical differential conductance trace of a $N-S$ tunnel junction hosting a Majorana bound state at zero temperature. The zero-bias conductance peak of quantized height $2e^2/h$ serves as a signature of the Majorana states. The peaks at $|eV| = \Delta$ originate from the BCS singularity in the superconductor's density of states.

3.3.1. Conductance signatures

Current experimental efforts to detect signatures of Majorana bound states mainly focus on conductance measurements. As predicted in [Law 09, Flen 10] tunneling into a Majorana end state yields a quantized conductance of $2e^2/h$. Consider a junction of a normal metal (N) and a superconductor (S) with a tunnel barrier in between. Such a setup can be realized, for instance, by tunneling from an STM tip or by contacting the quantum wire with a normal electrode at one end and inducing a tunnel barrier with gates.

There are two principle mechanisms responsible for transport through an $N-S$ junction: tunneling of single-electrons and Andreev reflection. At subgap voltages the superconductor can only accommodate single electrons by exciting subgap quasiparticles and a dc current requires relaxation of these quasiparticle states (so-called quasiparticle poisoning), e.g., by phonon-induced transitions to the continuum. Tunneling spectroscopy measurements in $N-S$ and $S-S$ junctions including such relaxation processes are discussed in detail in Sec. 8. At low temperatures we may neglect quasiparticle poisoning and only consider Andreev reflection as the dominant transport mechanism.

Bound states resonantly enhance Andreev reflection and therefore appear as peaks in the differential conductance as a function of bias voltage V. Resonant Andreev reflection

is equivalent to tunneling between two reservoirs through a resonant level as depicted in Fig. 3.6(a), where the tip serves as the lead for the incoming electrons at energy eV and the outgoing holes at $-eV$ [Law 09] (see also [Mart 13] and Sec. 8). The peak height of such a resonance is given by the usual expression for resonant tunneling [Naza 09]

$$\left(\frac{dI}{dV}\right)_{\text{reson.}} = \frac{2e^2}{h}\frac{4T_eT_h}{(T_e+T_h)^2}, \tag{3.9}$$

where $T_{e/h}$ are the electron and hole tunneling probabilities. When the superconductor is in a topological phase the junction harbors a Majorana state at zero energy which thus appears as a zero-bias peak. Since the Majorana is a quasiparticle with an equal superposition of electrons and holes the incoming electrons and outgoing holes, both at zero energy, have equal transmission probability through the barrier $T_e = T_h$. As a result the conductance is equal to the superconducting conductance quantum $2e^2/h$ independent of the tunneling strength. The differential conductance as a function of bias voltage for a normal metal–topological superconductor junction is shown in Fig. 3.6(b).

Such a quantized zero-bias peak in the differential conductance can serve as an experimentally accessible fingerprint of a Majorana bound state. Indeed, in several experiments a zero-bias peak appearing at finite magnetic fields has been observed in the conductance of superconducting quantum wires [Mour 12, Das 12, Deng 12a, Lee 12, Chan 13, Finc 13, Chur 13, Lee 14], although not all of the reports attribute the observations to Majorana bound states. In all cases the reported zero-bias conductance is much smaller than the conductance quantum. Such a reduction in height can be explained by a combination of temperature broadening and multichannel effects. A detailed discussion of the peak height in a general multichannel wire is given in Sec. 4. At the same time a nonquantized peak at zero-bias can have various origins other than topological superconductivity:

(a) The Kondo effect in superconductors can result in a zero-bias peak above a certain strength of magnetic field. In normal metals the Kondo effect leads to screening of an impurity spin by electrons at the Fermi level and manifests itself as a zero-bias peak without requiring an external magnetic field. By contrast, in a superconductor the condensate depletes the density of states at the Fermi level leaving the Kondo impurity unscreened. An applied magnetic field reduces pairing and when the Kondo temperature is large enough screening is established once the density of states at the Fermi level becomes finite. In this case the zero-bias peak only appears at finite fields mimicking the behavior of a Majorana peak only appearing beyond a critical magnetic field. Importantly, quasiparticle subgap states or a soft gap can lead to coexistence of a Kondo peak and superconductivity as observed in Refs. [Lee 12] and [Chan 13].

(b) Disorder can result in a spectral peak at the center of the gap resulting in a zero-bias peak. In disordered topological superconductor wires (in class D) close to the critical point disorder-induced subgap levels cluster at zero-energy [Bagr 12, Neve 13]. At the end of the superconducting domain, e.g., in the $N-S$ junction possibly hosting Majorana states, this leads to the formation of a small region (an effective "quantum dot" in the language of Ref. [Bagr 12]), where a gapless diffusion mode forms. This mode originates from coherent scattering off order parameter fluctuations due to disorder and it appears as a zero-bias peak in the conductance. The same phenomenon can alternatively be understood in terms of weak antilocalization in class D [Piku 12]. At zero energy the Andreev-reflected holes are the phase conjugate of the incident electrons leading to constructive interference which enhances the conductance. The phase conjugation relies on particle-hole symmetry only present at zero energy and therefore weak antilocalization leads to a zero-bias peak. The general statements above only apply to ensemble averages rather than individual disorder realization. Nevertheless, it can be argued [Bagr 12, Piku 12, Neve 13] that the zero-bias excess conductance of the ensemble average originates mainly from certain disorder configurations. Thus a zero-bias peak occurs in specific samples and may even persist upon a variation of parameters.

One instance where a disorder-induced zero-bias peak could persists for a certain range of magnetic field occurs in disordered proximity-coupled quantum wire. When the gap is smaller than a certain threshold the density of states of such wires develops a Dyson singularity at zero energy [Brou 11b]. Since the gap is small in the vicinity of the topological critical point, a zero-bias peak can occur in a finite range of magnetic field on *both* sides of the topological phase transition. This effect is exclusively due to clustering of disorder-induced subgap states near zero energy but mimics the typical magnetic field dependence of Majorana peaks in finite wires.

(c) Pairs of Andreev bound states can be close to zero energy resulting in a zero-bias conductance peak. Usually Andreev bound states can be identified from their magnetic field dependence as they disperse as $g\mu_B B/2$. The usually very large g factor makes such states easily discernible as in Ref. [Mour 12]. Nevertheless, it is possible for Andreev states to remain near zero energy in a finite range of magnetic field with a much weaker field dependence than the Zeeman energy. This occurs due to a combination of level repulsion and a decreasing superconducting gap, which pushes all subgap levels towards the center of the gap. This effect was observed experimentally and supported by theoretical calculations in Ref. [Lee 14]. Moreover, the authors comment that the presumed conductance signatures of Majorana particles in Ref. [Das 12] are consistent with weakly dispersing Andreev bound states.

Such zero-bias peaks originating from Andreev bound states can be ruled out by us-

ing, e.g., InSb wires with a g factor $g \sim 50$ ensuring a strong dispersion of Andreev states.

(d) Pairs of end states in trivial s-wave superconducting wires can be close to zero energy. A 1d s-wave superconductor is topologically equivalent to two copies of a p-wave wire with indices ± 1. Such a wire hosts two bound states at a single end, which can be thought of as two coupled Majorana states originating from the two p-wave channels. For an abruptly terminated wire the coupling energy is usually of the order of the gap but when the confining potential is smooth the coupling can become exponentially suppressed [Kell 12b]. Similar low-energy subgap states appear in quasi one-dimensional p-wave wires [Kell 12a, Pott 12, Ried 12]. If close enough to zero energy such states can appear as zero-bias peaks in the differential conductance although the system is in a trivial phase.

A different setup has been investigated in Ref. [Deng 12a], where a zero-bias conductance peak has been observed in an $S-S$ junction and attributed to the presence of Majorana bound states. One likely origin of such a peak is a supercurrent flowing across the Josephson junction. The supercurrent originating from the Majorana states, however, cannot be distinguished from the ordinary bulk supercurrent or current through Andreev bound states in conductance measurements.[2] On the other hand, tunneling from the continuum into the zero-energy Majorana state produces a peak at $eV = \Delta$ and not zero. Unfortunately, a peak at Δ can also originate from pure Andreev reflection without Majoranas and it thus does not provide unambiguous evidence for the Majorana.

Nevertheless, it is possible to differentiate between the two processes. At moderate temperatures single electron tunneling into the Majorana state is possible due to phonon induced relaxation (see Ch. 8 for a general discussion of tunneling into bound states in a superconductor). As a consequence in the limit of very weak tunneling the Majorana peak height should be linear in the junction transmission T, whereas an Andreev process involves two tunneling events and scales as $\sim T^2$. The presence of single-electron tunneling processes proves the existence of a bound state at zero energy. Showing furthermore that this state appears only at finite magnetic fields and then remains at $eV = \Delta$ for larger fields constitutes a strong signature of a Majorana. In this sense the $S-S$ setup may be advantageous compared to an $N-S$ junction, since, for instance, weak antilocalization can be ruled out as a possible origin of the peak.

[2] In Sec. 3.3.2 we discuss how the Majorana mediated supercurrent can be differentiated by phase-sensitive methods.

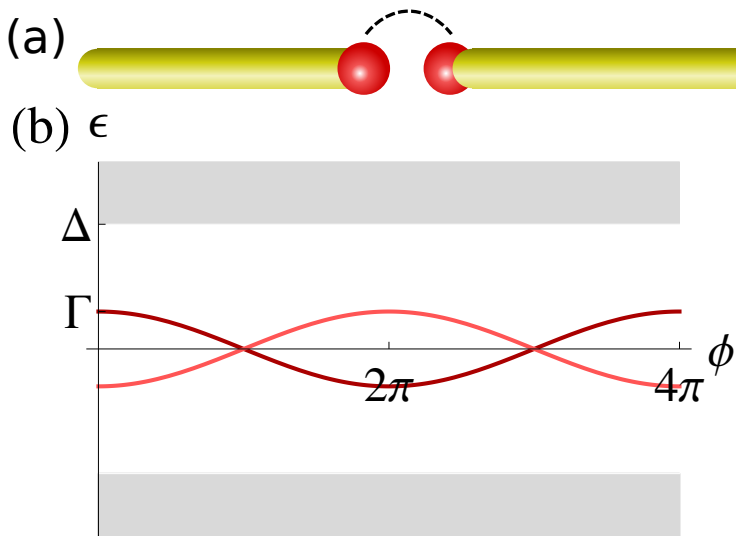

Figure 3.7.: (a) A Josephson junction between two topological superconductors hosting two Majorana bound states. (b) Spectrum of a topological Josephson junction. The two Majorana excitations have period 4π in the superconducting phase difference.

3.3.2. The 4π Josephson effect

Tunnel junctions between two superconductors exhibit the Josephson effect, where a supercurrent flows only due to a phase difference between the superconductors. This phase difference can be controlled, for instance, by threading a flux through a superconducting ring. The Josephson current is periodic in the superconducting phase difference corresponding to a flux period of $h/2e$. This period reflects the charge $2e$ of Cooper pairs carrying the supercurrent. The Josephson current flowing between two superconductors in the topological phase is obviously affected by the Majorana bound states located at the junction shown in Fig. 3.7(a). The Majorana states form single-particle states at zero energy allowing individual quasiparticles with charge e to cross the junction giving rise to a flux period h/e. In terms of the phase difference the Josephson current becomes 4π periodic [Kita 01].

In order to substantiate this heuristic argument we consider the spectrum of two Majorana bound states γ_1 and γ_2 on two sides of an initially impenetrable barrier. We can construct a zero-energy fermionic excitation $d_0 = \gamma_1 + i\gamma_2$ from the two Majoranas. Now consider an operation that adiabatically tunes the phase of the order parameter ϕ in the right superconductor from 0 to 2π. This effects the rotation $\gamma_2 \to e^{i\pi}\gamma_2 = -\gamma_2$ and the fermion d_0 then evolves to $d_{2\pi} = \gamma_1 - i\gamma_2$. Now we allow for a finite coupling through the barrier, which is weak enough that the operators d are a good description of the excitations. At zero phase difference the Majoranas acquire an energy splitting and the

fermion d_0 annihilates an excitation of energy E_0. By virtue of particle-hole symmetry $d_0^\dagger = \gamma_1 - i\gamma_2$ annihilates an excitation of energy $-E_0$. The same is true at phase difference $\phi = 2\pi$, but now $d_\pi = d_0^\dagger$ annihilates an excitation of energy $-E_0$. Thus the positive energy state at $\phi = 0$ becomes negative at $\phi = \pi$ as illustrated in Fig. 3.7(b). This shows that the excitation d has an odd number of zero-energy crossings when tuning the phase difference by 2π and hence the current $J \propto \partial_\phi E$ is 4π periodic, since fermion-parity conservation forbids transitions between the two states.

In Sec. 2.3 we discussed that an odd number of crossing points and the change of fermionic parity of the ground state associated with it is a topological property. Therefore, although the above argument assumes coupling through a weak link, the 4π-periodic Josephson effect is present for any junction as long as the two banks are in the topological phase and serves as a signature of topological superconductivity. The zero-energy crossings can also be understood from the phase diagram of the p-wave superconductor in Fig. 2.3. A phase difference $\phi = \pi$ corresponds to a junction between two p-wave superconductors with positive and negative pairing. The two banks thus have topological indices ± 1 which signals that there are two zero-energy Majorana bound states at the interface,[3] and thus the crossing occurs at $\phi = \pi$.

For the p-wave superconductor in Eq. (2.3) the bound state energy is given by $E_0^{(p)} = \Delta' p_F \sqrt{D} \cos \phi/2$, where D is the junction transparency and p_F the Fermi momentum [Kwon 04], reflecting the robust zero-energy crossings. In contrast, the energy of an Andreev bound state in a trivial s-wave superconductor junction reads $E_0^{(s)} = \Delta[1 - D \sin^2 \phi/2]^{1/2}$. Incidentally, in the case of unit transmission the two dispersions are identical with a zero-energy crossing at π. The fermion parity of the s-wave superconductor, however, does not change when the phase advances by 2π resulting in an unprotected crossing which opens for $D < 1$.

Observing this 4π periodicity in experiment requires the conservation of fermionic parity. If the parity is allowed to change, e.g. by phonon-induced transitions, the system will relax to the ground state at each value of the flux restoring 2π periodicity. Hence the observation of the 4π-periodic current in a typical junction via the dc Josephson effect might be difficult. A way out is provided in Sec. 5, where the Josephson current in mesoscopic topological superconductor rings is investigated in detail. Such systems exhibit a 4π dc Josephson effect even without fermion parity conservation. The required setup has already been realized in a recent experiment [Forn 13], where a semiconductor ring in proximity to a superconductor has been fabricated by etching techniques.

In an ac measurement the current may be 4π periodic for several cycles [Kwon 04], but

[3] The interface between two phases characterized by topological quantum numbers ν and ν' hosts $|\nu - \nu'|$ bound states.

switching events induced by the finite bias leads to a 2π-periodic average current. Signatures of the 4π periodicity can still be accessed in the finite-frequency noise [Badi 11]. A different possibility to access the 4π signature consists of a Shapiro step measurement [Jian 11b, Houz 13], where a dc and an ac voltage are applied. Resonances between the ac voltage and the phase winding due to the dc voltage result in so-called Shapiro steps in the $I - V$ characteristic [Shap 63, Tink 75]. The 4π periodicity of the bound states leads to an enhancement of every second step. Such an enhancement might be hard to detect on top of large steps due to the conventional 2π Josephson effect mediated by the bulk states (for a detailed discussion see [Houz 13]). This problem can be circumvented in a three-leg junction as described in Ref. [Jian 11b]. In this perhaps experimentally challenging setup only the 4π-periodic contribution to the current survives and the odd (conventional) Shapiro steps vanish.

The first experimental signatures of the 4π Josephson effect have been claimed in a Shapiro step measurement in Ref. [Rokh 12], where current-biased Josephson junctions in InSb quantum wires have been investigated. Instead of an enhancement of even steps the authors observed a vanishing of the first step, which they attribute to single charge transfer via Majorana bound states. Numerical results for a current-biased junction indeed indicate the vanishing of odd steps [Domi 12], but more detailed investigations are needed to rule out other possible explanations for single-charge transfer.

In Sec. 3.2.1 we have pointed out a duality of superconducting and magnetic quantities of the TI edge model in Eq. (3.1). This duality has remarkable manifestations in the Josephson effect. The dual of the superconducting phase is the angle of the magnetic field in a plane perpendicular to the effective spin-orbit field. Since the Δ dominated phase of the TI edge model is topologically equivalent to a p-wave superconductor it also exhibits a 4π Josephson effect. By virtue of the duality the B dominated phase supports a magneto-Josephson effect, which is 4π periodic in the magnetic field angle [Jian 13]. This corroborates the view that neither phase of the TI edge model is trivial as discussed in Sec. 3.2.1. The magneto-Josephson effect for the quantum wire model in Eq. (3.4) is investigated in detail in Sec. 6. In contrast to the TI edge the quantum wire has a trivial phase, which is topologically connected to the vacuum. In that phase both types of Josephson effects are trivial. The topological phase, on the other hand, displays a 4π periodicity in both the conventional and the magneto-Josephson effect.

3.4. Other signatures and physical realizations

An overwhelming number of topological superconductor realizations in one dimension has been put forward since the pioneering work of Fu and Kane [Fu 08], ranging

from variants of the three proposals presented in the previous chapters over halfmetals [Duck 11, Chun 11], 3d topological insulator nanowires [Cook 11], cold atomic systems [Jian 11a], and proximity-coupled integer quantum Hall edges to parafermions on edges of fractional topological insulators or fractional quantum hall systems [Lind 12, Chen 12, Clar 13, Vaez 13]. In addition a series of proposals to realize time-reversal invariant topological superconductors in class DIII have been made [Fu 10b, Wong 12, Deng 12b, Zhan 13, Kese 13, Nako 13a, Gaid 14, Haim 14]. In these systems the ends support Kramers pairs of zero-energy Majorana bound states protected by time-reversal and particle-hole symmetry. According to a recent work [Wolm 14] adiabatic qubit manipulations are not protected against local perturbations making Majorana Kramers pairs inept for topological quantum computing.

Many experimental signatures of Majorana bound states in addition to the ones discussed here have been predicted including the conductance of quantum point contacts [Wimm 11], thermal and magneto conductance [Akhm 11], signatures of the nonlocal transport in the correlated current [Nils 08, Fu 10a], shot noise in tunneling experiments [Bole 07], and interferometry [Fu 09b, Akhm 09, Hass 10, Benj 10, Stru 11]. Finally a list of proposals exists to realize braiding of Majoranas including spatially moving domain walls and braiding in T-junctions by means of gates [Alic 11, Halp 12] or supercurrents [Romi 12], manipulating couplings between different Majoranas with gates [Sau 11] or fluxes [Heck 12], and changing the parity of various Majorana qubits using quantum dots [Flen 11]. Moving domain walls hosting Majorana bound states have been investigated in [Karz 13].

The above compilation illustrates the large variety of condensed matter systems supporting topological superconducting phases, which can be traced back to the generic requirements for such a phase to be realized: s-wave superconductivity in conjunction with broken spin degeneracy and spin-rotation symmetry. To obtain undisputed evidence for the existence of Majorana bound states, however, remains a challenging task. For instance, a proximity-coupled quantum wire is typically hard to control using gates or magnetic fields due to screening from the nearby superconductor. Moreover the combination of superconductivity as well as time-reversal and spin-rotation symmetry breaking gives rise to a number of distinct physical phenomena which are expected to appear under similar conditions as Majorana bound states. We have encountered a few examples such as the Kondo effect, Andreev bound states or weak antilocalization in the discussion of the conductance signatures in Sec. 3.3.1. This demonstrates that signatures associated with a single Majorana state may have various possible origins, which must be ruled out to verify the existence of Majorana bound states. One goal of this thesis is to improve the theoretical understanding of various experimental setups currently under investigation in order to clarify how Majoranas can be uniquely identified. We

finally remark that bullet-proof evidence for Majorana states requires the observation of their nonlocal properties (e.g., in current correlations) or even braiding.

4. Zero-bias Majorana peak in disordered multi-subband quantum wires

A recent experiment [Mour 12] reports the realization of proximity-induced topological superconductivity and the formation of Majorana bound states in InSb quantum wires. Following the theoretical suggestions reviewed in Sec. 3.2.2, superconducting order is induced in an InSb quantum wire by proximity to a Nb lead attached alongside the wire. At the other end, the quantum wire is contacted to a normal lead via a gate-induced tunnel junction. Evidence for the formation of Majorana bound states is found through measurements of the differential conductance, which exhibits a zero-bias peak when a magnetic field is applied in certain directions (cf. Sec. 3.3.1). In subsequent experiments similar results have been reported for the same system [Chur 13] and for normal-metal–superconductor structures based on InAs quantum wires [Das 12, Finc 13].

At zero temperature and in single-subband quantum wires, the Majorana-induced zero-bias peak is predicted to have a height of $2e^2/h$ [Flen 10, Law 09]. At finite temperature, the zero-bias peak broadens with its weight fixed, so that the peak height is no longer expected to reach $2e^2/h$. The expected suppression is given by the ratio of the tunnel coupling to the lead and temperature. In the experiment reported in [Mour 12] a zero-bias peak of height $\sim 0.05e^2/h$ was observed. Such a strong suppression cannot be explained within this simple theory in view of the small temperature ($T = 60mK$) and fairly high contact transparency ($\sim 25\%$) in the experiment. Furthermore, the experimental data showed no signature of a gap closing and reopening associated with the emergence of the zero-bias peak although creating a Majorana bound state requires tuning through a topological phase transition. A plausible interpretation of the observed zero-bias peak as originating from Majorana bound states necessitates resolving these apparent contradiction between theory and experiment.

In this chapter (previously published as [Pien 12b]), we consider the current-voltage characteristic of multi-subband wires — a situation which is presumably relevant to the experiment of Ref. [Mour 12]. Importantly, we find that the zero-bias peak as well the closing of the gap, which marks the topological phase transition, are suppressed under realistic conditions in clean multi-subband wires. This result provides a natu-

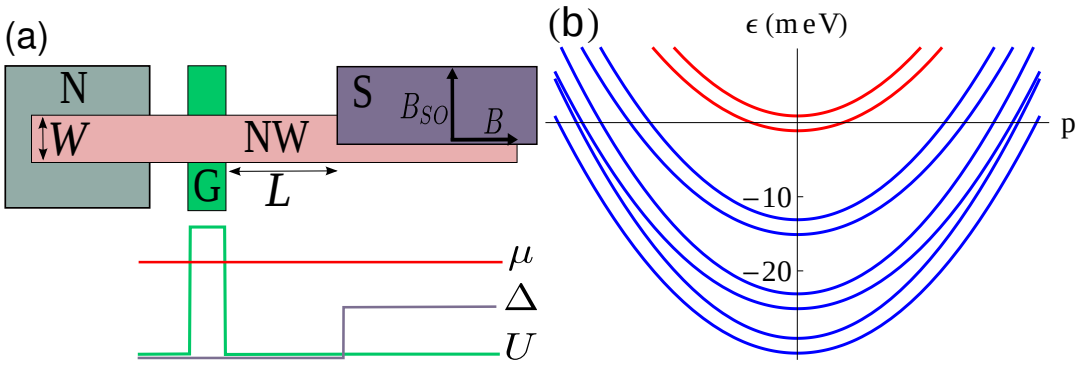

Figure 4.1.: (a) Setup of multi-subband quantum nanowire (NW) with gate-induced tunnel barrier (G) and proximity coupled s-wave superconductor (S). As in Ref. [Mour 12] we consider the conductance between the normal lead (N) and the superconductor. Subband mixing is induced through disorder in the short segment of length L between the tunnel barrier and superconductor. (b) Normal-state dispersion in the absence of disorder for four subbands with $B = 1$ meV and $m\alpha^2/2 = 50$ μeV.

ral explanation for the experimental findings in [Mour 12] and rehabilitate Majoranas as a possible origin of the zero-bias peak. Furthermore we show that, remarkably, the weight of the Majorana-induced zero-bias peak is typically enhanced as the tunnel junction becomes more disordered. The basic idea is that disorder couples the topological channel, which itself is only weakly transmitted through the barrier, with the other non-topological subbands which have higher transmission coefficients. This coupling broadens the conductance peak and hence, in the presence of a finite temperature, enhances the zero-bias conductance. The intentional inclusion of disorder in or near the barrier, either during the fabrication process of the InSb nanowires used in the experiment, or after fabrication of the device, could thus lead to an additional, strong signature of the Majorana end state. It is important to note that the mechanism discussed here is different from reflectionless tunneling [Kast 91, Quir 02, Been 92] induced by disorder on the normal side of NS tunnel junctions. A similar effect is expected if the tunnel barrier is replaced by a point contact [Wimm 11], provided the point contact is non-adiabatic.

4.1. Model system

We consider a geometry close to that of the experiment in Ref. [Mour 12] shown schematically in Fig. 4.1a. It consists of a two-dimensional multi-subband semiconducting wire with spin-orbit velocity α, chemical potential μ, and width W. At one end, the semiconductor is coupled laterally to a superconducting lead. At the other end, it is contacted to a normal metal via a tunnel barrier defined by the gate potential U. The system is

placed in a magnetic field parallel to the wire direction with Zeeman energy B. Taking the x direction to be along the wire, the system is then described by the Bogoliubov–de Gennes Hamiltonian [Oreg 10, Lutc 10, Lutc 11, Alic 12, Been 13]

$$\mathcal{H} = \left(\frac{\mathbf{p}^2}{2m} + \alpha p_x \sigma_y - \alpha_y p_y \sigma_x + U(x) + V_{\rm dis}(\mathbf{r}) - \mu \right) \tau_z - B\sigma_x + \Delta(x)\tau_x, \tag{4.1}$$

where the Pauli matrices σ and τ operate on the spin and particle-hole degrees of freedom, respectively. The parameter α_y is included for future reference and equals α for the case of Rashba spin-orbit coupling. The lateral contact to the superconductor covers the region $x > 0$, so that we set $\Delta(x) = \Delta$ for $x > 0$ and $\Delta(x) = 0$, otherwise, where Δ is the proximity-induced gap for $B = 0$. The disorder potential $V_{\rm dis}(\mathbf{r})$ is nonzero in the region $-L < x < 0$ between the gate-defined tunnel barrier and the superconducting contact only. In this region, we choose a Gaussian random potential with $\langle V_{\rm dis}(\mathbf{r}) \rangle = 0$ and

$$\langle V_{\rm dis}(\mathbf{r}) V_{\rm dis}(\mathbf{r}') \rangle = \frac{v_F^2}{k_F l_{\rm 2d}} \delta(\mathbf{r} - \mathbf{r}'), \tag{4.2}$$

where $v_F = \sqrt{2\mu/m}$ and $l_{\rm 2d}$ are the Fermi velocity and mean free path.

We numerically calculate the normal and Andreev reflection matrices $r_{\rm ee}(\varepsilon)$ and $r_{\rm he}(\varepsilon)$ for the Hamiltonian (4.1), using the technique described in Ref. [Brou 11b]. The differential conductance $G(V)$ is then evaluated according to [Blon 82]

$$G(V) = \frac{e^2}{h} \mathrm{tr} \left[1 + r_{\rm he}(eV) r_{\rm he}(eV)^\dagger - r_{\rm ee}(eV) r_{\rm ee}(eV)^\dagger \right],$$

where the trace is in spin and channel space. In a wire of width W lateral momenta are quantized as $p_{y,n} = \hbar n \pi / W$ with $n = 1, 2, \ldots$. In our numerical calculations we use an effective mass $m = 0.015 m_e$, m_e being the bare electron mass, proximity induced gap $\Delta = 250$ μeV, spin-orbit energy $m\alpha^2/2 = 50$ μeV, and width $W = 110$ nm.[1]. This choice corresponds to the parameters of the InSb quantum wires used in Ref. [Mour 12]. The chemical potential in the nanowire is chosen as $\mu = 32.1$ meV, corresponding to $N = 4$ occupied channels (cf. Fig. 4.1b). The subbands in the nanowire are therefore separated by several meV and for Zeeman energies less than 1.5 meV (corresponding to $B < 1$ T for InSb) only the highest channel (subband index $n = N = 4$) can be in the topological phase.

[1] Here we assume the same induced gap in all subbands. We have confirmed numerically that different induced gaps (cf. Ref. [Faga 05]) lead only to minor changes in the peak width, leaving our conclusions qualitatively unchanged.

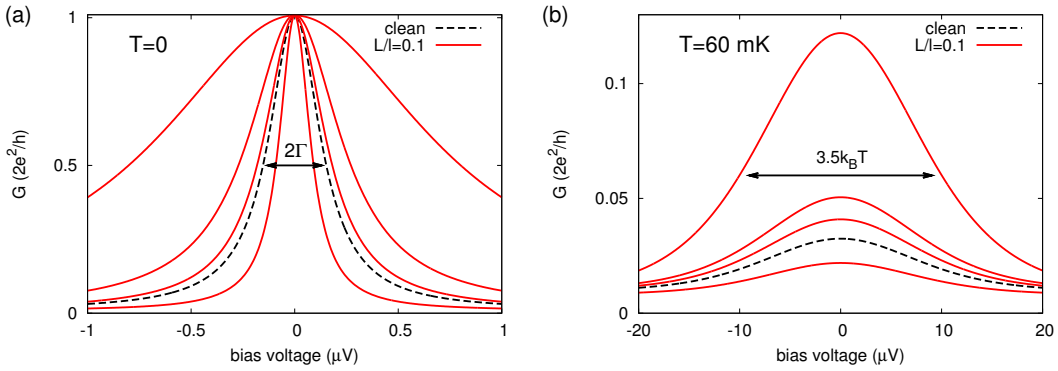

Figure 4.2.: (a) Zero-bias conductance peak at zero temperature in a quantum wire with $B = 0.5$ meV and $N = 4$ transverse subbands, one of which is in the topological phase with barrier transmission $T_4 = 0.01$. The three nontopological subbands have transmissions $20T_4$, $10T_4$, and $4T_4$. The red curves show the conductance for four different disorder configurations with $l = 10L$. The black dashed line shows the peak shape for the clean wire. (b) Same as in (a), but for a temperature $T = 60$ mK, larger than the zero-temperature peak width.

4.2. Clean multi-subband quantum wires

We first consider a clean multi-subband wire with $\alpha_y = 0$. To a good approximation, a gate-induced tunnel barrier exposes the electrons to a potential which depends only on the coordinate x along the wire. Consequently, the tunnel barrier does not mix the transverse subbands (channels) of the quantum wire and the subbands can effectively be considered as independent. Each subband is characterized by a Fermi velocity $v_{F,n} = \frac{1}{m}(2m\mu - p_{y,n}^2)^{1/2}$, an excitation gap Δ_n, and a transmission coefficient T_n of the gate-induced tunnel barrier. Since the highest occupied subband $n = N$ determines whether the wire is in the topological phase, we refer to this subband as the "topological subband." A nontrivial topological phase exists if $B^2 > B_N^2 = \Delta^2 + (\mu - p_{y,N}^2/2m)^2$ [Lutc 10, Oreg 10]. At the topological phase transition, *i.e.*, for $B = B_N$, the topological gap Δ_N vanishes, whereas the excitation gaps for the other subbands remain finite.

The topological phase is characterized by a zero-bias conductance peak

$$G(V) = \frac{2e^2}{h}\frac{\Gamma^2}{\Gamma^2 + (eV)^2}, \tag{4.3}$$

with width $\Gamma = \beta_0 \Delta_N T_N$ if $L \ll \xi = \hbar v_{F,N}/\Delta_N$. The numerical constant β_0 takes the value $\beta_0 \approx 0.375$ for the range of parameters we investigated ($T_N \ll 1$, Δ between 0 and 60 μeV). This width may be very small, since the transmission coefficient T_N of the topological subband is typically much smaller than the transmission coefficients of the

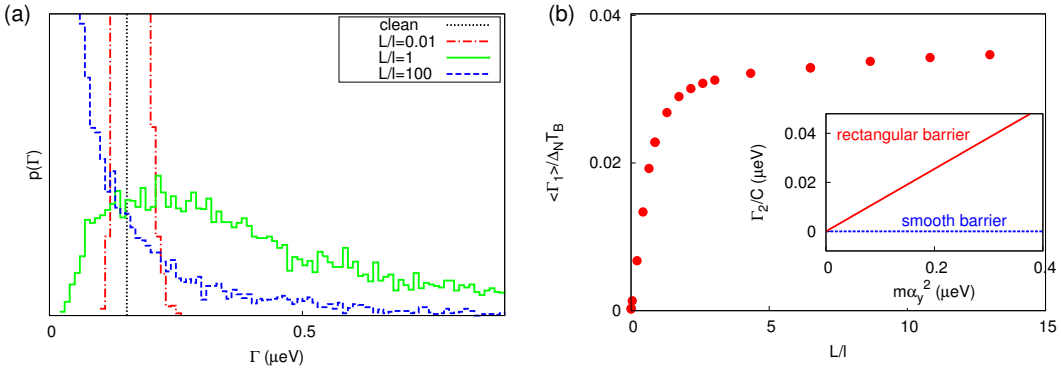

Figure 4.3.: (a) Probability distribution of the zero-bias peak width Γ in the presence of disorder in the nanowire segment $-L < x < 0$ between the superconducting part and the barrier for a multi-channel wire with the same choice of parameters as in Fig. 4.2. With increasing disorder, Γ increases on average (red and green curve) due to subband mixing. For $L \gg l$ Anderson localization reduces the overall transparency of the junction, causing Γ to decrease again in the case of very strong disorder (blue curve). (b) Ensemble average of the contribution Γ_1 from disorder-induced subband mixing to the width Γ of the zero-bias peak as a function of disorder strength in the segment $-L < x < 0$. The peak width is normalized by the normal state conductance $G_B \equiv (2e^2/h)NT_B$ to focus on the effects of subband mixing and to eliminate changes in the overall transparency by Anderson localization. Inset: Contribution Γ_2 to the peak width from lateral spin-orbit coupling for a rectangular barrier (red crosses) and a Gaussian barrier (blue dashed line). In both figures the parameters of the barrier potential have been chosen such that only T_1 differs appreciably from zero.

other channels. (For the Nth subband to be topological, it is important that its band bottom be close to the chemical potential.) At finite temperature, the conductance peak is thermally broadened,

$$G(V,T) = \int_{-\infty}^{\infty} d\varepsilon G(\varepsilon,0)\frac{df}{d\varepsilon}(eV-\varepsilon,T), \tag{4.4}$$

where $f(\epsilon,T)$ is the Fermi distribution function at temperature T. Thermal broadening preserves the weight of the zero-bias peak. For $k_\mathrm{B}T \gg \Gamma$, the peak width is of order $k_\mathrm{B}T$, whereas the height $(2e^2/h)(\pi\Gamma/4k_\mathrm{B}T)$ is inversely proportional to temperature. Both regimes are illustrated in Fig. 4.2.

4.3. Effect of disorder

If the disorder is limited to the segment of the semiconductor wire that is not in contact with the superconductor, i.e., to $-L < x < 0$ (cf. Fig. 4.1), it has no effect on the existence

of the topological phase [Brou 11a]. However, impurity scattering in the "normal" part of the wire has profound consequences for the weight of the zero bias peak associated with the existence of the topological phase. The underlying reason is the large disparity in the transparencies of the different subbands, with the topological subband having the smallest transparency T_N. Mixing of subbands by impurity scattering allows for the coupling of the topological subband to the normal lead via the lower subbands with higher transparency.

The effect is illustrated in Fig. 4.2, where we show the shape of the zero-bias peak for various disorder configurations, such that the distance L between gate-induced tunnel barrier and the superconducting contact equals one tenth of the characteristic scattering length

$$l = l_{2\mathrm{d}} v_{F,1} v_{F,N} / v_F^2. \tag{4.5}$$

A systematic dependence on disorder strength can be seen in Fig. 4.3. Panel (a) shows the probability distribution of the zero-temperature peak width for different values of the ratio L/l. We conclude that already a moderate amount of disorder causes subband mixing and an increase in the peak width. At very strong disorder, $L \gg l$, Anderson localization suppresses the overall coupling to the normal lead, leading to a decrease of the weight of the zero-bias peak. This effect is not related to subband mixing and can be removed by normalizing the peak weight to the normal-state conductance $G_B \equiv (2e^2/h) N T_B$ of the device; see Fig. 4.3(b). The average peak width from disorder-induced subband mixing saturates for $L/l \gg 1$ to $\langle \Gamma_1 \rangle = \beta_1 T_B \Delta_N$, where β_1 is a numerical factor of the order of 0.1, the exact value depending on the barrier transparencies for different subbands and spin mixing due to the magnetic field.

4.4. Other causes of subband mixing

The lateral spin-orbit term proportional to α_y in Eq. (4.1) may be an additional source of subband mixing. For small α_y its contribution to the width of the zero-bias peak is

$$\Gamma_2 = \beta_2 C m \alpha_y^2, \qquad C = \frac{\Delta_N T_B}{W^2 k_F^3 v_{F,N}} \tag{4.6}$$

proportional to α_y^2, with a numerical prefactor β_2 that depends on the precise shape of the barrier. In the inset of Fig. 4.3(a) we show its effect on the conductance of a clean wire for a long and low tunnel barrier, so that only the lowest subband $n = 1$ has an appreciable transmission. For a rectangular barrier, the subband mixing caused by lateral spin-orbit coupling is maximal, but still weak in comparison to the maximal subband

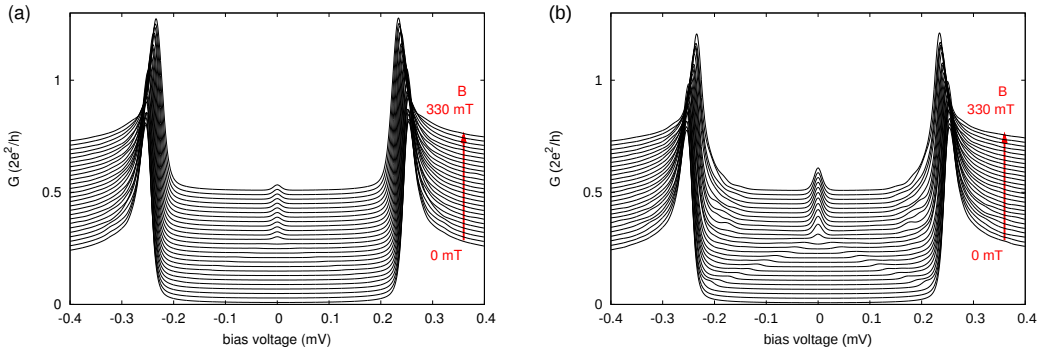

Figure 4.4.: (a) Differential conductance vs bias voltage in a clean multichannel nanowire for increasing B from 0 to 0.5 meV (750 mT in InSb) in steps of 0.02 meV with the realistic parameters [Mour 12] $\alpha_y = 0$, $T = 60$ mK ($k_{\mathrm{B}}T = 5$ μeV), $L = 10$ nm, and $T_N = 0.01$. The $B > 0$ traces are offset vertically for clarity. The formation of a Majorana bound states is reflected in the emergence of a zero-bias peak. The corresponding closing of the topological gap is hardly discernible due to the low transparency of the topological channel. For $B = 0$ there are coherence peaks at the proximity induced gap $\Delta = 0.25$ meV. For larger Zeeman fields the bulk gap of the lower channels is decreased consistently with expectations. (b) Same as (a) but with weak disorder in the region $-L < x < 0$ adjacent to the barrier. All traces are calculated for the same disorder configuration with a scattering length $l = 10L$. The zero-bias peak and the signature of the topological gap closing are considerably enhanced.

mixing obtained from disorder, since for $B = 0.5$ meV we obtain $C \approx 10^{-4}$. For a smooth barrier, which is the experimentally relevant limit, the numerical prefactor β_2 becomes vanishingly small and lateral spin-orbit coupling does not give any appreciable subband mixing. Subbands may also be mixed by a gate-defined barrier that is not perpendicular to the direction of the wire. The mixing effect is maximal if the barrier is rectangular, and effectively absent for smooth barriers.

4.5. Current-voltage characteristic and topological gap

Unlike in single-channel models for spinless p-wave superconductors, multi-subband models are characterized by the coexistence of multiple superconducting gaps in different sections of the Fermi surface. Specifically, the proximity-induced gaps in the lower subbands are only weakly affected by the applied magnetic field. In contrast, the highest occupied subband should have a gap closing when it enters into the topological superconducting phase at the critical magnetic field. Thus, it is interesting to investigate to which degree the differential conductance contains signatures of the gap closing at the

topological phase transition and how disorder near the barrier affects these signatures.

In Fig. 4.4(a), we show the differential conductance versus bias voltage for a clean multichannel quantum wire at $T = 60$ mK. At the critical Zeeman field of the topmost channel $B_c = 0.27$ meV a peak appears at zero bias voltage. Since the topological channel is only weakly transmitted through the barrier, its contribution to the conductance is weaker than that of the other channels. In conjunction with density of states effects [Stan 12], this explains the very weak signature of the topological gap closing in transport in Fig. 4.4(a), consistent with the absence of the topological gap in the experimental measurements of Ref. [Mour 12]. As for the zero-bias peak, the gap-closing feature in the differential conductance will also be significantly enhanced by disorder in the barrier region. This is shown in Fig. 4.4(b) where both the zero-bias peak and the peaks associated with the topological gap for $B < B_c$ are much more pronounced than in Fig. 4.4(a). Indeed, the topological gap originates from the same subband as the zero-bias peak and its visibility is thus enhanced by the same mechanism. Given that the predictions of the multiband model (4.1) are consistent with the experimental data of Ref. [Mour 12], the deliberate introduction of subband mixing would be an instructive probe of Majorana bound states.

5. Signatures of topological phase transitions in mesoscopic superconducting rings

The 4π-periodic Josephson effect can provide strong evidence for the presence of Majorana bound states in a Josephson junction. The 4π periodicity in the superconducting phase difference arises as a consequence of single-particle tunneling mediated by the Majorana bound states—a process forbidden in conventional Josephson junctions. As discussed in Sec. 3.3.2, this signature of Majorana bound states is masked by relaxation processes that change fermion parity. In this chapter (previously published as [Pien 13c]) we investigate Josephson currents in mesoscopic superconducting rings with a weak link which are in or near a topological phase. Such a systems may, for instance, be realized in proximity-coupled semiconductor rings as have been fabricated and characterized in [Forn 13]. We show that even when fermion parity is *not* a good quantum number the periodicity of the Josephson current in such rings provides signatures of the topological phase transition and the emergence of Majorana bound states situated on both sides of the weak link.

We furthermore show that weak disorder can drive a trivial p-wave superconductor close to the phase transition into the topological phase in stark contrast to the detrimental effect of disorder deep inside the topological phase. We use these results on disordered superconductors close to the topological phase transition to demonstrate the robustness of the Josephson signature in mesoscopic rings.

5.1. Introduction

The current flowing through a weak link in a ring made of a conventional superconductor is a periodic function of flux with period $h/2e$ (corresponding to 2π periodicity in the phase difference), associated with the transfer of Cooper pairs across the junction. In a ring made of a topological superconductor, there is a MBS on each side of the junction and the tunneling current obtains a component that is h/e periodic (corresponding to 4π periodicity in the phase difference). This doubling of the flux period with respect to the ordinary Josephson effect due to the MBS is dubbed fractional Josephson

effect. The h/e-periodic Josephson current is observed as long as the fermion number parity of the system is conserved. Once the system is in strict thermodynamic equilibrium, including relaxation processes which change fermion parity, the Josephson current reverts to the conventional $h/2e$ periodicity. Indeed, the h/e-periodic Josephson current has equal magnitude but opposite signs for even and odd fermion parities, so that it averages to zero in the presence of fermion-parity changing processes. Possible workarounds that do not require strict parity conservation rely on the ac Josephson effect [Kwon 04, Jian 11b], or finite-frequency current noise [Badi 11]. Experimental signatures of a fractional Josephson effect in Shapiro step measurements have been claimed recently [Rokh 12].

Here we show that in mesoscopic rings with a weak link, the presence of Majorana bound states can lead to an h/e-periodic Josephson current even in thermodynamic equilibrium and in the presence of fermion-parity-breaking relaxation processes. This h/e-periodic contribution exists in the topological superconducting phase and peaks in magnitude near the topological phase transition, providing an experimental signature of the phase transition. We investigate this signature for a spinless p-wave superconductor wire, the Kitaev chain [Motr 01, Kita 01], which is a paradigmatic model exhibiting a topological phase transition. This model also arises as an effective low-energy theory in more realistic situations such as the quantum-wire proposals of [Lutc 10] and [Oreg 10]. In a ring geometry, the Majorana bound states hybridize not only due to the tunneling across the weak link but also through the superconducting interior of the ring. The latter overlap is exponentially small in the ratio of the ring circumference and the superconducting coherence length governing the spatial extent of the Majorana bound states. As one approaches the topological phase transition, the superconducting coherence length diverges and the interior overlap between the Majorana bound states becomes significant. This causes a peak of the h/e-periodic Josephson current near the topological phase transition [1].

After discussing this effect in clean rings, we extend our considerations to disordered rings. We show that the signature of the topological phase transition is robust and survives under more realistic conditions. This issue also leads us to study the influence of disorder in the vicinity of the topological phase transition of the Kitaev chain which had not been discussed previously. Previous work [Motr 01, Pott 10, Brou 11b, Brou 11a] on disorder effects in the Kitaev chain or models of quantum wires focused on the regime of large chemical potential (measured from the lower band edge), $\mu \gg m\Delta'^2$, where Δ' denotes the effective p-wave order parameter of the Kitaev chain in the continuum limit.

[1] This peak in the h/e-periodic current should not be confused with the peak in the h/e-periodic magnetoconductance discussed in [Akhm 11]. The former originates from the MBS whereas the latter is a bulk effect.

In this regime, the topological region in the phase diagram shrinks with increasing disorder [Brou 11b]. In contrast, the topological phase transition in the Kitaev chain occurs for $\mu = 0$ and thus in the opposite regime of $\mu \ll m\Delta'^2$. Remarkably, we find that in this regime disorder *increases* the topological region in the phase diagram.

This chapter is organized as follows. In Section 5.2 we review the Kitaev model for a one-dimensional spinless p-wave superconductor and its various regimes. We also discuss how this model is related to quantum-wire based realizations, focusing on the modeling of the magnetic flux through a quantum wire ring in proximity to a bulk superconductor. Section 5.3 is dedicated to the flux-periodic Josephson currents in clean rings, focusing on the flux-periodicity as a signature of the topological phase transition. The basic effect is discussed in Sec. 5.3.2, analytical considerations on the magnitude of the effect are given in Sec. 5.3.3, and a comparison with numerical results is given in Sec. 5.3.4. Sec. 5.4 extends the considerations to disordered rings. Besides a discussion of the effects of disorder on the Josephson currents, we also study the phase diagram of the disordered wire near the topological phase transition.

5.2. Model

5.2.1. Kitaev model of a one-dimensional spinless p-wave superconductor

Our analysis starts with the Kitaev model of a one-dimensional spinless p-wave superconductor [Kita 01, Motr 01]

$$H_{\mathrm{TB}} = -\mu_{\mathrm{TB}} \sum_{j=1}^{N} c_j^\dagger c_j - \sum_{j=1}^{N-1} (t c_j^\dagger c_{j+1} + \Delta_{\mathrm{TB}} c_j c_{j+1} + \mathrm{h.c.}), \tag{5.1}$$

which describes a wire of N sites. Electrons on site j are annihilated by c_j, hop between neighboring sites with hopping amplitude t, and have chemical potential μ_{TB}. For all numerical calculations in this chapter we choose $t = 1$. The p-wave pairing strength is given by Δ_{TB}. Here, we label both the chemical potential and the pairing strength by the subscript TB to distinguish these parameters of the tight-binding model (5.1) from their analogs in the continuum model introduced below. The wire can be closed into a ring with a weak link by an additional hopping term between sites 1 and N,

$$H_{\mathrm{T}} = -t' c_N^\dagger c_1 + \mathrm{h.c.}, \tag{5.2}$$

with hopping amplitude t'. We assume that charging effects are weak and can be neglected (see Refs. [Heck 11, Zoch 12] for consequences of charging in ring-like structures).

For an infinite and uniform wire, the Kitaev Hamiltonian (5.1) exhibits a phase transition when the chemical potential μ_{TB} crosses one of the band edges. The system is in a topological (nontopological) superconducting phase when the chemical potential is within (outside) the interval $[-2t, 2t]$, i.e., within (outside) the band at vanishing pairing $\Delta_{\mathrm{TB}} = 0$. The spectrum exhibits a superconducting gap on both sides of the topological phase transition while the gap closes at the topological critical points $|\mu_{\mathrm{TB}}| = 2t$. It is thus natural to introduce the chemical potential measured from the lower band edge, i.e., $\mu = \mu_{\mathrm{TB}} + 2t$.

In the vicinity of the band edges (say the lower band edge) and thus of the topological phase transition, we can make a continuum approximation to the tight-binding model (5.1). We will mostly employ the tight-binding model in the first part of the manuscript, while we partially find it more convenient to rely on the continuum approximation in dealing with effects of disorder in Sec. 5.4. The continuum model is formulated in terms of the corresponding Bogoliubov–de Gennes Hamiltonian [Motr 01, Kita 01]

$$H = \begin{bmatrix} \frac{p^2}{2m} + V(x) - \mu & \frac{1}{2}\{\Delta'(x), p\} \\ \frac{1}{2}\{\Delta'(x), p\} & -\left(\frac{p^2}{2m} + V(x) - \mu\right) \end{bmatrix}, \tag{5.3}$$

where $\Delta'(x)$ is the p-wave pairing strength and the curly brackets denote the anticommutator. Here, we have included a disorder potential $V(x)$ which we will return to in more detail in Sec. 5.4. For $V(x) = 0$ the bulk spectrum of the continuum model is given by

$$\epsilon_p = \pm \left[\left(\frac{p^2}{2m} - \mu \right)^2 + |\Delta'|^2 p^2 \right]^{1/2}, \tag{5.4}$$

which becomes gapless for $\mu = 0$. This indicates the above-mentioned topological phase transition between a topological phase with $\mu > 0$ and a nontopological phase for $\mu < 0$.

In a semi-infinite wire, the topological phase is characterized by a Majorana bound state localized near its end point. The Majorana bound state has zero energy and a wave function that decays exponentially into the wire on the scale of the superconducting coherence length ξ. In a finite wire, the Majorana bound states localized at the two ends of the wire hybridize and form a conventional Dirac fermion whose energy ϵ_0 scales like the overlap of the two Majorana end states which is exponentially small in the length L of the wire. The wavefunction of the Majorana bound state depends on the parameter regime (see, e.g., [Halp 12]). This is easily seen by determining the allowed wavevectors

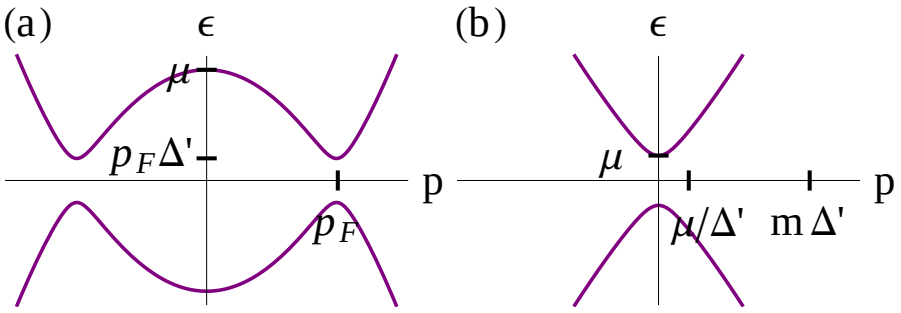

Figure 5.1.: Bulk spectrum Eq. (5.4) of Kitaev's model for a spinless p-wave superconductor in the regimes (a) $\mu \gg m\Delta'^2$ and (b) $0 < \mu \ll m\Delta'^2$.

at zero energy from Eq. (5.4), which yields

$$p_0 = \pm im|\Delta'| \pm \sqrt{2m\mu - m^2|\Delta'|^2}. \tag{5.5}$$

(i) $\mu \gg m\Delta'^2$: Deep in the topological phase, the bulk excitation spectrum Eq. (5.4) has two minima around $\pm p_F = \pm\sqrt{2m\mu}$ with a gap $\Delta_{\text{eff}}^{(i)} \approx p_F\Delta'$ (see Fig. 5.1a). According to Eq. (5.5), the Majorana wavefunctions decay on the scale $\xi = 1/m\Delta'$ and oscillate with a much shorter period $1/p_F$. In a finite wire the hybridization energy is given by (cf. appendix A) $\epsilon_0 = 2\Delta' p_F |\sin(p_F L)| \exp(-L/\xi)$, which has accidental degeneracies at integer values of $p_F L/\pi$.

(ii) $\mu \ll m\Delta'^2$: Near the topological phase transition at $\mu = 0$, the excitation spectrum has only a single minimum at $p = 0$ with a gap of order μ (see Fig. 5.1b). At low energies, we can neglect the kinetic energy in Eq. (5.3) and the spinless p-wave superconductor can be approximately described by the Dirac Hamiltonian

$$H \simeq -\mu\tau_z + \Delta' p\tau_x. \tag{5.6}$$

Equation (5.5) gives $p_0 \approx \pm i\mu/\Delta'$, so that the spatial extent of the Majorana wavefunction is governed by the coherence length $\xi = \Delta'/\mu$, which diverges at the topological phase transition. In contrast to the previous regime, the end-state energy does not exhibit oscillations, $\epsilon_0 \propto \exp(-L/\xi)$.

5.2.2. Magnetic flux

In the presence of a magnetic flux threading the ring, both the tunneling amplitude and the pairing strength become complex and acquire a phase. The precise nature of these phases depends on the physical realization of the Kitaev chain. We illustrate this point

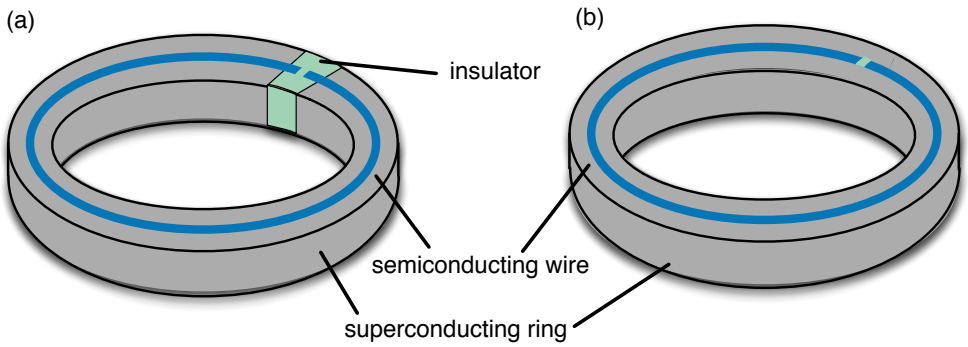

Figure 5.2.: Two possible setups for a quantum wire with a tunneling junction in proximity to an s-wave superconductor. (a) The bulk superconductor is interrupted by an insulating region underneath the weak link in the wire. (b) The bulk superconductor forms a continuous ring and only the wire contains a weak link.

by discussing two possible setups based on the proposal to realize the Kitaev chain in a semiconductor wire proximity coupled to an s-wave superconductor [Lutc 10, Oreg 10], as illustrated in Fig. 5.2:

(a) The s-wave superconductor is interrupted underneath the weak link in the quantum wire. Current can flow around the loop only through the semiconductor weak link.

(b) The s-wave superconductor forms a closed ring and a weak link exists only in the semiconductor wire. The current through the weak link of the semiconductor will in general be only a small perturbation of the current flowing through the superconductor.

We assume that the thickness of the superconducting ring is small compared to both its London penetration depth and its superconducting coherence length ξ_{SC}. The supercurrent flowing in the superconductor is given by [Tink 75]

$$J_s = \frac{2e}{m^*}|\psi|^2 \left(\hbar\nabla\varphi - 2eA\right), \tag{5.7}$$

where m^* and $|\psi|^2$ are the effective mass and density of the superconducting electrons and φ denotes the phase of the s-wave order parameter. The p-wave pairing potential in the quantum wire inherits its phase φ from the s-wave superconductor underneath via the proximity effect. (The effective p-wave order parameter may have an additional phase shift that depends on geometric details such as the direction of the Zeeman field and the spin-orbit coupling; however, these contributions lead to constant offsets of the phase which are unaffected by the magnetic flux.) The vector potential $\mathbf{A}$ oriented along

the wire is related to the Aharonov–Bohm flux ϕ through

$$\phi = \oint \mathrm{d}x A(x), \tag{5.8}$$

where the integral is taken around the ring of circumference L.

The phase of the order parameter φ is different for the two setups illustrated in Fig. 5.2. In setup (a), no supercurrent is able to flow since the loop is interrupted, $J_s = 0$. If we choose a gauge in which the vector potential is uniform around the ring, $A(x) = \phi/L$, the phase φ of the order parameter becomes $\varphi(x) = 4\pi(\phi/\phi_0)(x/L)$ in terms of the normal-metal flux quantum $\phi_0 = h/e$. In setup (b), the supercurrent around the ring is governed by fluxoid quantization $\varphi(x+L) = \varphi(x) + 2\pi n$, with the integer n labeling the fluxoid states. In a gauge in which $A(x) = \phi/L$, this implies that $\nabla\varphi = 2\pi n/L$, yielding a supercurrent of $J_s = (2e/m^*)|\psi|^2[2\pi\hbar n/L - 2eA]$. Here, $[x]$ denotes the integer closest to x. In thermodynamic equilibrium, the system realizes the fluxoid state of lowest energy and thus of lowest supercurrent, i.e., $n = [\phi/(\phi_0/2)]$.

Within the chosen gauge, in setup (a) the hopping amplitude and the pair potential in the tight binding Hamiltonian in Eq. (5.1) take the form $t \to te^{i2\pi\phi/N\phi_0}$ and $\Delta_{\mathrm{TB}} \to \Delta_{\mathrm{TB}} e^{i4\pi(\phi/\phi_0)(j/N)}$. Alternatively one can perform the gauge transformation $c_j \to c_j e^{-i(j-1/2)2\pi\phi/N\phi_0}$ which eliminates the phase from the pair potential. In this new gauge, both the pair potential and the hopping amplitude t in the interior of the ring are real while the hopping amplitude across the weak link acquires a phase factor, $t' \to t' e^{i2\pi\phi/\phi_0}$. Our numerical results will be obtained for this representation of the tight-binding model. In contrast, in setup (b), we find $\Delta_{\mathrm{TB}} \to \Delta_{\mathrm{TB}} e^{i2\pi[\phi/(\phi_0/2)](j/N)}$ for the pair potential (notice the closest integer symbol [.] in the exponent), while $t \to te^{i2\pi\phi/N\phi_0}$ as well as $t' \to t' e^{i2\pi\phi/N\phi_0}$. As in the previous case (a), we can eliminate the phase of the pair potential by a gauge transformation. However, this no longer eliminates the phase of the hopping matrix element t. Instead, one finds $t \to te^{i(\pi/N)\{\phi/(\phi_0/2) - [\phi/(\phi_0/2)]\}}$ and $t' \to t' e^{i(\pi/N)\{\phi/(\phi_0/2) + (N-1)[\phi/(\phi_0/2)]\}}$. The fact that we can no longer eliminate the magnetic flux from the bulk of the wire is a manifestation of the fact that supercurrents in the s-wave superconductor modify the spectrum of the quantum wire [Romi 12].

Clearly, the effective Kitaev chain is quite different for setups (a) and (b). In the remainder of this chapter, we will focus on setup (a) where the flux enters only into the tunneling Hamiltonian representing the weak link. In this setting, the current in the semiconductor wire of interest here is experimentally more accessible since there is no background current in the bulk s-wave superconductor unlike in setup (b).

5.3. Clean rings

5.3.1. Infinite wire

We first briefly review the Josephson effect of two semi-infinite wires connected at their ends through a weak link (or equivalently, a ring of infinite circumference), as originally considered by Kitaev [Kita 01]. The corresponding low-energy excitation spectrum as a function of flux is sketched in Fig. 5.3a. Due to the Majorana end states, there are two subgap states whose energies are governed by the tunneling amplitude across the weak link. While each individual level is periodic in flux with period h/e, the overall spectrum is $h/2e$ periodic. As a result, the thermodynamic ground state energy of the system – and thus the Josephson current in strict thermodynamic equilibrium – are $h/2e$ periodic.

At the same time, the h/e periodicity of the individual subgap states is a direct consequence of the Majorana nature of the end states. This signature of Majorana bound states can be brought out in measurements of the Josephson current if the fermion parity of the system is a good quantum number. The level crossing of the two Majorana subgap states in Fig. 5.3a is then protected by fermion parity conservation. As a result, since there is only a single level crossing per superconducting flux quantum, the system necessarily goes from the ground state to an excited state (or vice versa) when changing the flux by $h/2e$. During this process, the excited state is unable to relax to the ground state since this would require a change in fermion parity. Thus, the system only returns to its initial state after a change in flux of h/e, which corresponds to the fractional Josephson effect.

5.3.2. Finite size ring

For rings with finite circumference, the two Majorana bound states localized at the two banks of the weak link hybridize not only through the tunnel coupling across the weak link but also because of the overlap of their wavefunctions in the topological superconductor. In the previous subsection, we considered the situation in which this interior hybridization is vanishingly small compared to tunneling across the weak link. Conversely, when tunneling across the weak link is negligible compared to the interior hybridization, the splitting of the Majoranas due to the interior overlap does not depend on flux. Weak tunneling across the junction will then cause a small h/e-periodic modulation of the split Majorana levels with flux. In this situation, even the *thermodynamic* ground state energy becomes h/e periodic, regardless of the presence or absence of fermion parity violating processes. In fact, of the two h/e-periodic levels, the negative-

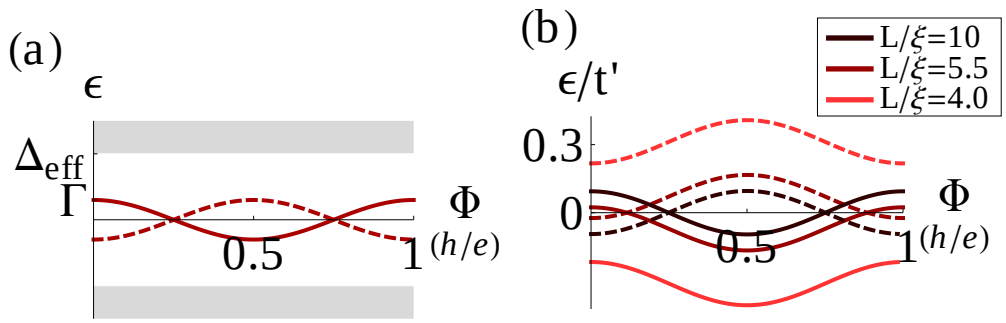

Figure 5.3.: (a) Typical Bogoliubov–de Gennes spectrum as a function of phase difference across the junction between two semi-infinite wires in the topological phase with the tunneling amplitude Γ and the gap Δ_{eff}. The two low-energy Majorana states represented by the dashed and solid lines are related by particle-hole symmetry. The continuum of states outside the gap is displayed in gray. The thermodynamic ground state has period $h/2e$. (b) Numerical results for the subgap spectrum of a mesoscopic ring with finite circumference for $\Delta = 1$, $\mu = -1.8$, $t' = 0.01$. We set $t = 1$ for all numerical calculations in this chapter. The parameters correspond to $\xi = 9.5$ and the different curves display data for ring circumferences $L = 95, 52, 38$ all in units of the lattice spacing. As the circumference of the wire decreases the overlap through the topological superconductor in Eq. (5.12) increases. Note that the equilibrium ground state always has h/e periodicity in rings of finite circumference.

energy level (which is occupied in equilibrium) corresponds to an even-parity ground state while the positive-energy level is occupied in the odd-parity first excited state. Weak fermion parity violating processes will not destroy the h/e-periodic Josephson current as the two levels no longer cross as function of flux.

The full crossover of the Bogoliubov–de Gennes spectrum as the interior overlap of the Majorana bound states increases is illustrated with numerical results in Fig. 5.3b (see Sec. 5.3.4 for details on the numerical calculations). They confirm the above picture for the limit of strong overlap. But they also show that an h/e-periodic contribution to the equilibrium Josephson current exists even when the interior splitting is of the order of or smaller than the tunnel coupling across the weak link. Indeed, the interior overlap essentially pushes one of the two states (dashed line) up in energy, while it pushes its particle-hole conjugate state (solid line) down. At small interior overlaps, this shifts the two level crossings (initially at $\phi_0/4$ and $3\phi_0/4$) outwards towards a flux of zero and one flux quantum ϕ_0. Note that the level crossings remain intact, protected by fermion parity conservation. However, once the level crossings reach a flux of zero and ϕ_0, respectively, the levels merely touch at these points. Thus, fermion parity no longer protects the levels from splitting, and indeed one state remains at finite and negative energies at all

values of flux while, symmetrically, its particle-hole conjugate state remains at finite and positive energies.

Consider now the Josephson current as function of flux in the presence of weak but finite fermion parity violating processes. Specifically, we assume that the flux is varied by h/e on a time scale which is large compared to the relaxation time of the fermion parity while at the same time, the fermion parity violating processes are weak compared to the hybridization of the Majorana bound states so that the Bogoliubov-de Gennes spectra in Fig. 5.3 are relevant. In this case, the Josephson current is essentially $h/2e$ periodic deep in the topological phase, where $L \gg \xi$. However, as the system approaches the topological phase transition, ξ grows and hence, the hybridization of the Majorana bound states through the interior of the ring increases. As a result, the h/e-periodic contribution to the current increases. Conversely, the Majorana bound states disappear on the nontopological side of the phase transition where the Josephson current thus reverts to $h/2e$ periodicity. As a result, we expect a *peak* in the h/e-periodic Josephson current near the topological phase transition, whose measurement would constitute a clear signature of the topological phase transition and the formation of Majorana bound states.

This expectation is confirmed by the numerical results shown in Fig. 5.4a, where the corresponding Fourier coefficient $A_{h/e} = (2e/h)\int_0^{h/e} \mathrm{d}\phi I(\phi)\sin(2\pi e\phi/h)$ of the *equilibrium* Josephson current $I(\phi)$ is plotted as a function of chemical potential. $A_{h/e}(\mu)$ exhibits a peak in the topological phase ($\mu > 0$), which moves closer to the topological phase transition at $\mu = 0$ as the ring circumference increases (see Fig. 5.4b).

Deep in the topological phase the Majorana bound states are localized at the weak link. Approaching the phase transition at $\mu = 0$, the MBS delocalize. On the one hand, this causes an increase in the overlap of the MBS in the interior of the topological superconductor. As discussed above, this leads to an increase of the h/e-periodic Josephson current. On the other hand, however, the probability density of the Majorana bound state near the weak link decreases, causing a suppression of the hybridization of the Majorana bound states across the weak link and hence of the h/e-periodic Josephson current. Thus, the peak occurs for the value of μ where the interior overlap splitting is equal to the tunnel coupling. Since the interior overlap is exponentially small in L/ξ while the hybridization across the weak link is roughly independent of the ring's circumference L, the peak position shifts towards the phase transition point at $\mu = 0$ with increasing L (cf. Fig. 5.4c). Since at the same time the h/e-periodic Josephson current becomes suppressed when the systems is approaching the phase transition, the peak is more pronounced in shorter rings.

5.3.3. Low-energy Hamiltonian

A more quantitative description can be developed by restricting the Hamiltonian to the low-energy subspace spanned by the two Majorana bound states. The projection of the tunneling Hamiltonian across the weak link onto this subspace yields

$$H_{\mathrm{T}} = -\Gamma \cos(2\pi\phi/\phi_0)(d_{\mathrm{M}}^{\dagger} d_{\mathrm{M}} - 1/2), \tag{5.9}$$

where d_M is the Dirac fermion constructed from the two Majorana bound states. The parameter Γ measures the tunnel coupling of the Majorana bound states across the weak link and is given by (cf. Eq. (A.3) in appendix A)

$$\Gamma = \frac{t'\mu(4t-\mu)\Delta_{\mathrm{TB}}}{t(t+\Delta_{\mathrm{TB}})^2}. \tag{5.10}$$

Here the factor of μ accounts for the probability density of the Majorana wavefunction at the junction, which vanishes at the phase transition.

The overlap of the Majorana end-states in the interior of the wire leads to an additional coupling (cf. appendix A)

$$H_{\mathrm{overlap}} = \epsilon_0 \left(d_M^{\dagger} d_M - 1/2 \right),$$

where

$$\epsilon_0 = 2\mu \exp(-L/\xi) \tag{5.11}$$

measures the strength of the overlap.

Combining these two contributions for a mesoscopic ring near the topological phase transition ($\mu \ll m\Delta'^2$), the effective low-energy Hamiltonian reads as

$$H_{\mathrm{eff}} = \left[\epsilon_0 - \Gamma \cos\left(\frac{2\pi\phi}{\phi_0} \right) \right] \left(d_{\mathrm{M}}^{\dagger} d_{\mathrm{M}} - 1/2 \right). \tag{5.12}$$

The Bogoliubov–de Gennes spectrum of this Hamiltonian reproduces the numerically calculated subgap spectra depicted in Fig. 5.3b.

In principle, both the negative energy continuum states as well as the negative energy subgap state contribute to the equilibrium Josephson current. If we denote the sum over all negative excitation energies by $E_0(\phi)$, we can write the equilibrium Josephson current as $I(\phi) = -\partial_\phi E_0(\phi)$. However, it is natural to expect and will be corroborated by our numerical results that the Josephson current is dominated by the contribution of the subgap state $I(\phi) \simeq \partial_\phi |\epsilon_0 - \Gamma \cos(2\pi\phi/\phi_0)|/2$. Thus, it is straight-forward to compute

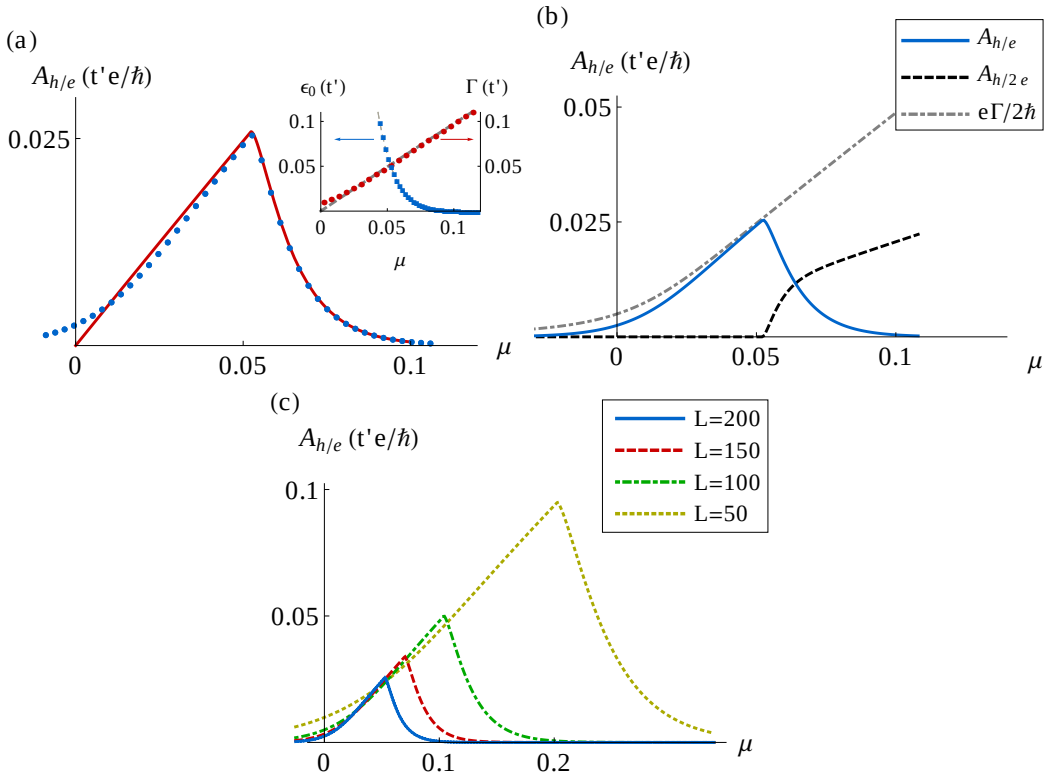

Figure 5.4.: (a) Numerical results for the h/e-periodic Fourier component of the Josephson current, $A_{h/e}$, as a function of chemical potential in a ring with $\Delta_{\mathrm{TB}} = 1$ and $L = 200$ (blue dots) together with analytical expression Eqs. (5.13) (red solid line). Inset: numerical results for ϵ_0 (blue squares) and Γ (red circles) together with the corresponding analytical expressions (gray dashed curves) Eqs. (5.11) and (5.10). (b) h/e-periodic Fourier component (solid), $h/2e$-periodic Fourier component (dashed), and the maximum tunneling current of the MBS, $e\Gamma/h$. (c) $A_{h/e}$ for different ring circumferences L.

the h/e-periodic Fourier component of the Josephson current,

$$A_{h/e} = \begin{cases} \frac{e\Gamma}{\pi\hbar}\left[\frac{\epsilon_0}{\Gamma}\sqrt{1-\frac{\epsilon_0^2}{\Gamma^2}} + \arcsin\left(\frac{\epsilon_0}{\Gamma}\right)\right], & \epsilon_0 < \Gamma \\ \frac{e\Gamma}{2\hbar}, & \epsilon_0 > \Gamma \end{cases}. \tag{5.13}$$

In the next section, we compare this analytical result with numerics and find nice agreement.

5.3.4. Numerical Results

To obtain numerical results for the Josephson current, we solve the Hamiltonian defined in Eqs. (5.1) and (5.2) by exact diagonalization. Fig. 5.4a compares the amplitude of the h/e-periodic component as a function of chemical potential with the analytical

result in Eq. (5.13). The numerical results agree well with the behavior predicted by the low-energy model, except for small deviations in the immediate vicinity of the phase transition at $\mu = 0$. In the inset of Fig. 5.4a we compare the analytical and numerical results for the quantities Γ and ϵ_0 appearing in the low-energy Hamiltonian. While the model correctly captures ϵ_0 in the regime of interest, there are deviations of Γ near $\mu = 0$. These discrepancies are readily understood as a consequence of the finite circumference of the ring. Although the coherence length diverges at the phase transition, the Majorana bound states can delocalize at most throughout the entire length of the ring there remains a finite probability density of the Majorana bound state wavefunction at the weak link.

Figure 5.4b shows that the left flank of the peak of $A_{h/e}$ and $e\Gamma/h$ deviate slightly. This deviation is a measure of the size of the bulk contribution to the h/e-periodic current. The latter can thus be seen to be small, justifying our focus on the low-energy Hamiltonian (12) describing the Majorana bound states only. In the same figure, the $h/2e$ component is plotted, showing that the h/e-periodic Josephson current exceeds the $h/2e$ component. This is a consequence of the tunneling regime that favors single-electron tunneling over the tunneling of Cooper pairs.

In Fig. 5.4c, we show how the position of the peak in $A_{h/e}$ depends on the circumference of the ring. We find that the value of μ where the peak occurs scales as $1/L$. This result can be understood as follows. Γ is essentially independent of the length of the ring, while ϵ_0 scales as $\sim \exp(-L/\xi)$. As we have seen above the peak occurs at $\epsilon_0 = \Gamma$. For given t, Δ_{TB}, and t', Γ is fixed and the peak occurs at a constant value of the ratio L/ξ. Since $\xi \sim 1/\mu$, the value of μ where the peak occurs scales as $1/L$. Also note that the above-mentioned tail of the peak at $\mu \leq 0$ originating from finite-size corrections is more pronounced in shorter rings.

5.4. Effects of disorder

5.4.1. h/e-periodic Josephson current in disordered rings

In this section we investigate the fate of the peak in the equilibrium h/e-periodic Josephson current in the presence of disorder. Our main results are:

(i) The typical peak height is not affected by disorder as long as the mean free path is longer than the circumference of the ring. Thus the signature persists in the presence of moderate disorder.

(ii) For stronger disorder the peak height decreases and the peak position is shifted to lower chemical potentials.

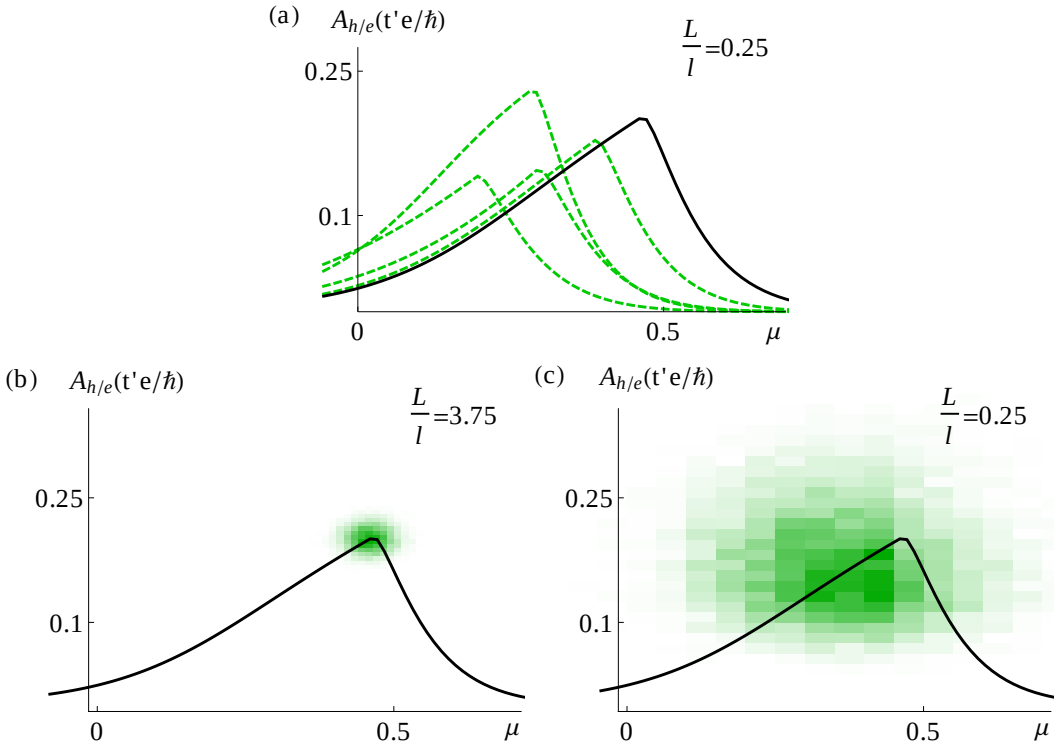

Figure 5.5.: (a) Numerical results for the h/e-periodic Fourier component of the Josephson current, $A_{h/e}$, as function of chemical potential for a clean ring (black solid line) and disordered rings with four disorder configurations (green dashed lines) corresponding to $l = 5$. (b) $A_{h/e}$ for a clean wire (black solid line) together with the histogram of the peak position in the presence of disorder for $l = 75$ as a color code (green (gray) area). (c) Same as (b) with $l = 5$. For all plots we chose $L = 20$ and $\Delta_{\mathrm{TB}} = 1$.

To study the effect of disorder we add a random onsite potential $\sum_i V_i c_i^\dagger c_i$ to the tight-binding Hamiltonian (5.1) and (5.2), where the V_i are taken from a uniform distribution over the interval $[-W, +W]$. The mean free path is then related to the disorder strength as $l \propto 1/W^2$.[2] To obtain numerical results we compute the spectrum by exact diagonalization. Disorder affects the h/e-periodic Josephson current by introducing fluctuations in the quantities ϵ_0 and Γ. While Γ is mainly affected by local fluctuations of the probability density of the Majorana wavefunction at the junction, ϵ_0 fluctuates due to the disorder potential in the entire ring. The interior overlap in disordered wires has been investigated previously for the continuum model (5.3) in regime (i), i.e., $\mu \gg m\Delta'^2$ [Brou 11a], where disorder leads to an increase of ϵ_0 and subsequently to a disorder-induced phase transition to the nontopological phase.

[2]For the numerical results for the tight-binding model we extract the mean free path from the variance of the normal distribution of $\ln(\epsilon_0)$ according to Eq. (5.21).

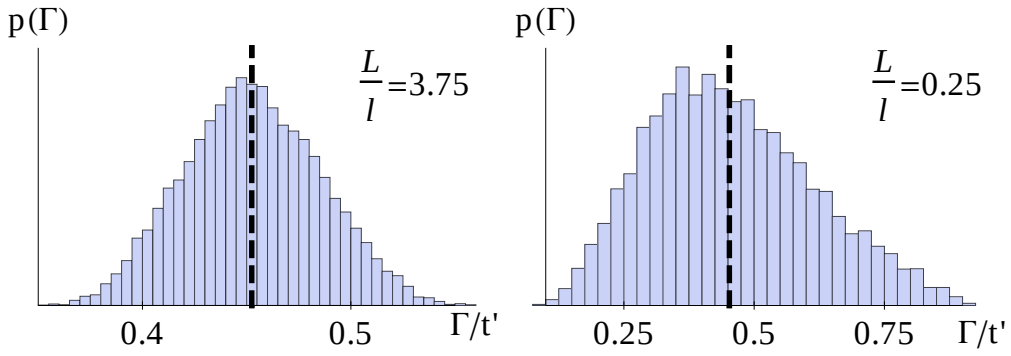

Figure 5.6.: Histogram of Γ for the same parameters as in Figs. 5.5b and c at $\mu = 0.4$. The dashed line denotes the value of Γ for the clean ring.

Fig. 5.5a shows numerical results for the h/e-periodic Josephson current for a few disorder configurations. The peaks in the presence of disorder (green dashed curves) are of comparable height as the peak in the clean ring (black solid curve). The peak shifts as a function of chemical potential which indicates fluctuations of the coherence length due to disorder.

Surprisingly, the peak shifts to lower chemical potentials, corresponding to a decrease in ϵ_0 with disorder in stark contrast to the known case of large μ. This implies that the topological phase is *stabilized* by disorder if the system is close to the phase transition. To investigate this further we plot the height and position of the peak maxima of many disorder configurations as a color code histogram for $l > L$ in Fig. 5.5b and $l < L$ in Fig. 5.5c. Indeed the average peak height is comparable to the one in the clean case for $l > L$. When $l \lesssim L$ the average peak height starts to decrease. The histogram in Fig. 5.5c confirms that the peak is shifted to lower chemical potentials on average.

To understand this behavior we analyze the probability distributions of ϵ_0 and Γ over the disorder ensemble. In Fig. 5.6 we show numerical results for the histogram of Γ corresponding to the two ensembles in Figs. 5.5b and c at $\mu = 0.4$. For weak disorder the distribution is symmetric with a mean near the zero-disorder tunnel coupling. For larger disorder when $l < L$ the distribution becomes wider and asymmetric and the average decreases.

In order to determine the probability distribution for ϵ_0 we now turn to the continuum Hamiltonian (5.3) for a wire of length L without tunnel junction. To model short-range correlated disorder in the continuum model, we include a disorder potential with zero average $\langle V(x)\rangle = 0$ and correlation function $\langle V(x)V(x')\rangle = \gamma\delta(x-x')$. For this model we employ a numerical method based on a scattering matrix approach [Brou 03, Bard 07, Brou 11b]. From the scattering matrix S we obtain the lowest energy eigenstate ϵ_0 by

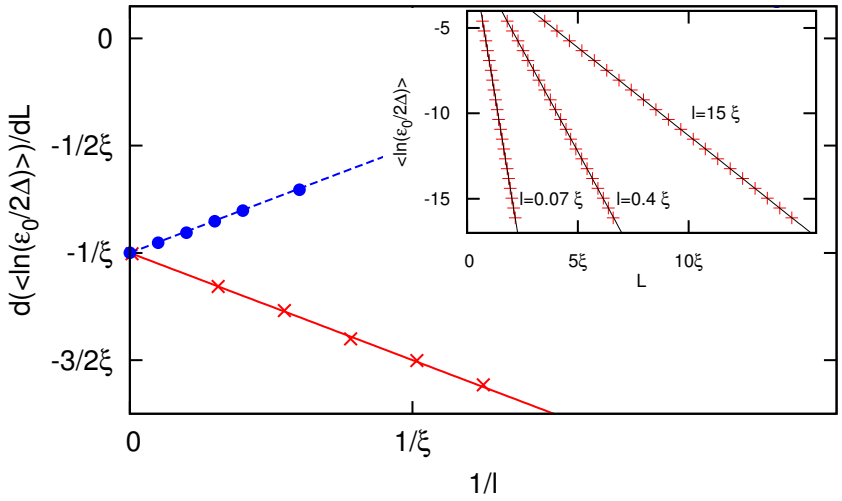

Figure 5.7.: Slope of $\langle \ln(\epsilon_0(L)/2\Delta_{\text{eff}}) \rangle$ (see inset) vs. disorder strength $1/l$ for regimes (i) with $\mu = 300\ \text{m}\Delta'^2$ (blue dots) and (ii) with $\mu = 3 \times 10^{-3}\ \text{m}\Delta'^2$ (red crosses) together with theoretical prediction according to Eqs. (5.14) (dashed line) and (5.15) with $\lambda = 1/2$ (solid line). Inset: numerical data (red crosses) and linear fit (solid) of the average of $\ln \epsilon_0$ as a function of L for different disorder strengths.

finding the roots of $\det(1 - S(\epsilon))$. In this model, the probability distribution of the hybridization energy ϵ_0 has been shown to be log-normal in [Brou 11a]. Specifically, it was shown that the log-normal distribution is governed by

$$\begin{aligned} \langle \ln(\epsilon_0/2\Delta_{\text{eff}}) \rangle &= -L\left(\frac{1}{\xi} - \frac{1}{2l}\right), \\ \text{var} \ln(\epsilon_0/2\Delta_{\text{eff}}) &= \frac{L}{2l} \end{aligned} \tag{5.14}$$

for regime (i). The distribution function reflects the disorder-induced phase transition to the nontopological state at $\xi = 2l$.

The numerical results are presented in Fig. 5.7. In the inset, we show that the mean of $\ln(\epsilon_0/2\Delta_{\text{eff}})$ is indeed linear in L with the slope depending on disorder strength. This slope is plotted as a function of inverse mean free path in Fig. 5.7. The data for $\mu = 300m\Delta'^2$ (blue dots) agrees well with the prediction Eq. (5.14) with the definitions $l = v_F^2/\gamma$ and $\xi = 1/m\Delta'$.

The same plot also shows data corresponding to regime (ii), i.e., $\mu \ll m\Delta'^2$, marked by red crosses. Here, we have $l = \Delta'^2/\gamma$ and $\xi = \Delta'/\mu$. Clearly, the behavior is qualitatively different from regime (i), since disorder decreases ϵ_0 rather than increasing it. This is consistent with the shift of the peak of $A_{h/e}$ to lower μ.

In order to gain analytical insight we now derive the probability distribution of ϵ_0 in regime (ii) extending the results of [Brou 11a]. The relevant momenta at low energies in this regime are near $p = 0$ (cf. Fig. 5.1b). Linearizing the dispersion around this point yields the Dirac Hamiltonian Eq. (5.6), where the disorder potential enters as a random mass term. Since the disorder potential is short-range correlated it couples high- and low-momentum degrees of freedom in the original Hamiltonian. Thus a proper linearization of the Hamiltonian requires one to project out the high-momentum states, which renormalizes the gap.

For a strictly linear model with a random mass term, the overlap ϵ_0 has a log-normal distribution [Brou 11a],

$$\begin{aligned} \langle \ln(\epsilon_0/2\Delta_{\text{eff}}) \rangle &= -\frac{L}{\xi}, \\ \operatorname{var} \ln(\epsilon_0/2\Delta_{\text{eff}}) &= \frac{L}{l}. \end{aligned} \tag{5.15}$$

Thus for the Dirac Hamiltonian the mean of $\ln(\epsilon_0/2\Delta_{\text{eff}})$ does not depend on disorder. A systematic linearization of the disordered spinless p-wave superconductor in the vicinity of the topological phase transition effectively renormalizes the chemical potential μ and hence the coherence length $\xi = \Delta'/\mu$.

We start by defining the projection operators $P = \sum_{|p|<p_1} |\psi_p\rangle \langle\psi_p|$ onto the low momentum subspace and $Q = 1 - P$, where $\{|\psi_p\rangle\}_p$ is a complete set of momentum eigenstates of the clean Hamiltonian. The relevant momentum scale for this projection is given by $p_1 = m\Delta'$, since for $p \ll p_1$, the term $p^2/2m$ constitutes the lowest energy scale of the Kitaev Hamiltonian. Furthermore, we assume that the disorder potential does not affect high momenta $p_1 \gg 1/l$. We can now project the clean Kitaev Hamiltonian H to the low- and high-energy subspaces,

$$PHP \simeq P\left[(-\mu + V(x))\tau_z + \Delta' p \tau_x\right] P, \tag{5.16}$$

$$QHQ \simeq Q\left(p^2/2m\right)\tau_z Q. \tag{5.17}$$

Both subspaces are exclusively mixed by the disorder potential $PHQ = PV(x)\tau_z Q$. To second order in V, the correction to the low-energy Hamiltonian is then given by

$$\begin{aligned} \delta H(p) &\simeq \left\langle \psi_p \middle| PHQ\left(\epsilon_p - QHQ\right)^{-1} QHP \middle| \psi_p \right\rangle \\ &\simeq \sum_{|p'|>p_1} V_{pp'} \frac{1}{\epsilon_p - p'^2/2m\tau_z} V_{p'p}. \end{aligned} \tag{5.18}$$

Here we used the short notation $V_{pp'} = \langle \psi_p \,|\, V(x) \,|\, \psi_{p'} \rangle$. Averaging over disorder, we obtain

$$\langle \delta H(p) \rangle \simeq - \sum_{|p'|>p_1} \frac{2m\gamma}{p'^2} \tau_z \sim -\frac{\gamma}{\Delta'} \tau_z. \tag{5.19}$$

Thus the renormalization produces a contribution to the low-energy Hamiltonian which has the same structure as the chemical potential term. Hence we find a renormalized chemical potential $\mu' = \mu + \lambda\gamma/\Delta'$ with a numerical factor $\lambda > 0$ that cannot be determined from this argument. Thus disorder enters the final result through the renormalized coherence length

$$\frac{1}{\xi} \to \frac{1}{\xi} + \frac{\lambda}{l}. \tag{5.20}$$

The data in Fig. 5.7 confirm Eqs. (5.15) and (5.20) and determine the unknown numerical prefactor to be $\lambda = 1/2$. Thus for $\mu \ll m\Delta'^2$, ϵ_0 has a log-normal distribution with mean and variance given by

$$\begin{aligned} \langle \ln(\epsilon_0/2\Delta_{\text{eff}}) \rangle &= -L \left(\frac{1}{\xi} + \frac{1}{2l} \right), \\ \operatorname{var} \ln(\epsilon_0/2\Delta_{\text{eff}}) &= \frac{L}{l}. \end{aligned} \tag{5.21}$$

This result is very similar to Eq. (5.14) where, however, the disorder correction to the decay length enters with opposite sign. This underlines the contrast between the two regimes, i.e., that disorder drives the system further into the topological phase when it is close to the phase transition, but away from it for larger chemical potentials. Specifically a spinless p-wave superconducting wire with negative chemical potential may exhibit edge states with an energy exponentially small in L as long as disorder is strong enough.

Combining the disorder-induced fluctuations of Γ and ϵ_0 we can understand the suppression of the peak in the h/e-periodic Josephson current in Fig. 5.5c for $l < L$. While ϵ_0 is decreased on average for a given μ with increasing disorder, Γ does not increase at the same time and thus the average peak height decreases. However the fluctuations of Γ and ϵ_0 become larger as disorder increases such that for single disorder configurations significant peaks are still possible even if the average peak height decreases.

5.4.2. Phase diagram of a disordered wire

Motivated by the contrasting probability distributions of ϵ_0 in the regimes of large and small μ we numerically calculate the phase diagram of the continuum model (5.3) as a

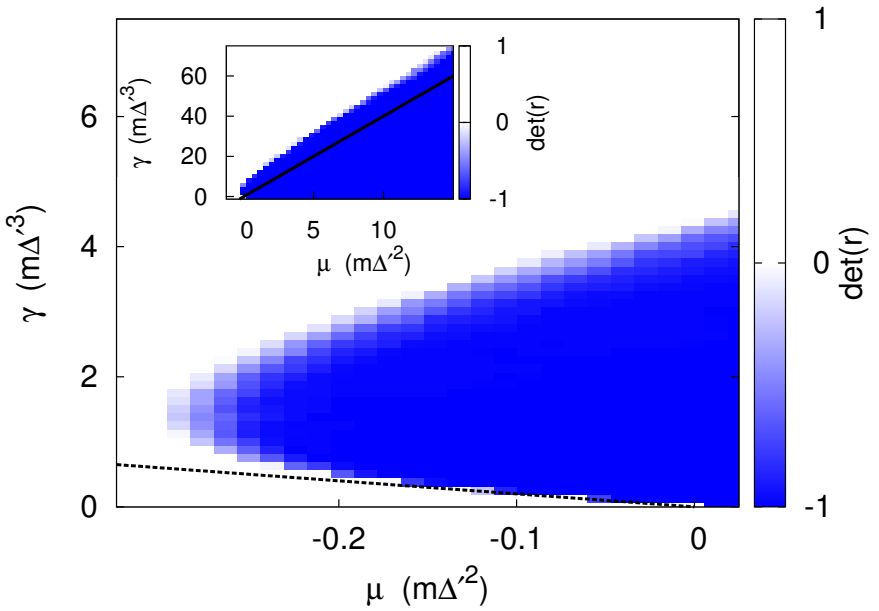

Figure 5.8.: Phase diagram of the continuum model (5.3) as function of disorder strength γ and chemical potential μ in the regime $\mu \ll m\Delta'^2$. The data has been averaged over 100 disorder configurations. For $\mu < 0$ disorder gives rise to a trivial-to-topological phase transition with a reentrant nontopological phase for stronger disorder. The dashed line denotes the phase transition line $\gamma_c^{(ii)}(\mu)$ valid for small $|\mu|$ given in Eq. (5.22). Inset: Phase diagram for a larger range of μ and γ. The solid line represents the predicted phase boundary $\gamma_c^{(i)}(\mu)$ for large μ. (The analytical phase boundary is only accurate at large μ up to sublinear corrections.)

function of μ and γ, particularly paying attention to the region near the topological phase transition of the clean model. By means of the scattering matrix approach also used in the last section we compute the determinant of the reflection matrix of a wire of length L at $\epsilon = 0$ which approaches the values $+1$ and -1 as $L \to \infty$ in the nontopological and topological phase, respectively [Merz 02, Akhm 11].

The resulting phase diagram is plotted in Fig. 5.8. From Eq. (5.14) we infer that the topological phase transition occurs for $\xi = 2l$ in the regime $\mu \gg m\Delta'^2$. Using the definitions of l and ξ in this regime, we obtain the phase boundary $\gamma_c^{(i)}(\mu) = 4\Delta'\mu$. This is compared with the numerical results in the inset of Fig. 5.8. The numerically calculated phase boundary $\gamma_c^{\mathrm{num}}(\mu)$ has only sublinear deviations from the predicted line, so that the ratio $\gamma_c^{\mathrm{num}}(\mu)/2\mu\Delta' = \xi/l$ approaches the value 2 for $\mu \to \infty$ as expected.

However, near $\mu = 0$ the behavior is qualitatively different. Here, disorder can induce a topological phase for $\mu < 0$ as well as a reentrant nontopological phase at larger disorder. From Eq. (5.21) we find the condition $\xi = -2l$ for the phase boundary. This

corresponds to

$$\gamma_c^{(ii)}(\mu) = -2\Delta'\mu, \tag{5.22}$$

which we find to agree well with the numerical results for the phase diagram (see dashed line in Fig. 5.8). Thus the phase diagram confirms that weak disorder leads to an enhancement of the chemical potential range of the topological phase, while for stronger disorder the range decreases again.

5.5. Conclusion

Even for conventional superconducting phases, the flux periodic currents have been widely studied for mesoscopic rings [Butt 86, Oppe 92, Schw 10, Kosh 07]. Here, we studied the Josephson currents across a weak link in a mesoscopic ring in a topological superconducting phase. As a paradigmatic model system, we studied Kitaev's model of a one-dimensional spinless p-wave superconductor, focusing on the parameter regime near the topological phase transition. We found that in mesoscopic rings, there is an h/e-periodic contribution to the tunneling current even if electron number parity is not conserved. This h/e-periodic contribution emerges due to the hybridization of the Majorana bound states localized on the two sides of the weak link through the interior of the ring and exhibits a pronounced peak just on the topological side of the topological phase transition. This peak provides an interesting signature for the existence of a topological phase transition and the formation of Majorana bound states at the junction.

We found that this effect remains robust in the presence of disorder in the wire. In fact, near the topological phase transition disorder can even stabilize the topological phase. When tuning, say, the chemical potential of the system to the nontopological side of the phase transition, there is a disorder-induced topological phase for moderate amounts of disorder, with a reentrant nontopological phase at even stronger disorder. This is in stark contrast to the behavior of the system far in the topological phase where disorder weakens and eventually destabilizes the topological phase.

6. Magneto-Josephson effects and Majorana bound states in quantum wires

Recent work established that topological insulator edges support a novel 'magneto-Josephson effect', whereby a dissipationless current exhibits 4π-periodic dependence on the relative orientation of the Zeeman fields in the two banks of the junction. In this chapter, we explore the magneto-Josephson effect in junctions based on spin-orbit-coupled quantum wires. In contrast to the topological insulator case, the periodicities of the magneto-Josephson effect no longer follow from an exact superconductor-magnetism duality of the Hamiltonian. To provide guidance to experiments, we also estimate the magnitude of the magneto-Josephson effects in realistic parameter regimes, and compare the Majorana-related contribution to the coexisting 2π-periodic effects emerging from non-Majorana states. This chapter has been previously published as [Pien 13b].

6.1. Introduction

One of the most direct but also challenging experimental confirmations of the existence of Majorana bound states is based on the periodicity of the Josephson effect. For junctions of topological superconductors, the Josephson effect is predicted to be 4π periodic in the phase difference of the order parameter, in sharp contrast to the conventional 2π periodicity (see Sec. 3.3.2). Recently it has been noticed that a topological-insulator edge, proximity coupled to an s-wave superconductor, exhibits an exact superconductivity-magnetism duality [Nils 08, Jian 13]. The duality transformation maps the phase of the superconducting order parameter to the direction of the applied magnetic field in the plane perpendicular to the spin–orbit field. As a consequence, the duality predicts a magneto-Josephson effect by which a rotation of the magnetic field across a junction induces a Josephson current even in the absence of a phase gradient [Jian 13, Meng 12, Kote 13].

Explicitly, proximity-coupled topological-insulator edges are described by the Bogo-

liubov-de Gennes Hamiltonian [Fu 08]

$$\begin{aligned}\mathcal{H}_{\mathrm{TI}} = v\hat{p}\tau^z\sigma^z - \mu\tau^z + \Delta\left(\cos\phi\,\tau^x - \sin\phi\,\tau^y\right) \\ - b\sigma^z + B\left(\cos\theta\,\sigma^x - \sin\theta\,\sigma^y\right).\end{aligned} \tag{6.1}$$

Here we have employed the Nambu spinor basis $\Psi^T = (\psi_\uparrow, \psi_\downarrow, \psi_\downarrow^\dagger, -\psi_\uparrow^\dagger)$ and introduced Pauli matrices σ^a and τ^a that act in the spin and particle-hole sectors, respectively. The edge-state velocity is given by v, $\hat{p}$ is the momentum, and the σ^z-direction represents the spin–orbit-coupling axis. We allow the chemical potential μ, superconducting pairing $\Delta e^{i\phi}$, longitudinal magnetic field strength b, transverse magnetic field strength B, and the transverse-field orientation angle θ to vary spatially. This Hamiltonian takes the same form upon interchanging the magnetic terms $\{b, B, \theta, \sigma^a\}$ with the superconducting terms $\{\mu, \Delta, \phi, \tau^a\}$. An important aspect of this duality is that it maps the two topologically distinct phases of the model into each other, mapping the 'Δ-phase' (occurring for $\Delta^2 - b^2 > \max\{B^2 - \mu^2, 0\}$) into the '$B$-phase' (occurring for $B^2 - \mu^2 > \max\{\Delta^2 - b^2, 0\}$) and vice versa.

For topological-insulator edges, the duality immediately allows one to derive the periodicity of the magneto-Josephson effect from the known periodicities of the Majorana Josephson effect [Jian 13, Meng 12, Kote 13]. To this end, we consider three-leg junctions [Jian 11b] with the phase arrangements $B-\Delta-B$ (with a 2π-periodic Majorana Josephson effect) and $\Delta - B - \Delta$ (with a 4π-periodic Majorana Josephson effect). The duality implies that the periodicities are reversed for the magneto-Josephson effect, which is 4π periodic in the magnetic-field orientation for $B - \Delta - B$ junctions but 2π periodic for a $\Delta - B - \Delta$ setup. Strictly speaking, the duality also maps charge Josephson currents into spin Josephson currents. At first sight, this may suggest that a change in direction of the magnetic field across a junction only drives a spin Josephson current. However, it was shown in Ref. [Jian 13] that as a result of the spin-momentum locking, there is also a conventional (and experimentally more accessible) charge current across the junction in addition to the spin current.

While the magneto-Josephson effect has been studied in some detail for topological insulator edges [Jian 13, Meng 12, Kote 13], much less is known about it for junctions based on semiconductor quantum wires. There are several reasons why this poses an interesting problem. Many of the ongoing searches for Majorana bound states are based on quantum-wire based structures. There are also several distinct differences between topological superconducting phases based on proximity-coupled topological insulators and semiconductor quantum wires. First, the kinetic energy of the quantum-wire Hamiltonian explicitly violates the duality, making the duality only of suggestive value for the quantum-wire situation. Second, the two topologically distinct phases of

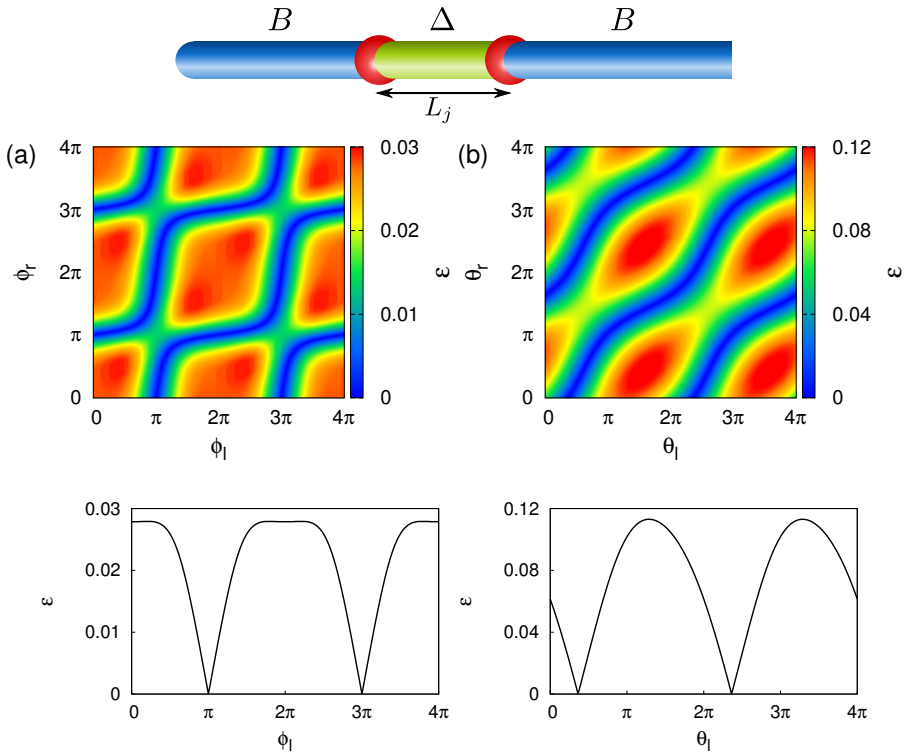

Figure 6.1.: Upper panels: Color scale plots of the low-energy Bogoliubov-de Gennes spectra (only $\epsilon > 0$) of a $B - \Delta - B$ junction vs. (a) the superconducting phases ϕ_l and ϕ_r and (b) the magnetic-field directions θ_l and θ_r. Lower panels: Corresponding line cuts along $\phi_r = 0$ and $\theta_r = 0$, respectively. Both line cuts exhibit cusps at zero energy, reflecting protected zero-energy crossings and thus, the Josephson current is 4π periodic in both ϕ and θ. The parameters for the three segments are $\Delta_{l/r} = 1.6$, $\Delta_m = 2$, $B_{l/r} = 2$, $B_m = 0.9$, $\mu_{l/m/r} = 0$, and $L_j = 2$ (length of the junction). We also set $\theta_l = \theta_r = \pi/2$, $\theta_m = 0$ in (a) and $\phi_l = \phi_r = \pi/2$, $\phi_m = 0$ in (b). Note that the parameters of the three segments are labeled by subscripts l, m, and r.

the topological insulator effectively trade places in the quantum wire. For instance, a 4π-periodic Majorana Josephson effect occurs in the $\Delta - B - \Delta$ arrangement in topological insulators, but in the $B - \Delta - B$ arrangement in quantum wires.

This motivates us to explore the magneto-Josephson effects in semiconductor quantum wires in more detail in this chapter. In Sec. 6.2, we present numerical results based on a recursive scattering-matrix approach and establish the periodicities of the magneto-Josephson effects. In Sec. 6.3, we provide further insight into the periodicities by analytical arguments and the analysis of limiting cases. Finally, Sec. 6.4 is concerned with numerical estimates of the magnitude of the effect and Sec. 6.5 collects our conclusions.

6.2. Numerical results

We now turn to semiconductor quantum wires proximity coupled to s-wave superconductors. The Hamiltonian for a clean, single-channel semiconductor quantum wire (QW) in the presence of a Zeeman field B, Rashba spin–orbit coupling u, and induced superconductivity Δ is [Lutc 10, Oreg 10]

$$\mathcal{H}_{\mathrm{QW}} = \left(\frac{\hat{p}^2}{2m} - \mu\right)\tau_z + u\hat{p}\sigma_z\tau_z + B\left(e^{i\theta}\sigma_+ + e^{-i\theta}\sigma_-\right) + \Delta\left(e^{i\phi}\tau_+ + e^{-i\phi}\tau_-\right) \qquad (6.2)$$

Other than dropping the longitudinal magnetic field term for lack of relevance in the following, this Hamiltonian differs from that of the topological insulator edge in Eq. (6.1) by the kinetic term $\hat{p}^2/2m$. This term explicitly breaks the duality present for the topological insulator edge and is responsible for key differences between the topological insulator edge and the quantum wire. Most importantly, the phases are in some sense effectively reversed in the two systems. Explicitly, in quantum wires, the topological (or B) phase occurs for $B^2 > \Delta^2 + \mu^2$, while the nontopological (or Δ) phase requires $B^2 < \Delta^2 + \mu^2$. In the quantum wire model, the identification of topological and nontopological phases is unique since the Δ-phase is continuously connected to the vacuum. The corresponding identification is less defined for the topological insulator as the model does not connect naturally to the vacuum due to the linear spectrum. Indeed, the duality of the model maps the two phases into each other, suggesting that they are topologically distinct but cannot be labeled as topological and nontopological. However, if we take the presence or absence of the fractional (4π-periodic) Majorana Josephson effect as the defining feature of a topological superconducting phase, we would crudely label the Δ phase as topological and the B phase as nontopological, which just reverses the assignments for the quantum wire model.

We consider quantum-wire junctions consisting of three segments, with phase arrangements $B - \Delta - B$ and $\Delta - B - \Delta$. It is well established that the periodicity in the superconducting phase difference across the junction is 4π in the $B-\Delta-B$ arrangement, but 2π for the $\Delta - B - \Delta$ setup [Lutc 10, Oreg 10]. These periodicities are reproduced in our numerical calculations of the low-energy Bogoliubov-de Gennes spectra shown in Figs. 6.1(a) and 6.2(a). Here, we restrict ourselves to $\mu = 0$ for simplicity. The calculations are based on a scattering-matrix approach which has been employed previously in the context of topological superconducting phases and Majorana bound states in quantum wires (see, e.g., [Brou 11b] and [Pien 12b]). In short, it is based on concatenating small slices of quantum wire to obtain the scattering matrix $S(\epsilon)$ of the entire wire. The spectrum can then be determined by solving the equation $\det[1 - S(\epsilon)] = 0$. A more detailed description of the method can be found in [Brou 11b].

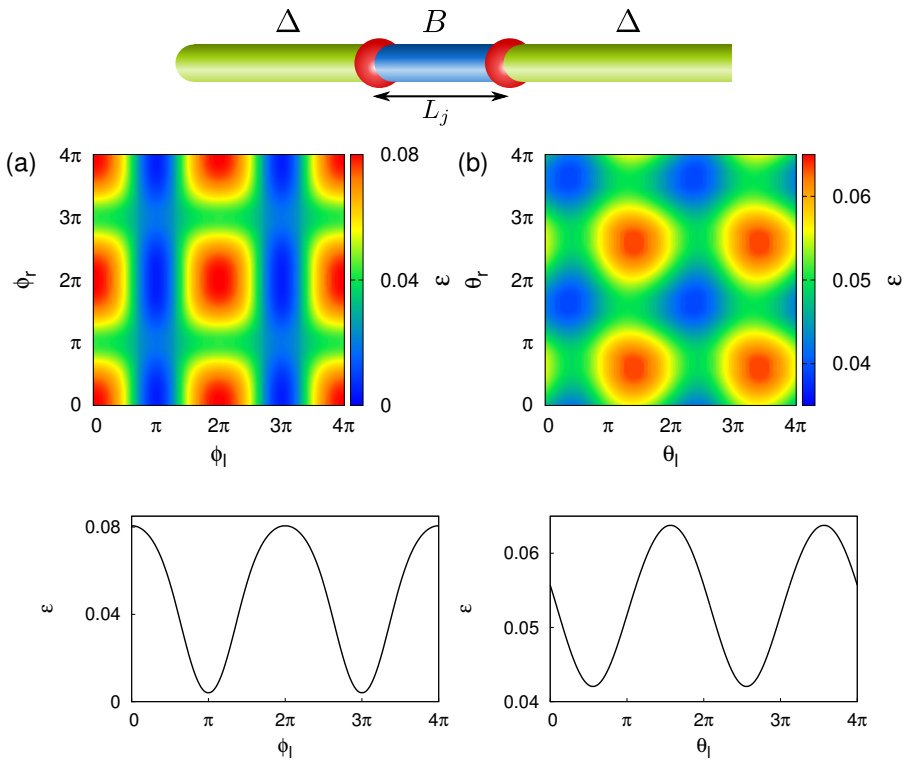

Figure 6.2.: Upper panels: Color scale plots of the low-energy Bogoliubov-de Gennes spectra (only $\epsilon > 0$) of a $\Delta - B - \Delta$ junction as a function of (a) superconducting phases and (b) magnetic field directions. Lower panels: Corresponding line cuts along $\phi_r = 0$ and $\theta_r = 0$, respectively. There are no zero-energy crossings and the current is 2π periodic. The parameters for the three segments are $\Delta_{l/r} = 2$, $\Delta_m = 1.6$, $B_{l/r} = 0.9$, $B_m = 2$, $\mu_{l/m/r} = 0$, and $L_j = 5$. We also set $\theta_l = \theta_r = \pi/2$, $\theta_m = 0$ in (a) and $\phi_l = \phi_r = \pi/2$, $\phi_m = 0$ in (b).

Fig. 6.1(a) shows the low-energy spectrum of a $B - \Delta - B$ junction as a function of the phases of the superconducting order parameters of the outer segments. The left and right segments are chosen much longer than the coherence length so that the Majorana bound states at the outer ends do not couple to the Majoranas at the junction and can be safely ignored. The low-energy spectrum shows protected zero-energy crossings, which makes the current 4π periodic as a function of ϕ. The corresponding spectrum of a $\Delta - B - \Delta$ junction is shown in Fig. 6.2(a). In contrast to the $B - \Delta - B$ case, the current is always 2π periodic. For both types of junctions, there are two Majorana bound states at the interfaces between the B and Δ regions. However, in the latter case the hybridization of the Majoranas does not generate a protected crossing at zero.

Representative results for the dependence of the low-energy Bogoliubov-de Gennes spectra of the junctions on the directions θ of the magnetic fields are shown in Figs. 6.1(b) and 6.2(b). We find that also the dependence on θ is 4π periodic for $B - \Delta - B$ junctions and 2π periodic for $\Delta - B - \Delta$ junctions, with the spectra exhibiting protected zero-

	$B-\Delta-B$		$\Delta-B-\Delta$	
	ϕ	θ	ϕ	θ
periodicity for QW	4π	4π	2π	2π
periodicity for TI edge	2π	4π	4π	2π

Table 6.1.: Periodicities of the Josephson energy as a function of the phase difference of the superconducting gap and the relative magnetic-field orientation θ. We list results for $B-\Delta-B$ and $\Delta-B-\Delta$ junctions realized in quantum wires (QW) and topological insulator edges (TI). The latter results are taken from [Jian 13].

energy crossings in the first case, but not in the second. We summarize the periodicities for the two types of junctions in quantum wires in Table 6.1. Remarkably, the magneto-Josephson effect has the same periodicity for the quantum wire and the topological-insulator edge. This is in stark contrast with the ordinary Josephson current which has different periodicities in the two models reflecting the reversed roles of topological and nontopological phases.

6.3. Limiting cases and analytical considerations

To gain more insight into the periodicities of the Josephson effects summarized in Table 6.1 and their relations, we now combine analytical arguments and an analysis of limiting cases. First, we use analytical arguments to derive the Josephson periodicities for quantum wires which are based on the well-established result that the dependence on the superconducting phase is 4π periodic for a $B-\Delta-B$ junction (fractional Josephson effect). This complements the arguments based on the magnetism-superconductivity duality for the topological insulator edge.

To gain a better understanding of the similarities of and differences between the topological insulator and quantum wire cases, we then study the limit of large spin–orbit coupling $\epsilon_{\mathrm{SO}} = mu^2$ for the quantum wire model (or equivalently large mass m), i.e. $\epsilon_{\mathrm{SO}} \gg \Delta \gg |B-\Delta|$. In this limit, there are strong similarities between the low-energy spectra of the topological-insulator edge and the quantum wire.

6.3.1. Analytical argument

In this section, we derive the periodicities in both ϕ and θ for the quantum-wire case by analytical arguments. Our arguments assume the well-established fractional Josephson effect (i.e. a 4π-periodic ϕ dependence) for a $B-\Delta-B$ junction and reproduce the numerically obtained periodicities summarized in Table 6.1. To this end, it suffices to

derive the number of protected zero-energy crossings considering particular limiting cases of the two types of junctions. By adiabatic continuity, these periodicities must then hold for junctions of the same kind with arbitrary parameters.

Consider first a quantum-wire junction in the $\Delta - B - \Delta$ configuration. The Δ phase of the quantum wire is adiabatically connected to the vacuum by making the chemical potential large and negative. At the same time, the B phase is adiabatically connected to a spinless p-wave superconductor by taking the limit of large Zeeman field B [Alic 11]. Consequently, a $\Delta - B - \Delta$ junction can be adiabatically deformed into an essentially finite segment of a p-wave superconducting wire with hard-wall boundary conditions. In this limit, the two Majorana bound states localized at the domain walls hybridize and split by some finite energy. Clearly, the two Majorana bound states will penetrate only very little into the Δ sections of the junctions, and consequently, they will be only weakly dependent on ϕ and θ as long as $|B|, |\Delta| \ll |\mu|$, where $\mu < 0$ is the chemical potential in the outer Δ segments of the wire. Thus, while there will be a variation of the energy splitting with ϕ and θ, it will be small compared to the magnitude of the splitting itself. Thus, there are no zero-energy crossings in this case and the Josephson current is 2π periodic both in θ and ϕ. These considerations are only valid for the quantum wire because the decay length of the Majorana states into the insulating segments on the outside is controlled by $|\mu|$. In a TI-edge junction the gap in the Δ segments is controlled by the pairing strength Δ and not by μ. Therefore, the effect of Δ in TI edges is never perturbative and the above argument does not hold for ϕ.

We now turn to the $B - \Delta - B$ junction for which the Majorana energy is 4π periodic both in ϕ and θ. The 4π periodicity as a function of ϕ represents the well-known fractional Josephson effect [Kita 01, Kwon 04, Fu 09a]. In the remainder of this section, we demonstrate that the parities of the number of protected zero-energy crossings of the Majorana energy dispersion as a function of ϕ and θ are equal for a $B - \Delta - B$ quantum wire junction. The basic observation is that we can again consider the limit in which the middle Δ section has a large and negative μ. In this insulating limit, the gap does not close when we take B and Δ equal to zero. In effect, we can thus replace the $B - \Delta - B$ junction by a $B - I - B$ junction, where the middle section is a conventional insulator (I).

We start by considering a $B - I$ interface between a B dominated phase with $\phi, \theta = 0$ and a normal insulator with $B, \Delta = 0$ and $\mu < 0$. This interface harbors one zero-energy Majorana bound state with wavefunction ψ. We can tune the left region to the phase ϕ and the angle θ by performing the unitary transformation $U(\phi, \theta) = \exp(i\phi\tau_z/2 + i\theta\sigma_z/2)$ on the Majorana wavefunction, i.e., $\psi(\phi, \theta) = U(\phi, \theta)\psi$. It is crucial for our argument that we can effect the variation of ϕ and θ in the left region by a *global* transformation

$U(\phi, \theta)$, which is possible because the rotation of B and Δ does not affect the normal insulator on the right. We note that $U(2\pi, 0) = U(0, 2\pi) = -1$, which guarantees that the Majorana wavefunction evolves to the same final state, when either ϕ or θ advance by 2π.

We now consider weak coupling of two such interfaces in a $B - I - B$ junction. This coupling leads to a symmetric splitting of the two Majorana states about zero energy. When the coupling across the junction is sufficiently weak, we can obtain this subgap spectrum emerging from the Majorana modes localized at the junction accurately from first-order perturbation theory. Starting at $\phi = \theta = 0$ and tuning either ϕ or θ to 2π the initial wavefunction evolves to the same final state. Consequently, the initial and final subgap-energy spectra emerging from the hybridized Majorana modes will be identical for both processes. We know from the fractional Josephson effect that the positive-energy excitation at $\phi = 0$ becomes negative (and vice versa) when ϕ advances by 2π, and hence the associated Bogoliubov-de Gennes eigenenergy must cross zero energy an odd number of times in the process. Given that $U(2\pi, 0) = U(0, 2\pi) = -1$, this immediately implies that the positive- and negative-energy excitations also exhibit an odd number of zero-energy crossings when tuning θ from 0 to 2π instead, which proves the 4π periodicity as a function of θ.

It is worth noting that this argument fails for the TI edge model (6.1), as it should according to Table 6.1. The reason is that irrespective of μ, the corresponding spectrum is never gapped when setting $B, \Delta = 0$.

6.3.2. Strong spin–orbit coupling ($\epsilon_{\mathrm{SO}} \gg B > \Delta$)

The arguments in the previous subsection explain the periodicities of the magneto-Josephson effects for semiconductor quantum wires. When combined with the duality arguments for topological insulator edges, this explains the full set of periodicities collected in Table 6.1. How the periodicities of these two systems are related, however, remains an open question. This is particularly interesting in the limit $\epsilon_{\mathrm{SO}} \gg B > \Delta$, when the low-energy bulk spectrum of the quantum wire is nearly identical to the spectrum of a topological insulator edge.

When the spin–orbit energy is much larger than the Zeeman energy, the bulk spectrum of Eq. (6.2) depicted in Fig. 6.3 has three minima located at $p = 0$ and $p = \pm p_F$, where $p_F = 2mu$ when $\mu = 0$. Since p_F is large in the limit of strong spin–orbit coupling, the subspaces at $p = 0$ and at $p = \pm p_F$ effectively decouple for sufficiently smooth domain walls and the low-energy spectrum can be understood as arising from a super-

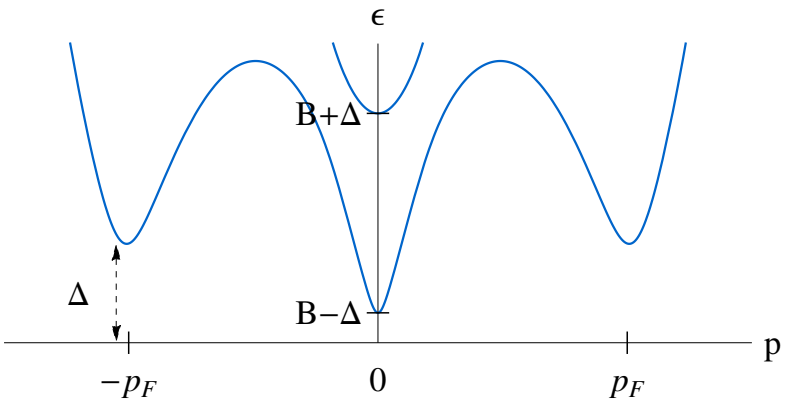

Figure 6.3.: Bulk spectrum of the quantum-wire Hamiltonian (6.2) in the limit of strong spin–orbit coupling.

position of two subspectra.[1] Near $p = 0$, the Hamiltonian (6.2) can be linearized and reduces to the Hamiltonian of the topological insulator edge (i.e., Eq. (6.1) with $\mu = b = 0$). Near $p = \pm p_F$, the Hamiltonian can be linearized, as well, and reduces to that of a spinless p-wave superconductor (cf. App. B). This describes a topological superconductor by itself. Since the topologically distinct phases are labeled by a $\mathbf{Z}_2$ index, this provides an explanation for the effective reversal of phases between the quantum-wire and the topological-insulator Hamiltonian.

The high-momentum subspace near $p = \pm p_F$ has a gap of size Δ. In contrast, the low-momentum subspace near $p = 0$ has a gap equal to $|B - \Delta|$, which is controlled by the competition of Zeeman and pairing energies and which is much smaller when the system is close to the topological phase transition, $|B - \Delta| \ll \Delta$. Zeros of the gap in the low-momentum subspace trigger the topological phase transition and thus, the Majorana bound states, localized at domain walls between B- and Δ-dominated regions, predominantly reside in this subspace. Consequently, in this subspace the relevant subgap spectrum of a short junction is determined by the hybridization of the Majorana bound states and the periodicities as a function of ϕ and θ are those for the topological-insulator edge. This seems consistent with Table 6.1 for the dependences on θ, but not for those on ϕ.

To understand the full set of periodicities in Table 6.1, we thus need to also consider the high-momentum subspace at $\pm p_F$. In this subspace where the Hamiltonian reduces to that of a spinless p-wave superconductor, the effective spin–orbit field is large and hence, the magnetic field is only a small perturbation. The corresponding spectrum should thus depend only weakly on θ. At the same time, variations in ϕ can result in a

[1] Note that the superconducting pairing couples the states near $+p_F$ with those near $-p_F$ so that these momenta cannot be considered separately.

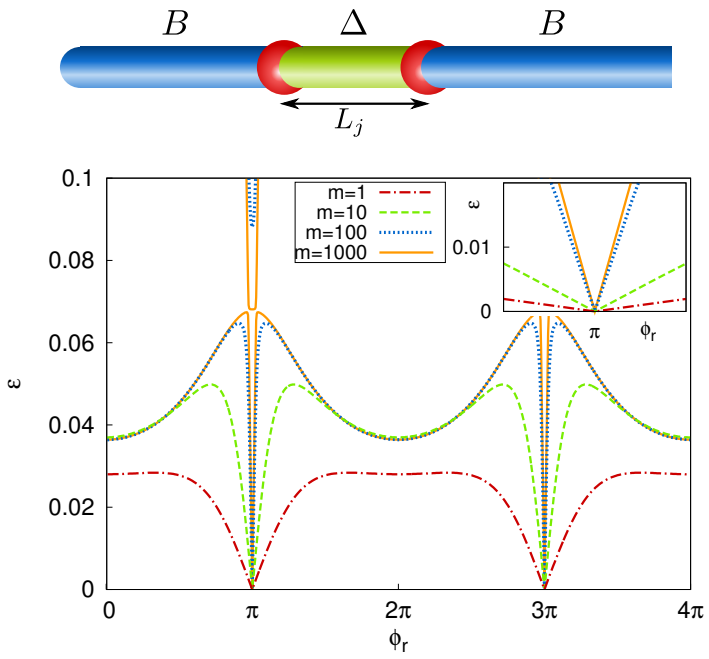

Figure 6.4.: Low-energy spectrum of a $B - \Delta - B$ junction as a function of ϕ_r for different masses m (and hence spin–orbit energies $\epsilon_{\mathrm{SO}} = mu^2$). For large ϵ_{SO}, the dispersion of the hybridized Majorana bound states becomes 2π periodic while additional Andreev bound states cross zero energy at $\phi_r = \pi, 3\pi$. The avoided crossings between the Andreev and Majorana bound state excitations vanish in the limit $\epsilon_{\mathrm{SO}} \gg B$. The inset shows that the zero-energy crossing at $\phi = \pi$ persists for all values of m. Parameters: $B_{l/r} = \Delta_m = 2$, $\Delta_{l/r} = B_m = 1$, $u = 1$, $\mu_{l/m/r} = 0$, $L_j = 2$, and $\theta_{l/m/r} = \phi_{l/m} = 0$.

considerable Josephson current. In fact, as the high-momentum subspace by itself constitutes a model of a topological superconductor, the ϕ dependence of the corresponding Bogoliubov-de Gennes spectrum exhibits protected zero-energy crossings.

We now use these insights to understand the similarities and differences of the Josephson periodicities in topological insulators and quantum wires in more detail. First consider a quantum wire in a $B-\Delta-B$ configuration. Such junctions exhibit a 4π-periodic Josephson current in the superconducting phase, with a protected zero-energy crossing of the Bogoliubov-de Gennes spectra. This contrasts with the 2π periodicity for the same junction made of topological-insulator edges. To understand this difference in periodicity, Fig. 6.4 shows how the low-energy spectrum changes with increasing spin–orbit energy. As expected based on the general arguments above, the spectrum develops two distinct types of subgap states as the spin–orbit energy increases, $\epsilon_{\mathrm{SO}} \gg B$ (seen most clearly in the traces for $m = 1000$ in Fig. 6.4). The first type of state has an approximately sinusoidal ϕ dependence, an offset from zero energy, and 2π periodicity. This state can

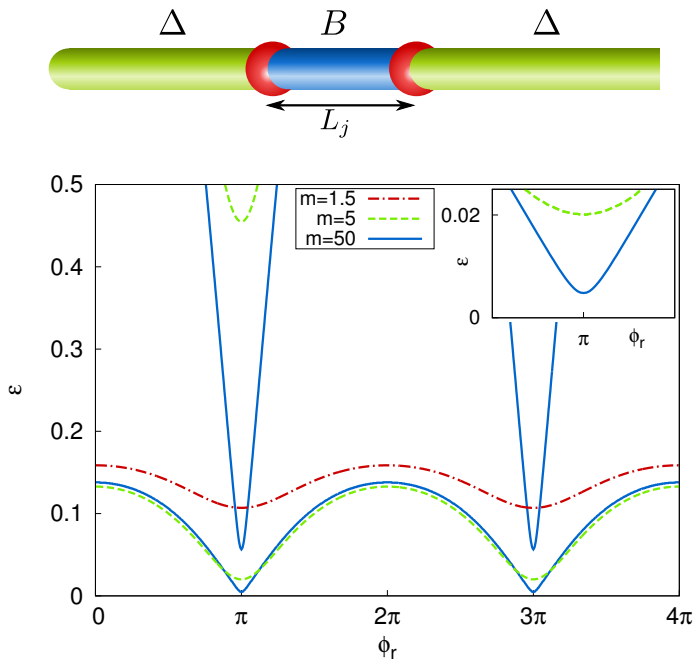

Figure 6.5.: Low-energy spectrum of a $\Delta - B - \Delta$ junction as a function of ϕ_r for different masses m (and hence spin–orbit energies $\epsilon_{\mathrm{SO}} = mu^2$). As indicated by Table 6.1, the spectrum approaches 4π periodicity for $\epsilon_{\mathrm{SO}} \to \infty$. For strong spin–orbit coupling, Andreev bound states appear. Their energy has a phase dependence $\epsilon_A \sim \Delta\cos(\phi/2)$. Inset: Close-up near $\phi = \pi$ showing the avoided crossing at $\epsilon = 0$. Parameters: $B_{l/r} = \Delta_m = 1$, $\Delta_{l/r} = B_m = 2$, $u = 1$, $\mu_{l/m/r} = 0$, $L_j = 2$, and $\theta_{l/m/r} = \phi_{l/m} = 0$.

be identified with the hybridized Majorana bound states in the low-momentum subspace. The second type of state crosses zero energy at $\phi = \pi, 3\pi$ with a $\pm E_0\cos(\phi/2)$ dispersion, where E_0 is of the order of Δ. This excitation corresponds to an Andreev bound state at $p = \pm p_F$. As seen in Fig. 6.4, there is an avoided crossing between these states which disappears as the spin–orbit energy and, with it, the momentum mismatch diverge.

This now allows one to understand the periodicities of Table 6.1 for the case of $B-\Delta-B$ junctions. In the quantum wire, only the low-momentum subspace has an interesting θ dependence. Thus, the θ dependence remains the same between quantum wires and topological-insulator edges. At the same time, both subspaces contribute to the dependence on ϕ. Indeed, the above considerations show that the protected zero-energy crossing in the quantum-wire spectrum is associated with states which converge entirely on the high-momentum subspace as the spin–orbit energy increases. These states do not exist for the topological-insulator edge whose ϕ dependence is thus 2π periodic.

In a $\Delta - B - \Delta$ junction, the change of periodicities is opposite. While the quan-

tum wire is 2π periodic in ϕ, the topological-insulator edge is 4π periodic. The evolution of the low-energy spectrum for the quantum wire with increasing spin–orbit energy is shown in Fig. 6.5. The sinusoidal 2π-periodic dependence of the Majorana states present for $\epsilon_{\mathrm{SO}} \simeq B$ becomes a $\pm\cos(\phi/2)$ dispersion with avoided crossings at π and 3π for $\epsilon_{\mathrm{SO}} \gg B$. In the limit of large spin–orbit energy, these states reside in the low-momentum subspace and reflect that the topological insulator model displays a topological Josephson effect in this subspace. Similarly, there are also Andreev states in the high-momentum subspace, similar to the ones in $B-\Delta-B$ junctions with the same $\pm E_0\cos(\phi/2)$ dispersion. At large but finite values of the spin–orbit energy, the levels in the low- and high-momentum subspaces mix, resulting in avoided crossings at $\phi=\pi,3\pi$ and a 2π-periodic spectrum. The avoided crossings close as the spin–orbit energy diverges, explaining the difference in ϕ periodicities of the quantum wire and topological insulator. Finally, the absence of change in the θ dependence between quantum wire and topological insulator has the same explanation as for $B-\Delta-B$ junctions.

6.4. Magnitude of the magneto-Josephson effect

In experiments aimed at detecting the 4π-periodic Josephson effect, a 2π-periodic background current originating from the conventional Josephson effect of the continuum states may mask the signature of the unconventional Josephson current. In the following, we provide quantitative estimates for the 4π- and 2π-periodic contributions to the current and show that the magneto-Josephson effect may be favorable over the conventional Josephson effect with regard to the relative magnitude of 2π- and 4π-periodic currents.

In order to obtain quantitative estimates, we consider a junction with a conventional insulating barrier between two semi-infinite quantum wires in the B-dominated phase. In the barrier, we set $B=\Delta=0$ and $\mu=-V_0<0$, so that there are no unconventional 4π-periodic Josephson currents originating from splitting Cooper pairs in the barrier into the two topological superconducting phases on the left and right [Jian 11b]. Thus, the Josephson currents in this setup are only due to the phase difference $\phi=\phi_l-\phi_r$ or the difference $\theta=\theta_l-\theta_r$ in magnetic-field orientations of the left and right bank. The total energy E (and hence the Josephson current) includes contributions from the above-gap continuum and the Andreev bound states with a 2π-periodic dispersion (jointly referred to below as continuum contribution for brevity) as well as Majorana bound states whose energy is 4π periodic.

For junctions with a low transmission probability $D \ll 1$, we find the energy of the

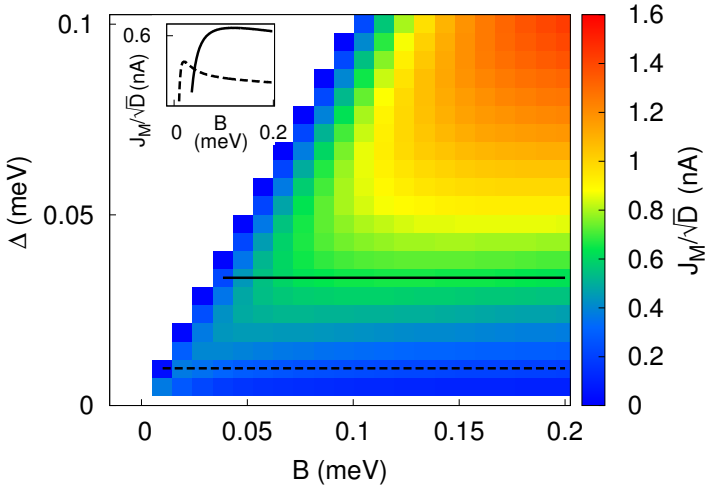

Figure 6.6.: Maximum Majorana Josephson current J_M for a $B-I-B$ junction normalized by the normal-state transmission coefficient $\sqrt{D}$ of the junction as a function B and Δ. We set $\mu = 0$ in the superconductor, which thus supports a topological phase for $B > \Delta$. Inset: cuts along the dashed and solid lines in the color scale plot. The parameters are $\epsilon_{SO} = 0.05$meV, $m = 0.015m_e$, $V_0 = 250$meV, $L_j = 3.2$nm.

Majorana states to be

$$E_{\text{Majorana}}(\phi, \theta) = E_M \cos(\phi/2) \cos[\theta/2 + \theta_0(\phi)]. \tag{6.3}$$

The θ dependence of the energy involves a phase shift, whereas the ϕ dependence is always symmetric with respect to $\phi = 0$ (cf. the lower panels of Figs. 6.1 and 6.2). The largest energy splitting is given by $E_M \sim \sqrt{D}E_{\text{gap}}$, where E_{gap} denotes the magnitude of the gap in the two banks of the junction. The size of the splitting is determined by the single-electron tunneling amplitude $\propto \sqrt{D}$.

The critical current of the junction depends on θ with a maximum critical current of $J_M = (e/\hbar)E_M$. In Fig. 6.6, we show numerical results for J_M, normalized by $\sqrt{D}$ to make the results insensitive to detailed properties of the tunnel junction, as a color scale plot. This normalized Majorana current roughly corresponds to $(e/\hbar)E_{\text{gap}}$. Thus for a fixed Δ, there is an optimal value of B for which the ratio $J_M/\sqrt{D}$ is maximized.

In Fig. 6.7, we compare the amplitudes of the 4π- and 2π-periodic currents originating from the Majorana and continuum states, respectively. We distinguish between the modulation of the continuum current with ϕ and θ. According to our numerical results,

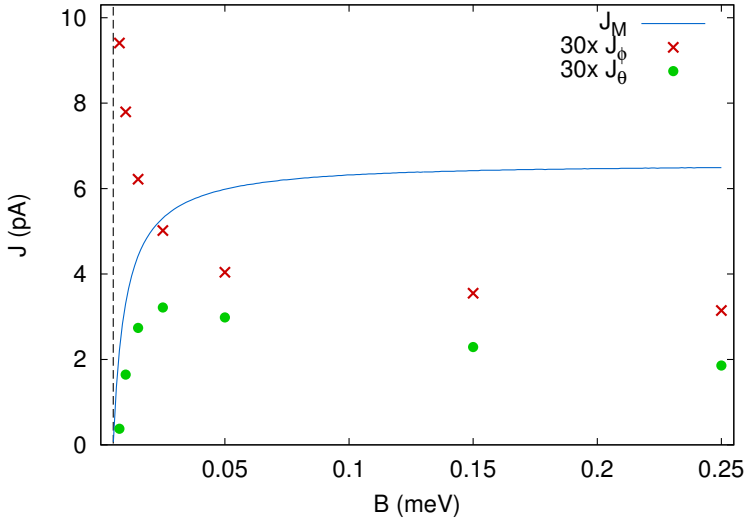

Figure 6.7.: Numerical results for the Majorana (J_M) and continuum (J_ϕ, J_θ) current oscillation amplitudes as a function of B. For presentation the continuum current has been multiplied by 30. The calculations have been performed with the same parameters as in Fig. 6.6 with $\Delta = 5\mu$eV. Transmission probabilities range from 0.1% to 0.4%. The vertical dashed line denotes the critical magnetic field.

the phase dependence of the continuum energy can be well described by

$$\begin{aligned} E_{\text{cont}}(\phi,\theta) =& E_0 \cos(\phi)\left\{\alpha + (1-\alpha)\cos\left[\theta + \theta_1(\phi)\right]\right\} \\ &+ \text{const.}, \end{aligned} \tag{6.4}$$

where $\alpha \in [0,1]$ is a parameter-dependent constant. Hence for $\alpha > 0$, the amplitude of the oscillations as a function of θ is smaller than the amplitude of the ϕ-oscillations. We numerically calculate the largest amplitudes of the Josephson current oscillations as a function of ϕ and θ,

$$\begin{aligned} J_\phi &= eE_0/\hbar \\ J_\theta &= (eE_0/\hbar)(1-\alpha) \end{aligned} \tag{6.5}$$

and plot them in Fig. 6.7 as a function of B along with the amplitude of the 4π-periodic Majorana current J_M. The latter is much larger than the continuum contribution for a large range of parameters. For a p-wave-superconductor junction the 2π-periodic current involves tunneling of Cooper pairs with amplitude $\propto D$ [Alic 11], in contrast to single-electron tunneling $\propto \sqrt{D}$ responsible for the 4π-periodic current. Hence in the large B limit, we expect J_M to exceed the 2π-periodic current by a factor of $1/\sqrt{D}$, which is ~ 20 for the parameters used in Fig. 6.7.

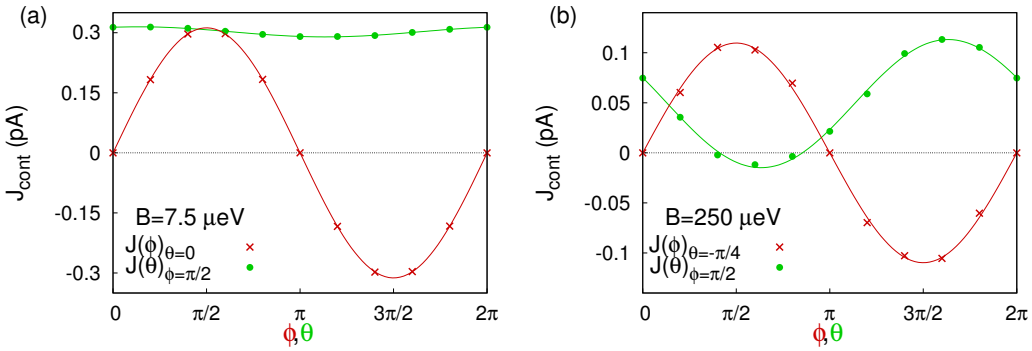

Figure 6.8.: Numerical results for the continuum contribution to the Josephson current as a function of ϕ (red crosses) and θ (green dots). The solid lines are fits to the ϕ-derivative of Eq. (4), $\partial_\phi E_{\mathrm{cont}}(\phi,\theta)$. All parameters are the same as in Fig. 6.7. The fixed angle is chosen such that the current is maximized. In this way, the oscillation amplitudes can be used to obtain J_ϕ and J_θ plotted in Fig. 6.7. The ϕ dependence is simply $J(\phi) = J_\phi \sin(\phi)$. In contrast $J(\theta)$ has a large offset and only a weak θ dependence for $B \sim \Delta$ [panel (a)]. This corresponds to $\alpha \sim 1$. For $B \gg \Delta$ [panel (b)], the amplitude of J_θ approaches that of J_ϕ and α decreases.

Only very close to the phase transition, when $|B - \Delta| \ll \Delta$, can the continuum current exceed the Majorana contribution. This is consistent with numerical estimates for continuum and Majorana Josephson currents for the topological insulator edge (6.1) in [Jian 11b], which corresponds to the limit $|B - \Delta| \ll \Delta$ for the quantum wire model (6.2).

Comparing the Josephson and magneto-Josephson effects, we find in accordance with Eq. (6.5) that J_ϕ is larger than J_θ, in particular in the regime of small B. On the other hand, the amplitude J_M of the Majorana current oscillation is the same for ϕ and θ. Thus, near the critical magnetic field, the 4π-periodic magneto-Josephson current appears on top of a constant current background with a small 2π-periodic modulation from the continuum states (see Fig. 6.8a). This is favorable in experiments to discriminate the 4π-periodic Majorana current from the conventional Josephson current of the continuum, e.g., in the Shapiro-step-like pattern due to the interference of a rotating magnetic field and an ac voltage as described in [Jian 13].

6.5. Conclusions

The dedicated experiments [Mour 12, Das 12, Chur 13, Rokh 12, Deng 12a, Finc 13] to detect Majorana bound states in spin–orbit-coupled quantum wires raise the question of how the exotic signatures of Majorana zero modes manifest themselves in such wires.

In this work, we explored the magneto-Josephson effect which complements the remarkable Josephson physics that Majorana bound states entail.

Our principal goal was to determine the periodicities of the magneto-Josephson effect for the various domain configuration of the Josephson junction. For junctions made of topological insulator edge states, the 4π-periodic effects emerge in mutually exclusive configurations: the conventional Josephson effect (involving a phase difference of the superconducting order parameter across the junction) appears in the $\Delta - B - \Delta$ domain sequence, while the magneto-Josephson effect requires the complementary structure, $B - \Delta - B$. This indicates that, in a sense, both domain types are topological for a topological-insulator edge. In contrast, for spin–orbit-coupled wires, we found for both types of Josephson effects that a 4π periodicity requires the $B - \Delta - B$ configuration.

While we invoked both analytical arguments and numerical analysis to establish this result, it has a natural interpretation. We expect that 4π periodicity with a parameter which is normally defined between 0 and 2π (up to trivial shifts) can only emerge if the parameter pertains to a topological phase. In a spin–orbit-coupled wire, there is no ambiguity as to which phase is topological. The Δ-dominated phase is continuously connected to the vacuum by taking the limit of a large and negative chemical potential. The B-dominated phase, on the other hand, is a topological phase continuously connected to a spinless p-wave superconductor. In Sec. 6.3.1, this argumentation is made explicit using analytical arguments.

Despite these characteristic differences of the magneto-Josephson (as well as Josephson) periodicities between topological insulator edge and semiconductor quantum wire, both models can be connected explicitly in the limit of large spin–orbit coupling. We exploited this connection in Sec. 6.3.2 to understand the relation between the Josephson periodicities of the two models.

With a view towards experiments on Majorana Josephson phenomena, we also computed the 4π-periodic magneto-Josephson effect for typical parameters, and compared its magnitude to that of the more conventional 2π-periodic background. The above-gap continuum of states in the wire contributes to both the phase-controlled and the magneto-Josephson effect. In the low-transmission regime ($D \ll 1$), we found that both 4π-periodic Josephson effects yield currents of the order of $\frac{e}{\hbar}\sqrt{D}E_{gap}$, with E_{gap} the gap in the two banks of the Josephson junction. In contrast, the conventional effects are suppressed by an additional factor of $\sqrt{D}$. In order to measure a sizable 4π-periodic current in experiment, however, it may be necessary to work at large transmission probabilities. In this regime, the exotic and conventional current contributions are of the same magnitude, although the 4π periodicity is relatively more pronounced for the magneto-Josephson effect.

Josephson-related phenomena in spin–orbit-coupled wires can become more complex when considering, e.g., ac modulations and Shapiro steps. These may require one to take accurate account of the complicated spectrum of the quantum wires. Moreover, when the energy gap in the middle domain is not too large, additional Andreev bound states could be present, which contribute to the Josephson effect. In this work we refrain from discussing these topics as well as more complicated setups such as three-leg Josephson effects to keep the presentation concise. Nonetheless, these aspects may prove important (and maybe even beneficial) in experiments, and present interesting avenues for future research.

7. Topological superconducting phase in helical Shiba chains

Recently a third proposal to realize Majorana bound states besides proximity-coupled quantum wires and topological insulator edges has received considerable attention. As discussed in Sec. 3.2.3 a topological superconducting phase can form in a chain of magnetic impurities on the surface of an s-wave superconductor. Such an impurity chain forms a band in the gap of the substrate superconductor. There are, in principle, two ways to open a superconducting gap, when the particle and hole branches of the impurity band overlap at the Fermi level: either the impurity chain has a noncollinear spin configuration or spin-rotation symmetry is broken by the superconductor. The former possibility has been originally suggested in [Choy 11] (see also [Mart 12, Kjae 12]), while the latter is closely related to a halfmetallic wire on top of a spin-orbit-coupled superconductor studied in [Duck 11]. As mentioned in Sec. 3.2.3, these two realizations are intimately connected since a ferromagnetic chain on the surface of a superconductor with Rashba spin-orbit coupling can potentially be mapped onto a helical spin chain without spin-orbit coupling in the substrate. Recently, such spin helices have been studied by a number of authors [Nadj 13, Nako 13b, Klin 13, Brau 13, Vazi 13, Kim 14] with claims of self-tuned topological phases. A spin helix can form, for instance, as a result of the RKKY interaction mediated by the superconducting substrate. Ongoing experiments on impurity chains on superconductors in the group of A. Yazdani, Princeton University, are claimed to exhibit signatures of Majorana bound states although the spin configuration of the impurity chain in the experiment is not fully settled.

In this chapter we investigate a helical impurity chain theoretically by developing a tight-binding Bogoliubov-de Gennes description starting from the Shiba bound states induced by the individual magnetic impurities. While the resulting model Hamiltonian has similarities with the Kitaev model for one-dimensional spinless p-wave superconductors, there are also important differences, most notably the long-range nature of hopping and pairing as well as complex hopping amplitudes. We use both analytical and numerical approaches to explore the consequences of these differences for the phase diagram and the localization properties of the Majorana end states when the Shiba chain is in a topological superconducting phase.

Furthermore, we explore an unconventional topological critical point that occurs as a consequence of the long-range couplings and has no analogue in the case of the Kitaev chain. At the critical point, we find exponentially localized Majorana bound states with a short localization length unrelated to a topological gap. Away from the critical point, this exponential decay develops a power-law tail. Our analytical results have encouraging implications for experiment. This chapter is based on two separate articles. Sections 7.1-7.5 have been published as [Pien 13a] and Sec. 7.6 appeared as [Pien 14].

7.1. Introduction

Magnetic impurities placed in a conventional superconductor create localized, sub-gap Shiba states [Yu 65, Shib 68, Rusi 69, Bala 06]. When the magnetic impurities are brought close to one another, the individual localized Shiba states hybridize and may form a band. Electrons in such a band, in turn, may hybridize with the condensate of the bulk superconductor by Andreev reflection. The properties of the band and the strength of Andreev processes depend on the magnetic structure of the impurity chain. Assuming that the impurity spins form a helix, it is argued that the Shiba bands will effectively realize a topological superconducting phase, akin to one-dimensional spinless p-wave superconductors [Kita 01]. Indeed, the Shiba states are effectively spin polarized and the (spin-singlet) s-wave Cooper pairs of the superconducting substrate can induce p-wave superconducting correlations in the Shiba band since neighboring impurity spins are misaligned due to the helical spin order. A particularly attractive feature of this proposal is that the presence of Majorana end states could be probed directly by scanning tunneling spectroscopy [Yazd 97, Yazd 99].

Following the original suggestion [Nadj 13], some aspects of this proposal have been investigated by a number of authors [Nako 13b, Klin 13, Brau 13, Vazi 13, Kim 14]. However, a theory making the connection to the formation and hybridization of Shiba states explicit has not yet been given. It is the purpose of this chapter to provide such a theoretical description. We show that for the case of deep Shiba states, one can derive an effective tight-binding Bogoliubov-de Gennes Hamiltonian. While this tight-binding Hamiltonian shares important features with the paradigmatic Kitaev model for one-dimensional spinless p-wave superconductors [Kita 01], there are also several substantial differences: (i) Both the hopping and the pairing terms are long range, having a $1/r$-power-law decay with distance as long as r remains small compared to the coherence length ξ_0 of the host superconductor. (ii) The hopping terms generally involve complex phase factors which lead to dispersions which are asymmetric under momentum reversal $k \to -k$. We explore the consequences of these differences both for the

phase diagram and for the localization properties of Majorana end states present when the system is in a topological phase.

Our approach is based on the following physical picture. We start with a given static texture of the impurity spins along the chain. This texture is ultimately the result of the RKKY interaction between the impurity states as mediated by the superconducting host[1] [Nadj 13, Klin 13, Brau 13, Vazi 13]. It seems likely that the precise nature of the spin texture is sensitive to system-specific details such as the ratio of the impurity spacing to the Fermi wavelength of the superconductor or anisotropies of the exchange interaction at the surface of the superconductor. Hence, we consider general periodic and helical spin textures which need not be commensurate with the underlying impurity chain. As long as the magnetic impurities are sufficiently dilute, each of them binds a pair of Shiba states with energies in the superconducting gap which are symmetric about the chemical potential pinned to the center of the gap. Overlaps between the Shiba bound states lead to hybridization and the formation of bands whose bandwidth grows with decreasing spacing between the impurities. If the impurity states are shallow, i.e., their energies are close to the superconducting gap edges, the impurity band will in general merge with the quasiparticle continuum and simply smear the gap edge. Topological superconducting states can possibly still be realized when the impurity bands at positive and negative energies become wide enough to overlap around the center of the gap, i.e., when the bandwidth becomes comparable with the superconducting gap.

Here, we focus on the opposite limit in which the Shiba bound states are deep with energies near the center of the gap. In this case, the bands emerging from the positive- and negative-energy Shiba states start to overlap already for weak hybridization. Thus, the Shiba bands remain well separated from the quasiparticle continuum and we can derive an effective Hamiltonian within the subspace of Shiba states. As long as the bandwidth of the Shiba states remains smaller than the energy of the bare Shiba states, there are two well-separated Shiba bands and the system is in a nontopological superconducting state. Topological superconducting phases can occur when the Shiba bands overlap around the center of the gap. Since the Shiba states are spin polarized, the induced pairing amplitude within the subspace of Shiba states is necessarily odd in momentum and hence of p-wave nature. If the system enters such a topological phase, there will be a p-wave gap at the chemical potential within the overlapping Shiba bands, in addition to the original s-wave gap of the host superconductor. However, such a p-wave gap does not necessarily form for arbitrary parameters despite the presence of a finite p-wave pairing amplitude and overlapping Shiba bands. Elucidating this nontrivial phase diagram is

[1] In three dimensions, the formation of helical spin order as a consequence of the RKKY interaction between localized spins was originally investigated in the context of rare-earth metals, see, e.g., [Elli 61] and [Yosi 96]; for a consideration of fluctuation effects in one and two dimensions, see [Loss 11] and [Klin 13].

one of the central goals of this chapter.

For typical Shiba chains, the coherence length ξ_0 of the host superconductor is much larger than the impurity spacing a which is comparable to the lattice spacing of the host superconductor. In numbers, one has $\xi_0/a \sim 10^2 - 10^3$ making a model with a pure $1/r$ decay of hopping and pairing an excellent starting point. In the context of topological phases, this long-range coupling poses interesting questions. Most importantly, it is usually assumed [Hasa 10] that the boundary modes of topological phases, such as Majorana end states, fall off exponentially into the bulk which seems incompatible with long-range coupling.

In the last part of this chapter we provide an analytical theory for the surprising localization properties of the Majorana end states in the presence of long-range couplings, with important implications for experiment. We show that helical Shiba chains display an unconventional topological critical point as a function of the helix and Fermi wavevectors k_h and k_F as a consequence of the long-range coupling. The critical point is located exactly at $k_h = k_F$ in the limit $\xi_0 \to \infty$ and remains close to it for finite ξ_0. Thus right at or near the critical point, the spin helix satisfies the condition for Bragg reflection which induces a strong tendency towards localizing the Majorana end states, competing with the delocalizing tendency of the long-range coupling. This may result in a localization length of the order of a few impurity sites, making isolated Majoranas accessible in experimentally feasible chains containing only a few dozen atoms.

This chapter is organized as follows. In Sec. 7.2, we introduce the model and discuss the formation of the spin helix. In Sec. 7.3.1, we review the formation of Shiba states for a single magnetic impurity in an s-wave superconductor, employing a technique which readily generalizes to chains of magnetic impurities. The latter are discussed in Sec. 7.3.2, culminating in a tight-binding Bogoliubov-de Gennes equation for deep Shiba states. The tight-binding model is employed to analyze the phase diagram in Sec. 7.4 and the localization properties of the Majorana modes in Sec. 7.5. In Sec. 7.6 we discuss the unconventional topological phase transitions and the localization properties of the Majorana states in the vicinity of the critical point. We conclude in Sec. 7.7 and defer some technical details and derivations to Appendix C.

7.2. Model

Our starting point is the Bogoliubov-de Gennes Hamiltonian (BdG) of an s-wave superconductor. We assume that the superconductor is in the clean limit but hosts a chain of

magnetic impurities placed at locations $\mathbf{r}_j$,

$$\mathcal{H} = \xi_{\mathbf{p}}\tau_z - J\sum_j \mathbf{S}_i \cdot \boldsymbol{\sigma}\delta(\mathbf{r}-\mathbf{r}_j) + \Delta\tau_x. \tag{7.1}$$

Here, $\mathbf{p}$ and $\mathbf{r}$ denote the electron's momentum and position, $\xi_{\mathbf{p}} = \mathbf{p}^2/2m - \mu$ with the chemical potential μ, Δ is the superconducting gap, and J denotes the strength of the exchange coupling between the magnetic impurity with spin S and the electrons in the superconductor. The Pauli matrices σ_i (τ_i) operate in spin (particle-hole) space. The BdG Hamiltonian is written in a basis which corresponds to the four-component Nambu operator $\Psi = [\psi_\uparrow, \psi_\downarrow, \psi_\downarrow^\dagger, -\psi_\uparrow^\dagger]$ in terms of the electronic field operator $\psi_\sigma(\mathbf{r})$. In this basis, the time-reversal operator takes the form $T = i\sigma_y K$, where K denotes complex conjugation. The BdG Hamiltonian (7.4) obeys the symmetry $\{\mathcal{H}, CT\} = 0$, with $C = -i\tau_y$. Thus, if ψ is an eigenspinor of $\mathcal{H}$ with energy E, $CT\psi$ is an eigenspinor of energy $(-E)$.

We assume that the magnetic moments are classical and arranged along a linear chain with lattice spacing a. We can parametrize the impurity spins $\mathbf{S}_j$ through spherical coordinates, using the angles θ_j and ϕ_j in addition to S,

$$\mathbf{S}_j = S(\sin\theta_j\cos\phi_j, \sin\theta_j\sin\phi_j, \cos\theta_j). \tag{7.2}$$

In the BdG equation (7.1), we take the spins as frozen into a given spin texture $\mathbf{S}_j$. We also assume the impurity spacings $a \gg 1/k_F$ so that the bandwidth of the Shiba bands is small compared to the gap of the host superconductor.

The spin texture will in general be governed by the RKKY interaction between the impurity spins, as mediated by the superconducting host [Nadj 13, Klin 13, Brau 13, Vazi 13]. Magnetic impurities interact with each other via exchange by virtual electron-hole excitations in the host metal. If the host is in the normal state, this exchange leads to the familiar RKKY interaction between the impurities [Abri 88] whose sign alternates as a function of inter-impurity distance r_{ij} and which is of magnitude $J(i-j) \sim (J\nu_0)^2 v_F/(k_F^2 r_{ij}^3)$. Here, J denotes the exchange coupling between magnetic impurity and electrons, ν_0 is the electronic density of states at the Fermi energy, and v_F and k_F denote the Fermi velocity and wavevector, respectively. There is some evidence for normal-metal substrates [Menz 12] that the RKKY interaction between impurity spins can lead to the formation of a spin helix when the impurities form an ordered chain.[2]

In a clean system, the RKKY interaction between two magnetic impurities a distance

[2]The chirality of the helix is probably determined by the Dzyaloshinskii-Moriya component of the interaction. This component breaks the degeneracy between the two helicities and may be much smaller than the isotropic part $J(i-j)$ of the RKKY interaction.

r_{ij} apart involves virtual electron-hole pairs with characteristic energy $\hbar v_F/r_{ij}$. On the other hand, superconductivity prohibits pairs with energy less than the gap Δ. As a result, $J(i-j)$ is substantially affected by superconductivity if $r_{ij} \gtrsim \xi_0$, where ξ_0 is the coherence length of the host superconductor. A perturbative treatment of the exchange interaction indicates [Abri 88, Gali 02] that the correction to the normal-state value of $J(i-j)$ caused by superconductivity is antiferromagnetic. The magnitude of the correction is of order $\delta J(i-j) \sim \Delta/(k_F r_{ij})^2$ and thus small at any $r_{ij} \lesssim \xi_0$. The presence of deep Shiba states enhances the correction [Yao 13]; in the limit $\alpha \to 1$, its absolute value reaches a maximum of the order of $\Delta/(k_F r_{ij})$. [This estimate may be obtained from a consideration of the total energy of a superconductor containing a pair of impurities which create Shiba states according to Eqs. (23), (32), and (33) below.] Still, the "normal-state" RKKY wins over the correction at $k_F r_{ij} \lesssim (k_F v_F/\Delta)^{1/2}$. For a typical superconductor, the right-hand side gives a relatively mild limitation $\sim 10^2$ which is compatible with the assumption $k_F a \gg 1$. Note that at the border of that region, $k_F r_{ij} \sim (k_F v_F/\Delta)^{1/2}$, the energy scale important for the observation of Majorana states, Δ_{eff}, is already small, $\Delta_{\text{eff}} \sim \Delta^{3/2}/(k_F v_F)^{1/2}$. Placing the magnetic impurities closer to each other makes both, the band of Shiba states and the induced gap wider. At the same time, superconductivity of the host will hardly affect the mutual orientation of the magnetic moments.

In general, one would expect that the specifics of the spin helix such as the overall spin orientation or the pitch depend sensitively on the details of the system. Important parameters are the ratio of the impurity spacing and the Fermi wavelength of the host superconductor, the single-ion magnetic anisotropy, as well as the spatial structure and isotropy of the exchange interaction between the magnetic moments. For this reason, we consider a general class of helical spin textures of the form

$$\theta_j = \theta \quad ; \quad \phi_j = 2k_h x_j \tag{7.3}$$

with a constant opening angle θ and pitch π/k_h; here $x_j = ja$ denotes the position of the j-th impurity along the chain.

The possible values of k_h are determined by the maxima of the Fourier transform of $J(i-j)$ [Klin 13, Brau 13, Vazi 13]. Thus, for a simple isotropic model of the superconductor and at $k_F a \gg 1$, the RKKY interaction $J(i-j)$ results in a helix wavevector $2k_h = (2k_F a - 2\pi n)/a$ with a single value of n such that $|k_h a| \leq \pi$. While we investigate this simple case in some detail below, we will first discuss the phase diagram and the Majorana bound states for arbitrary spin helices as defined in Eq. (7.3). The reason is that the details of the band structure of the superconductor as well as possible spin-orbit coupling may allow for other relations between the Fermi wavevector k_F and the helix

wavevector k_h. Note also that if the Hamiltonian of the magnetic system is dominated by the exchange interaction with an isotropic exchange integral $J(i-j)$ [Gali 02], the spin helix is planar with $\theta = \pi/2$. In general, the value of the single-ion anisotropy depends strongly on the orbital moment of the magnetic ion and the coordination of the host lattice[3] [Fert 80, Gamb 03].

7.3. Shiba states

7.3.1. Single magnetic impurity

To provide necessary background and to fix notation, we briefly derive the Shiba states for a single magnetic impurity in a form which can be generalized to a chain of impurities. For a single impurity placed at the origin, the BdG Hamiltonian (7.1) simplifies to

$$\mathcal{H} = \xi_{\mathbf{p}}\tau_z - J\mathbf{S}\cdot\boldsymbol{\sigma}\delta(\mathbf{r}) + \Delta\tau_x. \tag{7.4}$$

We can choose the impurity spin $\mathbf{S}$ to point along the z direction. In this case, the 4×4 Hamiltonian in Eq. (7.4) separates into independent 2×2 Hamiltonians $\mathcal{H}_\pm$ for spin-up $(+)$ and spin-down $(-)$ electrons,

$$\mathcal{H}_\pm = \xi_{\mathbf{p}}\tau_z \mp JS\delta(\mathbf{r}) + \Delta\tau_x. \tag{7.5}$$

To solve for the bound-state spectrum of these Hamiltonians, we write the BdG equations in a way which isolates the impurity term on the right-hand side,

$$[E - \xi_{\mathbf{p}}\tau_z - \Delta\tau_x]\psi(\mathbf{r}) = \mp JS\delta(\mathbf{r})\psi(\mathbf{0}), \tag{7.6}$$

and pass to momentum space using $\psi(\mathbf{r}) = \int[d\mathbf{p}/(2\pi)^3]e^{i\mathbf{p}\cdot\mathbf{r}}\psi_{\mathbf{p}}$,

$$[E - \xi_{\mathbf{p}}\tau_z - \Delta\tau_x]\psi_{\mathbf{p}} = \mp JS\psi(\mathbf{0}). \tag{7.7}$$

Multiplying by $[E - \xi_{\mathbf{p}}\tau_z - \Delta\tau_x]^{-1}$ from the left, we obtain

$$\psi_{\mathbf{p}} = \frac{\mp JS}{E^2 - \xi_{\mathbf{p}}^2 - \Delta^2}[E + \xi_{\mathbf{p}}\tau_z + \Delta\tau_x]\psi(\mathbf{0}). \tag{7.8}$$

[3] The anisotropy energy extracted from various experiments ranges from $\lesssim 1\mu$eV for Mn (orbital moment $L = 0$) in bulk Cu [Fert 80] to ~ 9meV for Co atoms ($L = 1$) on the surface of Pt.[Gamb 03]

We can now turn this into an equation for the spinor $\psi(\mathbf{0})$ evaluated at the position of the impurity only,

$$\psi(\mathbf{0}) = \int \frac{d\mathbf{p}}{(2\pi)^3} \frac{\mp JS}{E^2 - \xi_{\mathbf{p}}^2 - \Delta^2} [E + \xi_{\mathbf{p}}\tau_z + \Delta\tau_x]\psi(\mathbf{0}). \tag{7.9}$$

The integral is readily evaluated (see Appendix C.1) and we obtain a linear set of equations for the BdG spinor at the position of the impurity,

$$\left\{ \mathbf{1} \mp \frac{\alpha}{\sqrt{\Delta^2 - E^2}} [E + \Delta\tau_x] \right\} \psi(\mathbf{0}) = 0. \tag{7.10}$$

Here we introduced the dimensionless impurity strength $\alpha = \pi\nu_0 JS$ in terms of the normal-phase density of states ν_0.

One readily finds from Eq. (7.10) that $H_\pm$ has a subgap solution at energy $\pm E_0$ with [Yu 65, Shib 68, Rusi 69, Bala 06]

$$E_0 = \Delta \frac{1 - \alpha^2}{1 + \alpha^2}. \tag{7.11}$$

The energies of the two Shiba states cross at $\alpha = 1$ where the ground state changes from even to odd electron number.

The corresponding eigenspinors (written in the four-spinor form of the original 4×4 BdG Hamiltonian)

$$\psi_+(\mathbf{0}) = \frac{1}{\sqrt{\mathcal{N}}} \begin{pmatrix} 1 \\ 0 \\ 1 \\ 0 \end{pmatrix} \quad ; \quad \psi_-(\mathbf{0}) = \frac{1}{\sqrt{\mathcal{N}}} \begin{pmatrix} 0 \\ 1 \\ 0 \\ -1 \end{pmatrix}. \tag{7.12}$$

Here, the normalization factor $\mathcal{N} = (1 + \alpha^2)^2 / 2\pi\nu_0 \Delta\alpha$ follows from the normalization condition $1 = \int d\mathbf{r} \sum_n |\psi_n(\mathbf{r})|^2 = \int [d\mathbf{p}/(2\pi)^3] \sum_n |(\psi_{\mathbf{p}})_n|^2$. Note that the solution starting out at positive energies for small exchange coupling corresponds to quasiparticles made up from spin-up electrons and spin-down holes, while the one which starts at negative energies consists of spin-down electrons and spin-up holes.

For later reference, it is useful to generalize these spinors to impurity spins pointing in arbitrary directions. Parameterizing the impurity spin in spherical coordinates, $\mathbf{S} = S(\sin\theta\cos\phi, \sin\theta\sin\phi, \cos\theta)$, the corresponding spin-up and spin-down Pauli spinors

are

$$|\uparrow\rangle = \begin{pmatrix} \cos(\theta/2) \\ \sin(\theta/2)e^{i\phi} \end{pmatrix} \;\; ; \;\; |\downarrow\rangle = \begin{pmatrix} \sin(\theta/2)e^{-i\phi} \\ -\cos(\theta/2) \end{pmatrix}. \tag{7.13}$$

In terms of these Pauli spinors, the BdG spinors in Eq. (7.12) generalize to

$$\psi_+(\mathbf{0}) = \frac{1}{\sqrt{\mathcal{N}}} \begin{pmatrix} |\uparrow\rangle \\ |\uparrow\rangle \end{pmatrix} \quad ; \quad \psi_-(\mathbf{0}) = \frac{1}{\sqrt{\mathcal{N}}} \begin{pmatrix} |\downarrow\rangle \\ -|\downarrow\rangle \end{pmatrix}. \tag{7.14}$$

Note that the Pauli spinors are related by time reversal symmetry, $|\downarrow\rangle = T|\uparrow\rangle$, so that the BdG spinors satisfy the relation $\psi_-(\mathbf{0}) = CT\psi_+(\mathbf{0})$ in accordance with the general symmetries of the BdG Hamiltonian.

7.3.2. Chain of magnetic impurities

General formulation

We now generalize the approach of the previous section to a chain of magnetic impurities $\mathbf{S}_j$ at sites $\mathbf{r}_j$ as described by the Hamiltonian in Eq. (7.1). As for a single impurity, we start by isolating the impurity terms on one side of the BdG equation and passing to momentum space. This yields

$$[E - \xi_{\mathbf{p}}\tau_z - \Delta\tau_x]\psi_{\mathbf{p}} = -J\sum_j \mathbf{S}_j \cdot \boldsymbol{\sigma} e^{-i\mathbf{p}\cdot\mathbf{r}_j}\psi(\mathbf{r}_j). \tag{7.15}$$

Multiplying from the left by $[E - \xi_{\mathbf{p}}\tau_z - \Delta\tau_x]^{-1}$ and evaluating $\psi(\mathbf{r}_i)$ yields a closed set of equations for the BdG spinors at the positions of the impurities,

$$\psi(\mathbf{r}_i) = -J\sum_j \int \frac{d\mathbf{p}}{(2\pi)^3} \frac{e^{i\mathbf{p}(\mathbf{r}_i - \mathbf{r}_j)}}{E - \xi_{\mathbf{p}}\tau_z - \Delta\tau_x} \mathbf{S}_j \cdot \boldsymbol{\sigma}\psi(\mathbf{r}_j). \tag{7.16}$$

We are searching for subgap states so that we need to evaluate the momentum integral on the RHS for energies $E < \Delta$. This integral is performed in Appendix C.1 and we find

$$\psi(\mathbf{r}_i) = -\sum_j J_E(\mathbf{r}_i - \mathbf{r}_j)\hat{\mathbf{S}}_j \cdot \boldsymbol{\sigma}\psi(\mathbf{r}_j), \tag{7.17}$$

where we defined the unit vector $\hat{\mathbf{S}}_j = \mathbf{S}_j/S$ and

$$J_E(\mathbf{r}) = -\frac{\alpha}{\sqrt{\Delta^2 - E^2}} \frac{e^{-r/\xi_E}}{k_F r} \times \begin{pmatrix} E\sin k_F r + \sqrt{\Delta^2 - E^2}\cos k_F r & \Delta \sin k_F r \\ \Delta \sin k_F r & E\sin k_F r - \sqrt{\Delta^2 - E^2}\cos k_F r \end{pmatrix} \quad (7.18)$$

in terms of $\xi_E = v_F/\sqrt{\Delta^2 - E^2}$.

Tight-binding model for deep impurities

We now specify to deep impurities with impurity strength α close to unity so that the energy $\epsilon_0 \simeq \Delta(1-\alpha)$ of the individual Shiba states is close to the center of the gap. Moreover, we assume that the impurities are sufficiently dilute that the resulting impurity band remains well within the superconducting gap. In this limit, we can expand to linear order in E [and hence in $(1-\alpha)$] as well as in the coupling between impurity sites.

We start by writing Eq. (7.17) as

$$\psi(\mathbf{r}_i) + J_E(\mathbf{0})\hat{\mathbf{S}}_i \cdot \boldsymbol{\sigma}\psi(\mathbf{r}_i) = -\sum_{j\neq i} J_E(\mathbf{r}_{ij})\hat{\mathbf{S}}_j \cdot \boldsymbol{\sigma}\psi(\mathbf{r}_j), \quad (7.19)$$

with the shorthand $\mathbf{r}_{ij} = \mathbf{r}_i - \mathbf{r}_j$. The RHS is already linear in the coupling between Shiba states so that we can evaluate it for $E = 0$ and $\alpha = 1$. The LHS is readily expanded using Eq. (7.18), so that we obtain

$$\{\mathbf{1} - [E/\Delta + \alpha\tau_x]\hat{\mathbf{S}}_i \cdot \boldsymbol{\sigma}\}\psi(\mathbf{r}_i) = \sum_{j\neq i} \frac{e^{-r_{ij}/\xi_0}}{k_F r_{ij}} [\tau_z \cos k_F r_{ij} + \tau_x \sin k_F r_{ij}]\hat{\mathbf{S}}_j \cdot \boldsymbol{\sigma}\psi(\mathbf{r}_j), \quad (7.20)$$

Multiplying by $\hat{\mathbf{S}}_i \cdot \boldsymbol{\sigma}$ and using the identity $(\hat{\mathbf{S}}_i \cdot \boldsymbol{\sigma})(\hat{\mathbf{S}}_i \cdot \boldsymbol{\sigma}) = 1$ yields

$$\{\hat{\mathbf{S}}_i \cdot \boldsymbol{\sigma} - [E/\Delta + \alpha\tau_x]\}\psi(\mathbf{r}_i) = \sum_{j\neq i} \frac{e^{-r_{ij}/\xi_0}}{k_F r_{ij}} [\tau_z \cos k_F r_{ij} + \tau_x \sin k_F r_{ij}](\hat{\mathbf{S}}_i \cdot \boldsymbol{\sigma})(\hat{\mathbf{S}}_j \cdot \boldsymbol{\sigma})\psi(\mathbf{r}_j), \quad (7.21)$$

We can now project this equation to the set of Shiba states in Eq. (7.14) localized at the impurities. If there are N impurities, the resulting equation is a tight-binding model

with a $2N \times 2N$ Hamiltonian which takes the form of a BdG equation,

$$\tilde{H}_{\rm eff}\phi = E\phi, \tag{7.22}$$

with an effective Hamiltonian

$$\tilde{H}_{\rm eff} = \begin{pmatrix} \tilde{h}_{\rm eff} & \tilde{\Delta}_{\rm eff} \\ \tilde{\Delta}^{\dagger}_{\rm eff} & -\tilde{h}^{T}_{\rm eff} \end{pmatrix}. \tag{7.23}$$

Here, $\tilde{h}^{T}_{\rm eff}$ denotes the time reverse of $\tilde{h}_{\rm eff}$. Taking matrix elements of Eq. (7.21), the entries of the effective Hamiltonian $\tilde{H}_{\rm eff}$ take the form

$$(\tilde{h}_{\rm eff})_{ij} = \begin{cases} \epsilon_0 & i = j \\ -\Delta \frac{\sin k_F r_{ij}}{k_F r_{ij}} e^{-r_{ij}/\xi_0} \langle \uparrow, i | \uparrow, j \rangle & i \neq j. \end{cases} \tag{7.24}$$

and

$$(\tilde{\Delta}_{\rm eff})_{ij} = \begin{cases} 0 & i = j \\ \Delta \frac{\cos k_F r_{ij}}{k_F r_{ij}} e^{-r_{ij}/\xi_0} \langle \uparrow, i | \downarrow, j \rangle & i \neq j. \end{cases} \tag{7.25}$$

In these expressions, the electronic spin states $|\sigma, i\rangle$ correspond to spin $\sigma = \uparrow, \downarrow$ with respect to the direction of the ith impurity spin. Parameterizing these impurity spin directions through angles θ_i and ϕ_i, we have

$$\langle \uparrow, i | \uparrow, j \rangle = \cos\frac{\theta_i}{2}\cos\frac{\theta_j}{2} + \sin\frac{\theta_i}{2}\sin\frac{\theta_j}{2} e^{i(\phi_j - \phi_i)} \tag{7.26}$$

$$\langle \uparrow, i | \downarrow, j \rangle = e^{-i(\phi_i + \phi_j)/2} \left[\cos\frac{\theta_i}{2}\sin\frac{\theta_j}{2} e^{-i(\phi_j - \phi_i)/2} - \sin\frac{\theta_i}{2}\cos\frac{\theta_j}{2} e^{-i(\phi_i - \phi_j)/2} \right] \tag{7.27}$$

Note that the pairing terms involve a site-dependent phase factor $\exp\{-i(\phi_i + \phi_j)/2\}$. It is convenient to eliminate this phase factor by a gauge transformation

$$\mathcal{U} = \begin{pmatrix} e^{i\phi/2} & 0 \\ 0 & e^{-i\phi/2} \end{pmatrix}, \tag{7.28}$$

where ϕ denotes a matrix in site space with matrix elements $\phi_{ij} = \delta_{ij}\phi_j$. Performing this unitary transformation, we find the effective Hamiltonian

$$\mathcal{H} = \mathcal{U}\tilde{\mathcal{H}}\mathcal{U}^{\dagger} = \begin{pmatrix} h_{\rm eff} & \Delta_{\rm eff} \\ \Delta^{\dagger}_{\rm eff} & -h^{T}_{\rm eff} \end{pmatrix} \tag{7.29}$$

with

$$(h_{\text{eff}})_{ij} = \begin{cases} \epsilon_0 & i = j \\ -\Delta \frac{\sin k_F r_{ij}}{k_F r_{ij}} e^{-r_{ij}/\xi_0} \left[\cos\frac{\theta_i}{2} \cos\frac{\theta_j}{2} e^{i(\phi_i - \phi_j)/2} + \sin\frac{\theta_i}{2} \sin\frac{\theta_j}{2} e^{-i(\phi_i - \phi_j)/2} \right] & i \neq j. \end{cases} \tag{7.30}$$

and

$$(\Delta_{\text{eff}})_{ij} = \begin{cases} 0 & i = j \\ \Delta \frac{\cos k_F r_{ij}}{k_F r_{ij}} e^{-r_{ij}/\xi_0} \left[\cos\frac{\theta_i}{2} \sin\frac{\theta_j}{2} e^{i(\phi_i - \phi_j)/2} - \sin\frac{\theta_i}{2} \cos\frac{\theta_j}{2} e^{-i(\phi_i - \phi_j)/2} \right] & i \neq j. \end{cases} . \tag{7.31}$$

Finally, we specify the Hamiltonian to a spin helix as defined in Eq. (7.3) and find

$$(h_{\text{eff}})_{ij} = \begin{cases} \epsilon_0 & i = j \\ -\Delta \frac{\sin k_F r_{ij}}{k_F r_{ij}} e^{-r_{ij}/\xi_0} \left[e^{ik_h x_{ij}} \cos^2\frac{\theta}{2} + e^{-ik_h x_{ij}} \sin^2\frac{\theta}{2} \right] & i \neq j \end{cases} \tag{7.32}$$

as well as

$$(\Delta_{\text{eff}})_{ij} = \begin{cases} 0 & i = j \\ i\Delta \frac{\cos k_F r_{ij}}{k_F r_{ij}} e^{-r_{ij}/\xi_0} \sin\theta \sin k_h x_{ij} & i \neq j, \end{cases} \tag{7.33}$$

where we use the notation $x_{ij} = x_i - x_j$. Note that in this form, the Hamiltonian is translationally invariant. Conveniently, ϵ_0 only enters the onsite terms and $-\epsilon_0$ effectively acts as a chemical potential for the band of Shiba states. While this BdG Hamiltonian is reminiscent of the Kitaev chain [Kita 01], there are several characteristic differences:

- The Hamiltonian involves long-range hopping terms. This is a consequence of the fact that the wavefunctions of the Shiba states fall off as $1/r$ with distance from the magnetic impurity as long as r is small compared to the superconducting coherence length.
- In general, the hopping terms involve complex phase factors. This reflects that there are (spin) supercurrents flowing in response to the spatially varying Zeeman field of the magnetic impurities, similar to the magneto-Josephson effect [Jian 13, Pien 13b]. These supercurrents induce a spatially varying phase of the effective p-wave paring strength which we then eliminated by the unitary transformation at the expense of introducing complex phase factors into the hopping terms (cf. [Romi 12]).

- The hopping amplitudes are real for a strictly planar spin helix with $\theta = \pi/2$ due to the additional reflection symmetry present in this case. This simplifies the site-off-diagonal hopping and pairing terms of the tight-binding Hamiltonian in Eqs. (7.32) and (7.33), which become

$$(h_{\text{eff}})_{ij} = -\Delta \frac{\sin k_F r_{ij}}{k_F r_{ij}} e^{-r_{ij}/\xi_0} \cos k_h x_{ij} \tag{7.34}$$

  as well as

$$(\Delta_{\text{eff}})_{ij} = i\Delta \frac{\cos k_F r_{ij}}{k_F r_{ij}} e^{-r_{ij}/\xi_0} \sin k_h x_{ij} \tag{7.35}$$

- While the pairing is odd and hence p-wave, it also involves long-range contributions which fall off as $1/r$ as long as r is small compared to the superconducting coherence length.

In the following, we explore the consequences of these differences for the phase diagram and the splitting of Majorana end states using both analytical and numerical approaches.

7.4. Phase diagram

We first consider an infinite chain of Shiba states and qualitatively explore the phase diagram of the effective tight-binding model. For an infinite chain, the Hamiltonian defined by Eqs. (7.32) and (7.33) is translationally invariant and can be solved by passing to momentum states. This yields the 2×2 BdG Hamiltonian

$$\mathcal{H} = \begin{pmatrix} h_k & \Delta_k \\ \Delta_k^* & -h_{-k}^* \end{pmatrix}. \tag{7.36}$$

Here, we introduced the Fourier transforms

$$h_k = \sum_j (h_{\text{eff}})_{ij} e^{ikx_{ij}} \tag{7.37}$$

and

$$\Delta_k = \sum_j (\Delta_{\text{eff}})_{ij} e^{ikx_{ij}}. \tag{7.38}$$

As detailed in Appendix C.2, the Fourier transforms can be performed explicitly and we find

$$h_k = \epsilon_0 + \frac{\Delta}{k_F a}\left[F(k+k_h)\cos^2\frac{\theta}{2} + F(k-k_h)\sin^2\frac{\theta}{2}\right] \tag{7.39}$$

in terms of the function

$$F(k) = -\left[\arctan\frac{e^{-a/\xi_0}\sin(k_F+k)a}{1-e^{a/\xi_0}\cos(k_F+k)a} + \arctan\frac{e^{-a/\xi_0}\sin(k_F-k)a}{1-e^{a/\xi_0}\cos(k_F-k)a}\right] \tag{7.40}$$

as well as

$$\Delta_k = \frac{\Delta\sin\theta}{4k_F a}\left[f(k_F+k_h+k) - f(k_F+k_h-k)\ -f(k_F-k_h+k) + f(k_F-k_h-k)\right] \tag{7.41}$$

in terms of

$$f(k) = -\ln\left[1+e^{-2a/\xi_0} - 2e^{-a/\xi_0}\cos ka\right]. \tag{7.42}$$

Both h_k and Δ_k depend sensitively on the superconducting coherence length. For ξ_0 small or of order a, the hopping and pairing amplitudes are essentially local. In contrast, the slow power-law decay with r_{ij} becomes relevant for large $\xi_0 \gg a$. In the following, we discuss these two limits separately.

7.4.1. Small coherence length

We first specify the problem to the limit of small coherence lengths $\xi_0/a \ll 1$. While this limit is presumably not very relevant experimentally, it is helpful in understanding the more realistic case $\xi_0/a \gg 1$ discussed in Sec. 7.4.2. For simplicity, we also assume $k_h a \ll 1$ which allows us to expand both h_k and Δ_k to linear order in this parameter.[4] This yields

$$h_k \simeq \epsilon_0 - \frac{2\Delta}{k_F a}e^{-a/\xi_0}\sin k_F a\left[\cos ka - k_h a\cos\theta\sin ka\right] \tag{7.43}$$

as well as

$$\Delta_k = \frac{2\Delta}{k_F a}e^{-a/\xi_0}(k_h a)\sin\theta\cos k_F a\sin ka. \tag{7.44}$$

[4] However, our conclusions remain qualitatively valid even without this assumption as illustrated by the numerical results in Fig. 7.1.

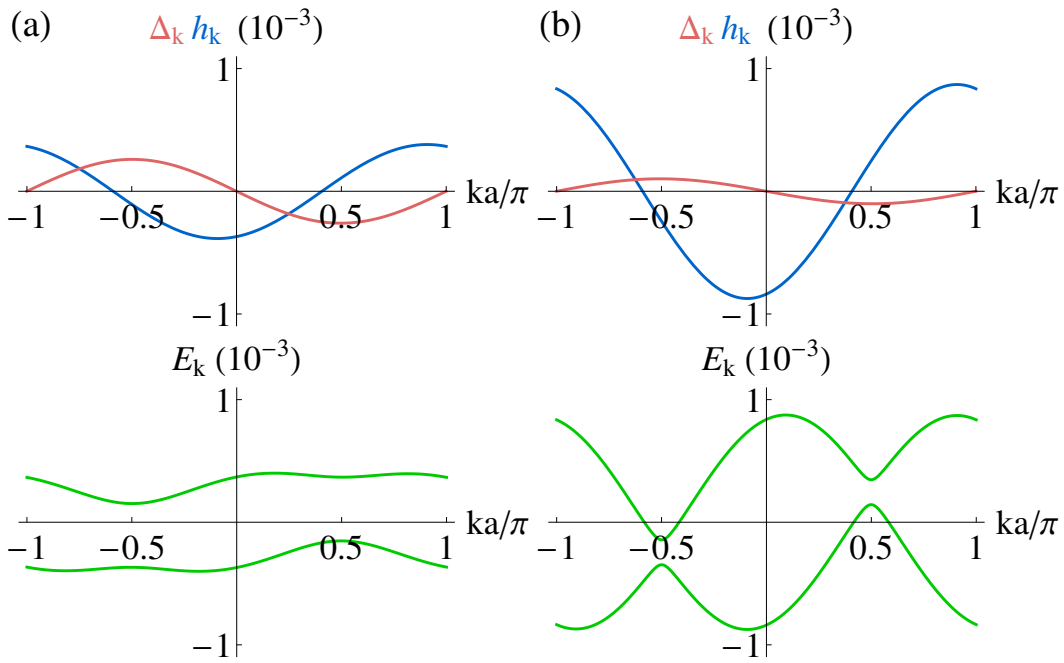

Figure 7.1.: Numerical results for h_k and Δ_k vs. momentum k (upper panels) and the corresponding quasiparticle excitation spectra E_k (lower panels) for a short coherence length $\xi_0/a = 0.2$, $\epsilon_0 = 0$, $\theta = \pi/4$, $k_h a = \pi/8$. The plots are for $k_F a = 4\pi + \pi/8$ in (a) and $k_F a = 4\pi + 3\pi/8$ in (b), illustrating the transitions between topological and gapless phases as a function of k_F. All energies are measured in units of Δ.

There are several noteworthy features of h_k and Δ_k: The scale of the effective bandwidth of the band of Shiba states is set by $t = (\Delta/k_F a)e^{-a/\xi_0}$. By comparison, the corresponding scale $\delta = 2t(k_h a)$ for the pairing strength is parametrically smaller by a factor of $k_h a$. It is important to note that h_k is asymmetric under $k \to -k$ unless $\theta = \pi/2$ and that the magnitude of the antisymmetric term is of the same order as the pairing. This asymmetry breaks the resonance between k and $-k$ states and hence suppresses Cooper pairing.

Diagonalizing the BdG equation (7.36), we thus find the subgap spectrum,

$$E_{k,\pm} = \delta \sin k_F a \cos\theta \sin ka \pm \sqrt{(\epsilon_0 - 2t \sin k_F a \cos ka)^2 + (\delta \cos k_F a \sin\theta \sin ka)^2}. \tag{7.45}$$

As the energy ϵ_0 of the Shiba states is reduced, the Shiba bands start to overlap and undergo a phase transition into a topological superconducting phase for appropriate parameters. Specifically, the Shiba bands cross the chemical potential at $\pm k_0$ determined by $\epsilon_0 = 2t \sin k_F a \cos k_0 a$. The pairing term opens p-wave gaps at $\pm k_0$ of magnitude $\delta|\cos k_F a \sin\theta \sin k_0 a|$. However, these gaps are shifted in energy by the shift

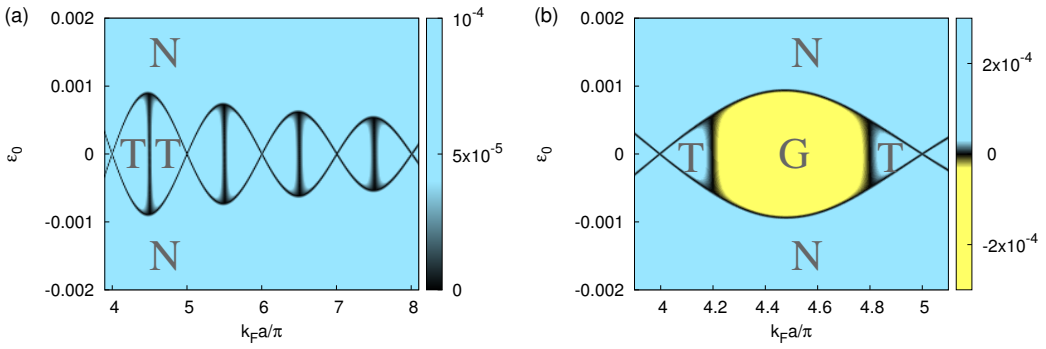

Figure 7.2.: Numerical results for the energy minimum of the upper band (color scale) vs. $k_F a$ and ϵ_0 for a short coherence length $\xi_0 = a/5$, $k_h a = \pi/8$, $\Delta = 1$, and (a) $\theta = \pi/2$, (b) $\theta = \pi/5$. The color scale has been chosen to highlight zeros of the band minimum (black regions), which indicate topological phase transitions. The light blue regions correspond to gapped phases, while yellow regions mark the gapless phase (G). We have identified the topological (T) and nontopological (N) gapped phases using the arguments in the main text as well as by checking that a single Majorana bound state exists at both ends of the wire. In (a) the band is symmetric under $k \to -k$ and the band minimum is always nonnegative. The topological phase is centered around $\epsilon_0 = 0$ and the transition to the nontopological phase is approximately described by $\epsilon_0 = \pm 2 \sin k_F a \, e^{-a/\xi_0} \cos k_h a / k_F a$. The topological phase is split in half by a vertical metallic line ($\Delta_k = 0$) at $k_F a \simeq n\pi + \pi/2$. At $k_F a = n\pi$ all hopping terms vanish and there can be no topological phase. In (b), the asymmetry of the spectrum expands the metallic line into a gapless phase.

term $\delta \sin k_F a \cos\theta \sin ka$ arising from the asymmetry of the dispersion h_k. The shifts are equal to $\pm\delta |\sin k_F a \cos\theta \sin k_0 a|$ at the two Fermi points. The system enters a topological superconducting phase only as long as these shifts do not close the gap:

- At $\theta = 0$, i.e., a ferromagnetic arrangement of the impurity spins, the p-wave gap vanishes and the system is gapless and nontopological.
- At $\theta = \pi/2$, i.e., when the spin helix of the impurity spins has zero average magnetization, the shift vanishes and the system always enters a topological superconducting phase as the Shiba bands start to overlap at the chemical potential.
- For intermediate $\theta \in (0, \pi/2)$, the system becomes gapless when the shift term becomes larger than the pairing term, i.e., when $|\sin k_F a \cos\theta| - |\cos k_F a \sin\theta| > 0$. This happens for $\theta < k_F a < \pi - \theta$ (mod 2π). Thus there are alternating topological and nontopological phases as a function of the Fermi momentum k_F of the superconductor.

This scenario is illustrated by the numerical results for the dispersion, the gap function, and the excitation spectrum in Fig. 7.1 and for the phase diagram in Fig. 7.2.

7.4.2. Large coherence length

The general Eqs. (7.39) and (7.41) for h_k and Δ_k can also be specified to the limit of large $\xi_0 \gg a$. The dispersion h_k follows from Eq. (7.39) with

$$F(k) = -\left[\arctan\left(\cot\frac{(k_F+k)a}{2}\right) + \arctan\left(\cot\frac{(k_F-k)a}{2}\right)\right] \tag{7.46}$$

Thus, the dispersion becomes steplike, reflecting the $1/r$ dependence of the hopping amplitudes, with bandwidths of order $\Delta/k_F a$. Depending on the Fermi wavevector k_F and the helix wavevector k_h, there are two cases which need to be distinguished. Representative dispersions h_k (referred to as *type 1* and *type 2* in the following) are shown in Fig. 7.3. Note that the sharp steps appear only in the limit $\xi_0 \to \infty$. For large but finite ξ_0, the steps are smoothened on the scale of $1/\xi_0$. In addition to the dispersions shown in Fig. 7.3, dispersions of *type 1* and *type 2* also include the case in which the dispersion differs by an overall minus sign. Then, the dispersion is of *type 1* when $n\pi + k_h a < k_F a < (n+1)\pi - k_h a$ for some integer n and of *type 2* when $n\pi - k_h a < k_F a < n\pi + k_h a$.

The pairing strength follows from Eq. (7.41), where $f(k)$ simplifies to

$$f(k) = -\ln\left[4\sin^2\frac{ka}{2}\right] \tag{7.47}$$

in the limit $\xi_0 \to \infty$. Thus, the paring strength develops logarithmic singularities which occur at those positions where the dispersion h_k develops steps as shown in Fig. 7.3. Specifically, the pairing strength becomes large and positive near the jumps in h_k which are associated with the $\cos^2\theta/2$ term in Eq. (7.39) (shown as large jumps in Fig. 7.3), and large and negative near the jumps which are associated with the $\sin^2\theta/2$ term in Eq. (7.39). Note that also for the pairing strength, the strict logarithmic divergences are cut off for large but finite ξ_0 on a scale of $1/\xi_0$.

In the following, we discuss the phase diagram separately for dispersions of *type 1* and *type 2*. To start with, whenever the positive- and negative-energy Shiba bands are nonoverlapping and the chemical potential falls in between the Shiba bands, the system is nontopological, with a large s-wave band gap of the host superconductor and a trivial gap between the positive- and negative-energy Shiba bands. The specifics of the dispersion become relevant once the positive- and negative-energy Shiba bands are overlapping (though still well separated from the continuum excitations).

Type 1.—As indicated in Fig. 7.3(c), the dispersion has three characteristic regions. Depending on the energy ϵ_0 of the Shiba states of the individual impurities, the chemical potential (center of the gap of the host superconductor) can be located in any of these regions. In regions I and III, the dispersion h_k is symmetric under $k \to -k$, with one pair

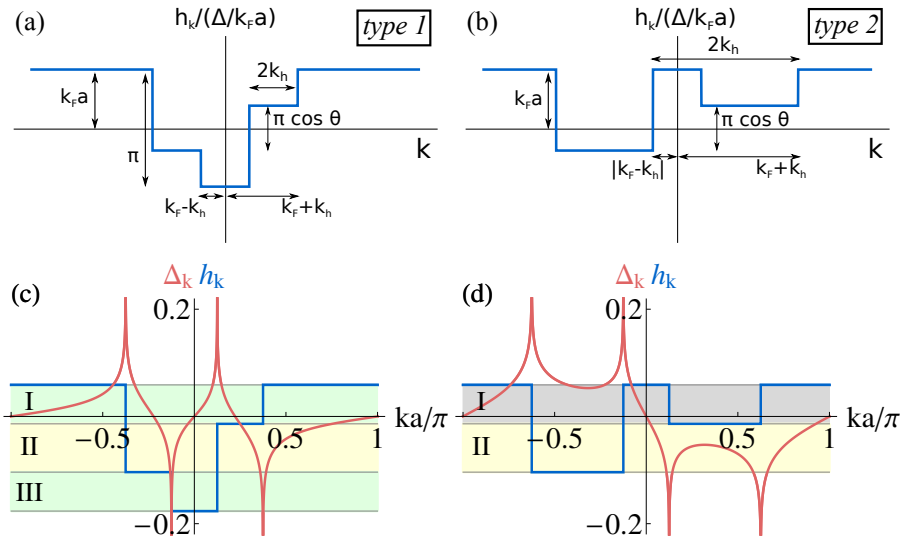

Figure 7.3.: (a,b) Schematic plot of the two representative classes of dispersions h_k in the limit of large coherence length $\xi_0 \gg a$ as given by the analytical expression in Eqs. (7.39) and (7.46). In the main text, the two classes are referred to as (a) *type 1* and (b) *type 2*. The form of the dispersion depends qualitatively on the value of the Fermi and the helix wavevector k_F and k_h. (All wavevectors labeling the arrows in (a) and (b) should be understood within the reduced-zone scheme.) The dispersion is fully symmetric under $k \to -k$ only for $\theta = \pi/2$. (c,d) Dispersions h_k and pairing strengths Δ_k of both classes for $\epsilon_0 = 0$, $k_F a = 4.25\pi$, $\theta = 3\pi/8$, and (c) $k_h a = \pi/8$, (d) $k_h a = 3\pi/8$ (energies are measured in units of Δ). A nonzero ϵ_0 would lead to an overall shift of the dispersion in energy which causes the chemical potential to pass through various regions as follows: In (c) (*type-1* dispersion), there are two regions (I and III, green area) with a symmetric dispersion, for which a topological phase forms. In contrast, in region II (yellow area) h_k is asymmetric and the excitation spectrum E_k becomes gapless. In (d) (*type-2* dispersion), h_k has two pairs of symmetric Fermi points in region I (grey area) and the system effectively behaves like a (nontopological) p-wave superconducting chain with two channels. In region II, the spectrum may be gapless or trivially gapped. Both classes are shown in the limit of $\xi_0 \to \infty$. A large but finite ξ_0 would smoothen the jumps in the dispersion and cut off the logarithmic divergences in the pairing strength on the scale of $1/\xi_0$.

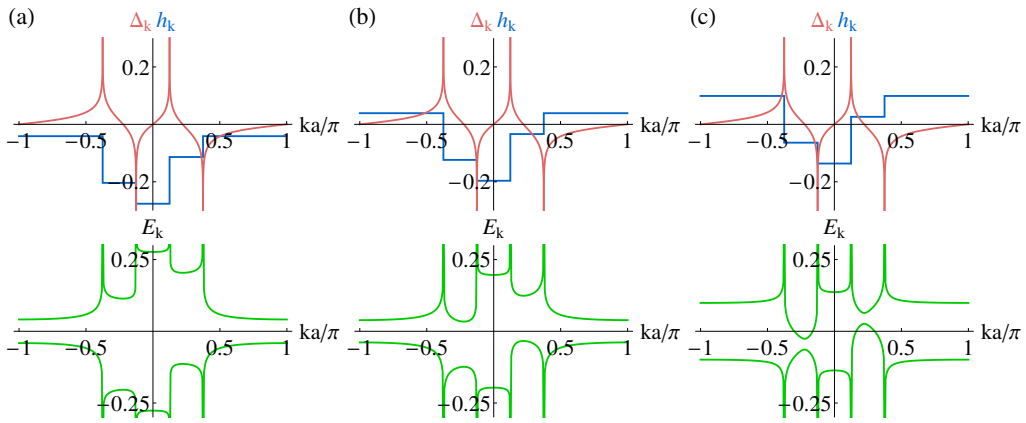

Figure 7.4.: *Type-1* dispersions h_k and gap functions Δ_k together with the corresponding excitation spectra [cf. Fig. 7.3(c)]. (a) Chemical potential lies outside the bands of Shiba states ($\epsilon_0 = 0.1$, gapped nontopological phase). (b) Chemical potential is inside region I ($\epsilon_0 = 0.02$, gapped topological phase). Analogous results are obtained when the chemical potential is located in region III. (c) Chemical potential is in region II ($\epsilon_0 = -0.04$, gapless nontopological phase). For all panels, the remaining parameters are $\xi_0 = \infty$, $k_F a = 4\pi + \pi/4$, $\theta = 3\pi/8$, and $k_h a = \pi/8$. Energies are measured in units of Δ.

of Fermi points. Thus, when the chemical potential falls into these regions, the effective p-wave pairing Δ_k will open a gap at the chemical potential and the Shiba chain enters into a topological superconducting phase. In contrast, when the chemical potential falls into region II, pairing is suppressed by the fact that the dispersion (and hence the two Fermi points) are asymmetric under $k \to -k$. Thus, the overlapping Shiba bands will remain gapless despite the effective p-wave pairing Δ_k. In fact, dispersions of *type 1* are always gapless in region II. To see this, we again compare the gap to the asymmetric energy shift. Since invariably, there are additional zeros of Δ_k for some pair $\pm k \neq 0, \pi$ [see Fig. 7.3(c)], the shift term always exceeds pairing for particular wavevectors, yielding a gapless spectrum at these points. These findings are illustrated by numerical results for the excitation spectra for various values of ϵ_0, as shown in Fig. 7.4.

Type 2.—In this case, the dispersion has two characteristic regions as indicated in Fig. 7.3(d). When the chemical potential falls into region I, there are two symmetric pairs of Fermi points. This is effectively analogous to a two-channel spinless p-wave superconducting wire and hence, the system is in a gapped nontopological phase. When the chemical potential falls into region II, the dispersion becomes strongly asymmetric under $k \to -k$. Correspondingly, pairing is suppressed and the system can enter a gapless nontopological phase. In contrast to *type-1* dispersions, a dispersion of *type 2* can still lead to a gapped (but nontopological) excitation spectrum in region II with asymmetric Fermi points, since Δ_k has no additional zeros. These conclusions are illustrated by

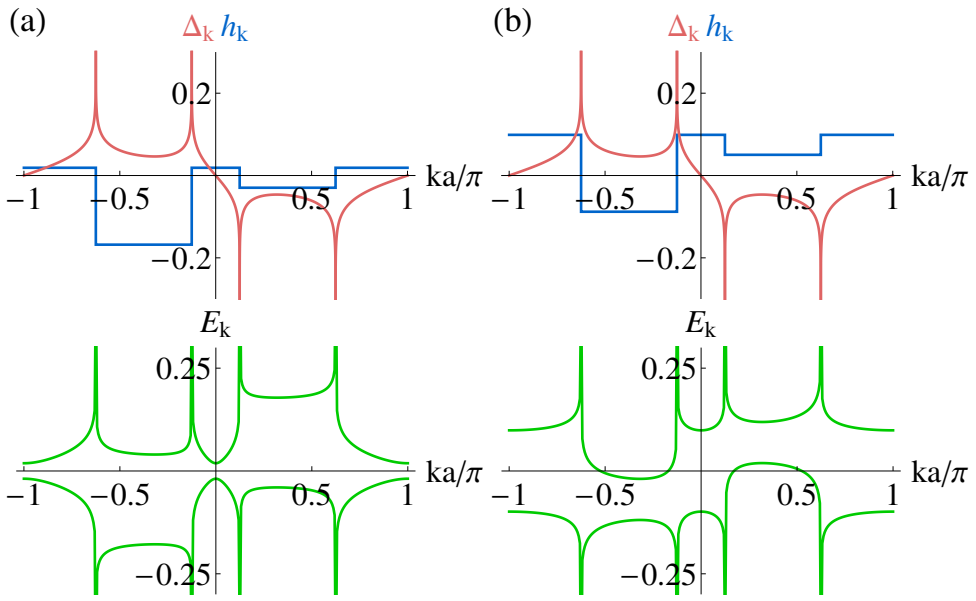

Figure 7.5.: Dispersions h_k, gap functions Δ_k, and excitation spectra for dispersions of the form shown in Fig. 7.3(d) (*type 2*). (a) Chemical potential lies inside region I in the band of Shiba states (gapped nontopological phase). (b) Chemical potential is in region II (gapless nontopological phase). The parameters are chosen as $\xi_0 = \infty$, $k_F a = 4\pi + \pi/4$, $\theta = 3\pi/10$, $k_h a = 3\pi/8$, and (a) $\epsilon_0 = -0.04$, (b) $\epsilon_0 = 0.04$. Energies are measured in units of Δ.

numerical results in Fig. 7.5.

Thus, we find a topological superconducting phase only for dispersions of *type 1*. The range of parameters over which the gapped topological phase extends becomes maximal for $\theta = \pi/2$ for which the hopping amplitudes $(h_{\text{eff}})_{ij}$ are real, resulting in a dispersion which is symmetric under $k \to -k$. The resulting phase diagram is plotted in Fig. 7.6 showing the alternation of topological and gapless phases as well as topological phase transitions as the dispersion changes between *type 1* and *type 2*. This alternation between topological and nontopological phases is similar to the case of small ξ_0.

7.5. Majorana bound states

Whenever the chain of Shiba states is in the topological phase, one expects localized Majorana bound states to form at the ends of finite chains. In a semi-infinite chain, the Majorana bound state has strictly zero energy. In a finite wire segment, Majorana bound states form at both ends and overlap in the interior of the wire, thereby acquiring a finite energy splitting. The overlap and hence the energy splitting is controlled by the decay of the Majorana wavefunctions.

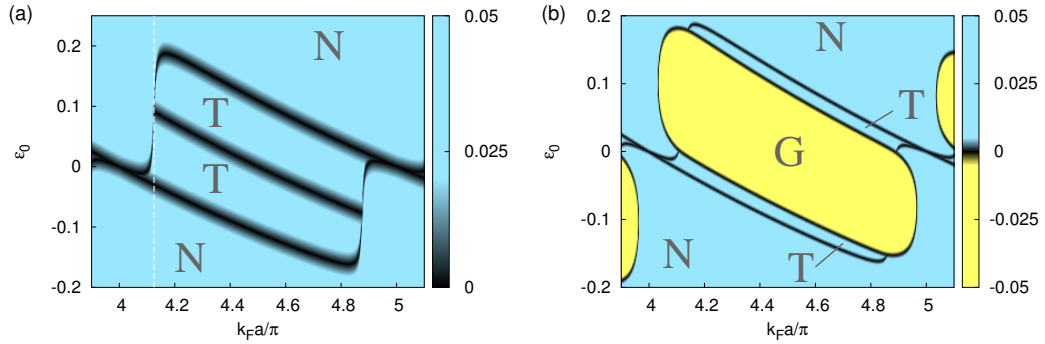

Figure 7.6.: Numerical results for the energy minimum of the upper band (color scale) vs. $k_F a$ and ϵ_0 for a long coherence length $\xi_0 = 50a$, $k_h a = \pi/8$, $\Delta = 1$, and (a) $\theta = \pi/2$, (b) $\theta = \pi/5$. Color scale and labels are as in Fig. 7.2. The topological phase transitions at the boundaries of regions I and III in Fig. 7.3(c) appear as diagonal black lines $\epsilon_0 = -(k_F a \bmod 2\pi)\Delta/k_F a$ in the phase diagram. The almost vertical transition lines between T and N in (a) are associated with the transition between *type-1* and *type-2* dispersions at $k_F a = 4\pi + k_h a = 4.125\pi$ (white dashed line) and $k_F a = 5\pi - k_h a = 4.875\pi$. As discussed in Sec. 7.5, this transition becomes infinitely sharp for $\xi_0 \to \infty$. For this reason the gap closing is hardly visible at this numerical resolution in some regions of parameter space. As in the short-ξ_0 limit, the topological phase for the symmetric spectrum in (a) is split in half by a metallic line. At this line, the chemical potential meets the middle plateaux in the dispersion h_k which are at the same height for $\theta = \pi/2$ [see Fig. 7.3(a)]. The excitation spectrum has two simultaneous gap closings at $\pm k_0$. For $\theta < \pi/2$ the spectrum becomes asymmetric and the energy at these two points is shifted in opposite directions. Thus, the metallic line is expanded into the gapless region marked by G in panel (b).

We now turn to a numerical analysis of the decay of the Majorana wavefunction and the corresponding energy splitting for the model given in Eqs. (7.32) and (7.33). In conventional models of 1d topological superconductors such as the Kitaev chain, the Majorana states decay exponentially into the bulk as controlled by the gap of the topological phase. This leads to an energy splitting which is exponentially small in the length of the chain. The Shiba chain differs in that hopping and pairing is long range, exhibiting a power-law decay for distances which are small compared to the coherence length ξ_0 of the underlying superconductor. This raises the question of the nature of the decay of the Majorana wavefunctions on scales short compared to ξ_0.

This issue is mute in the case of a short coherence length $\xi_0 \ll a$ in which the Shiba chain reduces to a Kitaev chain (with an additional phase gradient for general opening angles θ of the spin helix). Thus, one expects the conventional behavior in this case and indeed, in the topological phase, this model supports exponentially localized Majorana states whose decay length is determined by the parameters of the Kitaev chain in the usual way.

7.5.1. Type-1 dispersions

We now turn to the more interesting (and more realistic) case of large coherence lengths, $\xi_0 \gg a$, and parameters such that the dispersion is of *type 1*. Also in this case, the Majorana bound state decays exponentially on scales large compared to ξ_0. Indeed, given the effective bandwidth of the Shiba bands of order $\Delta/k_F a$ [cf. Eqs. (7.32)] and the smoothing of the steps in h_k of order $1/\xi_0$, we have an effective Fermi velocity of order $\Delta\xi_0/k_F a$. Combining this with the effective strength of the p-wave pairing of order $\Delta/k_F a$ [cf. Eqs. (7.33)], we find that the characteristic length scale (analogous to the relation $\xi_0 = \hbar v_F/\Delta$) is indeed of order ξ_0. Note that this is only a rough order-of-magnitude estimate which neglects the dependence on the opening angle θ, the energy ϵ_0 of the Shiba bound states, etc.

The decay of the Majorana bound states on length scales shorter than ξ_0 can be readily investigated numerically. To do so, we take the model defined by Eqs. (7.32) and (7.33) and formally set $\xi_0 = \infty$. As one readily checks numerically, the resulting model correctly reproduces the behavior of the Majorana bound states of the more complete model with finite ξ_0 on scales smaller than ξ_0. Numerical results for the $\xi_0 = \infty$ model and for parameters such that the system is in the topological phase are shown in Fig. 7.7. We find that asymptotically, the Majorana bound state decays approximately as a power law with logarithmic corrections. Indeed, the envelope of the Majorana wavefunction can be fit quite accurately by a decay of the type $1/[x \ln^2(x/x_0)]$ for a variety of parameter sets, cf. Fig. 7.7. While similar, this decay is faster than the decay of the hop-

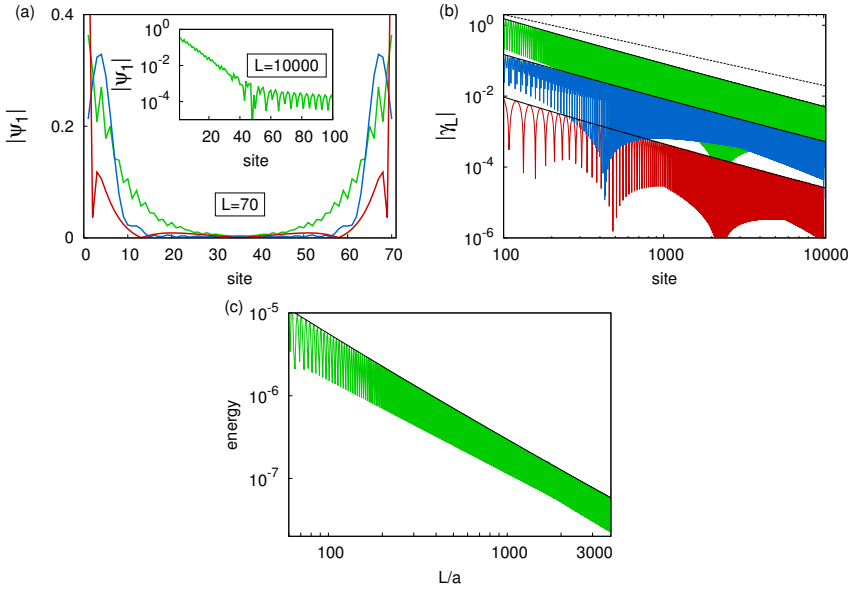

Figure 7.7.: (a) Spatial profile of the lowest-energy wavefunction $|\psi_1| = (\phi_1^2 + \chi_1^2)^{1/2}$, where ϕ_1 and χ_1 are the electron and hole components of the Nambu spinor ψ_1. All curves are for a chain length $L = 70$ and we have set $\xi_0 = \infty$, $\Delta = 1$, and $\theta = \pi/2$. The remaining parameters are $k_h a/\pi = 0.25; 0.1; 0.26$, $\epsilon_0 = -0.01; -0.13; 0$, and $k_F a/\pi = 4.5; 4.8; 4.3$ for the green, blue and red curve, respectively. Inset: Semi-log plot of the first 100 sites of $|\psi_1|$ in chain of length $L = 10000$. The parameters are the same as for the green curve in the main panel. The wavefunction initially decays exponentially and then crosses over to a much slower decay. The crossover point depends sensitively on the point in parameter space. (b) Log-log plot of the left Majorana wavefunction $|\gamma_L|$ for a chain of length $L = 10000$. (The first 100 sites are not shown.) The three curves are for the same set of parameters as in (a) and shifted vertically for clarity. The black solid lines represent $1/[x \ln^2(x/x_0)]$ fits to the envelopes of the curves. The dashed lines shows a $1/x$ power law for comparison. The Majorana wavefunctions can be obtained from the lowest energy wavefunction by a rotation in Nambu space[5] $\gamma_{L/R} = \chi_1 \pm i\phi_1$. The obtained fit parameters are $x_0/a \sim 0.17, 0.30, 0.55$ for the three curves. (c) Log-log plot of the Majorana energy splitting *vs* chain length for the same parameters as the green curve in (a) and (b). Similar to the wavefunction decay, the envelope of the energy splitting fits a $1/[x(\ln(x/x_0))^2]$ law (black line) with $x_0/a \sim 0.22$.

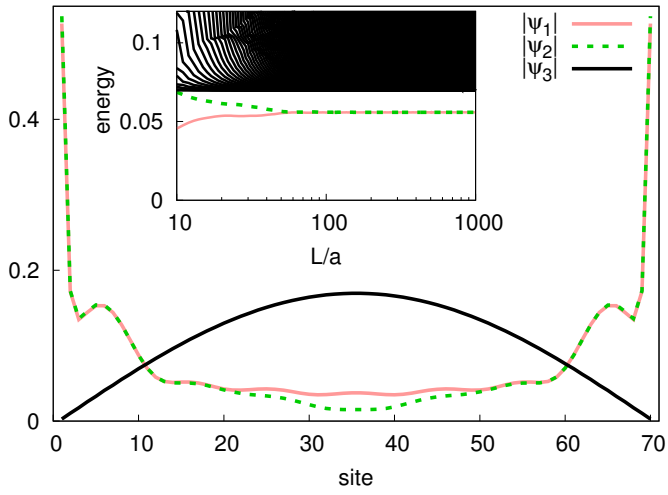

Figure 7.8.: Spatial wavefunction profile $|\psi|$ of the first three positive-energy states of a chain with 70 sites with a *type-2* dispersion in region I [see Fig. 7.3(d)]. There are two states localized at the ends of the chain. Inset: excitation spectrum of a finite chain as a function of chain length L. The plot shows that the two end states remain at a nonzero subgap energy for large L. This is the expected behavior of a two-channel p-wave superconducting chain with two coupled Majorana bound states at each end. The third state is a bulk state which defines the edge of the quasiparticle continuum. The parameters are: $\Delta = 1$, $\epsilon_0 = 0.05$, $\theta = \pi/2$, $k_h a = \pi/8$, $k_F a = 4.08\pi$.

ping and pairing amplitudes. Interestingly, this implies that in a finite wire of length $L \ll \xi_0$ (as may well be the case in an experiment) the energy splitting of the two Majorana bound states is not exponentially but merely power-law suppressed in L (with logarithmic corrections). This is illustrated numerically in Fig. 7.7(c).

7.5.2. Type-2 dispersions

In the discussion of the phase diagram for a large coherence length in Sec. 7.4.2, we showed that there is no topological phase for dispersions of *type 2*. Nevertheless, when the chemical potential is in region I [see Fig. 7.3(d)], the spectrum is analogous to that of a two-channel p-wave superconductor. Each of the channels individually supports one Majorana bound state at each end. The hard-wall boundary introduces scattering between the two channels and the Majoranas acquire a finite energy splitting, which is usually of the order of but smaller than the gap. Numerically, we indeed find two positive-energy subgap states in this regime, one for each end of the chain, as seen in

[5] One can only write the wavefunction ψ_1 in terms of real Majorana wavefunctions, which are located at only one end, in the case of $\theta = \pi/2$. For arbitrary θ the phase of ψ_1 varies spatially due to the complex long-range hopping terms and one cannot transform to a Majorana basis by a global rotation. We checked numerically that the decay of the wavefunction also obeys a $1/[x \ln^2(x/x_0)]$ law for $\theta < \pi/2$.

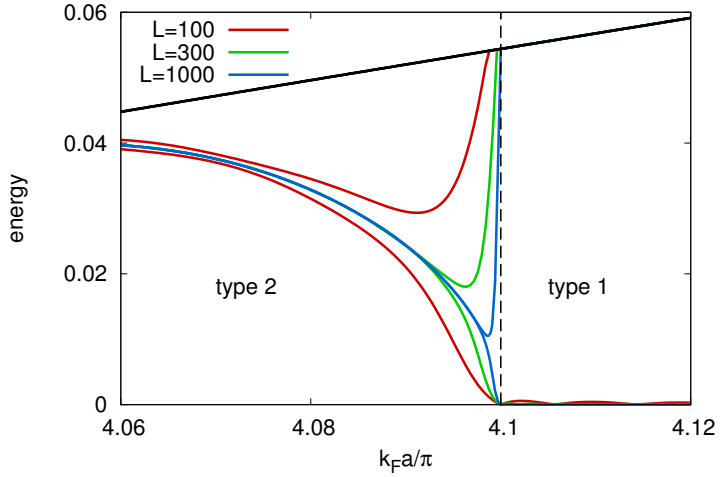

Figure 7.9.: Spectrum of subgap states (limited to positive energies in units of Δ) *vs* Fermi wavevector k_F near the phase transition from *type 2* to *type 1* at $k_F a = 4.1\pi$ (dashed line). The plot is for $\xi_0 \to \infty$ and chemical potential in region I so that at the transition, the system changes from a two-channel to a single-channel p-wave superconductor. The parameters are chosen as $k_h a = 0.1\pi$, $\xi_0 = \infty$, and $\epsilon_0 = 0.03$. The colored lines represent the two subgap states for various chain lengths (see legend) and the black line marks the lowest continuum excitation (which is indistinguishable for the different chain lengths). Just before the phase transition on the *type-2* side, the two subgap states split. While one state is absorbed into the continuum at the transition, the second state drops to near-zero energies and becomes a Majorana bound state.

Fig. 7.8. Their energy as a function of length is shown in the inset. The two states are clearly separated from the continuum, but they remain at a finite energy even at very large chain lengths. The energy depends on the boundary-induced coupling of the two channels. For long chains, the two subgap states become degenerate as the two ends of the chain are decoupled.

7.6. Unconventional topological phase transition at the Bragg point $k_h = k_F$

We now turn to a closer look at the transition point between dispersion of *type-1* and *type-2* and its immediate vicinity restricting the discussion to a planar helix. For $\xi_0 \to \infty$ the transition occurs at the Bragg point $k_F = k_h$,[6] where the spin helix satisfies the condition

[6] Additional Bragg points exist for $2k_F = \pm 2k_h + 2\pi n$.

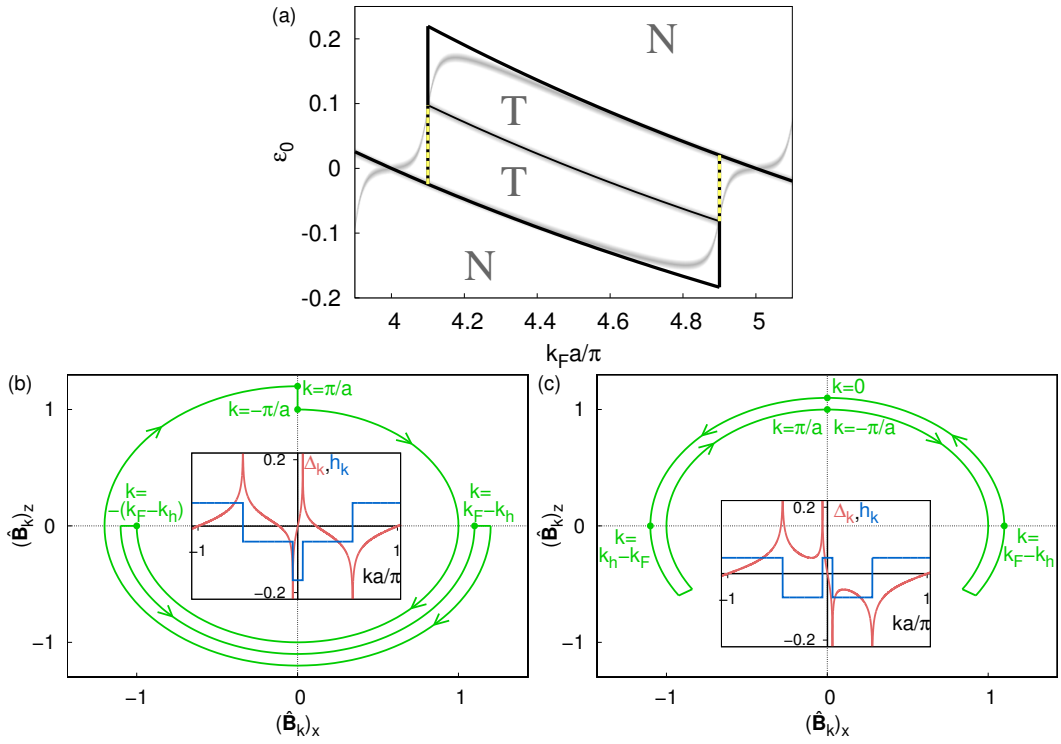

Figure 7.10.: (a) Phase diagram for $k_h = 0.1\pi/a$ and $\xi_0 = \infty$ (black phase boundaries) or $\xi_0 = 15a$ (gray lines), with topological (T) and nontopological (N) phases. (Energies are given in units of Δ_0.) The yellow dashed line indicates the Bragg point $k_F = k_h$ with exponentially localized Majorana states [$|\beta| < 1$ in Eq. (7.50)]. For $\xi_0 = \infty$, this coincides with the phase transition between the two- and single-channel phases. (b+c) Winding of the unit vector $\hat{\mathbf{B}}_k = \mathbf{B}_k/B_k$ as k is tuned across the Brillouin zone for (b) the single-channel and (c) the two-channel phase (partially shifted radially for visibility). While in the single-channel phase $\hat{\mathbf{B}}_k$ winds once around the origin; the winding is trivial in the two-channel phase, reflecting the topological phase transition. Insets: Dispersion h_k and pairing Δ_k in the two phases. The two-channel dispersion has a second pair of Fermi points.

for Bragg reflection.[7] We will see below that an effect similar to Bragg reflection indeed leads to strong localization of the Majorana state at this point. Figure 7.10(a) displays the phase diagram for $\xi_0 = \infty$. As discussed in Sec. 7.4.2 the topological phase boundaries which appear in the phase diagram as diagonal lines occur when the chemical potential leaves the Shiba bands. These transitions are equivalent to those of the Kitaev chain and reflect a continuous gap closing and reopening. A different type of topological phase transition which emerges from the long-range coupling and has no analog in the Kitaev chain, occurs at the Bragg point $k_h = k_F$ (vertical lines). For $\xi_0 = \infty$, this transition is abrupt and the bulk gap does not approach zero on either side of the transition as can be seen from Fig. 7.9. For finite ξ_0, the bulk gap closes smoothly as $|k_F a - (k_h a + n\pi)| \to 0$ on a scale of $1/\xi_0$. This is a discontinuous transition associated with the (dis)appearance of an additional pair of Fermi points near $k = 0$ [see region I in Fig. 7.3(c) and (d)] modifying the system between effective single-channel and two-channel phases. In the nontopological two-channel phase, the cumulative hopping strength is finite across an even number of sites but vanishes across an odd number so that one can roughly think of the even and odd sites as two channels (see App. C.3 for details). This happens for $k_F < k_h$, while even and odd sites are strongly coupled in the topological single-channel phase $k_F > k_h$. In some specific implementations, the RKKY interaction between the impurities is maximal at the wavevector $2k_F$, so that the helix wavevector realizes the Bragg point $k_h = k_F$ [Klin 13, Brau 09, Simo 08]. This would put the Shiba chain right at (for $\xi_0 \to \infty$) or near (for large but finite ξ_0) an unconventional topological critical point.

For a planar spin helix, the Shiba chain obeys chiral symmetry, $\{\mathcal{H}, \tau_y\} = 0$, which puts it in class BDI and in principle allows for a topological $\mathbb{Z}$-index [Ryu 10]. To explore the discontinuous transition at the Bragg point more closely, we analyze the topological index of the two adjacent phases. To this end, we rewrite the Hamiltonian in momentum space, $\mathcal{H}_k = h_k \tau_z + \Delta_k \tau_x$, and determine the winding number of the two-component vector $\mathbf{B}_k = (\Delta_k, h_k)$ in the xz-plane as k traverses the Brillouin zone from $-\pi/a$ to π/a [see Figs. 7.10(b) and 7.10(c)]. This confirms the identification of the topologically trivial ($k_F < k_h$) and nontrivial ($k_F > k_h$) phases.[8]

The transition between these phases at the Bragg point is reflected in the subgap states of long but finite chains. Their energies near $k_F = k_h$ are shown in Fig. 7.11(a). In the two-channel phase, one finds two subgap states for each end. These can be thought of as the hybridized Majorana states of the two channels. As $k_F \to k_h$, one subgap state merges with the quasiparticle continuum due to coupling with the opposite end of the chain, while the other approaches zero energy and connects smoothly with the Majorana

[7] Note that without the factor of two in the helix wavevector we introduced for notational convenience the condition would read $2k_F = k_h$ which is precisely the condition for Bragg reflection.

[8] Incidentally, the two topological phases in Fig. 7.10(a) differ by the winding direction and have topological indices ± 1. Thus, the intermediate phase transition involves two simultaneous gap closings.

end state in the topological phase. Thus, right at the Bragg point, there is exactly one zero-energy state for each end of the chain. We now turn to an analytical theory of the Majorana bound state and the subgap spectrum both at and near the Bragg point.

7.6.1. Majorana bound state at the Bragg point

We exploit the chiral symmetry of the Hamiltonian and rotate it into the Majorana basis in which $\mathcal{H}$ becomes purely off-diagonal in particle-hole space [Adag 99]. This is effected by a $\pi/2$-rotation about the x-axis which transforms $\tau_z \to -\tau_y$ and keeps τ_x unchanged so that $\mathcal{H} = -h_{\text{eff}}\tau_y + \Delta_{\text{eff}}\tau_x$ with h_{eff} and Δ_{eff} specified in Eqs. (7.34) and (7.35). Now, the equations for the zero-energy Majorana states with BdG spinor (u, v) take the simple form

$$u = 0 \quad \text{and} \quad (ih_{\text{eff}} + \Delta_{\text{eff}})v = 0 \tag{7.48}$$

for the Majorana localized at the left end of the chain, and $v = 0$ and $(-ih_{\text{eff}} + \Delta_{\text{eff}})u = 0$ for the Majorana localized at the right end. (Note that this consistently neglects finite-size effects). Specifying to the left-end states for definiteness, one readily finds for $\mathcal{H}_{12} = ih_{\text{eff}} + \Delta_{\text{eff}}$, from Eqs. (7.34) and (7.35), that $(\mathcal{H}_{12})_{jj} = i\epsilon_0$ and

$$(\mathcal{H}_{12})_{ij} = -\frac{i\Delta}{k_F r_{ij}} e^{-r_{ij}/\xi_0} \sin(k_F r_{ij} - k_h x_{ij}) \tag{7.49}$$

for $i \neq j$. Since $r_{ij} = |x_{ij}|$, the Bragg point $k_h = k_F$ has the remarkable property that $\mathcal{H}_{12}$ is a triangular matrix. This property immediately allows us to solve Eq. (7.48) by the ansatz $v_j = \beta^j$. Here, j enumerates the sites starting with the left end of the chain. Indeed, with this ansatz, all components of the equation $\mathcal{H}_{12}v = 0$ reduce to the same condition for β. Solving this condition (see App. C.4), we find

$$\beta = \frac{e^{a/\xi_0} \sin(k_F a \epsilon_0/\Delta)}{\sin[2k_F a + k_F a \epsilon_0/\Delta]}. \tag{7.50}$$

Obviously, this provides an exponentially localized Majorana solution as long as $|\beta| < 1$. One can convince oneself that this condition is satisfied wherever the line $k_F = k_h$ is inside the topological phase for finite ξ_0. This region is marked by a yellow dashed line in Fig. 7.10(a). As shown in Fig. 7.11(b), this exact analytical result is in excellent agreement with numerical simulations.

This constitutes a major result of this chapter with remarkable implications: (i) Helical Shiba chains display an unconventional topological critical point at or in the immediate vicinity of the Bragg point $k_F = k_h$. (ii) At the Bragg point, they have Majorana end

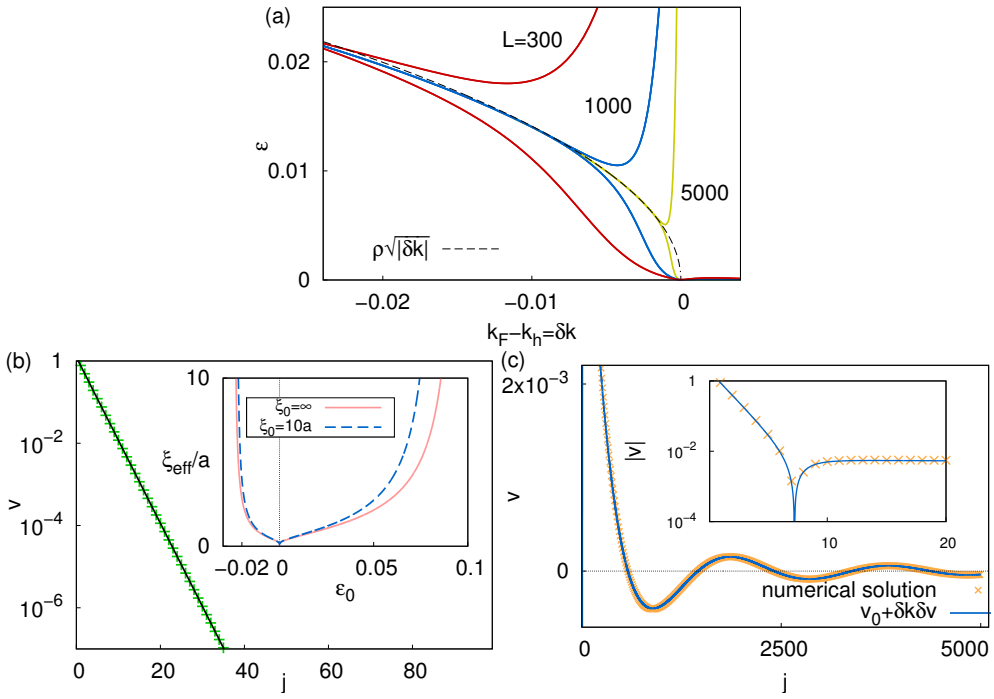

Figure 7.11.: (a) Energy of the two positive-energy subgap states (in units of Δ_0) in the nontopological two-channel phase ($\delta k < 0$) near the Bragg point, for $\xi_0 = \infty$ and various chain lengths L. As $L \to \infty$, the two states become degenerate with energy $\sim \sqrt{|\delta k|}$ near the phase transition. At the critical point, one subgap state merges discontinuously with the quasiparticle continuum. For finite L, the discontinuity is smeared and the degeneracy is lifted on the scale $1/L$. (b) Majorana wavefunction v_j at the Bragg point $k_F = k_h$. The exact numerical solution of the BdG Hamiltonian (green crosses) agrees with the analytical solution (black line) in Eq. (7.50). Inset: Localization length $\xi_{\text{eff}} = a/\ln|\beta^{-1}|$ along the yellow line in the phase diagram in Fig. 7.10(a). The localization length is of order a and decreases with increasing coherence length ξ_0. (c) Majorana wavefunction v_j for $k_F = k_h + \delta k$ with $\delta k = 0.003/a$. The numerical solution of the BdG Hamiltonian (orange crosses) agrees with the analytical solution (blue line) as obtained by numerical evaluation of the inverse Laplace transform in Eq. (7.53). Inset: Blowup near the end of the chain emphasizing the initial exponential decay. Parameters: $\epsilon_0 = 0.03\Delta_0$, $k_h = 0.1\pi/a$, and $k_F = 4.1\pi/a + \delta k$.

states which are exponentially localized even though the Hamiltonian allows for long-range hopping and pairing along the chain. (iii) The localization length $\xi_{\text{eff}} = a/\ln|\beta^{-1}|$ of the Majorana states is set by the spacing a between the magnetic impurities and thus much shorter than the coherence length ξ_0 of the superconducting host. (iv) The Majorana end states at the Bragg point remain well-defined and exponentially localized even in the limit $\xi_0 \to \infty$ where the Bragg point coincides with the topological critical point. (v) We will see below that away from the Bragg point, the Majorana wavefunctions develop a power-law tail in addition to the initial exponential decay.

Physically, the strong localization for $k_h = k_F$ can be traced back to Bragg reflection. Similar to a Bragg mirror, the resonance between the oscillations of the Shiba states and the spin helix leads to destructive interference in one direction which neutralizes the long-range coupling. This explains that the localization length becomes of the order of the lattice spacing. More explicitly, the hopping and pairing terms are generically of the same order, but their relative magnitude depends sensitively on the wavevectors k_F and k_h. At the resonance $k_F = k_h$, hopping and pairing between two arbitrary sites have equal magnitude but differ in parity. Hopping to left and right has the same sign and is thus even, whereas pairing is odd with opposite signs for the two directions.

7.6.2. Topological phase

When tuning away from the Bragg point, Bragg reflection is no longer perfect and the long-range character of the model is partially recovered. As a result, the wavefunction acquires a tail with a slow power-law decay as we will now show for the immediate vicinity of the Bragg point (in agreement with earlier numerical results in Sec. 7.5). Here we first focus on the topological phase ($k_F = k_h + \delta k$ with δk small and positive) and return to the nontopological phase ($k_F = k_h + \delta k$ with δk small and negative) further below.

For δk small and positive, the matrices $\mathcal{H}_{12}$ and $\mathcal{H}_{21}$ are no longer triangular, but we still expect a localized Majorana state in a semi-infinite chain. We expand the eigenvalue problem to linear order in δk and show that it reduces to an integral equation in a suitably taken limit when setting $\xi_0 \to \infty$. The integral equation can then be solved by standard methods. To first order in δk, we rewrite $\mathcal{H}_{12} v = 0$ as

$$(M + \delta M)(v_0 + \delta k \delta v) = 0 \tag{7.51}$$

(see App. C.5 for numerical support of this expansion). Here, M is the upper triangular part of $\mathcal{H}_{12}$ with $M_{ii} = i\epsilon_0$, $M_{ij} = (-i\Delta/k_F)\sin(Kr_{ij})/r_{ij}$ for $i < j$ in terms of $K = k_F + k_h$, and δM is the lower triangular part with $\delta M_{ij} = (-i\Delta/k_F)\sin(\delta k r_{ij})/r_{ij}$ for $i > j$.

To zeroth order in δk, we obtain $Mv_0 = 0$ and thus v_0 coincides with the exponentially decaying solution at the Bragg point.

Next, we rewrite δM as $\delta M_{i+j,i} = (-i\Delta/k_F)\delta k \sin y_j/y_j$ with $y_j = \delta k a j$. Thus δM_{ij} varies only on large scales $r_{ij} \sim 1/\delta k$ and we can take a continuum limit by considering $\delta k \to 0$ while keeping y_j fixed. In this limit, δM converges to a continuous matrix as a function of $y_j \to y$ and correspondingly, δv should also have a well-defined continuum limit $\delta v \to \delta v(y)$ as a function of the scaled variable y_j. The existence of this continuum limit is readily confirmed by numerics and to linear order in δk, Eq. (7.51) yields an integral equation for $\delta v(y)$ (see App. C.5 for the derivation),

$$A\delta v(y) + \int_0^y dz \frac{\sin(y-z)}{y-z}\delta v(z) = -B\frac{\sin y}{y}. \tag{7.52}$$

Here we defined $A = F(k_F + k_h) - \frac{k_F a \epsilon_0}{\Delta}$, $B = a \operatorname{sgn}\beta[(1+\beta)/(1-\beta)]^{1/2}$, and $F(x) = \arctan\cot(x/2)$. This integral equation can be solved in a standard manner by Laplace transform $\mathcal{L}$ which yields (see App. C.5)

$$\delta v(y) = -\mathcal{L}^{-1}\left[\frac{B \operatorname{arccot} s}{A + \operatorname{arccot} s}\right] \underset{y\to\infty}{\sim} -4AB\frac{\sin y}{y \ln^2 y}. \tag{7.53}$$

Corrections to the asymptote are suppressed by factors of $1/\ln y$. Although our analytical analysis focuses on the vicinity of the Bragg point, the asymptotic decay is characteristic of the Majorana states in the entire topological phase when $\xi_0 = \infty$ as previously established numerically in Sec. 7.5. Figure 7.11(c) shows that the analytical solution (7.53) is in excellent agreement with numerical results.

7.6.3. Nontopological phase

When the Bragg point $k_F = k_h$ falls into the topological phase for finite ξ_0 [i.e., along the yellow line in Fig. 7.10(a)], the nontopological side of the phase transition ($\delta k < 0$) can be understood as an effective two-channel wire (cf. Sec. 7.5.2). Thus, this phase exhibits two subgap states for each end. In long chains, $L \to \infty$, their wavefunction and energy can be obtained analytically by an extension of the technique used for $\delta k > 0$. Here, we sketch the results and defer details to the Appendix C.5.

The two positive-energy subgap states become degenerate for large L and to leading order in $|\delta k|$, we find that their energy scales as $\epsilon \sim |\delta k|^{1/2}$, consistent with the numerical results in Fig. 7.11(a). Similarly, the Nambu wavefunction (u, v) for the state at the left end[9] has $u_i \sim |\delta k|^{1/2}\exp(-\cot A|\delta k|ai)$ and $v \sim v_0 + |\delta k|\delta v$, with v_0 the exponential

[9] The second positive-energy subgap state is localized at the right end with electron and hole components exchanged. The two negative-energy states are related to the positive ones by chiral symmetry.

solution at the critical point and δv a power-law tail $\sim 1/y \ln^2 y$ as for $\delta k > 0$. The electron component u decays exponentially with a decay length which diverges for $\delta k = 0$, reflecting the phase transition and the disappearance of one subgap state. The hole component v smoothly evolves into the Majorana bound state on the topological side.

7.7. Conclusions

Chains of magnetic impurities placed on a conventional s-wave superconductor constitute a promising venue for Majorana physics. Assuming that the magnetic impurities form a spin helix, the bands of Shiba states formed in the host superconductor can enter into a topological superconducting phase. In this chapter, we considered the limit of dilute impurities inducing deep Shiba states in which the bands of Shiba states do not overlap with the quasiparticle continuum. Starting with the individual Shiba states, we derived an effective tight-binding Bogoliubov–de Gennes Hamiltonian. While this Hamiltonian has close similarities with the Kitaev model, it differs in important ways: (i) Both hopping and pairing are long range, falling off as $1/r$ for distances small compared to the superconducting coherence length ξ_0. (ii) For generic spin helices, the hopping amplitudes are complex (or, equivalently, the pairing amplitude involves a spatially varying phase). These differences have significant consequences, both for the phase diagram and for the decay (and hence the energy splitting) of Majorana bound states. Most importantly, the long-range nature of hopping and pairing implies that over a wide range of length scales, the spatial decay of the Majorana bound states is well fit by a power law with logarithmic corrections rather than an exponential dependence. Moreover, the complex hopping amplitudes tend to suppress topological superconductivity; they result in asymmetric dispersions under momentum reversal which suppresses Cooper pairing. As a result, fully planar spin helices whose additional reflection symmetry results in purely real hopping amplitudes, are optimal for realizing topological superconductivity.

As a consequence of the long-range coupling, helical Shiba chains display an unconventional topological critical point at the Bragg point $k_F = k_h$. We show that for finite chains, the Majorana end states persist at the critical point and display remarkable localization properties. By the competition between Bragg reflection and long-range coupling, the Majorana end states are exponentially localized at the critical point but develop a power-law tail in the topological phase. This contrasts in an interesting way with the decay of correlations around conventional critical points.

This is also an encouraging prediction for experiment, as the exponential localization at the critical point is on the scale of the lattice spacing and entirely unrelated to a topo-

logical gap. Thus, the Majorana end states may remain well localized even in chains whose length is comparable to the coherence length of the host superconductor. At the same time, the power-law localization within the topological phase raises interesting questions with regard to its stability against perturbations such as disorder.

Our approach can be extended in several directions. For instance, it might be relevant for experiment to include spin-orbit coupling within the superconducting host, since this also allows ferromagnetic chains to enter a topological phase. This is particularly interesting as ferromagnetic chains are presumably easier to realize than spin helices. Furthermore it would be interesting to extend our approach based on Shiba states to the limit of shallow impurities with narrow spacing in order to describe continuous chains.

8. Tunneling processes into localized subgap states in superconductors[1]

Tunneling spectroscopy has become an indispensable tool for the characterization of bound states in superconductors like Andreev or Shiba states [Baur 81, Yazd 97, Yazd 99, Pan 00, Huds 01, Ji 08, Deac 10, Pill 10, Fran 11, Pill 13, Lee 14]. As discussed in Sec. 3.3.1 and Ch. 4 tunneling conductance measurements are also a valuable technique in the search for Majorana bound states. In particular, ongoing experimental investigations on possible Majorana bound states in chains of magnetic impurities on top of superconductors forming a band of Shiba states [see Sec. 3.2.3 and Ch. 7] heavily rely on scanning tunneling microscopy and spectroscopy as diagnostic tools.

In general, tunneling into a localized state in a superconductor gives rise to resonances in the differential tunneling conductance. Typically the amplitude of the tunneling conductance is viewed as a measure of the local density of states. In this chapter, we perform a detailed study of the relevant mechanisms for tunneling into subgap states in a superconductor including quasiparticle relaxation mechanisms present at finite temperature. We combine our analysis with scanning tunneling microscopy and spectroscopy (STM/STS) experiments on single adatom Shiba states – employing superconducting tips for improved resolution. Interestingly, the experimental findings are inconsistent with a simple understanding of the conductance peaks in terms of the local density of states. We can explain the central features of the experimental data by analyzing the competition between single-particle and Andreev processes. Our results enable us to correctly determine the local density of states and yield information on the relaxation dynamics of the Shiba state.

8.1. Introduction

Impurity-induced subgap states provide a fruitful window into conventional and unconventional superconductors [Bala 06, Yazd 97, Yazd 99]. The Yu-Shiba-Rusinov states

[1] This chapter is based on a collaboration of M. Ruby, B. Heinrich, and K. Franke, who designed and performed the experiments and analyzed the experimental data, and Y. Peng, F. von Oppen, and the author of this thesis, who carried out the calculations. All collaborators interpreted the results.

[Yu 65, Shib 68, Rusi 69] bound by magnetic impurities in conventional s-wave superconductors are a simple model system for nonmagnetic impurity resonances in unconventional superconductors, probe the competition between superconducting and Kondo correlations [Fran 11, Baue 13, Yao 14], and might provide a platform for engineering topological superconducting phases with Majorana bound states [Nadj 13, Pien 13a, Pien 14].

Experimentally, Shiba states manifest themselves in scanning tunneling microscopy as resonances at positive and negative bias voltages [Yazd 97, Yazd 99, Ji 08]. Theoretically, these experiments have been interpreted in terms of single-electron tunneling into the localized subgap states [Bala 06], where the tunneling conductance represents a measure of the local density of states, with the electron (hole) component of the Shiba wavefunction governing the strength of the resonance at positive (negative) bias [Bala 06]. Recently, Martin and Mozyrsky [Mart 13] pointed out that this interpretation may be incomplete. They argue that an isolated subgap state cannot support a continuous current based on single-electron tunneling alone as current flow would stop once this state is occupied. They suggest Andreev reflections as alternative current-carrying processes which resonantly transfer Cooper pairs into the condensate. Importantly, these two processes can be distinguished experimentally for a normal-metal tip: Unlike the single-electron process, the Andreev process is symmetric under sign reversal of the bias voltage.

Here we shed light on this controversy for the case of a superconducting tip. We provide evidence that in general, both processes are required to understand the experimental differential conductance traces, with consequences for the interpretation of past and future experiments.

8.2. Basic processes

Consider a magnetic impurity which induces a single subgap Shiba state in the superconducting substrate. When probed by a superconducting tip (with the same gap Δ as the substrate), the following tunneling processes contribute to the current: (i) Single electrons can tunnel when the negative-energy quasiparticle continuum of the tip overlaps with the positive-energy continuum of the substrate (or vice versa). This requires a threshold bias $eV = \pm 2\Delta$. (ii) At finite temperature, there is a finite density of thermal quasiparticles (holes) in the positive (negative) energy quasiparticle continuum. Thus, a finite single-particle current can flow even near zero bias. When a Shiba state of energy ϵ_0 is present, a single-particle current can also flow when the negative- or positive-energy continuum of the tip overlaps with the Shiba state. This results in thresholds of

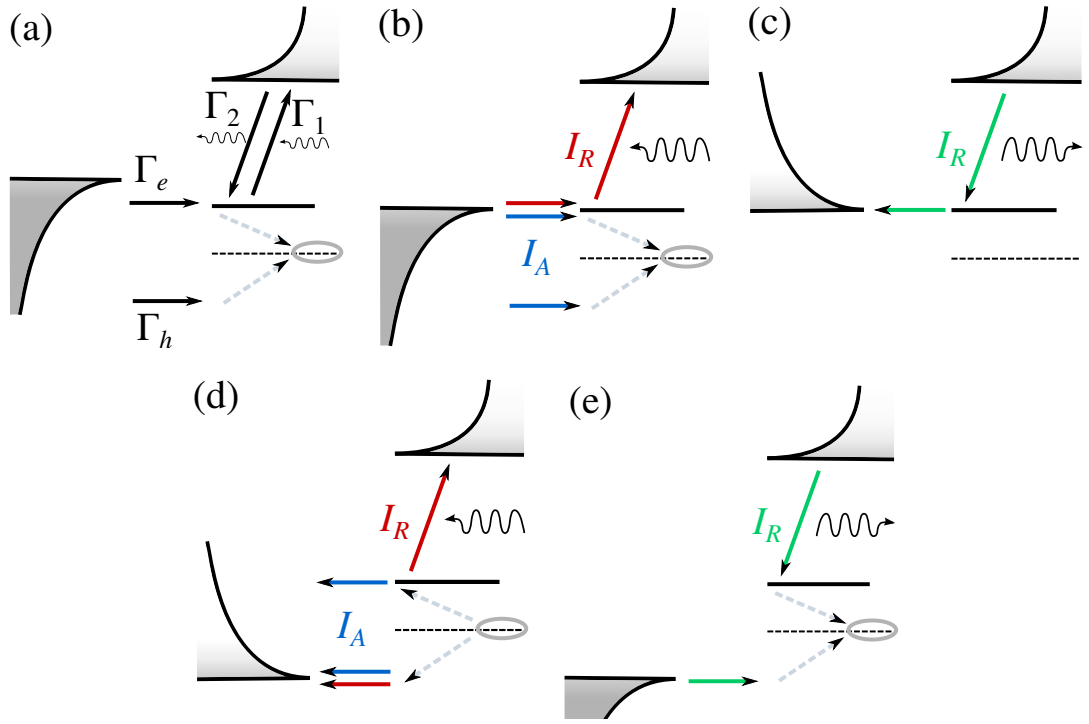

Figure 8.1.: (a) Principal tunneling and relaxation processes governing the occupation of the Shiba state. (b-e) Processes contributing to the threshold (b) at $eV = \Delta + \epsilon_0$ via Γ_e and Γ_1 (single-particle process) or Γ_e and Γ_h (Andreev process), (c) at $eV = -\Delta + \epsilon_0$ via Γ_e and Γ_2, (d) at $eV = -\Delta - \epsilon_0$ via Γ_h and Γ_1 (single-particle process) or Γ_h and Γ_e (Andreev process), and (e) at $eV = \Delta - \epsilon_0$ via Γ_h and Γ_2.

the bias voltage at $eV = \pm\Delta + \epsilon_0$. Similar processes involving an additional Andreev reflection are possible when the continuum of the tip overlaps with the symmetric energy $-\epsilon_0$. These processes give rise to additional thresholds $eV = \pm\Delta - \epsilon_0$. For continuous current flow, all of these processes necessarily require relaxation processes which empty the Shiba state after it is occupied from the tip (or occupy the empty Shiba state) [Mart 13]. At finite temperatures a quasiparticle in the Shiba state can be excited to continuum by absorption of a phonon. Conversely, a thermally excited quasiparticle can relax into the Shiba state emitting a phonon. The relaxation-induced current carrying processes for all four thresholds are depicted by the red and green arrows in Fig. 8.1(b-e). (iii) At $e|V| < 2\Delta$, an electron incident from, say, the tip can be reflected as a hole, transferring a Cooper pair to the substrate in the process. As both the electron and the hole gain an energy eV in this process, Andreev processes between the quasiparticle continua have thresholds $eV = \pm\Delta$. Additional processes involving multiple Andreev reflections lead to thresholds $eV = \pm 2\Delta/n$. These Andreev processes require two or more particles to cross the tunnel barrier and are therefore only relevant for strong tunneling. In the presence of Shiba states, an electron from the negative-energy contin-

uum of the tip can virtually tunnel into the Shiba state, reflect as a hole, and resonantly transfer a Cooper pair into the condensate of the substrate. Together with a similar process for reverse bias [see blue arrows in Figs. 8.1(b) and (d)], this leads to thresholds at $eV = \pm(\Delta + \epsilon_0)$ which *coincide* with two thresholds for the single-electron processes. Such Andreev processes mediated by Shiba states can occur at significantly lower tunneling rates compared to the nonresonant multiple Andreev reflections. The Andreev processes allow for continuous current flow even in the absence of relaxation processes as they do not change the occupation of the Shiba states but merely transfer electron pairs into the condensate.

8.3. Experiment

The thresholds at $e|V| = \Delta \pm \epsilon_0$ can be observed in experiment, confirming this basic picture. Specifically, we have performed STM experiments probing Mn adatoms on a Pb(111) single crystal surface. The experiments were carried out in a Specs JT-STM at the base temperature of $1.2\,\mathrm{K}$ as well as at $4.8\,\mathrm{K}$. Spectra of the differential conductance $\mathrm{d}I/\mathrm{d}V$ were recorded using a conventional lock-in technique with a modulation amplitude of $15\,\mu\mathrm{V}$ at a frequency of $912\,\mathrm{Hz}$. The lead single crystal surface was cleaned by repeated sputter/anneal cycles until a clean, atomically flat and superconducting surface was obtained (critical temperature $T_c = 7.2\,\mathrm{K}$). Mn adatoms were evaporated onto the clean sample at a temperature below $10\,\mathrm{K}$ resulting in a density of 30 atoms per $100 \times 100\,\mathrm{nm}^2$. Importantly, our STM experiments are carried out with a lead-covered, superconducting tip (see Ref. [Fran 11] for the preparation procedure). This results in an experimental resolution far beyond the Fermi-Dirac limit ($\approx 400\,\mu\mathrm{V}$ at $1.2\,\mathrm{K}$ [Hein 13, Ruby]), and contributes the additional thermal thresholds $eV = \pm(\Delta - \epsilon_0)$ in the spectra which strongly facilitate the analysis.

Figure 8.2 shows $\mathrm{d}I/\mathrm{d}V$ traces (normalized to the normal state conductance) as a function of V, acquired at different tip–sample distances and thus different tunneling strengths. Accounting for the improved energy resolution, our spectra at large distances compare well with earlier experiments [Ji 08]. The thresholds for the basic processes contributing to the tunneling current manifest themselves as peaks in $\mathrm{d}I/\mathrm{d}V$. The peaks at $e|V| = 2\Delta \simeq 2.7\,\mathrm{meV}$ are the coherence peaks associated with the gap edges and coincide with the peaks observed on a clean surface (top *grey* trace in Fig. 8.2). For weak tunneling, there are several subgap peaks which originate from Shiba states induced by the adatom. The most pronounced peaks are due to the deepest Shiba state with $\epsilon_0 \simeq 0.2\,\mathrm{meV}$. This state leads to the two *main* peaks at $eV = \pm(\Delta + \epsilon_0)$ (with peak height $\alpha_\pm$) and the two *thermal* peaks at $eV = \pm(\Delta - \epsilon_0)$ (with peak height $\beta_\pm$). In the

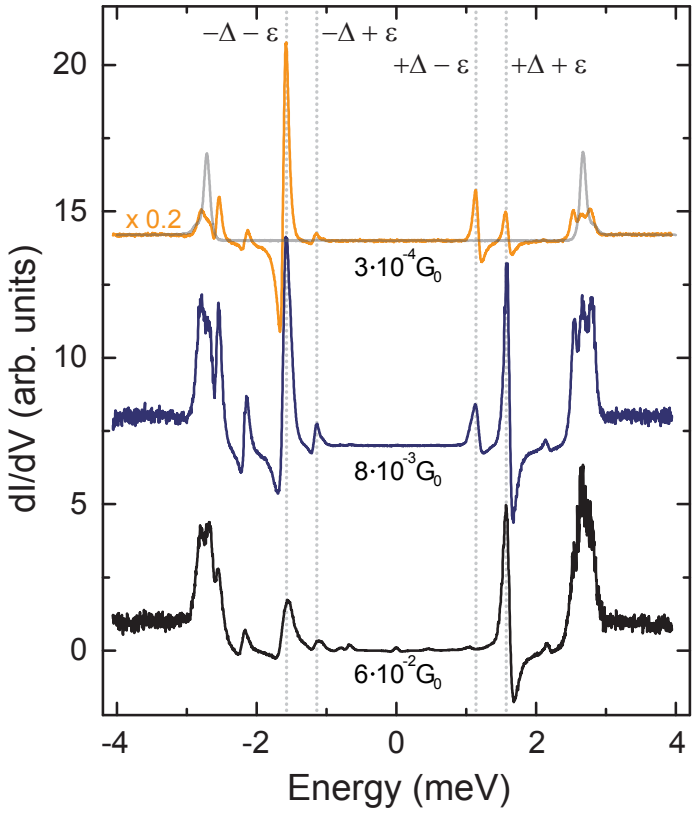

Figure 8.2.: $\mathrm{d}I/\mathrm{d}V$ spectra measured on an isolated Mn adatom on Pb(111) for increasing tunneling strength from top to bottom. Spectra are normalized to the normal-state conductance (noted in the graph in units of $2\,e^2/h = G_0$), curves are offset for clarity, top curves divided by 5 to increase visibility. The distance to the closest neighboring Mn atom was larger than 5 nm. As Guide for the eye a spectrum acquired above the clean Pb(111) surface is overlaid in the case of smallest conductance (top curve). The four peaks originating from the deepest Shiba level are marked by dashed lines at $e|V| = \pm(\Delta \pm \epsilon)$. With increasing tunnel coupling the asymmetry of the peak height changes. The lowest curve shows signatures of multiple Andreev reflections and a Josephson peak at zero bias.

following, we focus on this Shiba state as the associated peaks are most pronounced experimentally and their theoretical interpretation turns out to be least affected by the presence of the other Shiba states.

The heights of the peaks associated with this Shiba state are plotted *vs* normal-state conductance in Fig. 8.3 over several orders of magnitude in tunneling strength. We first draw attention to two important features of these data. First, the peak heights are linear over a wide range in tunneling strength before turning sublinear at stronger tunneling. Second, the asymmetry in the peak heights $\alpha_\pm$ between positive and negative biases

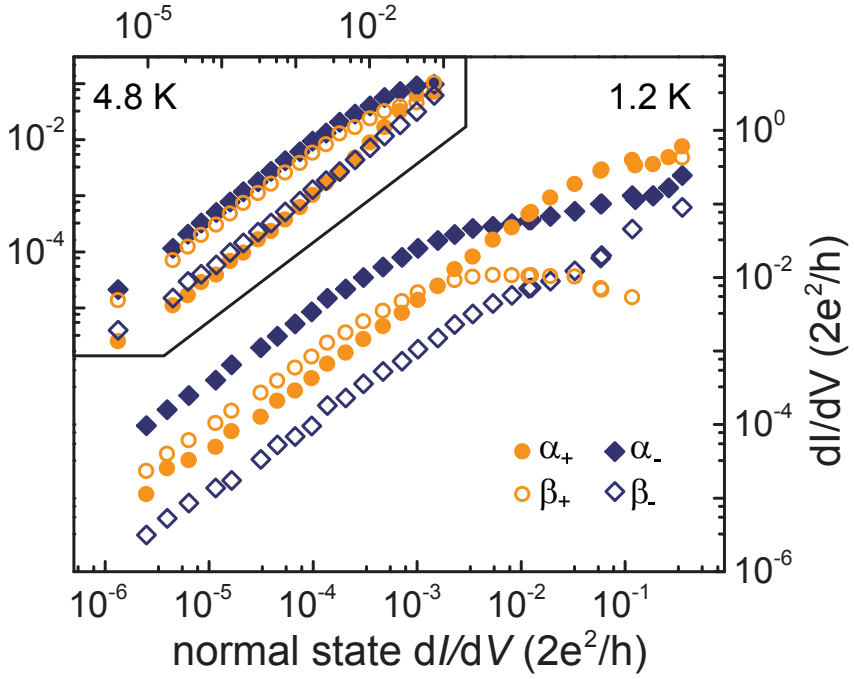

Figure 8.3.: Measured peak heights $\alpha_\pm$ and $\beta_\pm$ of the four resonances associated with the deepest Shiba level (marked by dashed lines in Fig. 8.2) *vs* normal state conductance at $T = 1.2\,\mathrm{K}$ (main panel) and $T = 4.8\,\mathrm{K}$ (inset).

inverts as a function of tunneling strength: At small tunneling rates, $\alpha_+ < \alpha_-$, while at large tunneling rates, $\alpha_+ > \alpha_-$. It is also evident that the inversion of the peak heights occurs at the crossover between the linear and sublinear regimes.

8.4. Theoretical results for the tunneling current

The inversion of peak heights implies that the peak heights cannot generally be a direct measure of the electron and hole components u and v of the Shiba wavefunction. To gain further insight into these observations, we have derived the differential conductance theoretically within the Keldysh Green's function formalism. A detailed derivation is included in App. D. Here, we focus on the physics underlying the results. Our calculation includes single-electron and Andreev processes involving the Shiba state as well as a phenomenological description of relaxation processes between the Shiba state and the quasiparticle continuum. We neglect Andreev reflections at the superconducting tip (and thus multiple Andreev reflections), which is justified except in the regime of very strong tunneling. With this approximation, we can write the tunneling current

as a sum of single-particle and Andreev currents, $I = I_R + I_A$, where

$$I_R = \frac{2e}{h}\int d\omega \left\{ \frac{2\Gamma_1[\Gamma_e n_F(\omega_-) - \Gamma_h n_F(\omega_+)]}{(\omega-\epsilon_0)^2+\Gamma^2} - \frac{2\Gamma_2[\Gamma_e(1-n_F(\omega_-)) - \Gamma_h(1-n_F(\omega_+))]}{(\omega-\epsilon_0)^2+\Gamma^2} \right\}, \tag{8.1}$$

$$I_A = \frac{2e}{h}\int d\omega \frac{4\Gamma_h\Gamma_e[n_F(\omega_-) - n_F(\omega_+)]}{(\omega-\epsilon_0)^2+\Gamma^2}. \tag{8.2}$$

Here, $\omega_\pm = \omega \pm eV$ and $\Gamma = \Gamma_e + \Gamma_h + \Gamma_1 + \Gamma_2$.

The expressions for I_R and I_A can be understood in terms of the basic processes discussed above. The Andreev current I_A involves tunneling of an electron, described by $\Gamma_e(\omega) = \pi|u|^2\rho(\omega - eV)|t|^2$, and a hole, described by $\Gamma_h(\omega) = \pi|v|^2\rho(\omega + eV)|t|^2$. Here, t is the amplitude for tunneling between tip and substrate. The rates Γ_e and Γ_h are strongly ω-dependent through the tip's BCS density of states $\rho(\omega)$. The denominator in Eq. (8.2) describes the intermediate virtual occupation of the Shiba state. It includes the rates Γ_1 for depopulating the Shiba state by excitation to the continuum and Γ_2 for occupying the Shiba state by a thermally excited quasiparticle. The latter processes are possible, e.g., via phonon or photon emission and can be assumed ω-independent to a good approximation. The four contributions to the single-particle current I_R directly correspond to the peaks α_+ [term $\propto \Gamma_1\Gamma_e$, see Fig. 8.1(b)], α_- [term $\propto \Gamma_1\Gamma_h$, see Fig. 8.1(d)], β_- [term $\propto \Gamma_2\Gamma_e$, see Fig. 8.1(c)], and β_+ [term $\propto \Gamma_2\Gamma_h$, see Fig. 8.1(e)].

Eqs. (8.1) and (8.2) provide the following basic picture consistent with the data in Fig. 8.3: At weak tunneling, the relaxation rates Γ_1 and Γ_2 are faster than the tip-substrate tunneling. Once an electron tunnels into the Shiba state from the lead, it is rapidly excited to the quasiparticle continuum. In this regime, the tunnel current is dominated by the single-electron current I_R which is proportional to $|t|^2$ and thus to the normal-state conductance. The Andreev current I_A is merely a small correction scaling as $|t|^4$. This explains the wide linear regime in Fig. 8.3. At stronger tunneling, the tunneling rates become comparable to and eventually larger than the relaxation rates Γ_1 and Γ_2. Here, the t-dependence of the broadening Γ leads to a sublinear or even a decreasing dependence of the peak heights on the normal state conductance (i.e., on $|t|^2$).

8.5. Linear regime

This picture is substantiated by a quantitative analysis of the linear regime. For weak tunneling and $\Gamma_1 \gg \Gamma_2$, the ω-integral in Eq. (8.1) yields (see App. D)

$$\alpha_+ \sim (2e^2/h)(|u|^2|t|^2\nu_0)(\sqrt{\Delta}/\Gamma_1^{3/2}), \tag{8.3}$$

$$\beta_- \sim (2e^2/h)(|u|^2|t|^2\nu_0)(\sqrt{\Delta}/\Gamma_1^{3/2})(\Gamma_2/\Gamma_1) \tag{8.4}$$

for the peak heights. The expressions for α_- and β_+ simply differ by the substitution $u \leftrightarrow v$. Thus, in this regime, the peak height is indeed a measure of the Shiba wavefunction at the tip position. From the data in Fig. 8.3, we extract $|u/v|^2 \approx 0.13$. This asymmetry between u and v implies that the impurity is associated with a scalar potential in addition to the exchange coupling [Bala 06].

All four peaks are related by the relation $\alpha_+\beta_+ = \alpha_-\beta_-$. This is readily checked against the data in Fig. 8.3 and indeed, we find that this identity is well satisfied in the linear regime. Moreover, the thermal and main peaks in Eqs. (8.3) and (8.4) differ only through a ratio of relaxation rates, $\alpha_+/\beta_- = \Gamma_1/\Gamma_2 = \exp(\epsilon_0/k_BT)$. Here, the last equality follows when assuming detailed balance. This is in perfect agreement for the data at $T = 4.8\,\mathrm{K}$. For the data at $T = 1.2\,\mathrm{K}$, we back out a slightly higher temperature of $T = 1.6\,\mathrm{K}$ from the ratio of peak heights. Still, these considerations point to a relaxation process involving thermal activation rather than the quasiparticle bath suggested in Ref. [Mart 13].

As Γ_1 increases with temperature, Eqs. (8.3) and (8.4) also predict the peak heights in the linear regime to decrease with T. This is consistent with the data by comparing the data in the main panel and the inset in Fig. 8.3.

8.6. Regime of strong tunneling

$$\alpha_+ \sim (2e^2/h)\frac{|v|^2}{|u|^{4/3}}\frac{|t|^{2/3}\rho(\Delta+2\epsilon_0)}{(\nu_0\sqrt{\Delta})^{2/3}}, \tag{8.5}$$

$$\beta_- \sim (2e^2/h)\Gamma_2/(|u|^2|t|^2\nu_0\sqrt{\Delta})^{2/3}, \tag{8.6}$$

as well as α_- and β_+ which differ again by $u \leftrightarrow v$. Note that indeed, in the strong-tunneling regime the main peaks $\alpha_\pm$ increase sublinearly as a function of normal state conductance.

First focus on the asymmetry of the main peaks $\alpha_\pm$. Unlike for normal-metal tips [Mart 13], the Andreev contribution remains asymmetric and inverts for a supercon-

ducting tip. While we have $\alpha_+/\alpha_- = |u/v|^2$ in the linear regime, Eq. (8.5) predicts $\alpha_+/\alpha_- = |v/u|^{10/3}$ in the Andreev-dominated regime. Indeed, an inversion of the peak heights $\alpha_\pm$ is seen in Fig. 8.3, as pointed out above.

Eq. (8.6) also predicts that the thermal peaks invert, from $\beta_-/\beta_+ = |u/v|^2$ in the linear regime to $\beta_-/\beta_+ = |v/u|^{4/3}$ in the sublinear regime. This is also consistent with the data. However, the theory predicts that both β_+ and β_- exhibit a peak as a function of normal-state conductance, while we observe such a peak only for β_+. For β_-, the peak is expected to occur only at a rather large normal-state conductance. First, our approximation of neglecting Andreev reflections at the tip presumably starts to break down in this regime. Second, it becomes difficult to reliably extract the peak height in this regime due to the substantial background conductance which we attribute to multiple Andreev reflections.

We can also estimate the crossover points between the linear and sublinear regimes. In the linear regime, $\alpha_- > \alpha_+$ and $\beta_+ > \beta_-$. Thus, the tunneling rates reach the relaxation rates already at smaller normal-state conductance for α_- and β_+ than for α_+ and β_-. This is consistent with the data in Fig. 8.3 where the crossovers for α_- and β_+ occur at smaller normal-state conductance than those for α_+ and β_-. More quantitatively, the crossover points for α_+ and β_- can be obtained by equating Eqs. (8.4) and (8.6) which yields the estimate $|u|^2|t|^2\nu_0\sqrt{\Delta} \sim \Gamma_1^{3/2}$. The crossover condition for α_- and β_+ follows by the replacement $u \leftrightarrow v$. This predicts the ratio of the crossover conductances to be of order $|u/v|^2$. We previously deduced $|u/v|^2 \approx 0.13$ from the ratio of the main peaks which is consistent with the ratio of crossover conductances in Fig. 8.3. As Γ_1 grows with temperature, we also expect the crossover points to move to larger normal-state conductances for higher temperatures. This is consistent with experiment, as seen from a comparison of the main panel and the inset of Fig. 8.3.

Relaxation mechanism.—Our analysis implies that STM experiments on subgap states in superconductors can not only image the wavefunctions of the subgap states but also provide access to relevant relaxation processes. Here, we illustrate this capability by comparing the data at the two experimental temperatures in Fig. 8.3. The peak heights depend on Γ_1 which one expects to obey an Arrhenius law for a thermally activated relaxation process. If the relaxation process relied on directly exciting a quasiparticle from the Shiba state to the continuum, we would predict a ratio of the peak heights at the two temperatures of order $\sim 10^6$. This differs from the experimentally observed suppression of order 10 by several orders of magnitudes. We can account for a substantial part of this apparent discrepancy by recalling that there are additional Shiba states associated with the magnetic impurities. Assuming that relaxation to the continuum proceeds via a multistep process which first excites to the second Shiba state dramatically reduces

the discrepancy to little more than an order of magnitude, which is presumably within the accuracy of our model considerations.

8.7. Conclusions

STM experiments on subgap states in superconductors are typically assumed to measure the local density of states, as in the normal state. Here, we show that for superconducting tips, this is true only at sufficiently weak tunneling where we find single-particle tunneling to dominate. We provide evidence that there is a considerable Andreev contribution to the tunneling current at larger tunneling strengths which becomes increasingly important as the temperature is reduced. This clarifies the physical processes underlying STM experiments on superconductors and has important ramifications for interpreting corresponding experiments.

Our conclusions are based on a comprehensive comparison between experimental data and a theoretical analysis of the single-particle and Andreev currents. There are several interesting directions for future work. First and foremost, it would be highly desirable to gain a better understanding of the underlying relaxation processes. A reasonable phenomenological description would even be necessary for an analogous analysis of the higher Shiba states present for Mn on Pb. In addition, it should be rewarding to include Andreev processes at the tip in the theoretical description to investigate the importance of multiple Andreev processes in STM measurements.

9. Conclusions

In this thesis we investigate signatures of Majorana bound states in topological superconductors. Recent theoretical advances have put the realization of topological superconductors within the range of state-of-the-art experiments. For manifold reasons discussed at length in Sec. 3.3 a feasible way to obtain bullet-proof evidence for Majorana bound states remains an open issue. Signatures of Majoranas may be obscured by non-ideal conditions. Additionally other effects may produce similar features in experiments impairing the unambiguous identification of Majorana states.

We specifically address this lack of unique signatures by examining a variety of experiments in different systems following two different strategies. On the one hand this work (Chs. 4, 7, and 8) aims to improve the theoretical understanding of recent experiments searching for Majorana bound states with a particular focus on the specific experimental conditions. Employing realistic model Hamiltonians we are able to predict several intriguing phenomena which differ qualitatively from existing theories. On the other hand we propose novel measurement schemes exhibiting distinct signatures of Majorana bound states and the topological superconducting phase in Chs. 4, 5 and 6. We discuss the viability of these experiments and give estimates for the expected outcome. In the following we summarize the various projects pursued in this thesis before commenting on possible future research avenues.

In Ch. 4 we investigate the zero-bias peak as a signature of Majorana bound states in the tunneling conductance. We show that in multisubband quantum wires the Majorana peak can be significantly suppressed compared to the strictly one-dimensional case. This finding provides a simple and realistic explanation for the small peak height found in experiments such as [Mour 12]. Furthermore we propose to deliberately introduce disorder into a certain part of the system introducing scattering between subbands and thereby enhancing the peak height significantly. We determine the optimal conditions for this effect and also discuss other mechanisms for subband mixing.

Chapter 5 predicts signatures of the topological phase transition in the Josephson current through a weak link in a mesoscopic superconducting ring. Inevitable quasiparticle transitions that violate fermion parity conservation in the superconductor typically conceal signatures of the topological phase in the dc Josephson effect. Nevertheless, they

can lead to a peak in the Majorana-specific 4π-periodic supercurrent as the system is tuned through the topological phase transition. This signature is shown to be robust in the presence of disorder. As a byproduct of these considerations we find that weak disorder surprisingly drives a p-wave superconductor further into the topological phase contrary to the effect of strong disorder.

The 4π Josephson effect is revisited in Ch. 6, which explores the so-called magneto-Josephson effect, a supercurrent induced by twisting the magnetic field directions in the two banks of the junction. This work extends previous results for proximity-coupled topological insulator edges to the quantum-wire realization of topological superconductors. We derive the periodicities of the Josephson and magneto-Josephson effect for all possible Josephson junctions showing that the signatures of Majorana states occur in different domain configurations for the quantum wire and TI edge realizations. This difference between the two closely related models can be explained in terms of the effective low-energy theories. We can describe the quantum wire model at low energies by a superposition of a TI edge and a p-wave superconductor, which explains the reversal of the topological and trivial phases between the quantum wire and TI edge model. We close the chapter by evaluating the magnitude of the ordinary and magneto-Josephson effects under realistic conditions. While the Majorana states carry equal current in both cases the background contribution from the bulk states maybe considerably lower for the magneto-Josephson effect.

The last two chapters of this thesis investigate Shiba bound states in superconductors. In Ch. 7 we develop an effective description of helical chains of magnetic impurities in superconductors possibly hosting Majorana bound states. This realization of a topological superconductor has only recently been predicted [Choy 11, Nadj 13] and is the subject of ongoing experimental efforts. Our model describes the topological superconductor as an impurity band in the superconductor formed by Shiba states bound to the individual impurities. The long-range tails of the Shiba wavefunctions give rise to a series of unusual phenomena unique to this system such as power-law rather than exponential localization of Majorana bound states and an unconventional topological phase transition without smooth closing of the gap. We furthermore identify a possible destructive interference akin to Bragg reflection leading to extremely strong (exponential) localization of the Majorana bound states near or at a topological critical point.

Finally we part from Majorana-specific investigations in Ch. 8 and consider the tunneling spectroscopy of arbitrary bound states in superconductors with a focus on Shiba states but applicable also to Majorana and Andreev states. A general theoretical analysis of the competition between different resonant tunneling processes and the resulting peaks in the differential tunneling conductance is supported by actual measurements

for Shiba states carried out by experimental collaborators. The theory is compared to the experimental data, which allows us to determine central properties of the bound states and the nature of quasiparticle relaxation mechanisms present in the system. Although this chapter does not directly address Majorana bound states it fits well within the scope of this thesis. On the one hand it is motivated by the helical Shiba chains hosting Majorana bound states as discussed in Ch. 7, since tunneling spectroscopy is the most important diagnostic tool for such systems. On the other hand the study applies to generic bound states in superconductors and may therefore provide useful information about spectroscopic signatures of Majorana bound states.

In conclusion we would like to point out an interesting feature of the results summarized above. In various situations we find that deviations from ideal experimental conditions can lead to new interesting physics and may even be beneficial for the desired outcome. Although imperfections are generally regarded as a nuisance necessarily present in experiment they can also be used as an additional tool to manipulate the system. For instance, we show that the presence of disorder can enhance signatures of Majoranas in conductance experiments (Ch. 4) or even extend the range of the topological superconducting phase (Ch. 5). Furthermore, typically unwanted quasiparticle relaxation of subgap states in superconductors present at finite temperature may greatly facilitate the determination of the density of states when measuring the differential tunneling conductance (Ch. 8) and give rise to a compelling signature of the topological phase transition in topological superconductor rings (Ch. 5). Finally, we argue that, counterintuitively, long-range *power-law* couplings in helical Shiba chains (Ch. 7) can lead to a very strong *exponential* localization of Majorana bound states on short scales. Thus by taking into account realistic experimental conditions, which at first glance appear to be detrimental to the desired outcome, we have been able to predict novel phenomena with important implications for experiment.

The unequivocal observation of Majorana bound states in topological superconductor would represent a milestone in condensed matter physics and beyond. On the one hand, topological superconductors with protected zero-energy Majorana bound states constitute a novel flavor of topological phases, which have fascinated condensed-matter physicist for the past three decades. In particular, the nonlocal nature of the topological phase promises interesting applications such as a Cooper pair splitter [Nils 08] or a Thouless pump [Thou 83], i.e., pumping of quantized charge, in one dimension. Even more remarkable, on the other hand, are the phenomenal nonabelian exchange statistics of Majorana bound states which could revolutionize many-body physics and quantum information alike. Majorana bound states in superconductors can be manipulated by gates, magnetic fields, and supercurrents among others and are therefore much easier to control that nonabelian anyons in exotic fractional quantum Hall systems.

These special properties set the two major challenges in this field of research: to identify realistic measurement schemes sensitive to the nonlocal character of Majorana bound states and as a second step to design experimentally feasible protocols for braiding Majoranas. Several proposals addressing these problems have been put forward, however, mostly on an abstract level. We have mentioned some of the proposals in Sec. 3.4. Clear estimates on parasitic mechanisms such as the quasiparticle poisoning time or the influence of impurities or nonadiabatic manipulations on a braiding cycle in specific realization are often unavailable (notable exceptions are [DeGo 11, Chen 11, Tsve 12, Perf 13, Karz 13]).

Until now, the existing experiments have addressed neither nonlocal signatures nor braiding of Majoranas, but instead focused on spectral signatures of single Majoranas or the Josephson current through a pair of Majoranas in a narrow junction. The topological character of these bound states can at best be probed indirectly in such measurements. Nevertheless, the detection of local properties provides a valuable tool even in more sophisticated experiments. While local signatures of Majoranas are typically more accessible in experiments than, for instance, nonlocal correlations or interference patterns, such detection schemes are impaired by other effects. As we have discussed in Sec. 3.3, distinct physical phenomena unrelated to topology can mask or mimic local Majorana signatures. Thus neither the pure presence nor absence of a signal can yield a definite answer on the existence of Majorana states.

A promising strategy to circumvent this problem is to combine different measurements and methods in a single experiment. This allows one to rule out artifacts plaguing a particular experimental approach. An inspiring realization of this paradigm has been reported in [Bret 13], where the Andreev spectrum of a conventional Josephson junction has been measured by a combination of microwave absorption and supercurrent spectroscopy. This technique could be equally useful in the quest for Majorana bound states. As another example, one could measure the tunneling conductance simultaneously at both ends of a long superconducting wire, thus combining two copies of the same experiment at different locations. True Majorana signatures must appear and vanish in conjunction at both ends, whereas signals of trivial origin should be susceptible to manipulations of local parameters at one end.

Finally, we comment on several more concrete future research topics motivated by the individual projects presented in the main part. The most recently predicted platform for Majorana bound states currently investigated in experiments are chains of impurities on a superconductor. Here the fundamental question about the conditions for a topological phase persists. In Ch. 7 we have investigated a helical chain of impurities, but, for instance, a ferromagnetic chain in conjunction with spin-orbit interaction in the substrate

can also lead to a nontrivial topology (this is similar to a halfmetal wire in proximity to a spin-orbit-coupled superconductor [Duck 11, Chun 11]). Furthermore the role of disorder and inhomogeneities in such a chain as well as the robustness of braiding operations remains unclear due to the long-range couplings. An interesting proposal for braiding in impurity rings has been made in [Li 14], which could provide a good starting point for such investigations.

Another focus of this work has been the 4π Josephson effect considered in Chs. 5 and 6. A broad range of theoretical work has investigated the dc and the voltage-biased ac Josephson effect as well as Shapiro step measurements. Recent experiments aiming to detect signatures of Majoranas in the Josephson effect, however, are performed under current bias [Rokh 12], which has received only little attention in theoretical work (see, e.g., [Domi 12]). The dynamics of current-biased junctions are complex due to nonlinear effects possibly leading to different results than the voltage bias case. Indeed, there is a discrepancy between experimental findings and theoretical prediction on the odd-even effect in Shapiro step measurements [Houz 13], which motivate revisiting the current-biased 4π Josephson effect.

The Josephson effect on the edge of a two-dimensional topological insulator has been observed in [Hart 13, Prib 14]. In these beautiful experiments two opposite edges of a rectangular topological insulator have been contacted by superconductors and the supercurrent has been used to prove the pure edge transport in the topological phase by analyzing the Fraunhofer pattern. At the same time this constitutes the first demonstration of induced superconductivity in helical edge channels. Intriguingly, the Josephson current may also carry information about Majorana states in the junction, for instance in the current–phase relationship, although further investigation are needed to clarify the role of the two parallel junctions present in the experiments. We note in passing that a proximity-coupled topological insulator edge naturally has a ring shape. This system may therefore provide an appropriate setting for the signature of Majoranas in mesoscopic superconducting rings discussed in Ch. 5.

Triggered by realistic theoretical proposals and recent experimental advances, Majorana states have received considerable attention over the past few years. On the one hand, topological superconductors promise manifold applications associated with emerging Majorana bound states. Interesting physical phenomena arise due to the underlying topology such as quantized transport properties (e.g, conductance or charge pumping) or due to the nonlocal nature of the zero-energy fermion formed by two distant Majoranas such as teleportation [Fu 09a] or splitting of Cooper-pairs [Nils 08]. This line of thought that topology gives rise to quantization and nonlocality has been initiated with the quantum Hall effect more than thirty years ago. It has regained impor-

tance with the discovery of topological insulators and recently the prediction of topological superconductors and it is likely to continue with the discovery of exciting new facets such as topological phases protected by crystalline symmetries [Fu 11], induced by external driving [Lind 11], or in interacting topological systems [Fidk 10, Gura 11, Turn 11, Fidk 11, Manm 12].

On the other hand, topological superconductors host Majorana bound states, a manifestation of nonabelian anyons. Miraculously, these exotic particles predicted more than twenty years ago in strongly correlated 2d fractional quantum Hall systems [Moor 91] might finally be realized in weakly correlated 1d superconductors described by a mean field theory. Given this surprising similarity between two very different physical systems first pointed out by Read and Green [Read 00], one may wonder whether even more sophisticated nonabelian anyons realized in other exotic quantum Hall states may also be realized in more mundane systems. Another example for nonabelian anyons in hybrid structures are parafermions occurring on the edge of conventional fractional quantum Hall systems (or equivalently fractional topological insulators) in proximity to an s-wave superconductor [Lind 12, Chen 12, Clar 13, Vaez 13]. Regarding the substantial progress on topological hybrid systems in only a few years and the enormous power of designing hybrid systems that combine all desired properties one may hope for many new and exciting phenomena awaiting discovery.

A. Effective energy splitting and Josephson coupling of Majorana end-states in p-wave superconductor rings

We present here the analytical estimation of the Majorana energy splitting, ϵ_0, and the effective Josephson coupling, Γ, in the Hamiltonian (5.12). For sake of simplicity we will first present our calculation for the effective Josephson coupling Γ, obtained by working in the tight-binding model. We will then describe the calculation of ϵ_0 through an alternative approach working directly in the continuum limit both in both regimes $\mu \ll m\Delta'^2$ and $\mu \gg m\Delta'^2$ discussed in Sec. 5.2.

Effective Josephson coupling. In order to compute the effective Josephson coupling we neglect the effect of the overlap of the two Majorana wavefunctions in the topological part of the ring. We therefore consider the limit of a junction between two half-infinite topological sectors of the wire, the right one on sites $j \in [1, \infty)$ and the left one on $j \in (\infty, -1)$. They are both described by the Hamiltonian (5.1) with paring strength $\Delta_{\rm TB} e^{i\phi_a}$ with $a = L, R$ for the left and right sector, respectively. The hopping between the two sectors from Eq. (5.2) now simply reads $H_{\rm T} = -t'(c^\dagger_{-1}c_1 + c^\dagger_1 c_{-1})$—cf. Fig. A.1.

We include the effect of the tunneling between the two wires perturbatively. The low energy excitations of this model for $t' = 0$ are represented by left and right zero energy Majorana operators [Kita 01]

$$b_R = A\sum_{j=1}^{\infty}(x_+^j - x_-^j)\gamma_{B,j}^{(R)} \tag{A.1}$$

$$b_L = A\sum_{j=-1}^{-\infty}(x_+^{-j} - x_-^{-j})\gamma_{A,j}^{(L)} \tag{A.2}$$

where $x_\pm = (-\mu_{\rm TB} \pm \sqrt{\mu_{\rm TB}^2 - 4t^2 + 4\Delta_{\rm TB}^2})/(2t + 2\Delta_{\rm TB})$, $A = (\sum_j |x_+^j - x_-^j|^2)^{-1/2}$ is a normalization constant, and the operators $\gamma_{A(B),j}$ are defined via $c_J = (\gamma_{B,j}^{(R)} e^{-i\phi_R/2} + i\gamma_{A,j}^{(R)} e^{i\phi_R/2})/2$. The projection of $H_{\rm T}$ onto the subspace spanned by the operators b_R, b_L leads to the effective coupling between the Majorana states. The Hamiltonian can

be rewritten in terms of ordinary fermion operators $d_M = (b_R + ib_L)/2$ to take the form presented in Eq. (5.9) with $\Gamma = t'A^2|x_+ - x_-|^2$. For simplicity, we consider $\mu < 2t\left(1 - \sqrt{1 - \Delta_{\rm TB}^2/t^2}\right)$ which corresponds to the condition $\mu < m\Delta'^2$ in the continuum model (5.3) and ensures that $x_\pm$ are real (see discussion of the continuum model in Sec. 5.2.1). Explicitly one obtains

$$\Gamma = \frac{t'\mu(4t-\mu)\Delta_{\rm TB}}{t(t+\Delta_{\rm TB})^2} \tag{A.3}$$

In the continuum limit, when $\mu \ll \Delta_{\rm TB} \ll t$ the expressions simplifies to

$$\Gamma \approx 4t'\mu\Delta_{\rm TB}/t^2\,. \tag{A.4}$$

Majorana energy splitting. In order to compute the energy splitting ϵ_0 we employ an alternative method working directly in the continuum limit. Similar to before, we neglect here the Majoranas interaction through the Josephson junction. The problem is then completely equivalent to calculating the energy splitting of two Majorana at the end of a wire of length L. We start considering the regime (ii) described by the Hamiltonian in Eq. (5.6), $H = \mu(x)\tau_z + \Delta'(x)p\tau_x$, with the specific choice of parameters (cf. Fig. A.1)

$$\begin{aligned}\mu(x) &= -V_0[\Theta(-x) + \Theta(x-L)] + \mu\Theta(x)\Theta(L-x)\,,\\ \Delta'(x) &= \Delta'\,,\end{aligned} \tag{A.5}$$

where $V_0 > 0$ and $\mu > 0$ guarantee that the wire is in a topological phase in $[0, L]$ and in a nontopological phase otherwise.

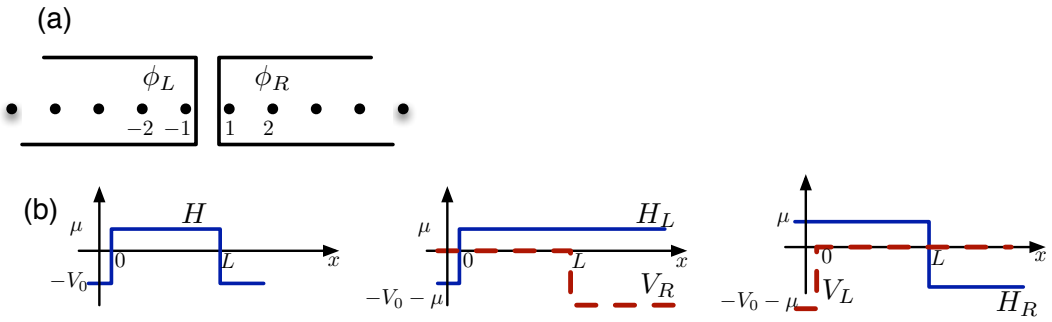

Figure A.1.: (a) Sketch of the Josephson junction between two topological segments of the wire and spatial dependence of the gate potential in the corresponding continuum realization. (b) Spatial dependence of the chemical potential, $\mu(x)$, in the Hamiltonian of the finite length wire and for the approximate Hamiltonians, H_L and H_R, used in the perturbative calculations

We determine the Majorana wavefunctions by a perturbative approach. We first find

the wavefunctions of the Majorana bound state localized at one of the interfaces between the topological and the insulating region, thus fully ignoring the existence of the other Majorana state. We label the corresponding states at the interfaces at $x = 0$ and $x = L$ as $|L\rangle$ and $|R\rangle$ respectively. We then project the Hamiltonian onto the Majorana subspace, to obtain their effective interaction, $H_{\text{overlap}} = \sum_{\alpha,\beta=L,R} \langle\alpha|H|\beta\rangle \ |\alpha\rangle \langle\beta|$. Eventually we will be interested in the limit $V_0 \to \infty$ corresponding to a high insulating barrier outside the wire.

The Majorana state at $x = 0$ is the zero-energy eigenstate of the Hamiltonian H_L, defined again by the same Hamiltonian as in Eq. (5.6), but with the choice of parameters

$$\begin{aligned} \mu(x) &= -V_0\Theta(-x) + \mu\Theta(x)\,, \\ \Delta'(x) &= \Delta'\,, \end{aligned} \tag{A.6}$$

as depicted in Fig. A.1. Solving this equation separately for $x > 0$ and $x < 0$ leads to zero energy states with imaginary momenta. Namely we can write

$$|L\rangle = \mathbf{v}_{-,L} e^{\alpha_0 x}\Theta(-x) + \mathbf{v}_{+,L} e^{-\alpha x}\Theta(x) \tag{A.7}$$

where $\alpha = \mu/|\Delta'|$ is the inverse coherence length in the wire, and $\alpha_0 = V_0/|\Delta'|$. The two-dimensional vectors $\mathbf{v}_{\pm,L}$ are determined by the continuity of the wavefunction and its derivative at the interface and by the wavefunction normalization. They are given by:

$$\mathbf{v}_{+,L} = \mathbf{v}_{-,L} = \sqrt{\frac{\alpha\alpha_0}{\alpha+\alpha_0}} \begin{pmatrix} 1 \\ -i \end{pmatrix}. \tag{A.8}$$

In the limit $V_0 \to \infty$ we are interested in, they reduce to

$$\mathbf{v}_{+,L} = \mathbf{v}_{-,L} = \sqrt{\alpha} \begin{pmatrix} 1 \\ -i \end{pmatrix}. \tag{A.9}$$

In a completely analogous way we can calculate the zero-energy eigenstate of the Hamiltonian H_R defined once more by the Hamiltonian in Eq. (5.6), now with (cf. Fig. A.1)

$$\mu(x) = -V_0\Theta(x-L) + \mu\Theta(L-x)\,, \tag{A.10}$$

$$\Delta'(x) = \Delta'\,. \tag{A.11}$$

In this case the zero-energy eigenstate reads

$$|R\rangle = \sqrt{\frac{\alpha\alpha_0}{\alpha+\alpha_0}} \begin{pmatrix} 1 \\ i \end{pmatrix} \left[e^{-\alpha_0(x-L)}\Theta(x-L) + e^{\alpha(x-L)}\Theta(L-x)\right]. \tag{A.12}$$

In the limit $V_0 \to \infty$ the prefactor reduces to $\sqrt{\alpha}$. Note that the particle-hole superposition has different phases in $|L\rangle$ and $|R\rangle$.

We can then project the full Hamiltonian onto the low-energy subspace spanned by the two Majorana states. In doing so, we conveniently rewrite $H = H_L + V_R = H_R + V_L$, where $V_R = -(V_0 + \mu)\Theta(x - L)\tau_z$ and $V_L = -(V_0 + \mu)\Theta(-x)\tau_z$, and the spatial dependence of the various terms is presented in Fig. A.1 We can then compute, e.g., $\langle L|H|L\rangle = \langle L|H_L|L\rangle + \langle L|V_R|L\rangle = \langle L|V_R|L\rangle$, and all the other matrix elements in a similar way, to get

$$H_{\text{overlap}} = \begin{pmatrix} \langle L|V_R|L\rangle & \langle L|V_L|R\rangle \\ \langle R|V_L|L\rangle & \langle R|V_L|R\rangle \end{pmatrix} = \begin{pmatrix} 0 & -2\mu e^{-\alpha L} \\ -2\mu e^{-\alpha L} & 0 \end{pmatrix} . \tag{A.13}$$

This leads to the energy splitting $\epsilon_0 = 2\mu e^{-\alpha L}$, as reported in Section 5.3.3.

In complete analogy, one can perform the calculation of the energy splitting in the regime $\mu \gg m\Delta'^2$. In this case the appropriate Hamiltonian, H, is that in Eq. (5.3), with the same choice of parameters as in Eq. (A.5). Again we start considering the left interface, looking for zero-energy solutions of the H_L, i.e., the Hamiltonian in Eq. (5.3) with the choice of parameters as in Eq. (A.6). We introduce $a_0 = V_0/(m\Delta'^2) > 0$ and $a = \mu/(m\Delta'^2) > 0$. We can write the solutions as

$$|L\rangle = \sqrt{m\Delta'}\sqrt{\frac{a}{1+2a}} \begin{pmatrix} 1 \\ -i \end{pmatrix} \left[(1+\eta)e^{i\kappa_- x}\Theta(-x) + \left(e^{ik_+ x} + \eta e^{ik_- x}\right)\Theta(x)\right] , \tag{A.14}$$

$$|R\rangle = \sqrt{m\Delta'}\sqrt{\frac{a}{1+2a}} \begin{pmatrix} 1 \\ i \end{pmatrix} \left[\left(e^{-ik_+(x-L)} + \eta e^{-ik_-(x-L)}\right)\Theta(L-x)\right. \tag{A.15}$$

$$\left. + (1+\eta)e^{-i\kappa_- x}\Theta(x-L)\right] , \tag{A.16}$$

where $\kappa_- = -im|\Delta'|(\sqrt{2a_0})$, $k_\pm = m|\Delta'|(\pm\sqrt{2a} + i)$ and $\eta = (\kappa_- - k_+)/(k_- - \kappa_-)$. In all the expressions we are neglecting $\mathcal{O}(\sqrt{a}/\sqrt{a_0}, 1/\sqrt{a_0})$, consistent with the condition $a_0 \gg a \gg 1$, reflecting the limit $V_0 \to \infty$ and the regime under consideration. The matrix elements of the effective Hamiltonian are, in this case, $\langle L|H|L\rangle = \langle R|H|R\rangle = 0$ and $\langle L|H|R\rangle = \langle R|H|L\rangle \equiv -\epsilon_0$, with

$$\epsilon_0 = \Delta'\sqrt{2m\mu}\left[\sin(\sqrt{2m\mu}L) - \sqrt{a/a_0}(\sqrt{2}-1)\cos(\sqrt{2}m\mu)L + \mathcal{O}(\sqrt{a}/a_0^2)\right] . \tag{A.17}$$

B. Proximity-coupled quantum wire in the limit of large spin–orbit coupling

In Sec. 6.3.2, we relied strongly on the statement that in the limit of strong spin–orbit coupling, the quantum-wire model (6.2) reduces at low energies to a combination of the topological-insulator-like low-momentum subspace and a spinless-p-wave-superconductor-like high-momentum subspace. In this appendix, we provide an explicit justification for this statement.

The statement is evident for the low-momentum subspace, so we will not consider it further. For $\mu = 0$, the Fermi points are located at $p = 0$ (low momentum) as well as $p = \pm p_F$ with $p_F = 2mu$ (high momentum). As the spin–orbit coupling (or equivalently, m) increases, p_F becomes large and so does the effective spin–orbit field in the high-momentum subspace. Thus, in this limit, we can first diagonalize the Hamiltonian in the absence of the induced pairing Δ and then treat the latter perturbatively. To do so, we perform the unitary transformation

$$\mathcal{U} = \exp\{i\alpha\sigma_y\tau_z/2\}\exp\{i\theta\sigma_z/2\} \tag{B.1}$$

on the wire Hamiltonian (6.2) with $\Delta = 0$. If we choose α such that $\tan\alpha = B/up$, the rotated Hamiltonian takes the form

$$\mathcal{H}_0 = \left(\frac{\hat{p}^2}{2m} + \sqrt{(up)^2 + B^2}\sigma_z\right)\tau_z. \tag{B.2}$$

The low-energy subspace at $p = \pm p_F$ is formed by the bands for which σ_z takes the value -1. We now reintroduce the pairing term $\Delta\tau_x$ and apply the transformation $\mathcal{U}$ to it. The projection of $\mathcal{H}_0$ onto the lower bands yields

$$\mathcal{H}_{\text{eff}} = \left(\frac{\hat{p}^2}{2m} - \sqrt{(up)^2 + B^2}\right)\tau_z + \frac{up\Delta}{\sqrt{(up)^2 + B^2}}\tau_x. \tag{B.3}$$

The condition $\epsilon_{SO} \gg \Delta$ guarantees that we can neglect the coupling to high-energy degrees of freedom near $\pm p_F$. Linearizing around the Fermi momenta and using $|up| \sim$

$\epsilon_{SO} \gg B$ the effective Hamiltonian takes the form

$$\mathcal{H}_{\text{eff}} = u\left(|p| - p_F\right)\tau_z + \text{sign}(p)\Delta\tau_x. \tag{B.4}$$

This describes a spinless p-wave superconductor.

C. Appendix for Chapter 7

C.1. Some integrals

In the following we evaluate and discuss the integral

$$I = \int \frac{d\mathbf{p}}{(2\pi)^3} \frac{e^{i\mathbf{pr}}}{E - \xi_{\mathbf{p}}\tau_z - \Delta\tau_x}, \tag{C.1}$$

which is used in Secs. 7.3.1 and 7.3.2. Note that we are interested in subgap energies $E < \Delta$. Explicitly inverting the matrix and changing integration variables to ξ_p and $x = \cos\theta_{\mathbf{p}}$ with the polar angle $\theta_{\mathbf{p}}$ measured relative to $\mathbf{r}$, we have

$$I = \frac{\nu_0}{2} \int d\xi_p \int_{-1}^{1} dx e^{iprx} \frac{E + \xi_{\mathbf{p}}\tau_z + \Delta\tau_x}{E^2 - \xi_{\mathbf{p}}^2 - \Delta^2}. \tag{C.2}$$

Here, ν_0 denotes the normal-state density of states per spin direction of the superconductor. Thus, we need to evaluate the integrals

$$I_0 = \frac{\nu_0}{2} \int d\xi_p \int_{-1}^{1} dx \frac{e^{iprx}}{E^2 - \xi_{\mathbf{p}}^2 - \Delta^2}, \tag{C.3}$$

$$I_1 = \frac{\nu_0}{2} \int d\xi_p \int_{-1}^{1} dx \frac{\xi_{\mathbf{p}} e^{iprx}}{E^2 - \xi_{\mathbf{p}}^2 - \Delta^2} \frac{\omega_D^2}{\xi_{\mathbf{p}}^2 + \omega_D^2}. \tag{C.4}$$

Note that we introduced a convergence factor $\omega_D^2/(\xi_{\mathbf{p}}^2 + \omega_D^2)$ into I_1. While the integral I_0 is automatically dominated by the vicinity of the Fermi surface, this is not the case for I_1 in the absence of the convergence factor. In that case, we need to account for the fact that the BCS model underlying the calculations is restricted to energies smaller than the Debye frequency ω_D. We will ultimately restrict attention to $r \gg v_F/\omega_D$. In this limit, we can formally eliminate the cutoff from the result by taking the limit $E_F, \omega_D \to \infty$ while keeping $\omega_D/E_F \ll 1$. Note that an accurate theory for $r \ll v_F/\omega_D$ would require one to develop a more microscopic theory of the underlying superconductor.

To evaluate the integrals, we first perform the integral over $\xi_{\mathbf{p}}$ and subsequently the x-integration. Writing $p = p_F + \xi_{\mathbf{p}}/v_F$, this can be done straightforwardly for I_0 and we

obtain

$$I_0 = -\frac{\pi\nu_0}{\sqrt{\Delta^2 - E^2}} \frac{\sin k_F r}{k_F r} e^{-\sqrt{\Delta^2 - E^2} r/v_F}. \tag{C.5}$$

Similarly, we can evaluate the integral for I_1. Taking the limit described above, we find

$$I_1 = -\pi\nu_0 \frac{\cos k_F r}{k_F r} e^{-\sqrt{\Delta^2 - E^2} r/v_F}. \tag{C.6}$$

More explicitly, the corrections to this result either decay exponentially with r on the scale v_F/ω_D or are suppressed as powers of ω_D/E_F, and thus vanish after taking the limit.

C.2. Momentum-space Bogoliubov-de Gennes Hamiltonian of helical Shiba chains

Here, we sketch the derivation of Eqs. (7.39) and (7.41). Inserting Eq. (7.32) into Eq. (7.37), we readily find Eq. (7.39) with

$$F(k) = -\Delta \mathrm{Im} \sum_{j=1}^{\infty} \frac{1}{k_F a j} e^{-aj/\xi_0} [e^{i(k_F + k)aj} + e^{i(k_F - k)aj}]. \tag{C.7}$$

Here, we have dropped the trivial term involving the Shiba energy ϵ_0 of the individual impurities. The sum over j can be readily performed by the identity

$$-\ln(1 - x) = \sum_{j=1} \frac{x^j}{j}, \tag{C.8}$$

which yields

$$\begin{aligned} F(k) \;=\; & \frac{\Delta}{k_F a} \mathrm{Im} \Big[\ln(1 - e^{-a/\xi_0 + i(k_F + k)a}) \\ & + \ln(1 - e^{-a/\xi_0 + i(k_F - k)a}) \Big]. \end{aligned} \tag{C.9}$$

Finally, we use the identity $\mathrm{Im} \ln z = i \arctan(\mathrm{Im} z / \mathrm{Re} z)$ to obtain the result given above in Eq. (7.40).

Similarly, inserting Eq. (7.33) into Eq. (7.38), we find Eq. (7.41) for Δ_k with

$$f(k) = \sum_{j=1}^{\infty} \frac{e^{-ja/\xi_0}}{j} [e^{ikaj} + e^{-ikaj}]. \tag{C.10}$$

Performing the sum over j using Eq. (C.8) yields Eq. (7.42) of the main text.

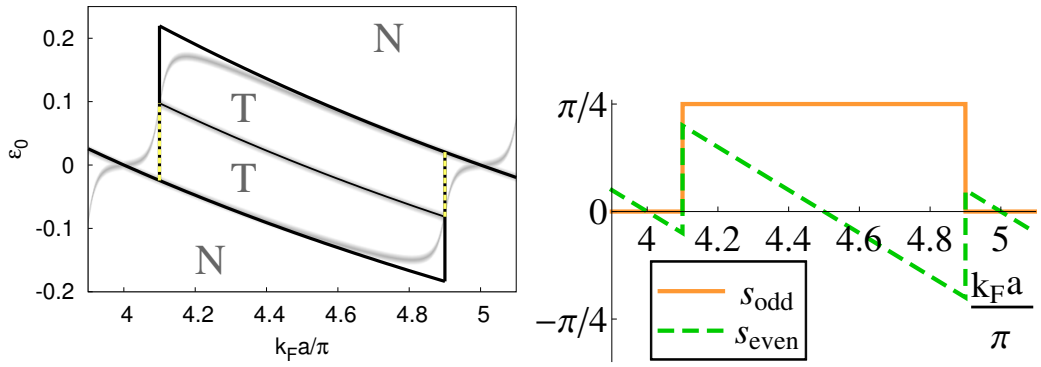

Figure C.1.: Phase diagram from Fig. 7.10(a) of the main text and corresponding cumulative hopping amplitudes across an odd and even number of lattice sites ($\xi_0 = \infty$, $k_h = 0.1\pi/a$): $s_{\mathrm{odd}} = \sum_n \sin[k_F a(2n+1)] \cos[k_h a(2n+1)]/(2n+1)$ and $s_{\mathrm{even}} = \sum_n \sin(2k_F an) \cos(2k_h an)/2n$. While s_{even} is always nonzero except for special points, s_{odd} changes from zero to $\pi/4$ at the transition between two-channel ($k_F < k_h$) and single-channel phase ($k_F > k_h$).

C.3. Origin of the two-channel phase

Roughly speaking, the two-channel phases arises because the even and odd sites of the chain form two independent channels. This can be traced back to the fact that for some ranges of the wavevectors k_F and k_h, hopping across an even number of lattice sites becomes stronger than across an odd number. To make this intuitive understanding more plausible, we consider the lattice Fourier transform $h_{k=0} = \sum_n h_{i,i+n}$ for the wavevector $k = 0$, at which the dispersion changes abruptly when $k_F = k_h$. The contribution to $h_{k=0}$ from hopping an odd number of sites is $\sum_n \sin k_F a(2n+1) \cos k_h a(2n+1)/(2n+1)$. This vanishes in the two-channel phase $k_F < k_h$ and equals $\pi/4$ in the single-channel phase $k_F > k_h$. The sum over all even hopping terms, on the other hand, varies between $-\pi/4$ and $\pi/4$. The cumulative hopping amplitudes for even and odd sites are illustrated in Fig. C.1. Thus, the phase transition occurs because hopping between even and odd sites becomes ineffective for $k_F < k_h$ and the chain effectively decomposes into two channels. This two-channel phase arises as a consequence of the long-range nature of the model. For finite ξ_0, the long-range hopping is cut off by the coherence length and the two-channel phase is restricted to a smaller region of parameter space.

C.4. Exponentially localized Majorana bound state at the Bragg point

We now provide further details of the derivation of Eq. (7.50) of the main text. At the Bragg point $k_F = k_h$, the off-diagonal block of the rotated Hamiltonian given in

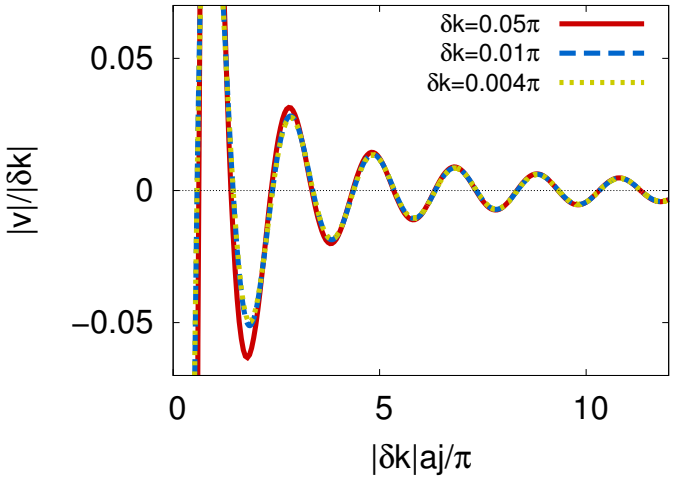

Figure C.2.: Scaling behavior of the Majorana wavefunction for $\delta k > 0$. In the limit $\delta k \to 0$ the slowly decaying tail $\delta k \delta v$ only depends on the scaled position variable $y_j = \delta k a j$. Due to the scaled axes all curves collapse. Note that the exponentially decaying zeroth-order term v_0 only dominates on the first few sites, which cannot be resolved in this graph. Similar results are obtained for $\delta k < 0$. The parameters used for numerical calculations in this appendix are all chosen as in Fig. 7.11 of the main text.

Eq. (7.49) reads

$$(\mathcal{H}_{12})_{ij} = \begin{cases} -\frac{i\Delta}{k_F a} e^{-(j-i)a/\xi_0} \frac{\sin[2k_F a(j-i)]}{j-i} & j > i, \\ i\epsilon_0 & j = i, \\ 0 & j < i. \end{cases} \tag{C.11}$$

Thus $\mathcal{H}_{12}$ is triangular and constant along the diagonals. In order to find Majorana end states we seek a solution of $\mathcal{H}_{12} v = 0$ which gives the set of equations

$$0 = \sum_{j=1}^{\infty} (\mathcal{H}_{12})_{ij} v_j \tag{C.12}$$

$$= i\epsilon_0 v_i - \frac{i\Delta}{k_F a} \sum_{j=i}^{\infty} e^{-(j-i)a/\xi_0} \frac{\sin 2k_F a(j-i)}{j-i} v_j. \tag{C.13}$$

Using the ansatz $v_j = \beta^j$ all of these equations reduce to the same condition

$$i\epsilon_0 = \frac{i\Delta}{k_F a} \sum_{j=1}^{\infty} e^{-ja/\xi_0} \frac{\sin(2k_F a j)}{j} \beta^j. \tag{C.14}$$

We can rewrite this as

$$i\epsilon_0 = \frac{\Delta}{2k_F a}\sum_{j=1}^{\infty}\left[\frac{(\beta e^{-a/\xi_0+i2k_F a})^j}{j} - \text{c.c.}\right] \tag{C.15}$$

and using the identity $\sum_{j=1}^{\infty} x^j/j = -\ln(1-x)$ we obtain

$$i\epsilon_0 = \frac{\Delta}{2k_F a}\ln\left[\frac{1-\beta e^{-a/\xi_0+i2k_F a}}{1-\beta e^{-a/\xi_0-i2k_F a}}\right] \tag{C.16}$$

$$= \frac{i\Delta}{k_F a}\arctan\frac{\beta e^{-a/\xi_0}\sin(2k_F a)}{1-\beta e^{-a/\xi_0}\cos(2k_F a)}. \tag{C.17}$$

Rearranging this as

$$\begin{aligned}&\beta e^{-a/\xi_0}[\sin(2k_F a)\cos\frac{k_F a\epsilon_0}{\Delta} + \cos(2k_F a)\sin\frac{k_F a\epsilon_0}{\Delta}]\\ &= \sin\frac{k_F a\epsilon_0}{\Delta},\end{aligned} \tag{C.18}$$

and solving for β finally yields Eq. (7.50).

C.5. Analytical solution near the Bragg point for $\xi_0 \to \infty$

Here we derive the corrections to the exponential Majorana wavefunction in the limit $\xi_0 \to \infty$ when tuning slightly away from the phase transition at $\delta k = 0$. To this end we expand the eigenproblem in $|\delta k|$ and construct a continuum limit in which the matrix equations for the wavefunction transform into integral equations that can be solved by standard methods. We present the solution for the more involved case $\delta k < 0$ (non-topological side). The calculation for the topological side $\delta k > 0$ is contained in the derivation presented here and can be obtained by simply setting u and ϵ in Eq. (C.19) to zero. On the nontopological side, there are two degenerate subgap states which exist at a finite energy. The eigenproblem reads

$$\begin{pmatrix} 0 & M+\delta M \\ M^\dagger + \delta M^\dagger & 0 \end{pmatrix}\begin{pmatrix} u \\ v \end{pmatrix} = \epsilon\begin{pmatrix} u \\ v \end{pmatrix} \tag{C.19}$$

with

$$M_{i,j} = \begin{cases} \frac{-i\Delta}{k_F a} \frac{\sin[Ka(j-i)]}{j-i} & j > i \\ i\epsilon_0 & j = i \\ 0 & j < i \end{cases} \tag{C.20}$$

$$\delta M_{i,j} = \begin{cases} 0 & j \geq i \\ \frac{-i\Delta}{k_F a} \frac{\sin[\delta k a(i-j)]}{i-j} & j < i \end{cases}. \tag{C.21}$$

and $K = 2k_F + \delta k$. The two degenerate subgap states are localized at opposite ends of the chain by an appropriate choice of basis. For definiteness we consider the Nambu spinor (u, v) to be localized at the left end and solve the eigenproblem for a semi-infinite chain. We start by expanding v to first order in $|\delta k|$,

$$v = v_0 + |\delta k| \delta v. \tag{C.22}$$

As detailed in Sec. 7.6.2 we find that in the limit $\delta k \to 0$ with $y_j = \text{const}$, the correction δv depends only on the scaled position variable $y_j = |\delta k| a j$. In this limit, the position variable becomes continuous $y_j \to y$ and the matrix equations (C.19) transforms into integral equations. The expansion and the scaling behavior of δv is corroborated by numerical results in Fig. C.2.

We can now obtain the scaling of the energy ϵ with δk by eliminating u from Eq. (C.19),

$$(M^\dagger + \delta M^\dagger)(M + \delta M) v = \epsilon^2 v. \tag{C.23}$$

As $\epsilon \to 0$ with $\delta k \to 0^-$ (which is supported by numerics in Fig. 7.11(a) of the main text), we obtain $M v_0 = 0$ in zeroth order, which is the eigenproblem at the Bragg point, i.e.,

$$v_{0,j} = \mathcal{N}_1 \beta^j, \tag{C.24}$$

with a normalization constant $\mathcal{N}_1$ and β given by Eq. (7.50). Normalization readily yields $\mathcal{N}_1 = (1 - \beta^2)^{1/2}/|\beta|$ for $\delta k > 0$. When $\delta k < 0$, the hole component u also enters into the normalization condition and we will determine $\mathcal{N}_1$ later.

From the next order in Eq. (C.23), we find that the energy scales as $\epsilon = \rho\sqrt{|\delta k|}$ with some constant ρ. This result is consistent with the numerical results in Fig. 7.11(a) of the main text. Since v_0 corresponds to the single solution at the Bragg point, u cannot have a zero-order term. In fact, due the $\sqrt{|\delta k|}$-dependence of ϵ, we have to expand $u = |\delta k|^{1/2} u_0 + O(|\delta k|^{3/2})$. Also u_0 is a function of y_i if we ignore terms at the very end of the chain where v_0 is dominating. The scaling $|\delta k|^{1/2} u(|\delta k| a i)$ is confirmed by

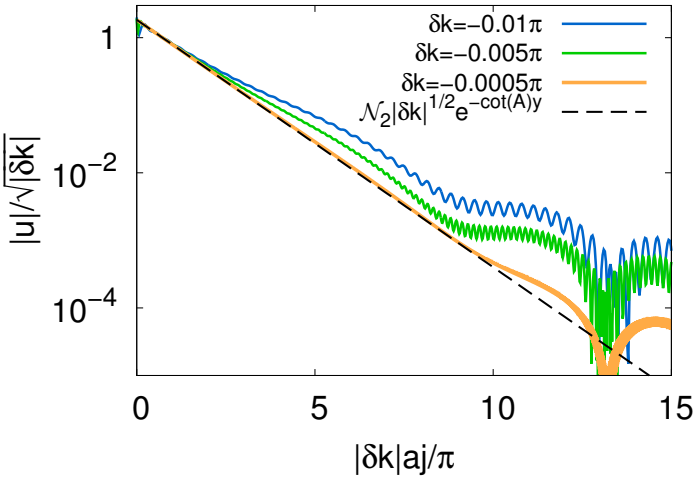

Figure C.3.: Nambu component u for various $\delta k < 0$. In the limit $\delta k \to 0$ the dominating contribution near the end of the chain is an exponential function which is well-described by our analytical solution (dashed line) given in Eq. (C.31). The results also show the scaling $|\delta k|^{1/2} u_0(|\delta k| aj)$. Further inside the chain u has a slowly decaying tail of order $|\delta k|^{3/2}$, which can be described by a similar power-law decay as δv. Since the tail of u is higher-order term we do not consider it further.

numerics as shown in Fig. C.3.

The next order $\sim |\delta k|^{1/2}$ of Eq. (C.19) is given by

$$|\delta k|^{1/2} \left(M^\dagger u_0 + \delta M^\dagger u_0 - \rho v_0 \right) = 0. \tag{C.25}$$

As mentioned above we ignore boundary terms of u_0 since they are of subleading order in $|\delta k|$. Hence we omit the last term $\sim v_0$ in the previous equation and take the limit $|\delta k| \to 0$ with $y_i = \text{const.}$ of the remaining terms by introducing the continuous position variable $y_i \to y$. This yields

$$\begin{aligned} [(M^\dagger + \delta M^\dagger) u_0]_i = &- \frac{i\Delta}{k_F a} \sum_{j=1}^{i-1} \frac{\sin[Ka(i-j)]}{i-j} u_0(y_j) \\ &+ i\epsilon_0 u_0(y_i) - \frac{i\Delta}{k_F a} \sum_{j=i+1}^{\infty} \frac{\sin[\delta k a(j-i)]}{j-i} u_0(y_j) = 0. \end{aligned} \tag{C.26}$$

The first sum can be rewritten as

$$\sum_{j=1}^{i-1} \frac{\sin(Kaj)}{j} u_0(y_i - y_j). \tag{C.27}$$

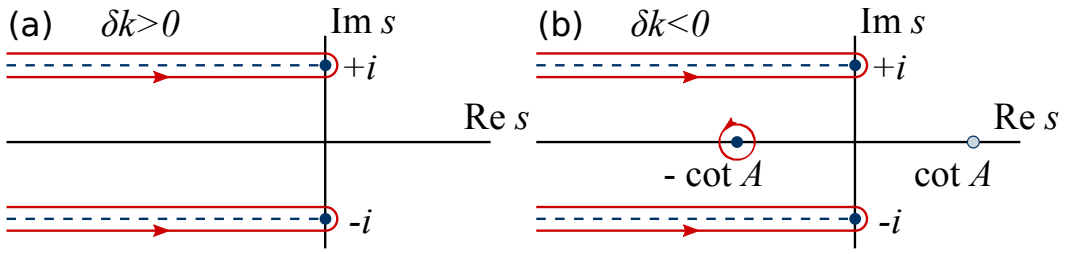

Figure C.4.: Branch cuts (dashed lines) and poles (dots) of the inverse Laplace transform for (a) positive δk and (b) negative δk. By writing $\operatorname{arccot} s = (1/2i)\ln(1+s)/(1-s)$ we have chosen the branch cuts along $s = \pm i - \sigma$ with $\sigma \in [0, \infty)$. With this choice there are no poles for $\delta k > 0$ (and $\rho = 0$). In the case $\delta k < 0$ there is a pole at $-\cot A < 0$. The pole in the positive real half plane at $+\cot A$ is regularized by a suitable choice of coefficients $\mathcal{N}_{1/2}$. The red lines with arrows denote the contour of integration in the inverse Laplace transform (C.39).

When $|\delta k|$ is small, $u_0(y_i - y_j)$ becomes a slowly varying function and the sum is dominated by the decay $\sin(Kj)/j$, i.e., only terms with $j \lesssim O(1/K)$ are relevant. Thus in the limit $\delta k \to 0$, $i \to \infty$ with $y_i = \text{const.}$ we can set $y_j \to 0$ and obtain

$$\sum_{j=1}^{i-1} \frac{\sin[Ka(i-j)]}{i-j} u_0(y_j) \to u_0(y) \sum_{j=1}^{\infty} \frac{\sin(Kj)}{j} \tag{C.28}$$

$$= u_0(y) \arctan\cot(K/2). \tag{C.29}$$

The other terms have a straightforward continuum limit and we obtain

$$A u_0(y) + \operatorname{sgn}(\delta k) \int_y^{\infty} dz \frac{\sin(z-y)}{z-y} u_0(z) = 0, \tag{C.30}$$

where $A = \arctan\cot(K/2) - k_F a \epsilon_0/\Delta$ as in Sec. 7.6.2. The solution of this homogeneous integral equation for $\delta k < 0$ is given by [Poly 12]

$$u_0(y) = \mathcal{N}_2 e^{-\cot(A) y}, \tag{C.31}$$

where the normalization factor $\mathcal{N}_2$ will be determined below. This result agrees well with a numerical solution of the tight-binding BdG Hamiltonian in the limit $\delta k \to 0$, as shown in Fig. C.3.

Finally we consider all terms in Eq. (C.19) which are linear in δk. This yields

$$\delta M v + |\delta k| M \delta v + |\delta k| \delta M \delta v = |\delta k| \rho u_0, \tag{C.32}$$

for which we evaluate each term separately. The first term becomes

$$(\delta M v)_i = \frac{i\Delta}{k_F a} \sum_{j=1}^{i-1} \frac{\sin[\delta k(i-j)]}{i-j} \mathcal{N}_1 \beta^j. \tag{C.33}$$

The sum is dominated by the first few terms due to the exponential decay β^j and since $i \to \infty$, we can safely set $i - j \to i$. Thus, the continuum limit yields

$$(\delta M v)_i \to \delta k \frac{i\Delta}{k_F} \mathcal{N}_1 \frac{\beta}{1-\beta} \frac{\sin y}{y}. \tag{C.34}$$

The continuum limit of the second and third term can be obtained in a similar manner as for Eq. (C.26),

$$(M \delta v)_i \to \frac{i\Delta}{k_F a} A \delta v(y) \tag{C.35}$$

$$(\delta M \delta v)_i \to \operatorname{sgn} \delta k \frac{i\Delta}{k_F a} \int_0^y dz \frac{\sin(y-z)}{y-z} \delta v(z). \tag{C.36}$$

Thus, we ultimately obtain the integral equation

$$\begin{aligned} &A\delta v(y) + \operatorname{sgn}(\delta k) \int_0^y dz \frac{\sin(y-z)}{y-z} \delta v(z) \\ &= -\frac{i\mathcal{N}_2 \rho k_F a}{\Delta} e^{-\cot(A) y} - \operatorname{sgn} \delta k \mathcal{N}_1 a \frac{\beta}{1-\beta} \frac{\sin y}{y}. \end{aligned} \tag{C.37}$$

For the case $\delta k > 0$ and with $\rho = 0$, this equation reduces to Eq. (7.52) of the main text. For both signs of δk, this integral equation (C.37) can be solved by Laplace transformation. Using $\mathcal{L}[e^{-\lambda y}] = 1/(s+\lambda)$ and $\mathcal{L}[\sin y/y] = \operatorname{arccot} s$ we find the solution of the integral equation to be

$$\begin{aligned} \delta v(y) = \mathcal{L}^{-1} \Bigg[&\frac{-1}{A + \operatorname{sgn} \delta k \operatorname{arccot} s} \\ &\left(\operatorname{sgn} \delta k \frac{\mathcal{N}_1 a \beta}{1-\beta} \operatorname{arccot} s + \frac{i\mathcal{N}_2 \rho k_F a}{\Delta} \frac{1}{s + \cot A} \right) \Bigg]. \end{aligned} \tag{C.38}$$

The inverse Laplace transform is defined as

$$\mathcal{L}^{-1} f(s) = \frac{1}{2\pi i} \int_{\lambda - i\infty}^{\lambda + i\infty} e^{sy} ds f(s), \tag{C.39}$$

where λ is a real number exceeding the real part of all singularities of f. For $\delta k > 0$, all branch cuts and poles of the Laplace transform in Eq. (C.38) can be chosen to lie in the negative real half plane (see Fig. C.4) and thus the weight e^{sy} is decaying for all $y > 0$. In contrast for $\delta k < 0$ the Laplace transform has a pole in the positive real half plane at

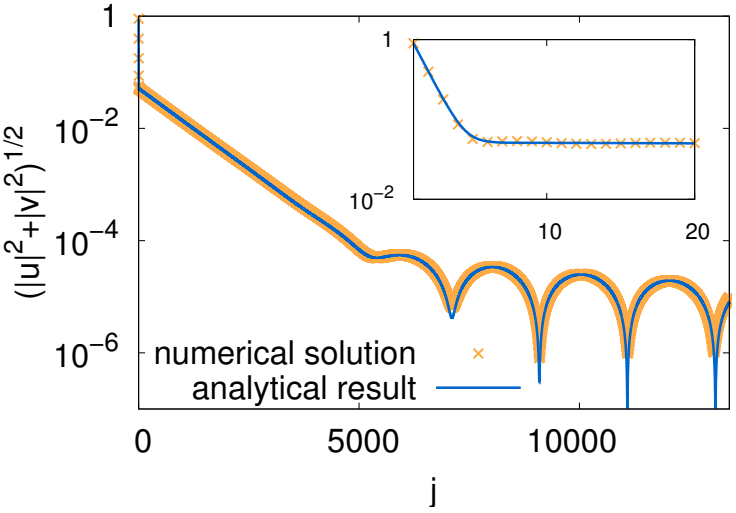

Figure C.5.: Wavefunction modulus $(|u|^2+|v|^2)^{1/2}$ in the nontopological phase ($\delta k<0$) exhibiting a two-exponential decay with a power-law tail. The numerical results from exact diagonalization of the tight-binding BdG Hamiltonian (orange crosses) agree well with the analytical solution $\left(\left|v_0+|\delta k|\delta v\right|^2+|\delta k|\cdot|u_0|^2\right)^{1/2}$ (blue line), where we obtained δv from the inverse Laplace transform (C.38) by numerically integrating along the branch cuts in Fig. C.4(b). For the plot we have chosen $\delta k=-5\times10^{-4}\pi$.

$s_p=\cot A$, which gives rise to an exponentially growing solution in $\delta v(y)$. In order for the wavefunction to be localized at the left end of the chain, we thus have to fix the ratio $\mathcal{N}_1/\mathcal{N}_2$ in a way that regularizes the Laplace transform at s_p, i.e.,

$$\frac{\mathcal{N}_2}{\mathcal{N}_1}=-2iA\cot A\frac{\Delta}{\rho k_F}\frac{\beta}{1-\beta} \tag{C.40}$$

for which the numerator in (C.38) vanishes at s_p. Thus by choosing a proper basis in the degenerate subspace, we have ensured that the wavefunction is localized at the left end. The coefficients $\mathcal{N}_{1/2}$ are now readily determined in terms of ρ from the overall normalization of the wavefunction $\sum_i(|v_{0,i}|^2+|u_{0,i}|^2)=1$ which is true in the limit $\delta k\to0$.

Finally we obtain $\delta v(x)$ from the inverse Laplace transform by integrating along the contour shown in Fig. C.4. The integral can be solved by expanding in $y\gg1$,

$$\delta v(y)\to\begin{cases}4aA\operatorname{sgn}\beta\sqrt{\dfrac{1+\beta}{1-\beta}}\dfrac{\sin y}{y\ln^2 y}, & \delta k>0\\[2ex] 4aA\mathcal{N}_1\dfrac{\beta}{1-\beta}\dfrac{\sin(y+2A)}{y\ln^2 y}, & \delta k<0\end{cases} \tag{C.41}$$

and neglecting terms of order $1/y\ln^3 y$.

In summary, we have found analytical expressions for the Nambu wavefunction of the subgap states close to the phase transition. For $\delta k < 0$, the bound state at one end of the chain has the form

$$\psi_i = \begin{pmatrix} \sqrt{|\delta k|} u_0 \left(i|\delta k|\right) \\ v_{0,i} + |\delta k| \delta v(i|\delta k|) \end{pmatrix} \tag{C.42}$$

which comprises the leading order terms in $|\delta k|$ for all sites. On the first few sites, ψ decays exponentially, then crosses over to a much slower exponential decay with amplitude $O(\sqrt{|\delta k|})$ and a decay length $O(1/|\delta k|)$. Further inside the chain the wavefunction decays as a power law with logarithmic corrections. For $\delta k > 0$, the wavefunction has a similar form with $u_0 = 0$.

In Fig. C.5 we compare the analytical solution to the tight-binding wavefunction obtained by exact diagonalization and find excellent agreement.

C.6. Localization of Majorana bound states for finite ξ_0

In this section, we briefly discuss in general how the localization of Majorana bound states is affected by a large but finite coherence length ξ_0 that limits the range of the hopping and pairing terms. In this case, the topological phase transition is shifted away from the Bragg point [see gray line in Fig. 7.10(a) of the main text], but Majorana bound states that are exponentially localized on short scales persist as long the Bragg point is inside the topological phase. In the dispersions h_k shown in the insets of Fig. 7.10(b) and (c) of the main text, a finite ξ_0 smoothens the steps on the scale $1/\xi_0$. As a consequence the gap closes continuously as a function of k_F in the immediate vicinity of the critical point and we can define an induced coherence length ξ_{ind} that diverges at the phase transition. Deep in the topological phase $\xi_{\mathrm{ind}} \sim \xi_0$ (see Sec. 7.5.1 for details). Thus a finite coherence length does not change the decay properties of Majorana bound states on scales shorter than ξ_0, i.e., both the exponential decay with a localization length comparable to the lattice spacing and the power-law tail persist. However, at larger distances the decay becomes exponential again on the scale of the induced coherence length, $\sim \exp(-ja/\xi_{\mathrm{ind}})$.

Right at the Bragg point, the tail is always eliminated by destructive Bragg interference and only the short exponential decay survives. Since finite ξ_0 reduces the extent of the Shiba wavefunction, this interference becomes less effective and the localization length increases compared to $\xi_0 = \infty$ [cf. inset of Fig. 7.11(b) of the main text]. In the vicinity of the Bragg point, the wavefunction acquires a small-amplitude tail as discussed in the previous paragraph, independent of the sign of δk. Since the power-law

tail $\sim 1/y \ln^2 y$ sets in only at rather large y, the tail is often completely dominated by the slow exponential $\sim \exp(-ja/\xi_{\mathrm{ind}})$.

D. Derivation of the Shiba peak height in the differential tunneling conductance for a superconducting tip

D.1. Derivation of the current formula

In this appendix we derive the formula for the tunneling current between a superconducting tip and a superconducting sample with a magnetic impurity given in Eqs. (8.1) an (8.2). We apply the nonequilibrium Green's function method used in [Cuev 96]. The system is described by the Hamiltonian $\hat{H} = \hat{H}_L + \hat{H}_R + \hat{H}_T$, where the three parts describe the tip, the substrate and the tunnel coupling. The superconducting tip is described by the BCS Hamiltonian

$$\hat{H}_L = \int \frac{d\mathbf{k}}{(2\pi)^3} \left[\sum_\sigma \xi_k \hat{c}^\dagger_{L,\mathbf{k}\sigma} \hat{c}_{L,\mathbf{k}\sigma} + (\Delta \hat{c}^\dagger_{L,\mathbf{k}\uparrow} \hat{c}^\dagger_{L,-\mathbf{k}\downarrow} + \text{h.c.}) \right], \tag{D.1}$$

where $\xi_k = k^2/2m - \mu$, μ is the chemical potential, Δ the superconducting gap, and $c_{L,\mathbf{k}\sigma}$ annihilates an electron with momentum $\mathbf{k}$ and spin σ. The Hamiltonian of the sample additionally contains a magnetic impurity at the origin with spin vector $\mathbf{S}$ and exchange coupling J

$$\hat{H}_R = \hat{H}_L - J\mathbf{S}(\hat{c}^\dagger_{R,\uparrow}, \hat{c}^\dagger_{R,\downarrow}) \boldsymbol{\sigma} \begin{pmatrix} \hat{c}_{R,\uparrow} \\ \hat{c}_{R,\downarrow} \end{pmatrix}, \tag{D.2}$$

where the operator $\hat{c}_{R,\sigma} = \int d\mathbf{k} \hat{c}_{R,\mathbf{k}\sigma}/(2\pi)^3$ annihilates an electron with spin σ at the origin of the sample and $\boldsymbol{\sigma}$ is the vector of Pauli matrices. One can always choose a gauge such that the superconducting order parameters in tip and sample are real. The superconducting phase difference $\phi(\tau)$ then enters the tunneling Hamiltonian

$$\hat{H}_T(\tau) = \sum_\sigma \left[t e^{i\phi(\tau)/2} \hat{c}^\dagger_{L\sigma}(\tau) \hat{c}_{R\sigma}(\tau) + t^* e^{-i\phi(\tau)/2} \hat{c}^\dagger_{R\sigma}(\tau) \hat{c}_{L\sigma}(\tau) \right], \tag{D.3}$$

where τ is the time argument and t the hopping strength. Note that we have assumed that the sample is contacted at the impurity location. The time-dependent phase dif-

ference between the tip and the sample $\phi(\tau) = \phi_0 + 2eV\tau$ depends on the voltage V applied to the junction. The current operator is obtained from the Heisenberg equation of motion $\hat{I} = -e\dot{\hat{N}}_L = ie[\hat{N}_L, \hat{H}_T]$, where $\hat{N}_L$ is the density operator in the tip. Then the current operator can be written as

$$\hat{I}(\tau) = ie \sum_{\sigma} \left[te^{i\phi(\tau)/2} \hat{c}^{\dagger}_{L\sigma}(\tau)\hat{c}_{R\sigma}(\tau) - t^* e^{-i\phi(\tau)/2} \hat{c}^{\dagger}_{R\sigma}(\tau)\hat{c}_{L\sigma}(\tau) \right]. \tag{D.4}$$

Taking the expectation value yields the current

$$I(\tau) = e \,\mathrm{Tr} \left\{ \tau_z \left[\hat{t}(\tau) G^{<}_{RL}(\tau,\tau) - G^{<}_{LR}(\tau,\tau)\hat{t}^{\dagger}(\tau) \right] \right\} \tag{D.5}$$

where we introduced the lesser Green's function $G^{<}_{\alpha\beta}(\tau_1,\tau_2) = i\langle \Psi^{\dagger}_{\beta}(\tau_2)\Psi_{\alpha}(\tau_1)\rangle$, in which $\Psi_\alpha(\tau)$ with $\alpha = L, R$ are the Nambu spinors in the two superconductors and τ_z is a Pauli matrix acting in Nambu space. The hopping matrix is defined by

$$\hat{t}(\tau) = \begin{pmatrix} te^{i\phi(\tau)/2} & 0 \\ 0 & -t^* e^{-i\phi(\tau)/2} \end{pmatrix}. \tag{D.6}$$

Since $\phi(\tau) = \phi(\tau + \frac{\pi}{eV})$, $\hat{I}$ and $\hat{H}$ are periodic functions of τ with period $2\pi/\omega_0$, where we introduced $\omega_0 = eV$. Thus the current can be expanded in a Fourier series

$$I(\tau) = \sum_m I_m e^{im\omega_0\tau}. \tag{D.7}$$

The nonequilibrium Green's functions have a generalized Fourier expansion

$$G(\tau_1,\tau_2) = \frac{1}{2\pi} \sum_n \int d\omega \, e^{-i\omega\tau_1} e^{i(\omega+n\omega_0)\tau_2} G(\omega, \omega + n\omega_0). \tag{D.8}$$

introducing Floquet indices n. We adopt the notation $G_{nm}(\omega) = G(\omega + n\omega_0, \omega + m\omega_0)$ for which the relation $G_{nm}(\omega) = G_{n-m,0}(\omega + m\omega_0)$ holds. The hopping matrix can be expanded as

$$\hat{t}(\tau) = \hat{t}_{01}e^{i\omega_0\tau} + \hat{t}_{10}e^{-i\omega_0\tau} = \begin{pmatrix} 1 & 0 \\ 0 & 0 \end{pmatrix} te^{i\omega_0\tau} - \begin{pmatrix} 0 & 0 \\ 0 & 1 \end{pmatrix} t^* e^{-i\omega_0\tau} \tag{D.9}$$

Hence the dc current

$$I_0 = \frac{e}{h} \int d\omega \ \mathrm{Tr} \left[\hat{\tau}_z \left(\hat{t}_{01} G^{<}_{RL,10} + \hat{t}_{0,-1} G^{<}_{RL,-1,0} - G^{<}_{LR,01}\hat{t}^{\dagger}_{10} - G_{LR,0,-1}\hat{t}^{\dagger}_{-1,0} \right) \right] \tag{D.10}$$

$$= \frac{e}{h} \int d\omega \ \left[tG^{<,ee}_{RL,10} + t^* G^{<,hh}_{RL,-1,0} - t^* G^{<,ee}_{LR,01} - tG^{<,hh}_{LR,0,-1} \right], \tag{D.11}$$

where the trace is taken in both Nambu space and Floquet space. Using the Langreth rule [Haug 08] yields

$$G^{<}_{RL} = G^{r}_{R}\hat{t}^{\dagger}g^{<}_{L} + G^{<}_{R}\hat{t}^{\dagger}g^{a}_{L}, \tag{D.12}$$

$$G^{<}_{LR} = g^{r}_{L}\hat{t}G^{<}_{R} + g^{<}_{L}\hat{t}G^{a}_{R}. \tag{D.13}$$

We do not consider multiple Andreev reflection processes and therefore neglect Andreev reflection in the superconducting tip, i.e. $g^{eh}_{L} = g^{he}_{L} = 0$. Importantly, we retain Andreev reflections in the sample as they may be resonantly enhanced due to the presence of Shiba bound states in the gap. We can now write the offdiagonal components of the Green's functions in Floquet space in terms of the diagonal components

$$G^{<,ee}_{RL,10} \simeq G^{r,ee}_{R,11}\hat{t}^{\dagger}_{10}g^{<ee}_{L,00} + G^{<,ee}_{R,11}\hat{t}^{\dagger}_{10}g^{a,ee}_{L,00}, \tag{D.14}$$

$$G^{<,hh}_{RL,-1,0} \simeq G^{r,hh}_{R,-1,-1}\hat{t}^{\dagger}_{-1,0}g^{<,hh}_{L,00} + G^{<,hh}_{R,-1,-1}\hat{t}^{\dagger}_{-1,0}g^{a,hh}_{L,00}, \tag{D.15}$$

$$G^{<,ee}_{LR,01} \simeq g^{r,ee}_{L,00}\hat{t}_{01}G^{<,ee}_{R,11} + \hat{g}^{<,ee}_{L,00}\hat{t}_{01}G^{a,ee}_{R,11}, \tag{D.16}$$

$$G^{<,hh}_{LR,0,-1} \simeq g^{r,hh}_{L,00}\hat{t}_{0,-1}G^{<,hh}_{R,-1,-1} + g^{<,hh}_{L,00}\hat{t}_{0,-1}G^{a,hh}_{R,-1,-1}. \tag{D.17}$$

Writing $G(\omega + neV) \equiv G_{nn}(\omega)$, and $g_L \equiv g^{ee}_{L} = g^{hh}_{L}$, we obtain for the current

$$I = \frac{e}{h}\int d\omega \left[tG^{<,ee}_{RL,10} + t^{*}G^{<,hh}_{RL,-1,0} - t^{*}G^{<,ee}_{LR,01} - tG^{<,hh}_{LR,0,-1}\right] \tag{D.18}$$

$$= \frac{e}{h}|t|^{2}\int d\omega$$

$$\left\{\left[G^{r,ee}_{R}(\omega+eV) - G^{a,ee}_{R}(\omega+eV)\right]g^{<}_{L}(\omega) + G^{<,ee}_{R}(\omega+eV)\left[g^{a}_{L}(\omega) - g^{r}_{L}(\omega)\right]\right. \tag{D.19}$$

$$\left. - \left[G^{r,hh}_{R}(\omega-eV) - G^{a,hh}_{R}(\omega-eV)\right]g^{<}_{L}(\omega) - G^{<,hh}_{R}(\omega-eV)\left[g^{a}_{L}(\omega) - g^{r}_{L}(\omega)\right]\right\}. \tag{D.20}$$

By using the relation $G^{<} - G^{>} = G^{a} - G^{r}$, we arrive at the current

$$I = \frac{e}{h}|t|^{2}\int d\omega \left\{G^{>ee}_{R}(\omega)g^{<}_{L}(\omega - eV) - G^{<ee}_{R}(\omega)g^{>}_{L}(\omega - eV)\right\}$$

$$- \frac{e}{h}|t|^{2}\int d\omega \left\{G^{>hh}_{R}(\omega)g^{<}_{L}(\omega + eV) - G^{<hh}_{R}(\omega)g^{>}_{L}(\omega + eV)\right\}. \tag{D.21}$$

To determine the Green's function of the sample G_R we first neglect the tunnel coupling to the tip. Without the magnetic impurity, the Green's function of a BCS superconductor in Nambu space evaluated at the origin is

$$g_{R0}(\omega) = -\frac{\pi\nu_0}{\sqrt{\Delta^2 - \omega^2}}\begin{pmatrix} \omega & \Delta \\ \Delta & \omega \end{pmatrix}. \tag{D.22}$$

We can include coupling to the impurity spin in Eq. (D.2) by means of the Dyson equation $g_R^{-1} = g_{R0}^{-1} + JS$, and obtain for the Green's function of the superconductor with impurity

$$g_R(\omega) = \frac{\pi\nu_0\sqrt{\Delta^2-\omega^2}}{(\omega+\alpha\sqrt{\Delta^2-\omega^2})^2-\Delta^2}\begin{pmatrix} \omega+\alpha\sqrt{\Delta^2-\omega^2} & \Delta \\ \Delta & \omega+\alpha\sqrt{\Delta^2-\omega^2}\end{pmatrix} \tag{D.23}$$

where $\alpha = JS\pi\nu_0 > 0$. The pole of the g_R gives the energy of the Shiba state $\epsilon_0/\Delta = (1-\alpha^2)/(1+\alpha^2)$. To calculate the tunneling into Shiba state, we only need to consider ω close to ϵ_0, where the Green's function has approximately the form

$$g_R(\omega) \equiv g_s(\omega) = \frac{1}{\omega-\epsilon_0}\begin{pmatrix} u^2 & uv \\ uv & v^2\end{pmatrix} \tag{D.24}$$

where u and v are electron and hole component of the Shiba state. Note that in general $u \neq v$ when potential scattering at the impurity is included. Coupling the Shiba state to the tip gives rise to the self energy $\Sigma_R = \hat{t}^\dagger g_L \hat{t}$. We write the retarded and advanced Shiba Green's function as

$$G_s^{r,a} = \frac{1}{(\omega-\epsilon_0)\mp i\Gamma}\begin{pmatrix} u^2 & uv \\ uv & v^2\end{pmatrix} \tag{D.25}$$

where $2i\Gamma = \Sigma^< - \Sigma^> = \Sigma^a - \Sigma^r$ defines the relaxation rate of the Shiba state (we neglect the shift of the resonance energy due to the self-energy). For a steady state, we obtain the relation [Haug 08]

$$G_s^{<,>} = G_s^r\Sigma^{<,>}G_s^a = \frac{-i\Sigma^{<,>}}{2\Gamma}(G_s^a - G_s^r) = \frac{\Sigma^{<,>}}{(\omega-\epsilon_0)^2+\Gamma^2} \tag{D.26}$$

and the Keldysh self energies are given by

$$\Sigma^< = 2i(\Gamma_e n_F(\omega_-) + \Gamma_h n_F(\omega_+) + \Gamma_2) \tag{D.27}$$

$$\Sigma^> = -2i(\Gamma_e(1-n_F(\omega_-)) + \Gamma_h(1-n_F(\omega_+)) + \Gamma_1) \tag{D.28}$$

where $\omega_\pm = \omega \pm eV$, $n_F(\omega) = [1+\exp(\omega/T)]^{-1}$ is the Fermi distribution, and $\Gamma = \Gamma_e + \Gamma_h + \Gamma_1 + \Gamma_2$. The tunneling rates Γ_e and Γ_h of electron and hole components are obtained from the self energy Σ_s in our model

$$\Gamma_e(\omega) = \pi t^2 u^2 \rho(\omega - eV) \tag{D.29}$$

$$\Gamma_h(\omega) = \pi t^2 v^2 \rho(\omega + eV) \tag{D.30}$$

where $\rho(\omega)$ is the density of state of the superconducting tip. Γ_1 and Γ_2 are rates for

quasiparticle transitions in the substrate that empty or occupy the Shiba state.

In fact, $\Sigma^<$ and $\Sigma^>$ can be interpreted as the self energies due to particles being scattered into the state and out of the state respectively. Denote $f = -i\Sigma^</2\Gamma$, then we can write

$$G_s^< = (G_s^a - G_s^r)f \tag{D.31}$$

$$G_s^> = -(G_s^a - G_s^r)(1-f). \tag{D.32}$$

Note that at equilibrium, the above equations are just the fundamental relations between Green's functions in which f is reduced to the Fermi distribution. Whereas in our nonequilibrium case, f can be interpreted as the nonequilibrium distribution, fulfills the steady state rate equation

$$\begin{aligned} 0 &= \frac{df}{dt} \\ &= (1-f)\left[\Gamma_e n_F(\omega_-) + \Gamma_h n_F(\omega_+) + \Gamma_2\right] - f\left[\Gamma_e(1-n_F(\omega_-)) + \Gamma_h(1-n_F(\omega_+)) + \Gamma_1\right]. \end{aligned} \tag{D.33}$$

Use the relation $g_L^<(\omega) = 2\pi i\rho(\omega)n_F(\omega)$ and $g_L^>(\omega) = -2\pi i\rho(\omega)(1-n_F(\omega))$, put them together into the current formula, we obtain the current $I = I_R + I_A$, where

$$\begin{aligned} I_R(\omega) = \frac{2e}{h}\int d\omega \Bigg\{ &\frac{2\Gamma_1[\Gamma_e(\omega)n_F(\omega_-) - \Gamma_h(\omega)n_F(\omega_+)]}{(\omega-\epsilon_0)^2 + \Gamma(\omega)^2} \\ &- \frac{2\Gamma_2[\Gamma_e(\omega)(1-n_F(\omega_-)) - \Gamma_h(\omega)(1-n_F(\omega_+))]}{(\omega-\epsilon_0)^2 + \Gamma(\omega)^2}\Bigg\}, \end{aligned} \tag{D.34}$$

$$I_A(\omega) = \frac{2e}{h}\int d\omega \frac{4\Gamma_e(\omega)\Gamma_h(\omega)}{(\omega-\epsilon_0)^2 + \Gamma(\omega)^2}\left[n_F(\omega_-) - n_F(\omega_+)\right]. \tag{D.35}$$

The current I_A originates from resonant Andreev reflection, whereas I_R describes single-particle tunneling and subsequent relaxation of quasiparticles in the Shiba state. These two equations are given in the main text as Eqs. (8.1) and (8.2).

Quasiparticle relaxation mechanisms can occur due to phonon scattering. This was studied in Ref. [Kozo 08] and it was shown that the two relaxation processes are given by

$$\begin{aligned} \Gamma_1 &\sim \sqrt{\frac{T}{\Delta}}e^{-\Delta/T}\left[(\Delta-\epsilon_0)e^{\epsilon_0/T} + (\Delta+\epsilon_0)\right] \\ \Gamma_2 &\sim \sqrt{\frac{T}{\Delta}}e^{-\Delta/T}\left[(\Delta-\epsilon_0) + (\Delta+\epsilon_0)e^{-\epsilon_0/T}\right]. \end{aligned}$$

The relaxation rate Γ_1 for leaving the Shiba state has a thermal factor $\exp[(\Delta-\epsilon_0)/T]$ involving the required phonon energy of the transition to the continuum $\Delta-\epsilon_0$, whereas

Γ_2 is limited by the thermal occupation $\exp(\Delta/T)$ of the excited quasiparticles in the continuum. The ratio of the two rate yields the thermal occupation of the Shiba state

$$\Gamma_2/\Gamma_1 = e^{-\epsilon_0/T}. \tag{D.36}$$

D.2. Calculation of the Shiba peak heights

In the following we calculate the differential conductance at the Shiba resonances at $e|V| = \Delta \pm \epsilon_0$ from Eqs. (D.34) and (D.35). We first focus on the positive-bias main peak α_+ at $eV = \Delta + \epsilon_0$. In the limit of weak tunneling and relaxation $t^2\nu_0, \Gamma_{1/2} \ll \epsilon_0$ the integral over ω is dominated by a narrow interval around ϵ_0. For α_+ the only sizable contribution to the differential conductance comes from the terms containing $\Gamma_e(\omega) \propto \rho(\omega - eV)$ with a square-root singularity at $\omega = \epsilon_0$. Using $n_F(\omega_+) = 0$ and $n_F(\omega_-) = 1$ in this region we obtain

$$\alpha_+ \sim \frac{2e}{h}\frac{d}{dV}\left[\int d\omega \frac{4\Gamma_e(\omega)\Gamma_h(\omega) + 2\Gamma_1\Gamma_e(\omega)}{(\omega-\epsilon_0)^2 + \Gamma(\omega)^2}\right]_{eV=\Delta+\epsilon_0}. \tag{D.37}$$

To perform the derivative it is convenient to set $eV = \epsilon_0 + \Delta + \delta x$. We furthermore shift the domain of integration introducing a new variable $z = \epsilon_0 + \delta x - \omega$. The BCS density of states ρ can be approximated in the region of interest as

$$\begin{aligned}
&\rho(\omega - eV) \to \rho(-z-\Delta) \sim \nu_0\sqrt{\frac{\Delta}{2z}}\Theta(z),\\
&\rho(\omega + eV) \sim \rho(\Delta + 2\epsilon_0 + 2\delta x) = \nu_0\frac{\Delta + 2\epsilon_0}{2\sqrt{\epsilon_0(\Delta+\epsilon_0)}} + O(\delta x/\epsilon_0).
\end{aligned}$$

Upon replacing all rates by their definitions the integral reads

$$\alpha_+ \sim \frac{2e^2}{h}$$
$$\frac{d}{d\delta x}\left[\int_0^\infty dz \frac{(4\pi t^2 v^2 \rho(\Delta + 2\epsilon_0 + 2\delta x) + 2\Gamma_1)\pi t^2 u^2 \nu_0\sqrt{\Delta/2z}}{(\delta x - z)^2 + [\Gamma_1 + \Gamma_2 + \pi t^2 u^2 \nu_0\sqrt{\Delta/2z} + \pi t^2 v^2 \rho(\Delta + 2\epsilon_0 + 2\delta x)]^2}\right]_{\delta x = 0}. \tag{D.38}$$

The function $\rho(\Delta + 2\epsilon_0 + 2\delta x)$ depends only weakly on δx and to lowest order in z/ϵ_0 only the first term in the denominator $\sim (\delta x - z)^2$ contributes to the derivative with

respect to δx. Introducing $\Gamma_{h,\text{eff}} = \pi v^2 t^2 \rho(\Delta + 2\epsilon_0)$ we find

$$\alpha_+ \sim \frac{2e^2}{h} \int_0^\infty dz \frac{(4\Gamma_{h,\text{eff}} + 2\Gamma_1)\pi t^2 u^2 \nu_0 \sqrt{2z\Delta}}{\left[z^2 + \left(\Gamma_1 + \Gamma_2 + \pi t^2 u^2 \nu_0 \sqrt{\Delta/2z} + \Gamma_{h,\text{eff}}\right)^2\right]^2}. \tag{D.39}$$

The integrand has the form of a resonance as a function of z and exhibits a peak at $z_{\max}$. The integral can be solved in two limiting cases:

(a) For $\Gamma_1 + \Gamma_2 + \Gamma_{h,\text{eff}} \gg \pi t^2 u^2 \nu_0 \sqrt{\Delta/2z_{\max}}$ the second term in the denominator does not depend on z and we can use the relation

$$\int_0^\infty dz \frac{\sqrt{z}}{(z^2 + \Gamma^2)^2} = \frac{\pi}{(2\Gamma)^{5/2}}$$

to find

$$\alpha_+ \sim \frac{2e^2}{h} \frac{(4\Gamma_{h,\text{eff}} + 2\Gamma_1)\pi^2 t^2 u^2 \nu_0 \sqrt{2\Delta}}{[2(\Gamma_1 + \Gamma_2 + \Gamma_{h,\text{eff}})]^{5/2}}. \tag{D.40}$$

(b) For $\Gamma_1 + \Gamma_2 + \Gamma_{h,\text{eff}} \ll \pi t^2 u^2 \nu_0 \sqrt{\Delta/2z_{\max}}$ the relation

$$\int_0^\infty dz \frac{\sqrt{z}}{(z^2 + a^2/z)^2} = \frac{\pi}{9a^{5/3}}$$

yields

$$\alpha_+ \sim \frac{2e^2}{h} \frac{(4\Gamma_{h,\text{eff}} + 2\Gamma_1)\pi^2 t^2 u^2 \nu_0 \sqrt{2\Delta}}{9(\pi t^2 u^2 \nu_0 \sqrt{\Delta/2})^{5/3}}. \tag{D.41}$$

We combine these two results and obtain

$$\alpha_+ \sim \frac{2e^2}{h} \frac{4\pi(2\Gamma_{h,\text{eff}} + \Gamma_1)\Gamma_{e,\text{eff}}^{3/2}}{\Gamma_{\max}^{5/2}}, \tag{D.42}$$

where $\Gamma_{\max} = \max\{2(\Gamma_1 + \Gamma_2), 9^{2/5}\Gamma_{e,\text{eff}}, 2\Gamma_{h,\text{eff}}\}$ and we have introduced the effective tunneling rate $\Gamma_{e,\text{eff}} = (\pi t^2 u^2 \nu_0 \sqrt{\Delta/2})^{2/3}$. This expression where one of the three terms in $\Gamma_{\max}$ dominates. It gives rise to three regimes as a function of normal state conductance. In Fig. D.1 the asymptotic expression (D.42) is compared to numerical evaluation of Eqs. (D.34) and (D.35).

The integral expression for β_- differs from Eq. (D.37) by $\Gamma_1 \to \Gamma_2$ and $\Gamma_h \to 0$, which can be understood from the comparison of Figs. 8.1(b) and (c) of the main text. Applying

D Derivation of the Shiba peak height in the differential tunneling conductance for a superconducting tip

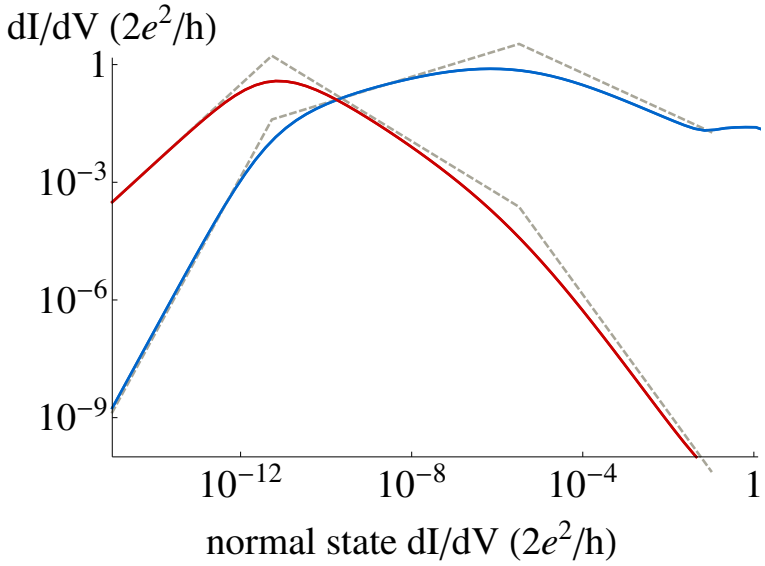

Figure D.1.: Relaxation (red) and Andreev current (blue) contribution to the differential conductance peak α_+ *vs* normal state conductance. The curves are obtained numerically from the derivatives of Eqs. (8.1) and (8.2). Both contributions have maxima at distinct values of normal state dI/dV. The maxima separate three regimes with dominating relaxation mechanisms Γ_1, $\Gamma_{e,\mathrm{eff}}$, and $\Gamma_{h,\mathrm{eff}}$ from low to high normal state conductances. The asymptotes in the three regimes (gray dashed lines) are given by Eq. (D.42). The system parameters are chosen such that all three regimes are visible. We have set $\Gamma_1 = 10^{-9}$, $\Gamma_2 = 0$, $u = 0.002$, $v = 0.7$, $\epsilon_0 = 0.3$, $\Delta = 1$, and $\nu_0 = 1$.

these substitutions to Eq. (D.42) yields

$$\beta_- \sim \frac{2e^2}{h} \frac{4\pi\Gamma_2\Gamma_{e,\mathrm{eff}}^{3/2}}{\widetilde{\Gamma}_{\mathrm{max}}^{5/2}}, \tag{D.43}$$

where $\widetilde{\Gamma}_{\mathrm{max}} = \max\{2(\Gamma_1+\Gamma_2), 9^{2/5}\Gamma_{e,\mathrm{eff}}\}$. The peaks α_- and β_+ can be obtained from α_+ and β_- by exchanging u and v. In the weak tunneling limit, where $\Gamma_{\mathrm{max}} = \widetilde{\Gamma}_{\mathrm{max}} = \Gamma_1 + \Gamma_2$ we find

$$\alpha_+^{(i)} \sim \frac{2e^2}{h} \frac{\pi^2 u^2 t^2 \nu_0 \sqrt{\Delta}\Gamma_1}{2(\Gamma_1+\Gamma_2)^{5/2}}, \tag{D.44}$$

$$\beta_-^{(i)} \sim \frac{2e^2}{h} \frac{\pi^2 u^2 t^2 \nu_0 \sqrt{\Delta}\Gamma_2}{2(\Gamma_1+\Gamma_2)^{5/2}}. \tag{D.45}$$

For stronger tunneling the broadening becomes dominated by tunneling to the BCS sin-

gularity of the tip $\Gamma_{\max} = \widetilde{\Gamma}_{\max} = 9^{2/5}\Gamma_{e,\text{eff}}$ and we find

$$\alpha_+^{(ii)} \sim \frac{2e^2}{h}\left[\frac{v^2}{u^{4/3}}\frac{4(2\pi)^{4/3}t^{2/3}\rho(\Delta+2\epsilon_0)}{9(\nu_0\sqrt{\Delta})^{2/3}} + \frac{4(2\pi)^{1/3}\Gamma_1}{9(t^2u^2\nu_0\sqrt{\Delta})^{2/3}}\right], \tag{D.46}$$

$$\beta_-^{(ii)} \sim \frac{2e^2}{h}\frac{4\pi\Gamma_2}{9(\pi t^2u^2\nu_0\sqrt{\Delta/2})^{2/3}}. \tag{D.47}$$

These four equations are given with out numerical prefactors as Eqs. (8.3-8.6) in the main text. A third regime could exists for even higher normal state conductances where $\Gamma_{h,\text{eff}}$ dominates Γ. This requires a very large asymmetry of u and v, i.e. $u \ll v$ for α_+. There is no signature of this regime in the experimental data shown in Fig. 8.3 of the main text as all peak heights should decrease in this regime (see Fig. D.1).

Bibliography

[Abri 88] A. Abrikosov. *Fundamentals of the theory of metals*. North Holland, Amsterdam, (1988).

[Adag 14] I. Adagideli, M. Wimmer, and A. Teker, *"Effects of electron scattering on the topological properties of nanowires: Majorana fermions from disorder and superlattices"*, Phys. Rev. B **89**, 144506 (2014).

[Adag 99] I. Adagideli, P. M. Goldbart, A. Shnirman, and A. Yazdani, *"Low-Energy Quasiparticle States near Extended Scatterers in d-Wave Superconductors and Their Connection with SUSY Quantum Mechanics"*, Phys. Rev. Lett. **83**, 5571 (1999).

[Akhm 09] A. R. Akhmerov, J. Nilsson, and C. W. J. Beenakker, *"Electrically Detected Interferometry of Majorana Fermions in a Topological Insulator"*, Phys. Rev. Lett. **102**, 216404 (2009).

[Akhm 11] A. R. Akhmerov, J. P. Dahlhaus, F. Hassler, M. Wimmer, and C. W. J. Beenakker, *"Quantized Conductance at the Majorana Phase Transition in a Disordered Superconducting Wire"*, Phys. Rev. Lett. **106**, 057001 (2011).

[Alic 10] J. Alicea, *"Majorana fermions in a tunable semiconductor device"*, Phys. Rev. B **81**, 125318 (2010).

[Alic 11] J. Alicea, Y. Oreg, G. Refael, F. von Oppen, and M. P. A. Fisher, *"Non-Abelian statistics and topological quantum information processing in 1D wire networks"*, Nat. Phys. **7**, 412 (2011).

[Alic 12] J. Alicea, *"New directions in the pursuit of Majorana fermions in solid state systems"*, Reports on Progress in Physics **75**, 076501 (2012).

[Altl 97] A. Altland and M. R. Zirnbauer, *"Nonstandard symmetry classes in mesoscopic normal-superconducting hybrid structures"*, Phys. Rev. B **55**, 1142 (1997).

[Ande 59] P. W. Anderson and H. Suhl, *"Spin Alignment in the Superconducting State"*, Phys. Rev. **116**, 898 (1959).

[Avig 08] F. T. Avignone, S. R. Elliott, and J. Engel, *"Double beta decay, Majorana neutrinos, and neutrino mass"*, Rev. Mod. Phys. **80**, 481 (2008).

[Badi 11] D. M. Badiane, M. Houzet, and J. S. Meyer, *"Nonequilibrium Josephson Effect through Helical Edge States"*, Phys. Rev. Lett. **107**, 177002 (2011).

[Bagr 12] D. Bagrets and A. Altland, *"Class D Spectral Peak in Majorana Quantum Wires"*, Phys. Rev. Lett. **109**, 227005 (2012).

[Bala 06] A. V. Balatsky, I. Vekhter, and J.-X. Zhu, *"Impurity-induced states in conventional and unconventional superconductors"*, Rev. Mod. Phys. **78**, 373 (2006).

[Bard 07] J. H. Bardarson, J. Tworzydło, P. W. Brouwer, and C. W. J. Beenakker, *"One-Parameter Scaling at the Dirac Point in Graphene"*, Phys. Rev. Lett. **99**, 106801 (2007).

[Baue 13] J. Bauer, J. I. Pascual, and K. J. Franke, *"Microscopic resolution of the interplay of Kondo screening and superconducting pairing: Mn-phthalocyanine molecules adsorbed on superconducting Pb(111)"*, Phys. Rev. B **87**, 075125 (2013).

[Baur 81] W. Bauriedl, P. Ziemann, and W. Buckel, *"Electron-Tunneling Observation of Impurity Bands in Superconducting Manganese-Implanted Lead"*, Phys. Rev. Lett. **47**, 1163 (1981).

[Been 05] C. W. J. Beenakker, *"Andreev billiards"*, Lect. Notes Phys. **667**, 131 (2005).

[Been 13] C. Beenakker, *"Search for Majorana Fermions in Superconductors"*, Annual Review of Condensed Matter Physics **4**, 113 (2013).

[Been 14] C. W. J. Beenakker, *"Annihilation of Colliding Bogoliubov Quasiparticles Reveals their Majorana Nature"*, Phys. Rev. Lett. **112**, 070604 (2014).

[Been 92] C. W. J. Beenakker, *"Quantum transport in semiconductor-superconductor microjunctions"*, Phys. Rev. B **46**, 12841 (1992).

[Benj 10] C. Benjamin and J. K. Pachos, *"Detecting Majorana bound states"*, Phys. Rev. B **81**, 085101 (2010).

[Blon 82] G. E. Blonder, M. Tinkham, and T. M. Klapwijk, *"Transition from metallic to tunneling regimes in superconducting microconstrictions: Excess current, charge imbalance, and supercurrent conversion"*, Phys. Rev. B **25**, 4515 (1982).

[Bole 07] C. J. Bolech and E. Demler, *"Observing Majorana bound States in p-Wave Superconductors Using Noise Measurements in Tunneling Experiments"*, Phys. Rev. Lett. **98**, 237002 (2007).

[Brau 09] B. Braunecker, P. Simon, and D. Loss, *"Nuclear Magnetism and Electronic Order in ^{13}C Nanotubes"*, Phys. Rev. Lett. **102**, 116403 (2009).

[Brau 13] B. Braunecker and P. Simon, *"Interplay between Classical Magnetic Moments and Superconductivity in Quantum One-Dimensional Conductors: Toward a Self-Sustained Topological Majorana Phase"*, Phys. Rev. Lett. **111**, 147202 (2013).

[Bret 13] L. Bretheau, C. O. Girit, C. Urbina, D. Esteve, and H. Pothier, *"Supercurrent Spectroscopy of Andreev States"*, Phys. Rev. X **3**, 041034 (2013).

[Brou 03] P. W. Brouwer, A. Furusaki, and C. Mudry, *"Universality of delocalization in unconventional dirty superconducting wires with broken spin-rotation symmetry"*, Phys. Rev. B **67**, 014530 (2003).

[Brou 11a] P. W. Brouwer, M. Duckheim, A. Romito, and F. von Oppen, *"Probability Distribution of Majorana End-State Energies in Disordered Wires"*, Phys. Rev. Lett. **107**, 196804 (2011).

[Brou 11b] P. W. Brouwer, M. Duckheim, A. Romito, and F. von Oppen, *"Topological superconducting phases in disordered quantum wires with strong spin-orbit coupling"*, Phys. Rev. B **84**, 144526 (2011).

[Butt 86] M. Büttiker and T. M. Klapwijk, *"Flux sensitivity of a piecewise normal and superconducting metal loop"*, Phys. Rev. B **33**, 5114 (1986).

[Caro 64] C. Caroli, P. D. Gennes, and J. Matricon, *"Bound Fermion states on a vortex line in a type II superconductor"*, Physics Letters **9**, 307 (1964).

[Cham 10] C. Chamon, R. Jackiw, Y. Nishida, S.-Y. Pi, and L. Santos, *"Quantizing Majorana fermions in a superconductor"*, Phys. Rev. B **81**, 224515 (2010).

[Chan 13] W. Chang, V. E. Manucharyan, T. S. Jespersen, J. Nygård, and C. M. Marcus, *"Tunneling Spectroscopy of Quasiparticle Bound States in a Spinful Josephson Junction"*, Phys. Rev. Lett. **110**, 217005 (2013).

[Chen 11] M. Cheng, V. Galitski, and S. Das Sarma, *"Nonadiabatic effects in the braiding of non-Abelian anyons in topological superconductors"*, Phys. Rev. B **84**, 104529 (2011).

[Chen 12] M. Cheng, *"Superconducting proximity effect on the edge of fractional topological insulators"*, Phys. Rev. B **86**, 195126 (2012).

[Cho 13] S. Cho, B. Dellabetta, A. Yang, J. Schneeloch, Z. Xu, T. Valla, G. Gu, M. J. Gilbert, and N. Mason, *"Symmetry protected Josephson supercurrents in three-dimensional topological insulators"*, Nat. Commun. **4**, 1689 (2013).

[Choy 11] T.-P. Choy, J. M. Edge, A. R. Akhmerov, and C. W. J. Beenakker, *"Majorana fermions emerging from magnetic nanoparticles on a superconductor without spin-orbit coupling"*, Phys. Rev. B **84**, 195442 (2011).

[Chun 11] S. B. Chung, H.-J. Zhang, X.-L. Qi, and S.-C. Zhang, *"Topological superconducting phase and Majorana fermions in half-metal/superconductor heterostructures"*, Phys. Rev. B **84**, 060510 (2011).

[Chur 13] H. O. H. Churchill, V. Fatemi, K. Grove-Rasmussen, M. T. Deng, P. Caroff, H. Q. Xu, and C. M. Marcus, *"Superconductor-nanowire devices from tunneling to the multichannel regime: Zero-bias oscillations and magnetoconductance crossover"*, Phys. Rev. B **87**, 241401 (2013).

[Clar 13] D. J. Clarke, J. Alicea, and K. Shtengel, *"Exotic non-Abelian anyons from conventional fractional quantum Hall states"*, Nat. Commun. **4**, 1348 (2013).

[Cook 11] A. Cook and M. Franz, *"Majorana fermions in a topological-insulator nanowire proximity-coupled to an s-wave superconductor"*, Phys. Rev. B **84**, 201105 (2011).

[Cuev 96] J. C. Cuevas, A. Martín-Rodero, and A. L. Yeyati, *"Hamiltonian approach to the transport properties of superconducting quantum point contacts"*, Phys. Rev. B **54**, 7366 (1996).

[Dam 06] J. A. van Dam, Y. V. Nazarov, E. P. A. M. Bakkers, S. De Franceschi, and L. P. Kouwenhoven, *"Supercurrent reversal in quantum dots"*, Nature **442**, 667 (2006).

[Das 12] A. Das, Y. Ronen, Y. Most, Y. Oreg, M. Heiblum, and H. Shtrikman, *"Zero-bias peaks and splitting in an Al-InAs nanowire topological superconductor as a signature of Majorana fermions"*, Nat. Phys. **8**, 887 (2012).

[Deac 10] R. S. Deacon, Y. Tanaka, A. Oiwa, R. Sakano, K. Yoshida, K. Shibata, K. Hirakawa, and S. Tarucha, *"Tunneling Spectroscopy of Andreev Energy Levels in a Quantum Dot Coupled to a Superconductor"*, Phys. Rev. Lett. **104**, 076805 (2010).

[DeGo 11] W. DeGottardi, D. Sen, and S. Vishveshwara, *"Topological phases, Majorana modes and quench dynamics in a spin ladder system"*, New J. Phys. **13**, 065028 (2011).

[Deng 12a] M. T. Deng, C. L. Yu, G. Y. Huang, M. Larsson, P. Caroff, and H. Q. Xu, *"Anomalous Zero-Bias Conductance Peak in a Nb–InSb Nanowire–Nb Hybrid Device"*, Nano Letters **12**, 6414 (2012).

[Deng 12b] S. Deng, L. Viola, and G. Ortiz, *"Majorana Modes in Time-Reversal Invariant s-Wave Topological Superconductors"*, Phys. Rev. Lett. **108**, 036803 (2012).

[Doh 05] Y.-J. Doh, J. A. van Dam, A. L. Roest, E. P. A. M. Bakkers, L. P. Kouwenhoven, and S. De Franceschi, *"Tunable Supercurrent Through Semiconductor Nanowires"*, Science **309**, 272 (2005).

[Domi 12] F. Domínguez, F. Hassler, and G. Platero, *"Dynamical detection of Majorana fermions in current-biased nanowires"*, Phys. Rev. B **86**, 140503 (2012).

[Duck 11] M. Duckheim and P. W. Brouwer, *"Andreev reflection from noncentrosymmetric superconductors and Majorana bound-state generation in half-metallic ferromagnets"*, Phys. Rev. B **83**, 054513 (2011).

[Elli 14] S. R. Elliott and M. Franz, *"Colloquium: Majorana Fermions in nuclear, particle and solid-state physics"*, arXiv:1403.4976 (2014).

[Elli 61] R. J. Elliott, *"Phenomenological Discussion of Magnetic Ordering in the Heavy Rare-Earth Metals"*, Phys. Rev. **124**, 346 (1961).

[Faga 05] G. Fagas, G. Tkachov, A. Pfund, and K. Richter, *"Geometrical enhancement of the proximity effect in quantum wires with extended superconducting tunnel contacts"*, Phys. Rev. B **71**, 224510 (2005).

[Fast 07] C. Fasth, A. Fuhrer, L. Samuelson, V. N. Golovach, and D. Loss, *"Direct Measurement of the Spin-Orbit Interaction in a Two-Electron InAs Nanowire Quantum Dot"*, Phys. Rev. Lett. **98**, 266801 (2007).

[Fert 80] A. Fert and P. M. Levy, *"Role of Anisotropic Exchange Interactions in Determining the Properties of Spin-Glasses"*, Phys. Rev. Lett. **44**, 1538 (1980).

[Fidk 10] L. Fidkowski and A. Kitaev, *"Effects of interactions on the topological classification of free fermion systems"*, Phys. Rev. B **81**, 134509 (2010).

[Fidk 11] L. Fidkowski and A. Kitaev, *"Topological phases of fermions in one dimension"*, Phys. Rev. B **83**, 075103 (2011).

[Finc 13] A. D. K. Finck, D. J. Van Harlingen, P. K. Mohseni, K. Jung, and X. Li, *"Anomalous Modulation of a Zero-Bias Peak in a Hybrid Nanowire-Superconductor Device"*, Phys. Rev. Lett. **110**, 126406 (2013).

[Flen 10] K. Flensberg, *"Tunneling characteristics of a chain of Majorana bound states"*, Phys. Rev. B **82**, 180516 (2010).

[Flen 11] K. Flensberg, *"Non-Abelian Operations on Majorana Fermions via Single-Charge Control"*, Phys. Rev. Lett. **106**, 090503 (2011).

[Forn 13] A. Fornieri, M. Amado, F. Carillo, F. Dolcini, G. Biasiol, L. Sorba, V. Pellegrini, and F. Giazotto, *"A ballistic quantum ring Josephson interferometer"*, Nanotechnology **24**, 245201 (2013).

[Fran 10a] S. D. Franceschi, L. Kouwenhoven, C. Schönenberger, and W. Wernsdorfer, *"Hybrid superconductor-quantum dot devices"*, Nat. Nano. **5**, 703 (2010).

[Fran 10b] M. Franz, *"Race for Majorana fermions"*, Physics **3**, 24 (2010).

[Fran 11] K. J. Franke, G. Schulze, and J. I. Pascual, *"Competition of Superconducting Phenomena and Kondo Screening at the Nanoscale"*, Science **332**, 940 (2011).

[Fran 13] M. Franz, *"Majorana's Wires"*, Nat. Nano. **8**, 149 (2013).

[Fu 06] L. Fu and C. L. Kane, *"Time reversal polarization and a Z_2 adiabatic spin pump"*, Phys. Rev. B **74**, 195312 (2006).

[Fu 08] L. Fu and C. L. Kane, *"Superconducting Proximity Effect and Majorana Fermions at the Surface of a Topological Insulator"*, Phys. Rev. Lett. **100**, 096407 (2008).

[Fu 09a] L. Fu and C. L. Kane, *"Josephson current and noise at a superconductor/-quantum-spin-Hall-insulator/superconductor junction"*, Phys. Rev. B **79**, 161408 (2009).

[Fu 09b] L. Fu and C. L. Kane, *"Probing Neutral Majorana Fermion Edge Modes with Charge Transport"*, Phys. Rev. Lett. **102**, 216403 (2009).

[Fu 10a] L. Fu, *"Electron Teleportation via Majorana Bound States in a Mesoscopic Superconductor"*, Phys. Rev. Lett. **104**, 056402 (2010).

[Fu 10b] L. Fu and E. Berg, *"Odd-Parity Topological Superconductors: Theory and Application to $Cu_xBi_2Se_3$"*, Physical Review Letters **105**, 097001 (2010).

[Fu 11] L. Fu, *"Topological Crystalline Insulators"*, Phys. Rev. Lett. **106**, 106802 (2011).

[Fulg 11] I. C. Fulga, F. Hassler, A. R. Akhmerov, and C. W. J. Beenakker, *"Scattering formula for the topological quantum number of a disordered multimode wire"*, Phys. Rev. B **83**, 155429 (2011).

[Fulg 12] I. C. Fulga, F. Hassler, and A. R. Akhmerov, *"Scattering theory of topological insulators and superconductors"*, Phys. Rev. B **85**, 165409 (2012).

[Gaid 14] E. Gaidamauskas, J. Paaske, and K. Flensberg, *"Majorana Bound States in Two-Channel Time-Reversal-Symmetric Nanowire Systems"*, Phys. Rev. Lett. **112**, 126402 (2014).

[Gali 02] V. M. Galitski and A. I. Larkin, *"Spin glass versus superconductivity"*, Phys. Rev. B **66**, 064526 (2002).

[Gamb 03] P. Gambardella, S. Rusponi, M. Veronese, S. S. Dhesi, C. Grazioli, A. Dallmeyer, I. Cabria, R. Zeller, P. H. Dederichs, K. Kern, C. Carbone, and H. Brune, *"Giant Magnetic Anisotropy of Single Cobalt Atoms and Nanoparticles"*, Science **300**, 1130 (2003).

[Genn 99] P. D. de Gennes. *Superconductivity of Metal and Alloys*. Westview Press, (1999).

[Grad 11] M. Gradhand, D. V. Fedorov, F. Pientka, P. Zahn, I. Mertig, and B. L. Györffy, *"Calculating the Berry curvature of Bloch electrons using the KKR method"*, Phys. Rev. B **84**, 075113 (2011).

[Grad 12] M. Gradhand, D. V. Fedorov, F. Pientka, P. Zahn, I. Mertig, and B. L. Györffy, *"First-principle calculations of the Berry curvature of Bloch states for charge and spin transport of electrons"*, J. Phys.: Condens. Matter **24**, 213202 (2012).

[Gura 11] V. Gurarie, *"Single-particle Green's functions and interacting topological insulators"*, Phys. Rev. B **83**, 085426 (2011).

[Haim 14] A. Haim, A. Keselman, E. Berg, and Y. Oreg, *"Time-reversal-invariant topological superconductivity induced by repulsive interactions in quantum wires"*, Phys. Rev. B **89**, 220504 (2014).

[Halp 12] B. I. Halperin, Y. Oreg, A. Stern, G. Refael, J. Alicea, and F. von Oppen, *"Adiabatic manipulations of Majorana fermions in a three-dimensional network of quantum wires"*, Phys. Rev. B **85**, 144501 (2012).

[Hart 13] S. Hart, H. Ren, T. Wagner, P. Leubner, M. Mühlbauer, C. Brüne, H. Buhmann, L. W. Molenkamp, and A. Yacoby, *"Induced Superconductivity in the Quantum Spin Hall Edge"*, arXiv:1312.2559 (2013).

[Hasa 10] M. Z. Hasan and C. L. Kane, *"Colloquium : Topological insulators"*, Rev. Mod. Phys. **82**, 3045 (2010).

[Hass 10] F. Hassler, A. R. Akhmerov, C.-Y. Hou, and C. W. J. Beenakker, *"Anyonic interferometry without anyons: how a flux qubit can read out a topological qubit"*, New J. Phys. **12**, 125002 (2010).

[Haug 08] H. Haug and A.-P. Jauho. *Quantum Kinetics in Transport and Optics of Semiconductors*. Springer, (2008).

[Heck 11] B. van Heck, F. Hassler, A. R. Akhmerov, and C. W. J. Beenakker, *"Coulomb stability of the 4π-periodic Josephson effect of Majorana fermions"*, Phys. Rev. B **84**, 180502 (2011).

[Heck 12] B. van Heck, A. R. Akhmerov, F. Hassler, M. Burrello, and C. W. J. Beenakker, *"Coulomb-assisted braiding of Majorana fermions in a Josephson junction array"*, New J. Phys. **14**, 035019 (2012).

[Hein 13] B. W. Heinrich, L. Braun, J. I. Pascual, and K. J. Franke, *"Protection of excited spin states by a superconducting energy gap"*, Nat. Phys. **9**, 765 (2013).

[Houz 13] M. Houzet, J. S. Meyer, D. M. Badiane, and L. I. Glazman, *"Dynamics of Majorana States in a Topological Josephson Junction"*, Phys. Rev. Lett. **111**, 046401 (2013).

[Huds 01] E. W. Hudson, K. M. Lang, V. Madhavan, S. H. Pan, H. Eisaki, S. Uchida, and J. C. Davis, *"Interplay of magnetism and high-Tc superconductivity at individual Ni impurity atoms in $Bi_2Sr_2CaCu_2O_{8+\delta}$"*, Nature **411**, 920 (2001).

[Hugh 11] T. L. Hughes, *"Majorana fermions inch closer to reality"*, Physics **4**, 67 (2011).

[Imam 04] H. Imamura, P. Bruno, and Y. Utsumi, *"Twisted exchange interaction between localized spins embedded in a one- or two-dimensional electron gas with Rashba spin-orbit coupling"*, Phys. Rev. B **69**, 121303 (2004).

[Ivan 01] D. A. Ivanov, *"Non-Abelian Statistics of Half-Quantum Vortices in p-Wave Superconductors"*, Phys. Rev. Lett. **86**, 268 (2001).

[Jack 81] R. Jackiw and P. Rossi, *"Zero modes of the vortex-fermion system"*, Nuclear Physics B **190**, 681 (1981).

[Ji 08] S.-H. Ji, T. Zhang, Y.-S. Fu, X. Chen, X.-C. Ma, J. Li, W.-H. Duan, J.-F. Jia, and Q.-K. Xue, *"High-Resolution Scanning Tunneling Spectroscopy of Magnetic Impurity Induced Bound States in the Superconducting Gap of Pb Thin Films"*, Phys. Rev. Lett. **100**, 226801 (2008).

[Jian 11a] L. Jiang, T. Kitagawa, J. Alicea, A. R. Akhmerov, D. Pekker, G. Refael, J. I. Cirac, E. Demler, M. D. Lukin, and P. Zoller, *"Majorana Fermions in Equilibrium and in Driven Cold-Atom Quantum Wires"*, Phys. Rev. Lett. **106**, 220402 (2011).

[Jian 11b] L. Jiang, D. Pekker, J. Alicea, G. Refael, Y. Oreg, and F. von Oppen, *"Unconventional Josephson Signatures of Majorana Bound States"*, Phys. Rev. Lett. **107**, 236401 (2011).

[Jian 13] L. Jiang, D. Pekker, J. Alicea, G. Refael, Y. Oreg, A. Brataas, and F. von Oppen, *"Magneto-Josephson effects in junctions with Majorana bound states"*, Phys. Rev. B **87**, 075438 (2013).

[Kall 12] C. Kallin, *"Chiral p-wave order in Sr_2RuO_4"*, Reports on Progress in Physics **75**, 042501 (2012).

[Karz 13] T. Karzig, G. Refael, and F. von Oppen, *"Boosting Majorana Zero Modes"*, Phys. Rev. X **3**, 041017 (2013).

[Kast 91] A. Kastalsky, A. W. Kleinsasser, L. H. Greene, R. Bhat, F. P. Milliken, and J. P. Harbison, *"Observation of pair currents in superconductor-semiconductor contacts"*, Phys. Rev. Lett. **67**, 3026 (1991).

[Kell 12a] G. Kells, D. Meidan, and P. W. Brouwer, *"Low-energy subgap states in multichannel p-wave superconducting wires"*, Phys. Rev. B **85**, 060507 (2012).

[Kell 12b] G. Kells, D. Meidan, and P. W. Brouwer, *"Near-zero-energy end states in topologically trivial spin-orbit coupled superconducting nanowires with a smooth confinement"*, Phys. Rev. B **86**, 100503 (2012).

[Kese 13] A. Keselman, L. Fu, A. Stern, and E. Berg, *"Inducing Time-Reversal-Invariant Topological Superconductivity and Fermion Parity Pumping in Quantum Wires"*, Phys. Rev. Lett. **111**, 116402 (2013).

[Kim 14] Y. Kim, M. Cheng, B. Bauer, R. M. Lutchyn, and S. Das Sarma, *"Helical order in one-dimensional magnetic atom chains and possible emergence of Majorana bound states"*, Phys. Rev. B **90**, 060401 (2014).

[Kita 01] A. Y. Kitaev, *"Unpaired Majorana fermions in quantum wires"*, Phys. Usp. **44**, 131 (2001).

[Kita 09] A. Y. Kitaev, *"Periodic table for topological insulators and superconductors"*, AIP Conf. Proc. **1134**, 22 (2009).

[Kitt 68] C. Kittel, in *Solid State Physics*, edited by F. Seitz, D. Turnbull, and H. Ehrenreich, Academic, New York, 1968.

[Kjae 12] M. Kjaergaard, K. Wölms, and K. Flensberg, *"Majorana fermions in superconducting nanowires without spin-orbit coupling"*, Phys. Rev. B **85**, 020503 (2012).

[Klin 13] J. Klinovaja, P. Stano, A. Yazdani, and D. Loss, *"Topological Superconductivity and Majorana Fermions in RKKY Systems"*, Phys. Rev. Lett. **111**, 186805 (2013).

[Kosh 07] N. C. Koshnick, H. Bluhm, M. E. Huber, and K. A. Moler, *"Fluctuation Superconductivity in Mesoscopic Aluminum Rings"*, Science **318**, 1440 (2007).

[Kote 13] P. Kotetes, G. Schön, and A. Shnirman, *"Engineering and manipulating topological qubits in 1D quantum wires"*, Journal of the Korean Physical Society **62**, 1558 (2013).

[Kozo 08] A. G. Kozorezov, A. A. Golubov, J. K. Wigmore, D. Martin, P. Verhoeve, R. A. Hijmering, and I. Jerjen, *"Inelastic scattering of quasiparticles in a superconductor with magnetic impurities"*, Phys. Rev. B **78**, 174501 (2008).

[Kurt 13] C. Kurter, A. D. K. Finck, Y. S. Hor, and D. J. V. Harlingen, *"Evidence for an anomalous current-phase relation of a dc SQUID with tunable topological junctions"*, arXiv:1307.7764 (2013).

[Kwon 04] H.-J. Kwon, K. Sengupta, and V. Yakovenko, *"Fractional ac Josephson effect in p- and d-wave superconductors"*, EPJB **37**, 349 (2004).

[Laug 81] R. B. Laughlin, *"Quantized Hall conductivity in two dimensions"*, Phys. Rev. B **23**, 5632 (1981).

[Law 09] K. T. Law, P. A. Lee, and T. K. Ng, *"Majorana Fermion Induced Resonant Andreev Reflection"*, Phys. Rev. Lett. **103**, 237001 (2009).

[Lee 12] E. J. H. Lee, X. Jiang, R. Aguado, G. Katsaros, C. M. Lieber, and S. De Franceschi, *"Zero-Bias Anomaly in a Nanowire Quantum Dot Coupled to Superconductors"*, Phys. Rev. Lett. **109**, 186802 (2012).

[Lee 14] E. J. H. Lee, X. Jiang, M. Houzet, R. Aguado, C. M. Lieber, and S. De Franceschi, *"Spin-resolved Andreev levels and parity crossings in hybrid superconductor-semiconductor nanostructures"*, Nat. Nano. **9**, 79 (2014).

[Li 14] J. Li, T. B. Neupert, A. Bernevig, and A. Yazdani, *"Majorana zero modes on a necklace"*, arXiv:1404.4058 (2014).

[Lind 11] N. H. Lindner, G. Refael, and V. Galitski, *"Floquet topological insulator in semiconductor quantum wells"*, Nat. Phys. **7**, 490 (2011).

[Lind 12] N. H. Lindner, E. Berg, G. Refael, and A. Stern, *"Fractionalizing Majorana Fermions: Non-Abelian Statistics on the Edges of Abelian Quantum Hall States"*, Phys. Rev. X **2**, 041002 (2012).

[Loss 11] D. Loss, F. L. Pedrocchi, and A. J. Leggett, *"Absence of Spontaneous Magnetic Order of Lattice Spins Coupled to Itinerant Interacting Electrons in One and Two Dimensions"*, Phys. Rev. Lett. **107**, 107201 (2011).

[Lutc 10] R. M. Lutchyn, J. D. Sau, and S. Das Sarma, *"Majorana Fermions and a Topological Phase Transition in Semiconductor-Superconductor Heterostructures"*, Phys. Rev. Lett. **105**, 077001 (2010).

[Lutc 11] R. M. Lutchyn, T. D. Stanescu, and S. Das Sarma, *"Search for Majorana Fermions in Multiband Semiconducting Nanowires"*, Phys. Rev. Lett. **106**, 127001 (2011).

[Maie 12] L. Maier, J. B. Oostinga, D. Knott, C. Brüne, P. Virtanen, G. Tkachov, E. M. Hankiewicz, C. Gould, H. Buhmann, and L. W. Molenkamp, *"Induced Superconductivity in the Three-Dimensional Topological Insulator HgTe"*, Phys. Rev. Lett. **109**, 186806 (2012).

[Majo 37] E. Majorana, *"Teoria simmetrica dell'elettrone e del positrone"*, Nuovo Cimento **14**, 171 (1937).

[Manm 12] S. R. Manmana, A. M. Essin, R. M. Noack, and V. Gurarie, *"Topological invariants and interacting one-dimensional fermionic systems"*, Phys. Rev. B **86**, 205119 (2012).

[Mao 11] L. Mao, J. Shi, Q. Niu, and C. Zhang, *"Superconducting Phase with a Chiral f-Wave Pairing Symmetry and Majorana Fermions Induced in a Hole-Doped Semiconductor"*, Phys. Rev. Lett. **106**, 157003 (2011).

[Mart 12] I. Martin and A. F. Morpurgo, *"Majorana fermions in superconducting helical magnets"*, Phys. Rev. B **85**, 144505 (2012).

[Mart 13] I. Martin and D. Mozyrsky, *"Non-equilibrium theory of tunneling into localized state in superconductor"*, arXiv:1312.2602 (2013).

[McMi 68] W. L. McMillan, *"Tunneling Model of the Superconducting Proximity Effect"*, Phys. Rev. **175**, 537 (1968).

[Meng 12] Q. Meng, V. Shivamoggi, T. L. Hughes, M. J. Gilbert, and S. Vishveshwara, *"Fractional spin Josephson effect and electrically controlled magnetization in quantum spin Hall edges"*, Phys. Rev. B **86**, 165110 (2012).

[Menz 12] M. Menzel, Y. Mokrousov, R. Wieser, J. E. Bickel, E. Vedmedenko, S. Blügel, S. Heinze, K. von Bergmann, A. Kubetzka, and R. Wiesendanger, *"Information Transfer by Vector Spin Chirality in Finite Magnetic Chains"*, Phys. Rev. Lett. **108**, 197204 (2012).

[Merz 02] F. Merz and J. T. Chalker, *"Two-dimensional random-bond Ising model, free fermions, and the network model"*, Phys. Rev. B **65**, 054425 (2002).

[Moor 91] G. Moore and N. Read, *"Nonabelions in the fractional quantum hall effect"*, Nucl. Phys. B **360**, 362 (1991).

[Motr 01] O. Motrunich, K. Damle, and D. A. Huse, *"Griffiths effects and quantum critical points in dirty superconductors without spin-rotation invariance: One-dimensional examples"*, Phys. Rev. B **63**, 224204 (2001).

[Mour 12] V. Mourik, K. Zuo, S. M. Frolov, S. R. Plissard, E. P. A. M. Bakkers, and L. P. Kouwenhoven, *"Signatures of Majorana Fermions in Hybrid Superconductor-Semiconductor Nanowire Devices"*, Science **336**, 1003 (2012).

[Nadj 13] S. Nadj-Perge, I. K. Drozdov, B. A. Bernevig, and A. Yazdani, *"Proposal for realizing Majorana fermions in chains of magnetic atoms on a superconductor"*, Phys. Rev. B **88**, 020407 (2013).

[Nako 13a] S. Nakosai, J. C. Budich, Y. Tanaka, B. Trauzettel, and N. Nagaosa, *"Majorana Bound States and Nonlocal Spin Correlations in a Quantum Wire on an Unconventional Superconductor"*, Phys. Rev. Lett. **110**, 117002 (2013).

[Nako 13b] S. Nakosai, Y. Tanaka, and N. Nagaosa, *"Two-dimensional p-wave superconducting states with magnetic moments on a conventional s-wave superconductor"*, Phys. Rev. B **88**, 180503 (2013).

[Naya 08] C. Nayak, S. H. Simon, A. Stern, M. Freedman, and S. Das Sarma, *"Non-Abelian anyons and topological quantum computation"*, Rev. Mod. Phys. **80**, 1083 (2008).

[Naza 09] Y. V. Nazarov and Y. M. Blanter. *Quantum transport*. Cambridge University Press, (2009).

[Nest 13] R. Nestler. "Jagd auf exotische Majorana-Teilchen". Tagesspiegel, Apr 4 (2013).

[Neve 13] P. Neven, D. Bagrets, and A. Altland, *"Quasiclassical theory of disordered multi-channel Majorana quantum wires"*, New J. Phys. **15**, 055019 (2013).

[Nils 08] J. Nilsson, A. R. Akhmerov, and C. W. J. Beenakker, *"Splitting of a Cooper Pair by a Pair of Majorana Bound States"*, Phys. Rev. Lett. **101**, 120403 (2008).

[Nils 09] H. A. Nilsson, P. Caroff, C. Thelander, M. Larsson, J. B. Wagner, L.-E. Wernersson, L. Samuelson, and H. Q. Xu, *"Giant, Level-Dependent g Factors in InSb Nanowire Quantum Dots"*, Nano Letters **9**, 3151 (2009).

[Nils 12] H. A. Nilsson, P. Samuelsson, P. Caroff, and H. Q. Xu, *"Supercurrent and Multiple Andreev Reflections in an InSb Nanowire Josephson Junction"*, Nano Letters **12**, 228 (2012).

[Nish 11] T. Nishio, T. Kozakai, S. Amaha, M. Larsson, H. A. Nilsson, H. Q. Xu, G. Zhang, K. Tateno, H. Takayanagi, and K. Ishibashi, *"Supercurrent through InAs nanowires with highly transparent superconducting contacts"*, Nanotechnology **22**, 445701 (2011).

[Oost 13] J. B. Oostinga, L. Maier, P. Schüffelgen, D. Knott, C. Ames, C. Brüne, G. Tkachov, H. Buhmann, and L. W. Molenkamp, *"Josephson Supercurrent through the Topological Surface States of Strained Bulk HgTe"*, Phys. Rev. X **3**, 021007 (2013).

[Oppe 92] F. von Oppen and E. K. Riedel, *"Flux-periodic persistent current in mesoscopic superconducting rings close to T_c"*, Phys. Rev. B **46**, 3203 (1992).

[Oreg 10] Y. Oreg, G. Refael, and F. von Oppen, *"Helical Liquids and Majorana Bound States in Quantum Wires"*, Phys. Rev. Lett. **105**, 177002 (2010).

[Pan 00] S. H. Pan, E. W. Hudson, K. M. Lang, H. Eisaki, S. Uchida, and J. C. Davis, *"Imaging the effects of individual zinc impurity atoms on superconductivity in $Bi_2Sr_2CaCu_2O_{8+\delta}$"*, Nature **403**, 746 (2000).

[Perf 13] E. Perfetto, *"Dynamical Formation and Manipulation of Majorana Fermions in Driven Quantum Wires in Contact with a Superconductor"*, Phys. Rev. Lett. **110**, 087001 (2013).

[Pien 12a] F. Pientka, M. Gradhand, D. V. Fedorov, I. Mertig, and B. L. Györffy, *"Gauge freedom for degenerate Bloch states"*, Phys. Rev. B **86**, 054413 (2012).

[Pien 12b] F. Pientka, G. Kells, A. Romito, P. W. Brouwer, and F. von Oppen, *"Enhanced Zero-Bias Majorana Peak in the Differential Tunneling Conductance of Disordered Multisubband Quantum-Wire/Superconductor Junctions"*, Phys. Rev. Lett. **109**, 227006 (2012).

[Pien 13a] F. Pientka, L. I. Glazman, and F. von Oppen, *"Topological superconducting phase in helical Shiba chains"*, Phys. Rev. B **88**, 155420 (2013).

[Pien 13b] F. Pientka, L. Jiang, D. Pekker, J. Alicea, G. Refael, Y. Oreg, and F. von Oppen, *"Magneto-Josephson effects and Majorana bound states in quantum wires"*, New J. Phys. **15**, 115001 (2013).

[Pien 13c] F. Pientka, A. Romito, M. Duckheim, Y. Oreg, and F. von Oppen, *"Signatures of topological phase transitions in mesoscopic superconducting rings"*, New J. Phys. **15**, 025001 (2013).

[Pien 14] F. Pientka, L. I. Glazman, and F. von Oppen, *"Unconventional topological phase transitions in helical Shiba chains"*, Phys. Rev. B **89**, 180505(R) (2014).

[Piku 12] D. I. Pikulin, J. P. Dahlhaus, M. Wimmer, and C. W. J. Beenakker, *"Zero-voltage conductance peak from weak antilocalization in a Majorana nanowire"*, arXiv:1206.6687 (2012).

[Pill 10] J.-D. Pillet, C. H. L. Quay, P. Morfin, C. Bena, A. L. Yeyati, and P. Joyez, *"Andreev bound states in supercurrent-carrying carbon nanotubes revealed"*, Nat. Phys. **6**, 965 (2010).

[Pill 13] J.-D. Pillet, P. Joyez, R. Žitko, and M. F. Goffman, *"Tunneling spectroscopy of a single quantum dot coupled to a superconductor: From Kondo ridge to Andreev bound states"*, Phys. Rev. B **88**, 045101 (2013).

[Poly 12] A. D. Polyanin and A. V. Manzhirov. *Handbook of integral equations*. Chapman & Hall/CRC Press, (2012).

[Pott 10] A. C. Potter and P. A. Lee, *"Multichannel Generalization of Kitaev's Majorana End States and a Practical Route to Realize Them in Thin Films"*, Phys. Rev. Lett. **105**, 227003 (2010).

[Pott 11] A. C. Potter and P. A. Lee, *"Engineering a $p+ip$ superconductor: Comparison of topological insulator and Rashba spin-orbit-coupled materials"*, Phys. Rev. B **83**, 184520 (2011).

[Pott 12] A. C. Potter and P. A. Lee, *"Topological superconductivity and Majorana fermions in metallic surface states"*, Phys. Rev. B **85**, 094516 (2012).

[Prib 14] V. S. Pribiag, A. J. Beukman, F. Qu, M. C. Cassidy, C. Charpentier, W. Wegscheider, and L. P. Kouwenhoven, *"Edge-mode Superconductivity in a Two Dimensional Topological Insulator"*, arXiv:1408.1701 (2014).

[Qi 08] X.-L. Qi, T. L. Hughes, and S.-C. Zhang, *"Topological field theory of time-reversal invariant insulators"*, Phys. Rev. B **78**, 195424 (2008).

[Quir 02] D. Quirion, C. Hoffmann, F. Lefloch, and M. Sanquer, *"Mesoscopic proximity effect in double-barrier superconductor/normal-metal junctions"*, Phys. Rev. B **65**, 100508 (2002).

[Read 00] N. Read and D. Green, *"Paired states of fermions in two dimensions with breaking of parity and time-reversal symmetries and the fractional quantum Hall effect"*, Phys. Rev. B **61**, 10267 (2000).

[Ried 12] M.-T. Rieder, G. Kells, M. Duckheim, D. Meidan, and P. W. Brouwer, *"End-states in multichannel spinless p-wave superconducting wires"*, Phys. Rev. B **86**, 125423 (2012).

[Ried 13] M.-T. Rieder, P. W. Brouwer, and I. Adagideli, *"Reentrant topological phase transitions in a disordered spinless superconducting wire"*, Phys. Rev. B **88**, 060509 (2013).

[Rokh 12] L. P. Rokhinson, X. Liu, and J. K. Furdyna, *"The fractional a.c. Josephson effect in a semiconductor-superconductor nanowire as a signature of Majorana particles"*, Nat. Phys. **8**, 795 (2012).

[Romi 12] A. Romito, J. Alicea, G. Refael, and F. von Oppen, *"Manipulating Majorana fermions using supercurrents"*, Phys. Rev. B **85**, 020502 (2012).

[Ront 14] J. Röntynen and T. Ojanen, *"Tuning topological superconductivity in helical Shiba chains by supercurrent"*, arXiv:1406.4288 (2014).

[Ruby] M. Ruby, B. W. Heinrich, J. I. Pascual, and K. J. Franke. (in preparation).

[Rusi 69] A. Rusinov, *"On the Theory of Gapless Superconductivity in Alloys Containing Paramagnetic Impurities"*, JETP **29**, 1101 (1969).

[Ryu 10] S. Ryu, A. P. Schnyder, A. Furusaki, and A. W. W. Ludwig, *"Topological insulators and superconductors: tenfold way and dimensional hierarchy"*, New J. Phys. **12**, 065010 (2010).

[Sau 10] J. D. Sau, R. M. Lutchyn, S. Tewari, and S. Das Sarma, *"Generic New Platform for Topological Quantum Computation Using Semiconductor Heterostructures"*, Phys. Rev. Lett. **104**, 040502 (2010).

[Sau 11] J. D. Sau, D. J. Clarke, and S. Tewari, *"Controlling non-Abelian statistics of Majorana fermions in semiconductor nanowires"*, Phys. Rev. B **84**, 094505 (2011).

[Schn 08] A. P. Schnyder, S. Ryu, A. Furusaki, and A. W. W. Ludwig, *"Classification of topological insulators and superconductors in three spatial dimensions"*, Phys. Rev. B **78**, 195125 (2008).

[Schw 10] G. Schwiete and Y. Oreg, *"Fluctuation persistent current in small superconducting rings"*, Phys. Rev. B **82**, 214514 (2010).

[Serv 11] R. F. Service, *"Search for Majorana Fermions Nearing Success at Last?"*, Science **332**, 193 (2011).

[Shap 63] S. Shapiro, *"Josephson Currents in Superconducting Tunneling: The Effect of Microwaves and Other Observations"*, Phys. Rev. Lett. **11**, 80 (1963).

[Shib 68] H. Shiba, *"Classical Spins in Superconductors"*, Progress of Theoretical Physics **40**, 435 (1968).

[Simo 08] P. Simon, B. Braunecker, and D. Loss, *"Magnetic ordering of nuclear spins in an interacting two-dimensional electron gas"*, Phys. Rev. B **77**, 045108 (2008).

[Soch 13] I. Sochnikov, A. J. Bestwick, J. R. Williams, T. M. Lippman, I. R. Fisher, D. Goldhaber-Gordon, J. R. Kirtley, and K. A. Moler, *"Direct Measurement of Current-Phase Relations in Superconductor/Topological Insulator/Superconductor Junctions"*, Nano Letters **13**, 3086 (2013).

[Spei 12] C. Speicher. "Ganz wie sein Antiteilchen". Neue Zürcher Zeitung, Aug 8 (2012).

[Stan 12] T. D. Stanescu, S. Tewari, J. D. Sau, and S. Das Sarma, *"To Close or Not to Close: The Fate of the Superconducting Gap Across the Topological Quantum Phase Transition in Majorana-Carrying Semiconductor Nanowires"*, Phys. Rev. Lett. **109**, 266402 (2012).

[Ster 04] A. Stern, F. von Oppen, and E. Mariani, *"Geometric phases and quantum entanglement as building blocks for non-Abelian quasiparticle statistics"*, Phys. Rev. B **70**, 205338 (2004).

[Ster 10] A. Stern, *"Non-Abelian states of matter"*, Nature **464**, 187 (2010).

[Stru 11] G. Strübi, W. Belzig, M.-S. Choi, and C. Bruder, *"Interferometric and Noise Signatures of Majorana Fermion Edge States in Transport Experiments"*, Phys. Rev. Lett. **107**, 136403 (2011).

[Thou 83] D. J. Thouless, *"Quantization of particle transport"*, Physical Review B **27**, 6083 (1983).

[Tink 75] M. Tinkham. *Introduction to Superconductivity*. McGraw-Hill, (1975).

[Tsve 12] A. M. Tsvelik, *"Riding a wild horse: Majorana fermions interacting with solitons of fast bosonic fields"*, EPL (Europhysics Letters) **97**, 17011 (2012).

[Turn 11] A. M. Turner, F. Pollmann, and E. Berg, *"Topological phases of one-dimensional fermions: An entanglement point of view"*, Phys. Rev. B **83**, 075102 (2011).

[Vaez 13] A. Vaezi, *"Fractional topological superconductor with fractionalized Majorana fermions"*, Phys. Rev. B **87**, 035132 (2013).

[Vazi 13] M. M. Vazifeh and M. Franz, *"Self-Organized Topological State with Majorana Fermions"*, Phys. Rev. Lett. **111**, 206802 (2013).

[Veld 12] M. Veldhorst, M. Snelder, M. Hoek, T. Gang, V. K. Guduru, X. L. Wang, U. Zeitler, W. G. van der Wiel, A. A. Golubov, H. Hilgenkamp, and A. Brinkman, *"Josephson supercurrent through a topological insulator surface state"*, Nat. Mater. **11**, 417 (2012).

[Volo 03] G. E. Volovik. *The Universe in a Helium Droplet*. Clarendon Press, (2003).

[Volo 99] G. E. Volovik, *"Fermion zero modes on vortices in chiral superconductors"*, JETP Letters **70**, 609 (1999).

[Wilc 09] F. Wilczek, *"Majorana returns"*, Nat. Phys. **5**, 614 (2009).

[Will 12] J. R. Williams, A. J. Bestwick, P. Gallagher, S. S. Hong, Y. Cui, A. S. Bleich, J. G. Analytis, I. R. Fisher, and D. Goldhaber-Gordon, *"Unconventional Josephson Effect in Hybrid Superconductor-Topological Insulator Devices"*, Phys. Rev. Lett. **109**, 056803 (2012).

[Wimm 11] M. Wimmer, A. R. Akhmerov, J. P. Dahlhaus, and C. W. J. Beenakker, *"Quantum point contact as a probe of a topological superconductor"*, New J. Phys. **13**, 053016 (2011).

[Wolm 14] K. Wölms, A. Stern, and K. Flensberg, *"Local Adiabatic Mixing of Kramers Pairs of Majorana Bound States"*, arXiv:1405.5104 (2014).

[Wong 12] C. L. M. Wong and K. T. Law, *"Majorana Kramers doublets in $d_{x^2-y^2}$-wave superconductors with Rashba spin-orbit coupling"*, Phys. Rev. B **86**, 184516 (2012).

[Yao 13] N. Y. Yao, L. I. Glazman, E. A. Demler, M. D. Lukin, and J. D. Sau, *"Enhanced anti-ferromagnetic exchange between magnetic impurities in a superconducting host"*, arXiv:1309.2633 (2013).

[Yao 14] N. Y. Yao, C. P. Moca, I. Weymann, J. D. Sau, M. D. Lukin, E. A. Demler, and G. Zaránd, *"Phase diagram and excitations of a Shiba molecule"*, arXiv:1403.4611 (2014).

[Yazd 97] A. Yazdani, B. A. Jones, C. P. Lutz, M. F. Crommie, and D. M. Eigler, *"Probing the Local Effects of Magnetic Impurities on Superconductivity"*, Science **275**, 1767 (1997).

[Yazd 99] A. Yazdani, C. M. Howald, C. P. Lutz, A. Kapitulnik, and D. M. Eigler, *"Impurity-Induced Bound Excitations on the Surface of $Bi_2Sr_2CaCu_2O_8$"*, Phys. Rev. Lett. **83**, 176 (1999).

[Yosi 96] K. Yosida. *Theory of Magnetism*. Springer Berlin, (1996).

[Yu 65] L. Yu, *"Bound state in superconductors with paramagnetic impurities"*, Acta Phys. Sin. **21**, 75 (1965).

[Zhan 13] F. Zhang, C. L. Kane, and E. J. Mele, *"Time-Reversal-Invariant Topological Superconductivity and Majorana Kramers Pairs"*, Phys. Rev. Lett. **111**, 056402 (2013).

[Zoch 12] B. Zocher, M. Horsdal, and B. Rosenow, *"Proposed Detection of the Topological Phase in Ring-Shaped Semiconductor-Superconductor Nanowires Using Coulomb Blockade Transport"*, Phys. Rev. Lett. **109**, 227001 (2012).

Acknowledgments

This thesis would not have been possible without the help of many people.

First I would like to express my gratitude to my supervisor Felix von Oppen, who supported my work on this thesis in every possible way during the past three and a half years. I benefited much from his expertise and guidance and always found working with him rewarding. I am also grateful for the collaborations with many great scientist he initiated and the scientific events I have been able to attend. Finally I would like to thank Felix for his support and understanding in the time of my parental leave.

I am indebted to all my collaborators who contributed to my work on this topic in numerous elightening discussions: Jason Alicea, Piet Brouwer, Mathias Duckheim, Katharina Franke, Leonid Glazman, Benjamin Heinrich, Liang Jiang, Torsten Karzig, Graham Kells, Yuval Oreg, David Pekker, Yang Peng, Gil Refael, Alessandro Romito, and Michael Ruby.

I would like to thank Piet Brouwer for refereeing this thesis as well as Piet, Felix, and all members of the Dahlem Center for creating a dynamic research environment and a congenial atmosphere. In particular I thank Niels Bode, Alexandra Junck, Silvia Viola Kusminskiy, Dganit Meidan, Maresa Rieder, Martin Schneider, and Mark Thomas for the many enjoyable and inspiring discussions and the nice time. Furthermore I am indebted to Brigitte Odeh for her administrative support.

I would like to acknowledge financial support by the Studienstiftung des dt. Volkes, the Dahlem Research School and the German Research foundation (DFG) through SPP 1459.

Finally, I am indebted to my parents for supporting me throughout my life and I am deeply grateful to Grit and Milan for their love, understanding, and support which carried me through this work.

Publications

This thesis comprises the following publications:

- F. Pientka, G. Kells, A. Romito, P. W. Brouwer, and F. von Oppen
  Enhanced Zero-Bias Majorana Peak in the Differential Tunneling Conductance of Disordered Multisubband Quantum-Wire/Superconductor Junctions
  Phys. Rev. Lett. **109**, 227006 (2012), http://dx.doi.org/10.1103/PhysRevLett.109.227006
- F. Pientka, A. Romito, M. Duckheim, Y. Oreg, and F. von Oppen
  Signatures of topological phase transitions in mesoscopic superconducting rings
  New J. Phys. **15**, 025001 (2013), http://dx.doi.org/10.1088/1367-2630/15/2/025001
- F. Pientka, L. Jiang, D. Pekker, J. Alicea, G. Refael, Y. Oreg, and F. von Oppen
  Magneto-Josephson effects and Majorana bound states in quantum wires
  New J. Phys. **15**, 115001 (2013), http://dx.doi.org/10.1088/1367-2630/15/11/115001
- F. Pientka, L. I. Glazman, and F. von Oppen
  Topological superconducting phase in helical Shiba chains
  Phys. Rev. B **88**, 155420 (2013), http://dx.doi.org/10.1103/PhysRevB.88.155420
- F. Pientka, L. I. Glazman, and F. von Oppen
  Unconventional topological phase transitions in helical Shiba chains
  Phys. Rev. B **89**, 180505(R) (2014), http://dx.doi.org/10.1103/PhysRevB.89.180505

The following publications have been completed in parallel to this thesis:

- M. Gradhand, D. V. Fedorov, F. Pientka, P. Zahn, I. Mertig, and B. L. Györffy
  Calculating the Berry curvature of Bloch electrons using the KKR method
  Phys. Rev. B, **84**, 075113 (2011).
- M. Gradhand, D. V. Fedorov, F. Pientka, P. Zahn, I. Mertig, and B. L. Györffy
  First-principle calculations of the Berry curvature of Bloch states for charge and spin transport of electrons
  J. Phys.: Condens. Matter **24**, 213202 (2012).
- F. Pientka, M. Gradhand, D. V. Fedorov, I. Mertig, and B. L. Györffy
  Gauge freedom for degenerate Bloch states
  Phys. Rev. B **86**, 054413 (2012).